MOLECULAR SIMULATION STUDIES OF DIESEL AND DIESEL ADDITIVES

ERASTOVA, VALENTINA

MOLECULAR SIMULATION STUDIES OF DIESEL AND DIESEL ADDITIVES

VALENTINA ERASTOVA

2012

SUBMITTED IN CONFORMITY WITH THE REQUIREMENTS FOR THE DEGREE OF DOCTOR OF PHILOSOPHY

Abstract

As diesel fuel is cooled down, waxes are deposited, which are made up from crystals of long chain *n*-alkanes. Wax depositions are undesirable, since they can block anything from filters in diesel engines to pipelines. It is already known that wax formation can be inhibited by the addition of wax crystal modifiers to diesel fuel. This thesis employs computational models at atomistic and coarse-grained levels to investigate the crystallisation of diesel fuel and the effect of additives upon the crystallisation process.

In the first results section, a model for diesel fuel is introduced and a strategy for investigating its crystallisation is developed. Crystallisation was observed from pure *n*-tricosane, binary and tertiary mixtures of paraffins of similar chain lengths. These systems were found to crystallise into hexagonally arranged lamellae. The presence of different length alkanes was found to create *gauche* disorders, leading to the formation of lamellar layers with softer edges. It was also found that crystal growth could be simulated more efficiently in the presence of a positionally restrained crystal, acting as a nucleation centre.

Subsequently, crystallisation of paraffins, and the solvent effect upon it, was studied. This allowed to establish behavioural trends characteristic for aromatic and aliphatic solvents. Finally, paraffin crystallisation in the presence of four common additives was investigated. A common mode of action for these additives was identified, based upon partial co-crystallisation of additive alkyl chains and paraffin molecules.

The main drawback of atomistic simulation is the computational cost, which limits both the time and length scales accessible on modern computers. In order to overcome these inherent limitations, a coarse grained model was developed for a range of *n*-alkanes. Remarkably, the model shows transferability over 120 K, preserving thermodynamic and structural properties of both melt and crystal.

In summary, this thesis provides a detailed picture of diesel crystallisation at a molecular level, and provides new insights into the mechanism of action of a number of common diesel additives.

Declaration

The material contained within this thesis has not previously been submitted for a degree at the University of Durham or any other university. The research reported within this thesis has been conducted by the author in the research group of Prof. Mark Wilson.

Copyright

Acknowledgements

First of all, I would like to thank Professor Mark Wilson for following every step of this project with his advice and support, and for always being in a contagious good mood.

I am thankful to my labmates, especially Dr. Tom Rodgers for his willingness to share his knowledge, and Dr. Michael Peach for his indispensable assistance. I would also like to thank Tom Prasitnok, Dr. Fatima Chami, Dr. Martin Walker and Dave Burnell for creating a great atmosphere.

I am grateful to ORSAS for giving an opportunity for foreign students, such as myself, to study in the UK. I am glad I was given a chance to collaborate with Infineum, who sponsored this project and contributed with experimental data and constructive discussions.

I also want to thank my great friends and in particular Dr. Matteo Degiacomi for helping and encouraging me, and especially for sharing his extensive knowledge of code development.

I am grateful to my parents Marina and Andrei, my grandma Galya and my grandpa Volodya for allowing me to have access to great education and supporting me. I also want to thank my scotty Shnaps and boxer Chingiz for setting a great example of courage and willpower.

Contents

List of Figures

List of Tables

Background Part I

1 Introduction

1.1 Brief history

Different types of fuel have been used by mankind for many years. Undoubtedly, the most widely used are fossil fuels, minerals that comes from the ground. Fossil fuels are derived from remains of former life, forming combustible materials, such as coal, oil and gas. In 1830s Karl von Reichenbach discovered a substance while studying wood-coke. He named it *paraffin* from latin *parum* "not very, too little" and *affinis* "associated with", as it was very distinct from anything known at a time [1]. Paraffin oil was found to be able to produce more energy than coal gas and form solid state wax. These properties made it a valuable material for candle making.

It is disputable when and where people started using mineral oil, but at about the same time as the discovery of paraffin, modern-type oil wells were drilled around the world. Initially the fuel was used purely for illumination and gasoline was undesirable, due to its high flammability. Only a few years after this, the first internal spark-ignition engines were engineered by Nicolas Otto (1876) and Karl Benz (1885) and implemented to power motorcycles [2].

In 1893, invention of the compression-ignition engine by Rudolph Diesel, allowed the use of heavier and more stable fractions of crude oil. The engine itself was of a higher efficiency and so was used to power trains and ships. With time diesel has gained popularity and is now used not only to power heavy machinery, but also to generate electricity and as a fuel for domestic cars. As of 2011 the World is currently consuming

88 million barrels of crude oil a day, that is approximately equivalent to 2 liters of oil per person each day [3].

Currently a lot of effort is being put into the production of alternative fuels, synthetic and biodiesels, as well as improving fuel properties. There are a large number of additives used in a modern fuel to improve its efficiency, ease of handling and transportation.

1.2 The problem of wax formation

Formation of wax can cause significant problems during extraction, transportation, processing and use of fuel. Figure 1.1 demonstrates an example of blockage caused by wax aggregation in a pipeline [4]. To minimise such problems a range of additives have been developed. The additives aim at the improving the fuel's cold flow properties. An example demonstrating the performance of such additives is shown in Figure 1.2.

A lot of effort has been made to further improve and extend the properties of additives. However, this progress is hindered by a limited understanding of the mechanism of action of additives at an atomic level.

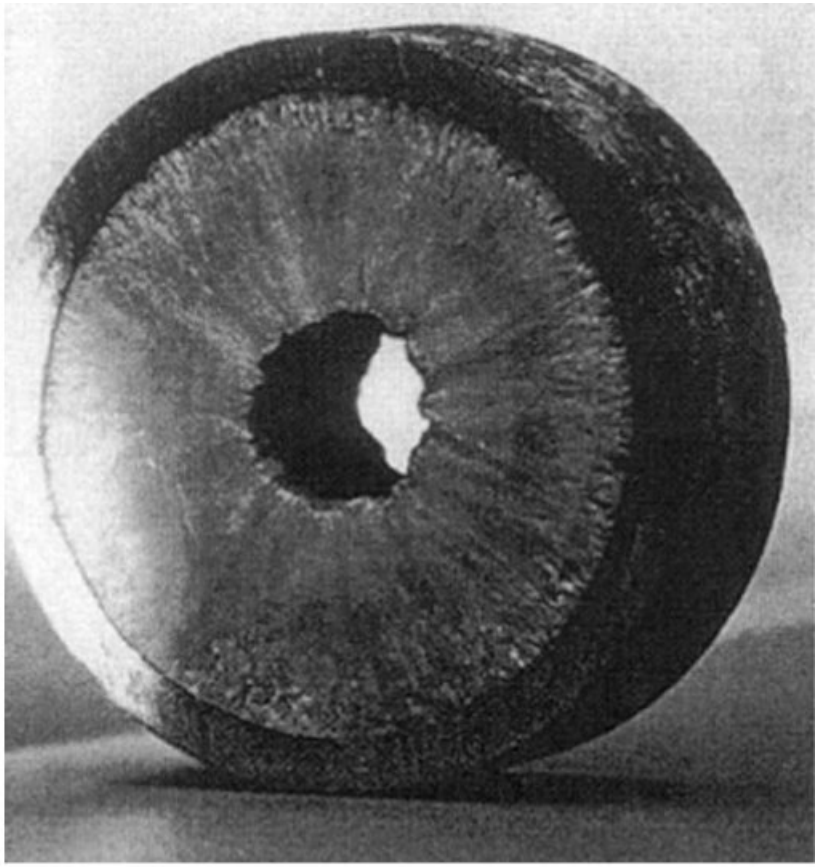

Figure 1.1: *Cross section of a pipeline blocked by wax [4].*

Figure 1.2: *The pouring properties of base fuel, without (right) and with (left) additive, cooled overnight to minus ten degrees Celsius, picture provided by Infineum.*

1.3 Aims and objectives

The work of this thesis is aimed at investigating the mechanism of action of common additives at atomic level. This is done by means of molecular dynamics simulations. Firstly, crystallisation of a model fuel in a variety of conditions is investigated at atomistic level. Subsequently, the effect of a range of common additives on its crystallisation is studied atomistically. Finally, for the purposes of studying larger molecular systems over longer timescales, we develop a coarse grained model for paraffins. Importantly, our model is capable of reproducing crystallisation in agreement with experimentally known temperatures, densities and structural features.

This thesis is structured as follows. In sections 1, 2 and 3, the experimental, computational and theoretical backgrounds of this work are described. In section 4 we create a fuel model and establish a cooling protocol leading to crystallisation. Additionally, paraffin mixtures and effects of solvents on crystallisation are studied. In section 5 we study paraffin crystallisation in the presence of four common additives. In sections 6 and 7 a coarse grained force field for modelling paraffin crystallisation is presented. Conclusions and further work are given in section 8.

2 Studies of paraffins

2.1 Diesel fuel

Diesel is extracted from crude oil. Crude oil is a mineral, formed under the ground at high temperatures and pressures from previously living fauna and flora. The main components of crude oil are hydrocarbons, but small amounts of oxygen, nitrogen, sulphur and traces of metals are also present. A large proportion of the the hydrocarbon component is composed of paraffins[1], as well as aromatic compounds, cycloalkanes, alkenes and alkynes. Crude oil is then separated by distillation into fractions, as given in the Table 2.1.

Table 2.1: *Products of distillations of crude oil*

Chain length	Distillate
C1-C2	Synthetic Natural Gas
C3-C4	Liquefied Petroleum Gas
	Naphtha:
C5-C7	Light
C8-C10	Heavy
	Middle distillate:
C11-C12	Kerosine
C13-C20	Diesel
C21-C30	Softwax
C31-C60+	Hardwax

Diesel fuel contains a range of *n*-alkanes. The distribution of the paraffins varies,

[1]Terms paraffins, linear alkanes and *n*-alkanes are interchangeably used in this thesis.

depending on the fuel. Figure 2.1 shows the typical example of the distribution in a base fuel [5].

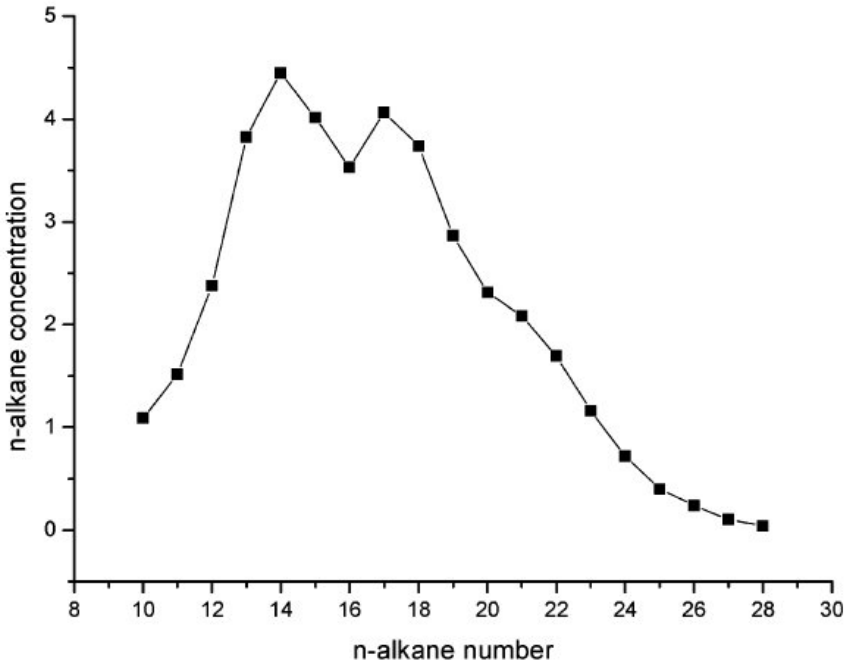

Figure 2.1: *n-Alkane distribution in base fuel [5]*

Under normal conditions *n*-alkanes of up to approximately 20 carbon-long chains are in liquid phase [2] [6] . As the temperature drops the formation of waxes occurs.

2.2 Paraffin wax crystals

The paraffin wax formed from fuels consists of a set of small crystals, locked together to form a solid domain [7]. Figure 2.2 shows an idealised representation of wax crystals at different levels of detail [4]. The crystal wax consists of plate like structures which stack together, Figure 2.2(a) and (b). The lateral lengths of such plates are hundreds of micrometers and thickness is within ten micrometers. Within each plate there is a multi-lamellar arrangement of extended *n*-alkane molecules, Figure 2.2 (b) and (c). The paraffin molecules are arranged perpendicular to the layers [8, 9].

[2] Melting temperature for eicosane, $C_{20}H_{42}$, at atmospheric pressure is 310 K.

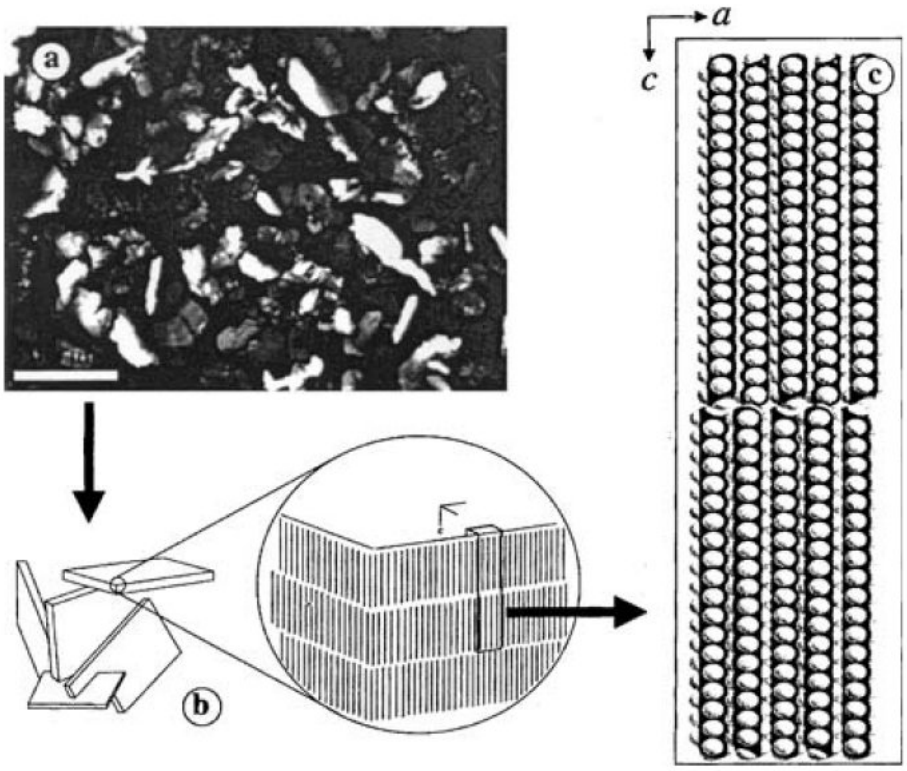

Figure 2.2: *Illustration of a wax at different resolutions: (a) micrograph, scale bar = 100 µm, (b) stacking of the crystal plates, formed by lamellar ordering of the extended linear alkane chains, (c) a multilayer packing within a 1-dimensional wax crystal [4]*

The length of the paraffin chains, defines the packing within the layer [10–13]:

- Triclinic – for alkane chains of 6 to 26 (even) carbon long.
- Monoclinic – for alkane chains of 28 to 36 (even) carbon long.
- Orthorhombic – for chains with odd number of carbons or over 36.

Figure 2.3 shows examples of the structures of triclinic (a), orthorhombic (b) and monoclinic (c) crystals. Alkane chains follow the discussed packing, up to 102 carbon long, after which the chains start folding on themselves within the crystal [14–16].

2.2.1 Crystal nucleation and growth

Crystallisation is a transition process from disordered phase into an ordered one. A successful crystallisation will take place in two steps: nucleation and crystal growth. Nucleation can be *homogeneous* or *heterogeneous*. Homogeneous nucleation starts with the formation of a first stable molecular association. This molecular cluster will dissolve if not stable enough. The association will be stable when a certain *critical size* is reached, i.e. when the free energy of the cluster formation compensates for the gain of free energy due to surface formation.

The free energy for a simple cubic molecular association is [18]:

$$\Delta G(n) = -n\Delta\mu + 6a^2 n^{\frac{2}{3}}\alpha \tag{2.1}$$

where α is the surface free energy, $\Delta\mu$ is the chemical potential, a is the side of a cube and n is a nucleus size. The free energy of nucleation is influenced by two terms: $-n\Delta\mu$, that describing the free energy loss due to the formation of a cluster in supersaturated solution, and $6a^2 n^{\frac{2}{3}}\alpha$ that is an energy gain due to cube surface formation. This dependance is illustrated on Figure 2.4.

The critical nucleus size can be calculated as a stationary point and is

$$n^* = \frac{64a^6\alpha^3}{\Delta\mu^3} \tag{2.2}$$

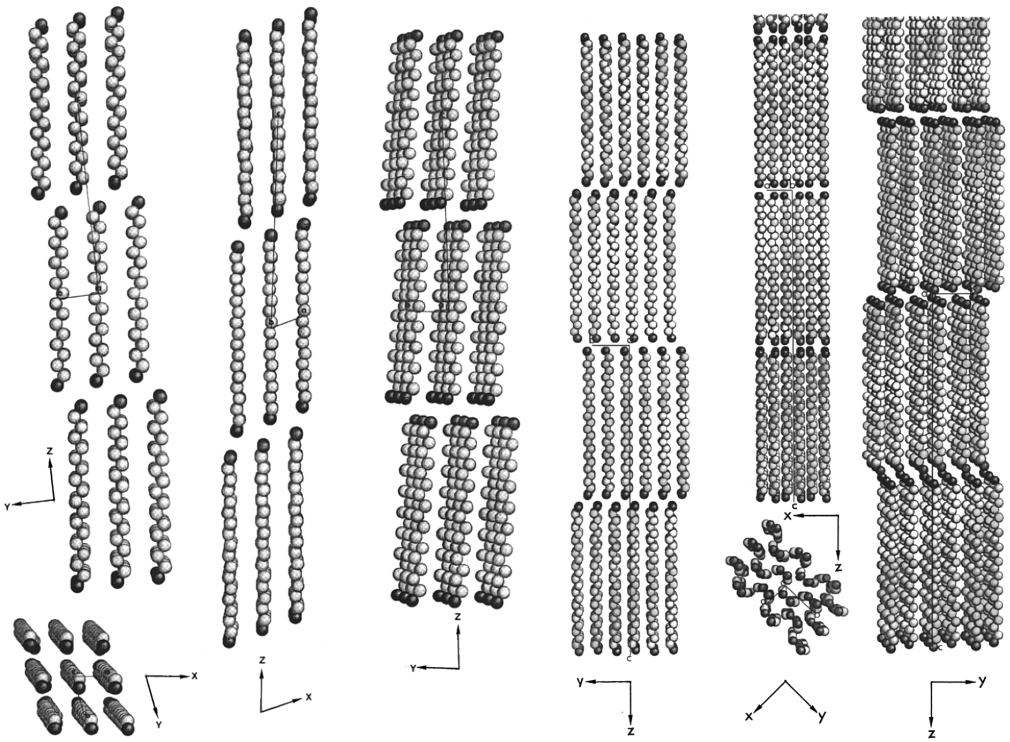

(a) Triclinic crystal

(b) Orthorhombic crystal

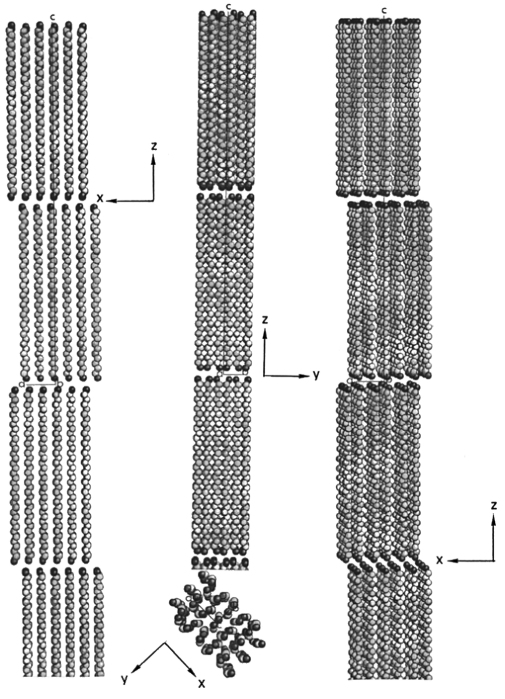

(c) Monoclinic crystal

Figure 2.3: *The layout of molecules in the crystal (a) triclinic crystal, formed by $C_{18}H_{38}$; (b) Orthorhombic crystal, formed by $C_{23}H_{48}$ and (c) monoclic crystal, formed by $C_{36}H_{74}$ [17]*

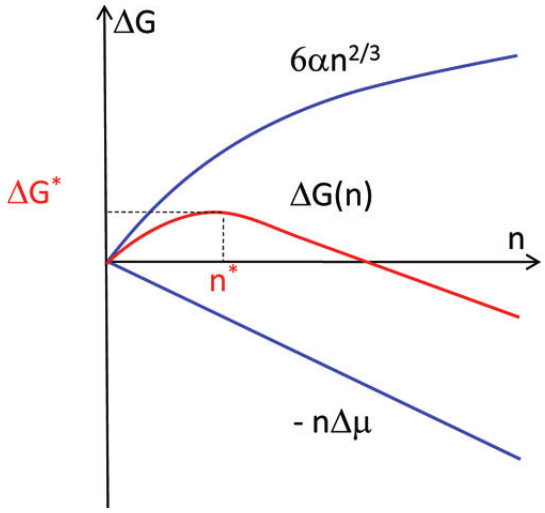

Figure 2.4: *Illustration of thermodynamics of crystal nucleus formation. Where n is a number of associated molecules, n* is a critical size cluster and Δ G* is free energy of the formation of critical size cluster [18]*

and therefore

$$\Delta G^* = \frac{32a^6\alpha^3}{\Delta\mu^2} = \frac{1}{2}n^*\Delta\mu \tag{2.3}$$

The nucleation rate is the number of nucleation centres appearing in solution per unit time and can be expressed as:

$$J = \Omega \exp\left(-\frac{\Delta G}{k_B T}\right) \tag{2.4}$$

where k_B is a Boltzmann constant and Ω is a pre-exponential factor and is nearly constant. The nucleation rate is dependant by ΔG, that is affected by factors such as temperature, concentration and pressure. The nucleation rate is very slow until the critical point is reached, where the rate substantially speeds up.

Heterogeneous nucleation occurs in the presence of foreign particles, such as surfaces, foreign crystals or interfaces. These foreign particles provide a nucleation site with a lower effective surface energy, by such reducing the free energy barrier.

Heterogeneous nucleation is most frequently observed. It allows for a faster crystallisation and often reduces the level of supercooling. Supercooling occurs in the region between the melting point and the pure substance freezing temperature. When crystallising pure paraffins the level of supercooling necessary to achieve nucleation is relatively low, due to their low interfacial tension.

Classical nucleation theory, discussed above, is limited in its applicability to real systems. Poor performances are observed when dealing with surface tensions, density, very small molecular association [19]. This approach also significantly overestimates energy barriers, that leads to an underestimating nucleation rates. Vekilov has shown that neither spinodal, nor the two step nucleation process is accounted for in classical nucleation theory [18].

2.2.2 Interactions within paraffin wax

The structure of a crystal is controlled by the intermolecular interactions. Alkanes comprise two types of groups: terminal CH_3 and central CH_2. The carbons in the alkanes are *sp3* hybridised and so, in a fully extended conformation, form a zig-zag structure. The total intermolecular forces between CH_2 groups are greater than the interaction of terminal CH_3. This induces the formation of well aligned, rapidly growing structures in the direction perpendicular to the molecular axis. This leads to the formation of lamellar structures.

The angle between the molecular axis and the layer, as well as the position and displacement between layers, are determined by molecular packing density [20]. The systems will aim at maximising this density. Figure 2.5 shows three different cases of theoretical superposition of layers. The case of two layers positioned without displacements over one other (a) will lead to low density, and so displacement will be necessary. Displacement can occur with (b) or without (c) tilt of the unit cell. The last two cases will lead to the structures observed in Figure 2.3.

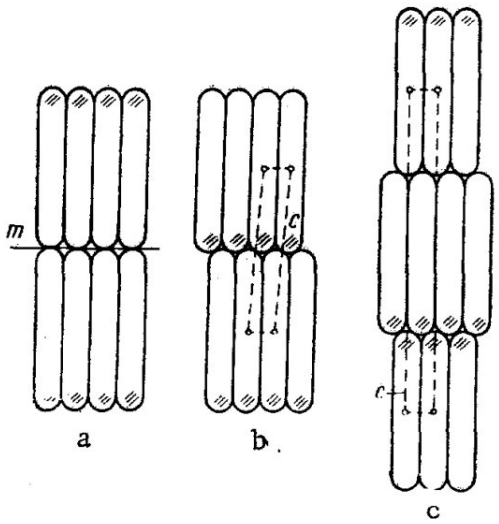

Figure 2.5: *Theoretical cases demonstrating superposition of layers in paraffin wax: (a) cubic, (b) triclinic, (c) monoclinic [20]*

2.2.3 Alkane mixes

Rules of interaction of *n*-alkane mixes were developed by Mnyukh in the 1960s: *Under otherwise similar conditions, n-paraffins with shorter chains will dissolve in n-paraffins with longer chains, while preserving the structure (modification) of the solvent, to a greater extent than in the reverse case* [20]. This rule holds for most liquid states and mixes.

This is not the case for the solid state, where two general behaviours are observed. Chains with the smallest difference in molecular weight, and hence melting point, will co-crystallise to form an orthorhombic structure. Some amount of disorder is also present to accommodate for differences in chain lengths within the lamellar structure [10, 21, 22]. Figure 2.6 shows the preferred arrangement in a crystal and their associated energy for a range of pure paraffins and their binary mixes [23].

When the *n*-alkanes in a mixture are of a significantly different molecular weight, the heaviest ones will separate out of the mixture, while shorter ones will act as a solvent. The study by Dorset *et al.* of crystallisation of a mixture of *n*-octacontane, *n*-dotriacontane and *n*-hexatriacontane has shown that initially a solid solution is

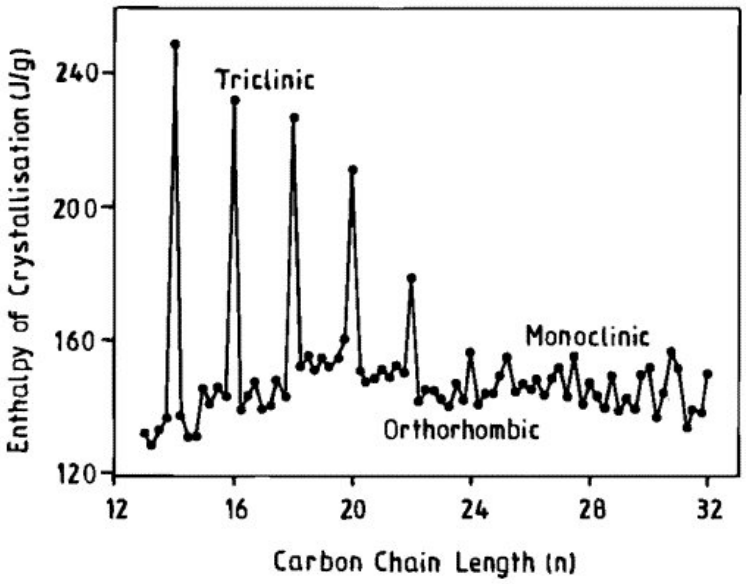

Figure 2.6: *Enthalpies of crystallization of pure n-alkanes and their binary mixtures (shown as mean carbon number) in the range $C_{13}H_{28}$ to $C_{32}H_{66}$ [23]*

formed, but within period of a few months the separation into domains is observed [24]. These behaviours occur also in diesel fuel, where the longest alkane chains co-crystallise to form the orthorhombic wax crystals while shorter ones stay mixed in a liquid state.

2.2.4 Disorder and rotator phase

In 1930 Muller suggested that *n*-alkanes undergo an intermediary phase between the liquid and crystal stage [25]. This phase is now known as *rotator* phase, due to molecules experiencing a rotational disorder along the molecular axis. This phase occurs as a result of accumulation of sufficient vibrational energy to rotate the molecules around the axis. This rotation distorts the packing within the lamellar structure, reducing the overall density of the layer and hence affecting the interactions between layers. This leads to pseudo-hexagonal structures with a slight tilt between molecular axes and the layer. Depending on whether the *n*-alkane chain is odd or even there are two transition schemes between states [26–30]. Figure 2.7 shows the transitions observed for even and odd *n*-alkanes.

With an increase of temperature, phases undergo disorder, increasing the spacing

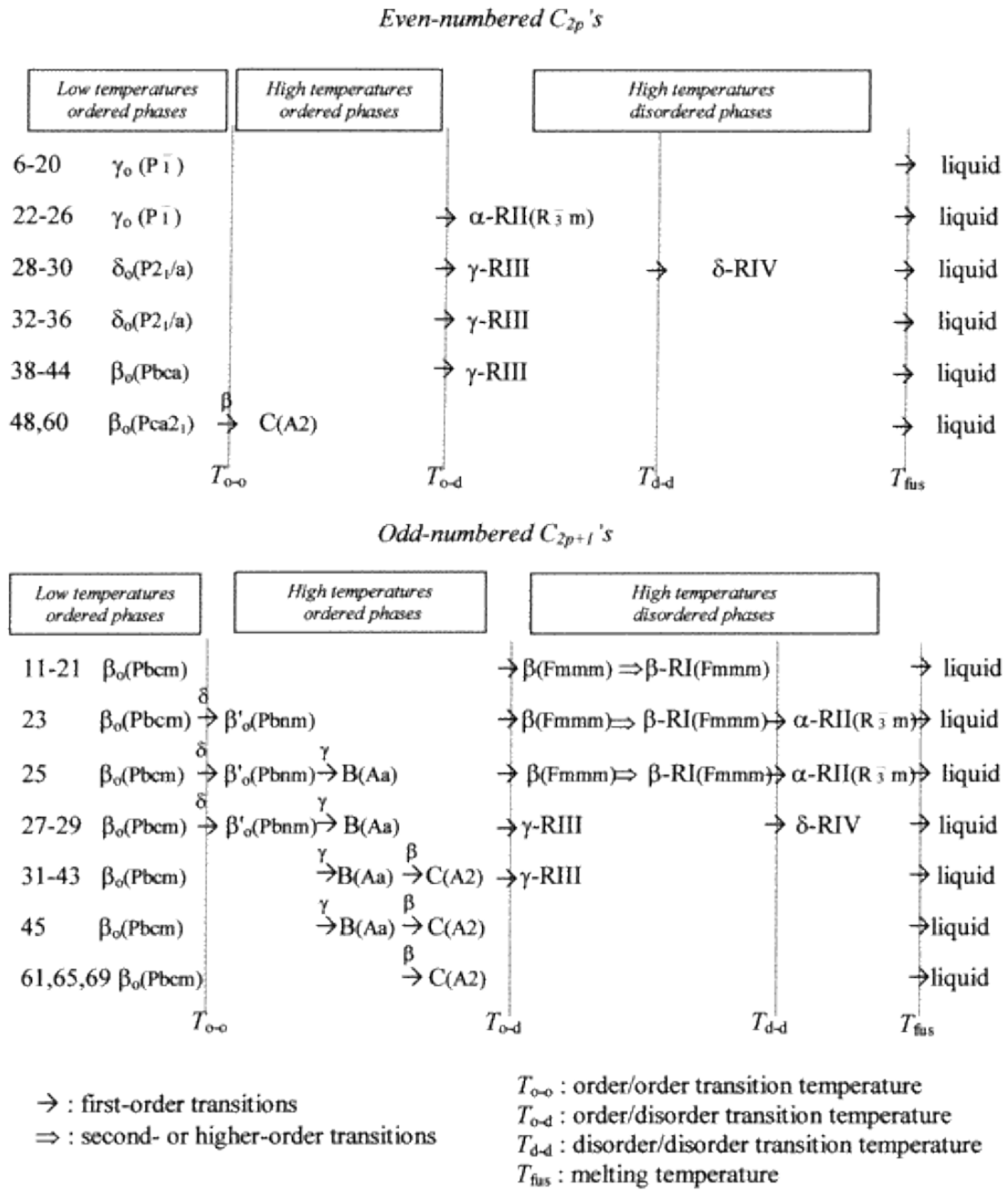

Figure 2.7: *Transitions in paraffins with increase of temperature [31]*

between lamellar layers and allowing molecules to move along the axis. This movement is a rigid body displacement and results in the formation of defects within the molecule. The different types of defects are illustrated on Figure 2.8. The kink defect (b) is the most commonly observed in the rotator phase, while end-*gauche* (a) and double end-*gauche* (c) are responsible for the separation between layers, as shown on Figure 2.9.

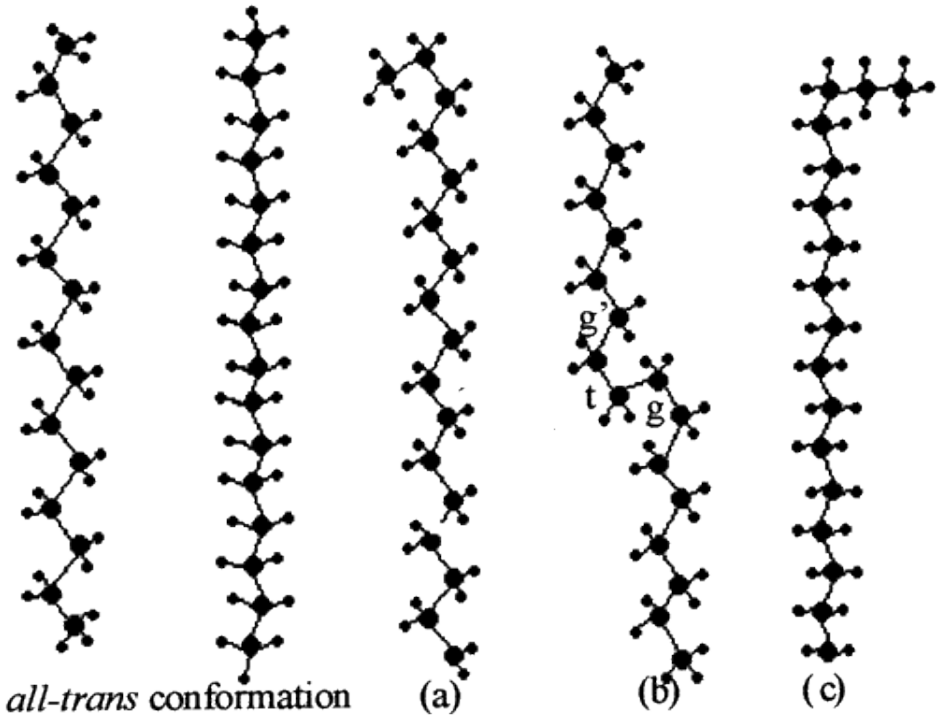

Figure 2.8: *Molecule conformation defects (a) end-gauche defect, (b) kink defect, (c) double end-gauche defect [17]*

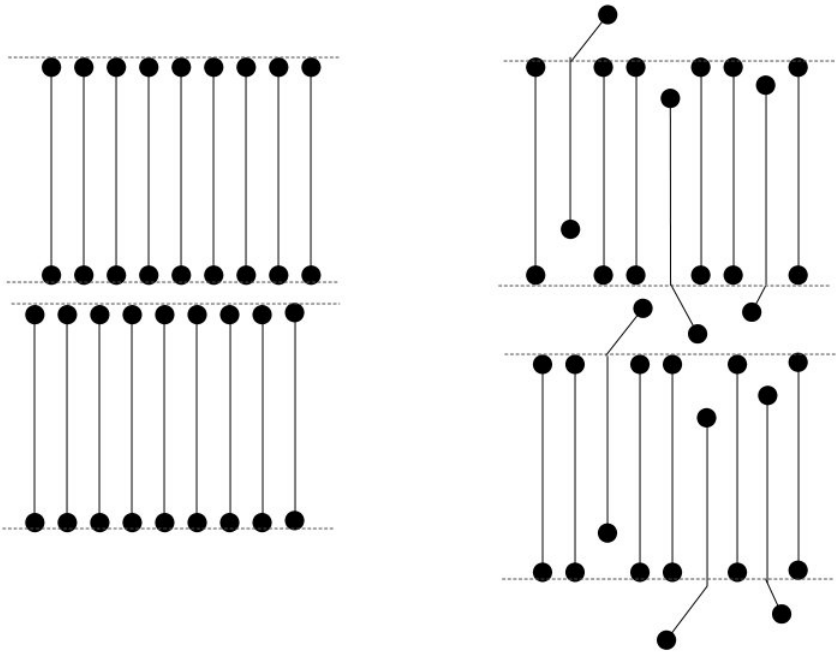

Figure 2.9: *Illustration of the disorder in lamellar structure upon heating*

2.3 Fuel additives

In past decades a lot of work has been put into developing additives for fuels. There are many types of additives aiming at improving the system's performance, controlling fuel contamination, increasing fuel stability and ease of handling. Common additives are antifoaming agents, lubricating additives, cetane number improvers, corrosion inhibitors, dispersants and cold flow improvers. Our research focuses on the latter. Cold flow improvers work by lowering the temperature of the cloud point, pour point or the cold filter plugging point of a fuel [32].

The *cloud point* is the temperature at which wax crystals begin forming. This leads to phase separation where wax particles get suspended in the solution. As a consequence, the solution loses its transparency [33].

The *pour point* is the lowest temperature at which the liquid will still pour or flow. At this temperature diesel fuel appears gel-like, due to the formation of an interlinked crystal network [34].

The *cold filter plugging point* is the temperature at which wax crystals are large enough to plug a 45 μm filter [35]. Figure 2.10 shows the wax crystals blocking a 100 μm car fuel filter.

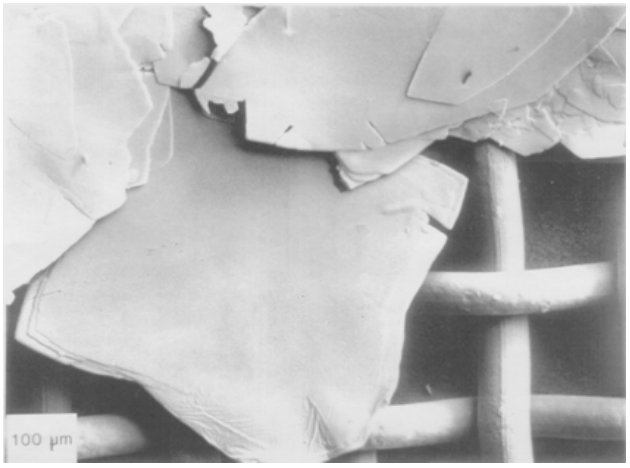

Figure 2.10: *Wax crystals over the fuel filter, picture provided by Infineum*

It can be difficult to assign an additive to a particular group since, for instance, dispersants can also act as cold flow improvers by preventing crystals from settling down. In most cases it is beneficial to introduce a number of additives, every one of which acts on a specific range of paraffins and/or temperatures. Frequently anti-settling agents are introduced in conjunction with other additives to further enhance their effect.

2.3.1 Mechanism of action of wax crystal modifiers

Many cold flow improvers act by altering the shapes of forming crystals, rather than postponing nucleation. Figures 2.11 and 2.12 show the difference in the shape of the crystals formed from the melt with and without additives. Figure 2.11 (a) shows the plate-like large crystals that form from a base fuel. Figure 2.11 (b) shows needle-like crystals formed under the same conditions in the presence of an ethylene vinyl acetate (EVA) additive. Figure 2.11 (c) shows small dispersed crystals formed in the presence of EVA and a wax anti-settling agent (WASA). On Figure 2.12 crystals precipitated from solution of tricosane (a) and crystals formed in the presence of polyoctadecylacrylate (PA-18) (b) are shown [36]. From these figures it can be clearly seen that the crystals

formed in the presence of additives are smaller and better dispersed than those from pure fuels. The use of additives modifies crystals allowing them to pass through the fuel filter, as illustrated on the Figure 2.13.

Usage of WASA allows the formed crystals to remain evenly dispersed through the fuel tank. It is essential to have long alkanes evenly distributed through the fuel. First, the longest chains generally provide the best cetane number (the measurement of the ignition quality). Second, dispersed crystals will not aggregate to form a gel, that can turn into a soft wax and hence cause blockage. Figure 2.14 shows the comparison in wax crystal settling of two fuels, both treated with EVA additive, but only the one on the right also containing WASA.

Depending on the mechanism of action, additives typically fall into two groups: wax crystal modifiers and nucleators [37]. As the name suggests, *wax crystal modifiers* change the shape of the forming crystal. The additive integrates into the forming crystal and introduces morphologies or restricts the growth of the crystal on a particular face.

The other type of additive is a *nucleator* or *promoter*. The additive precipitates out of the fuel just before the normal cloud point by creating a number of nucleation points. The crystallisation will start around them, leading to the formation of many small crystals. This will relieve the saturation caused by a temperature decrease. The heterogeneous centre created by the additive, can additionally affect the shape of the formed crystal to prevent co-crystallisation.

These mechanisms are not yet fully understood. Our work aims at better describing the interactions between fuels and additives. In the next section an up to date review of computational studies in the area is presented.

(a) Base fuel

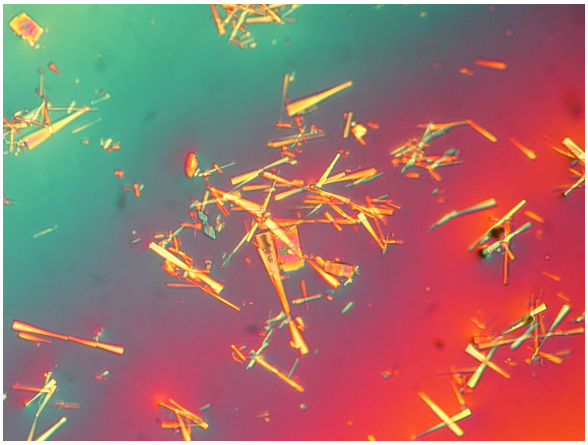

(b) Base fuel with EVA

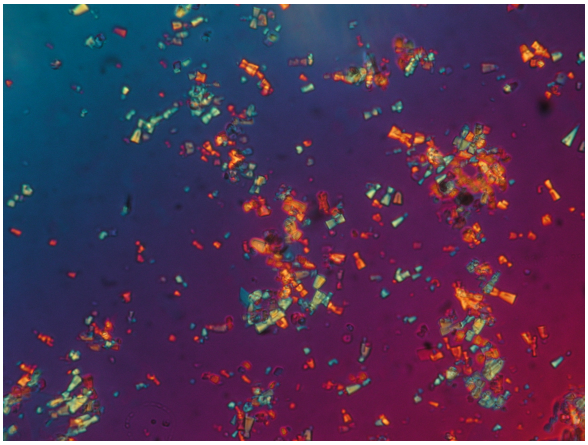

(c) Base fuel with EVA and WASA

Figure 2.11: *The formation of the wax crystals from diesel fuel (a) in the presence of EVA additive (b) and in the presence of both EVA additive and WASA (c), pictures provided by Infineum*

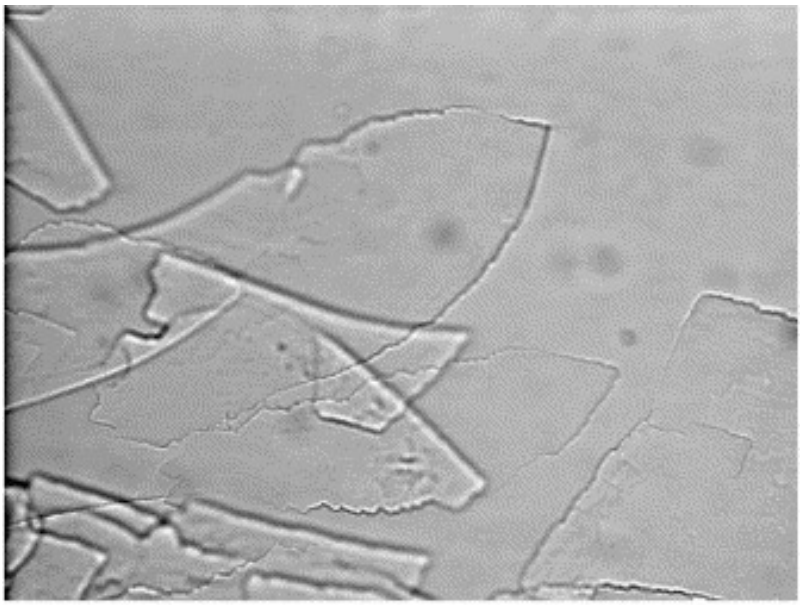

(a)

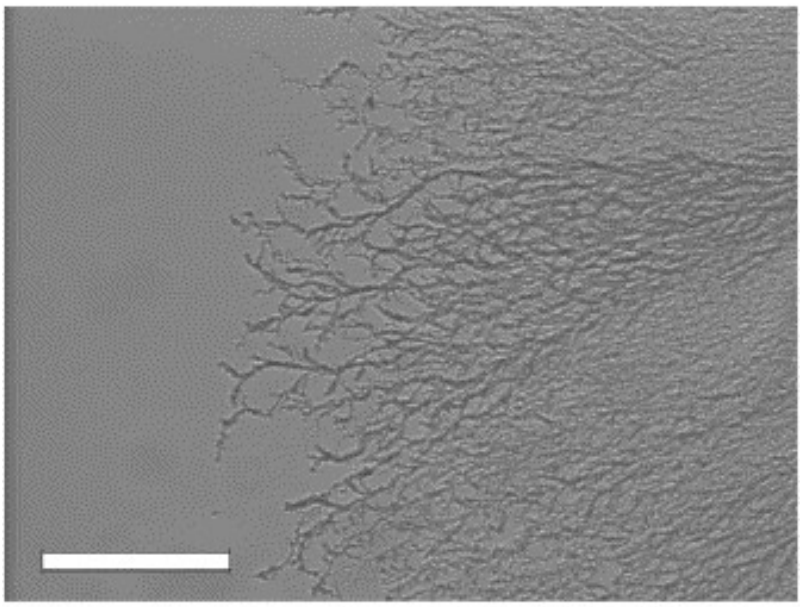

(b)

Figure 2.12: *The formation of the wax crystals from pure tricosane (a) and in the presence of PA-18 additive (b). Scale bar spans 100 µm [36]*

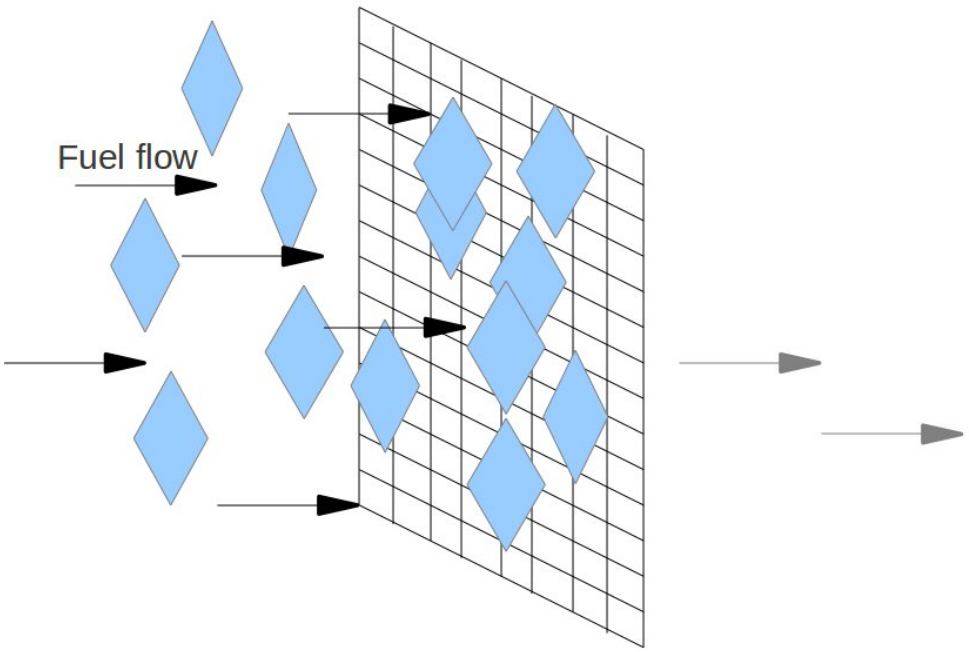

(a) Base fuel

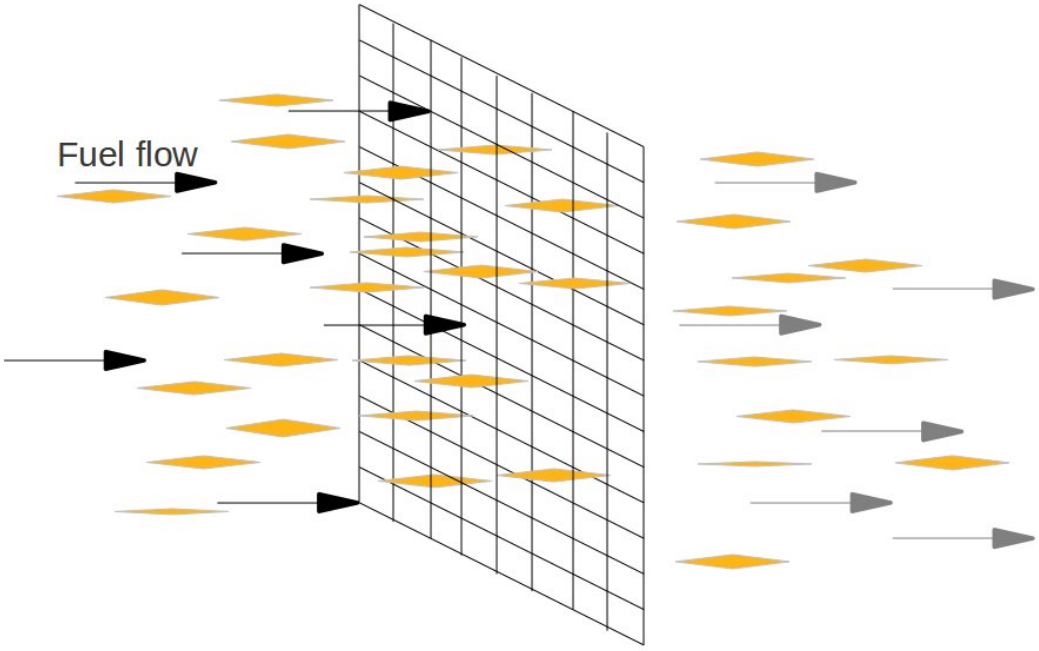

(b) Base fuel with additive

Figure 2.13: *Graphical illustration of wax formed from untreated fuels (a) and wax formed in the presence of additive (b) passing through the fuel filter*

Figure 2.14: *Wax crystals formed in the presence of EVA only (left); EVA and WASA (right), picture provided by Infineum*

2.4 Previous computational work

2.4.1 Studies of wax crystals

The first molecular dynamics studies of crystallisation in 3D were performed in 1970s [38]. However, theoretical studies of wax began only in 1980s, with the development of models describing wax formation [39, 40]. Larger scale simulations of wax only became computationally affordable in 1990s [41]. In the study by Esselink *et al.* [41] a range of short alkanes was crystallised and melted mimicking realistic conditions. The observed behaviour was consistent with experiment, including the temperature versus density graph showing the characteristic "kink", that was assumed to be a glass-rubber transition. In a later study by Waheed *et al.* the "kink", corresponding to the second order transition (Figure 2.15), was also observed upon heating of an initially crystallised *n*-eicosane. The authors also observed no presence of *gauche* conformations, but disturbance of the orientation along the intrinsic axes in the alkane chains [42].

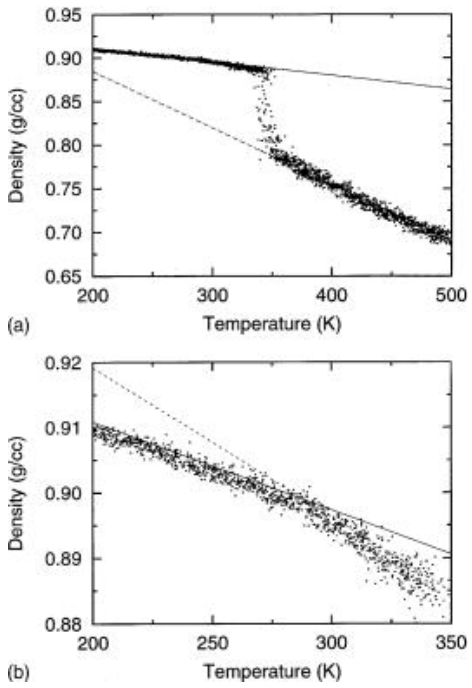

Figure 2.15: *(a) Density of the simulation cell as a function of temperature, during heating of n-eicosane, (b) magnification of the area of the "kink". Linear fits to the data are shown to illustrate the trends [42]*

The behaviour of the crystal observed in the two studies above can correspond to the rotator face, discussed in Section 2.2.4. Detailed studies of rotator phases were performed by a number of research groups [43–48]. The studies described a number of rotator phases. Wentzel *et al.* identified two, that were in agreement with experimentally observed data, as illustrated on Figure 2.7. However, the temperatures of the rotator phases found by computational techniques do not perfectly correspond to the experimental ones. This is to be expected due to the limitations in the calculation times and scales, imposed by computational methods. A study aimed at predicting the melting point produced the most accurate results, which deviated by 10 to 40 degrees from experimental results [49].

2.4.2 Studies of wax crystal modifiers

There are two popular groups of wax crystal modifiers: ethylene vinyl acetate (long branched polymers) and polyacrylates (comb type molecules). As discussed in Section 2.3.1 their mechanism of action is not fully understood. Few suggestions have been however made, based on experimental observations. In the past decade a few computational studies aimed at understanding the interaction between wax and the additive were performed.

Comb type polymers

Duffy *et al.* have performed molecular dynamics studies of the adsorption of comb-type polyoctadecylacrylate (PA-18) additive onto the wax surface [50–52]. The extended PA-18 was positioned onto the faces of wax, and liquid *n*-alkanes were added over it, Figure 2.16. The additive, as well as its variations, have shown to limit the growth of the crystal on the binding side.

Another study on comb-type polymers was performed by Jang *et al.* Four theoretical mechanisms were compared: Sequestering, Incorporation–Perturbation, Inhibitor Adsorption on Wax Crystals and Inhibitor Adsorption on Pipe Walls [53]. The study concluded that the most likely mechanism is Incorporation–Perturbation, rather than Inhibitor adsorption, as studied by Duffy *et al.* [50–52]. Figure 2.17 shows the mech-

anism proposed by Jang *et al.* The inhibitor (carbon atoms shown in yellow, oxygen atoms in red, hydrogen atoms are not show) is incorporated into the melt (1 –> 2) in an open coiled conformation, that is preserved upon formation of the soft wax (2 –> 3). The presence of the additive perturbs the further development of hard wax (4), that would form in the absence of an inhibitor (1 –> 4).

Ethylene vinyl acetate

The interaction of ethylene vinyl acetate (EVA) with wax was investigated with density functional theory and molecular mechanics by Zhang *et al* [54, 55]. Similarly to the studies of comb polymers performed by Duffy *et al.* [50–52], the additive was deposited onto common faces of the crystal and then relaxed. The research has shown that the carbon bonds adjacent to the vinyl acetate group in EVA are more rigid, as such promoting *n*-alkane molecules crystallisation along the non-polar segment. The polar vinyl acetate groups repel the *n*-alkane, creating as a consequence disorder in the forming crystal.

Based on the work by Zhang *et al.* discussed above, Wu *et al.* investigated the effect of side chains in the performance of EVA-type additives [56]. It was found that the introduction of a propylene branch adjacent to vinyl acetate would increase the affinity between additive and *n*-alkane, as such increasing the performance of EVA.

2.4.3 Summary

For many years, investigations of wax precipitation have been carried out, leading to many discoveries. In the last 50 years [57–60] a lot of work has been put into developing better additives for fuel. Nevertheless, wax formation still remains a problem. The exact mechanism behind the action of wax crystal modifiers is not well understood, limiting further additive development.

In the last decades, computational techniques and computer power became sophisticated enough to be able to perform necessary calculations. However, up to now only a few computational studies of wax crystal modifiers have been carried out. The

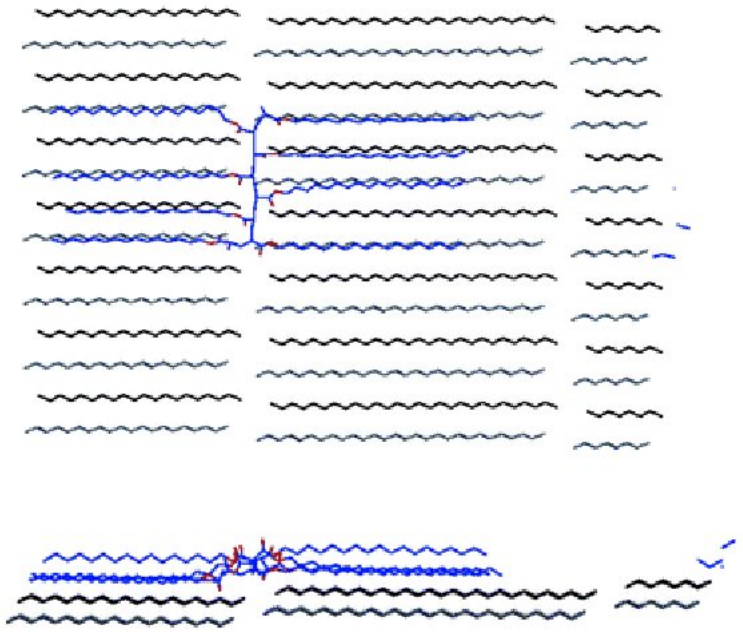

Figure 2.16: *The top and side views of the relaxed structure of the PA-18 octamer (blue carbons, red oxygens, hydrogens are not shown) on the (100) surface of an octacosane crystal (black) [50]*

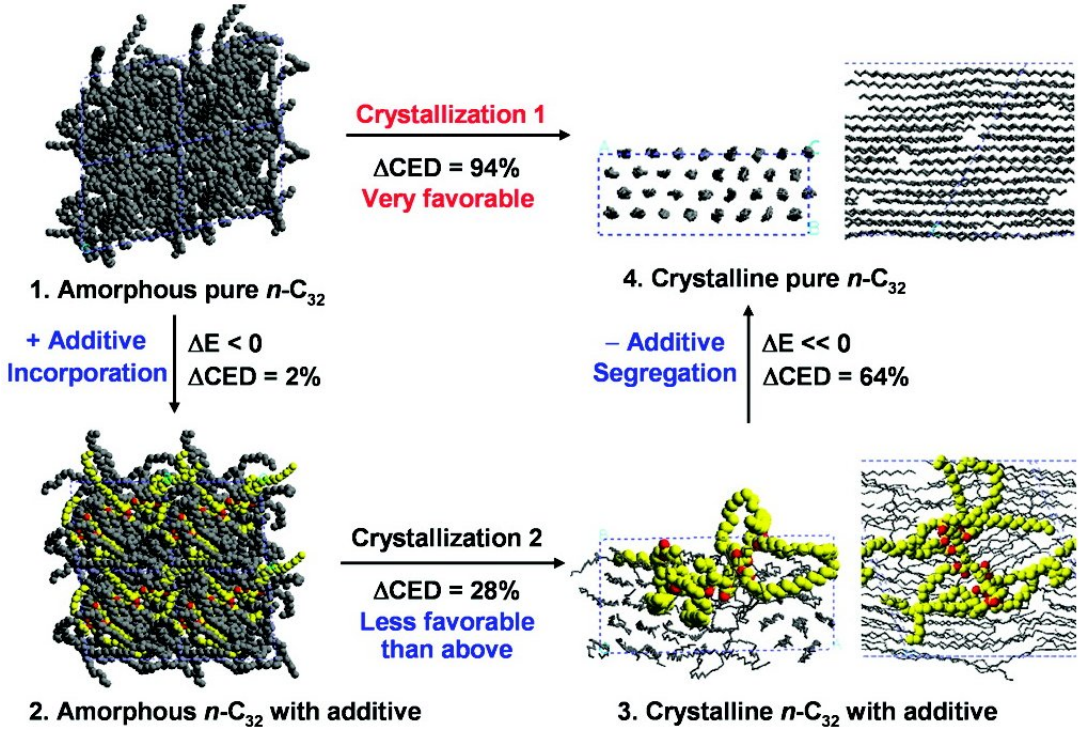

Figure 2.17: *Illustration of the mechanism of incorporation–perturbation. Wax is shown in grey and the inhibitor in yellow-red [53]*

interaction of EVA and PA-18 with wax surfaces was investigated by three independent groups, leading to a better understanding of the forces involved. Jang *et al.* [53] performed a comparison of theoretical mechanisms, showing that the additive can come into action before the crystal has formed.

With advances in simulation algorithms and computational power, further detailed investigation of the crystallisation process in the presence of additives is now possible. The aim of the work within this thesis will be to mimic realistic conditions of crystallisation, using molecular dynamics calculations and a combination of atomistic and coarse grained models for diesel and diesel additives.

3 Molecular Modelling

Molecular modelling is a computational approach, where the molecule is represented by a mathematical model and its behaviour is predicted by means of numerical calculations. This section provides an overview of the calculations carried out in this thesis, together with the theoretical background to the methods used.

There are a number of computational chemistry methods that are commonly used. The choice of the method is dependent on both the size of the system under study and the time scale required for the calculation. Figure 3.1 shows the relation between the choice of method, the size of the system and the time scale available. When increasing the size of the system and the simulated time scales, the level of detail of the calculation must typically be reduced in order to keep it computationally affordable [61–63].

The most detailed level of study is quantum mechanics, where the properties and geometry of a molecule are obtained by finding approximate solutions to the Schroedinger equation. As it is only possible to solve the equation for hydrogen and helium atoms, approximate solutions are required. This has led to the development of number of different methods. Methods directly derived from quantum mechanics are called *ab-initio*, while the ones that include parameters from experimental data are termed semi-empirical and empirical [61, 62].

Quantum mechanics calculations are computationally expensive. *Ab-initio* methods allow calculations for up to approximately 100 atoms and semi-empirical methods up to few hundred of atoms. These methods are often used to predict properties

of species that cannot be isolated, for example transition states and excited state geometries.

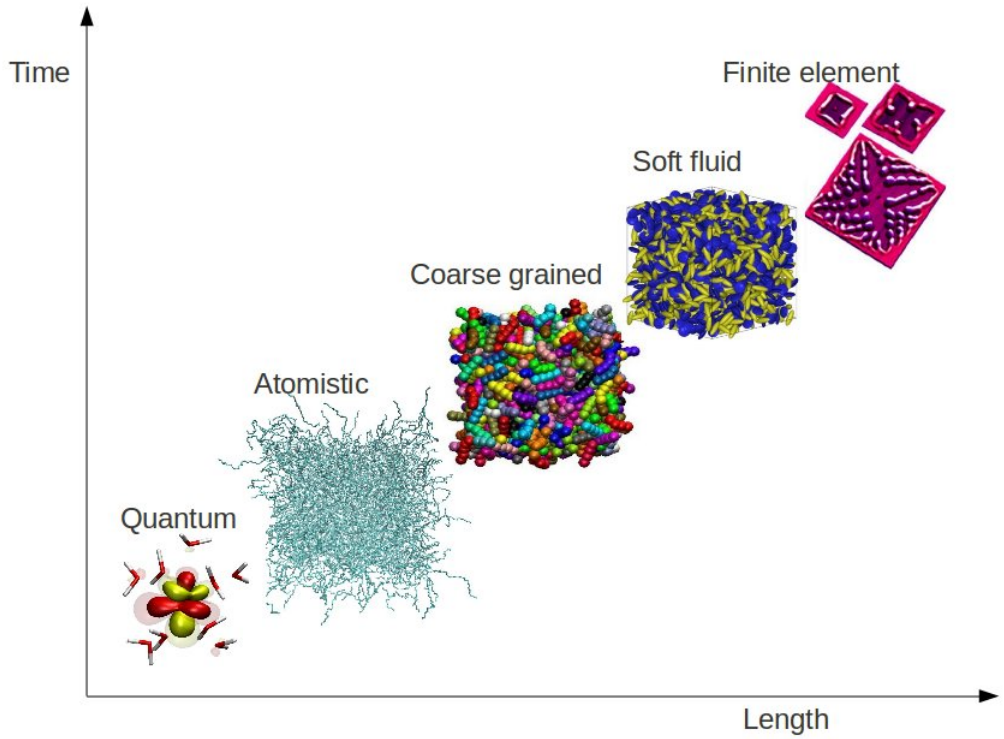

Figure 3.1: *Length scales, associated time scales and computational methods in molecular simulation. Images taken from author's work, group's work and Cecam website [64]*

The next level of modelling includes force field methods (atomistic models), where molecules are represented in terms of classical mechanics [63]. This allows the calculation of larger molecular systems, typically containing thousands of atoms. In this level of modelling, the molecular system is described atom by atom. To extend the available system size, it is possible to unite hydrogen atoms to the neighbouring heavier atom, creating an united atom representation.

Coarse grained methods are a further simplification of force field methods [65]. A number of atoms can be united together, creating a super-atom (also called a bead). This reduces the number of interactions to be calculated, thereby increasing the size of the system and the accessibility of longer time scales. There is no limit on how many

atoms can be united into a single super-atom, but presence of individual molecules is usually maintained.

When a whole molecule is represented as one bead, it is often regarded as a soft fluid. This is useful for studying the morphology of soft matter systems, like liquid crystals. For any further increase in the time and length scales the molecules are replaced with an equivalent-continuum model, often simulated by finite element models.

In recent years, lot of effort has been put into the development of effective multiscale methods, where two (or more) levels of theory are joined together [66]. The part of the system of highest interest, demanding therefore higher accuracy of calculation, is represented with a more exact method, while the bulk of the system is studied with a lower detail method. Typical combinations are quantum mechanics with all atom force fields (QM/MM), and all atom systems with coarse grained force fields.

3.1 Molecular mechanics force field methods

As discussed earlier, the choice of computational method is dependent on the size of the system and the required time scales. In this work, large systems (thousands of molecules) will be studied. Hence, the most computationally appropriate methods are based on molecular mechanics force fields.

In a molecular mechanics force field a molecule is represented by a set of balls, connected with springs, Figure 3.2. The energy of the system is dependent on the interactions within these. Any molecule can be represented in terms of *"balls and springs"*, allowing us to perform classical mechanics calculations on it.

To be able to represent the system in terms of classical mechanics, assumptions should be made:

- Nuclei and electrons are combined in an atom, represented by a ball.
- A ball has a radius and a constant charge. The ball can vary in softness.

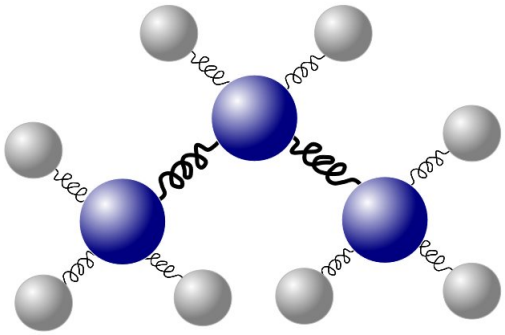

Figure 3.2: *Representation of propene, $CH_3-CH_2-CH_3$, in terms of "balls and springs" model: blue balls are carbon atoms, grey balls are hydrogen atoms, connected by springs with varying stiffness and length.*

- Bonds are represented by springs.
- Springs have an equilibrium length and can vary in stiffness.

The interactions are described by pre-assigned parameters, that are system dependent. These parameters can be obtained from experiment and/or higher level computational calculations, such as *ab-initio* methods.

3.1.1 Force field energy

The set of parameters used in classical mechanical calculations is called a force field. The potential energy of the system is described by the sum of all the interactions within the system:

$$E_{FF} = E_{str} + E_{bend} + E_{tors} + E_{VdW} + E_{el} + E_{Xterms} \tag{3.1}$$

where E_{str} is the energy function for stretching a bond between two atoms, E_{bend} is the energy required for bending an angle between three atoms, E_{tors} is the torsional energy for rotation around a bond, E_{VdW} is the Van der Waals energy, E_{el} is the electrostatic energy and E_{Xterms} represents coupling between the above terms. The first three terms represent the bonded interactions. The electrostatic and Van der Waals

energies are non-bonded interactions between atoms. To be able to calculate the force field energy it is necessary to know atomic coordinates, geometries and the relative energies of the atoms in the system.

3.1.2 Stretching energy

The stretching energy of a bond is the energy of the extension of the spring, bonding two atoms. The shape of the energy curve is well described by a Taylor expansion:

$$E_{str}(r^{AB} - r_0^{AB}) = E(r_0) + \frac{dE}{dr}(r^{AB} - r_0^{AB}) + \\ + \frac{1}{2}\frac{d^2E}{dr^2}(r^{AB} - r_0^{AB})^2 + \frac{1}{6}\frac{d^3E}{dr^3}(r^{AB} - r_0^{AB})^3 + ... \tag{3.2}$$

where r_0 is an equilibrium bond length for the given system and so correspond to the minimum energy.

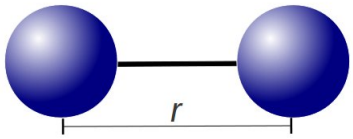

Figure 3.3: *Illustration of a bond with bond length r, formed between two atoms*

At $r = r_0$, $E(r_0)$ is zero and is used as the zero point on the energy scale, the second term is a first order derivative that is not symmetrical about r_0. The cubic term will drive the energy of the bond to negative value at infinity, so the expansion can be simplified to a harmonic approximation:

$$E_{str} = \frac{1}{2}k^{AB}(r^{AB} - r_0^{AB})^2 \tag{3.3}$$

where k^{AB} is the force constant for stretching the bond between atoms A and B and will change depending on the system.

Approximation to harmonic form is sufficient for most molecular dynamics calculations. For calculations of bond length dependent parameters, such as vibrational frequencies, or when the starting configuration is far from equilibrium, terms up to the fourth order may be included. The other common choice is the Morse potential [67]:

$$E_{str} = D^{AB}(1 - \exp(-\alpha(r^{AB} - r_0^{AB})^2) \tag{3.4}$$

where $\alpha = \sqrt{\frac{k}{2D^{AB}}}$ and D^{AB} is the bond dissociation energy, i.e. the depth of the well.

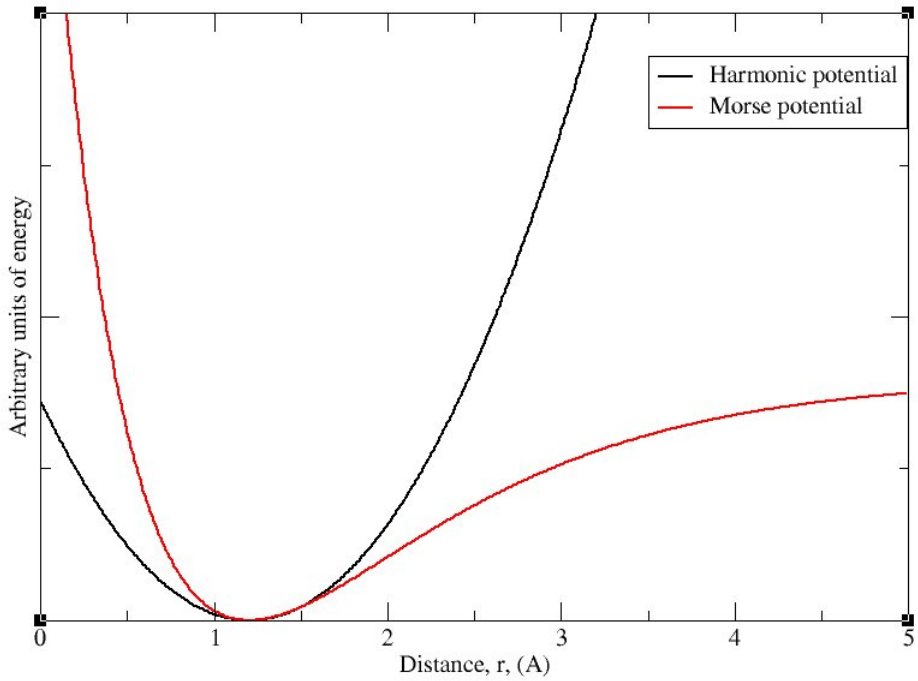

Figure 3.4: *Bond stretching energy, represented as harmonic and Morse potential*

The Morse potential reproduces stretching well over a wide range of distances, at long distances tends to zero. Hence, the Morse potential is slow in bringing atoms to equilibrium bond lengths, when the initial geometry has a large bond length. The comparison between harmonic and Morse potentials is shown on Figure 3.4.

The stretching energy has the highest contribution to overall energy of the system, followed by the bending energy.

3.1.3 Bending Energy

Similarly to the stretching energy, bending energy can also be expressed by a Taylor expansion, that can then be approximated to a harmonic potential.

$$E_{bend} = \frac{1}{2} k^{ABC} (\theta^{ABC} - \theta_0^{ABC})^2 \tag{3.5}$$

Here θ^{ABC} is an angle between three atoms *A, B* and *C*, as shown on the Figure 3.5. k^{ABC} is the force constant for the bending between three given atoms. When higher accuracy is required for the calculation, the next highest order term in the expansion can be included.

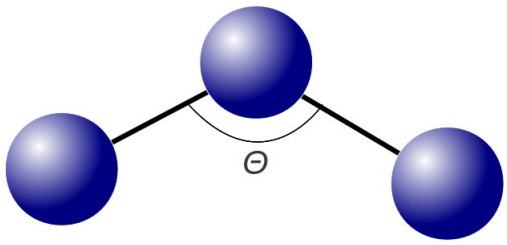

Figure 3.5: *Illustration of an angle,* Θ*, between three bonded atoms.*

Changes in the bending energy are usually smaller than the changes in stretching energy, so less energy is required to distort bond angles in comparison to bond length. Hence, force constants for bending are proportionally smaller than those for stretching.

When the central atom *B* is bonded to more than two other atoms, as shown on the Figure 3.6, a pyramidal structure is formed. The angle can no longer be calculated as

discussed above. A high force constant should be used to penalise out-of-plane bending, which would make planar structures very inflexible. By introducing a new term, the flexibility of the planar structure is maintained while out-of-plane movement is also taken into account.

The energy of such bending is referred to as the *out-of-plane bending energy*, or *improper torsional energy*. As the bending energy, it takes a form of a harmonic potential.

$$E_{oop} = \frac{1}{2} k^B (\alpha)^2 \tag{3.6}$$

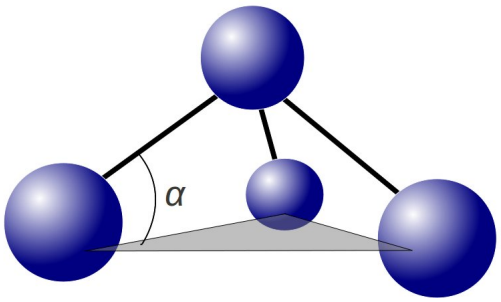

Figure 3.6: *Illustration of out-of-plane bending, created by three atoms bonded to sp^2 hybridised central atom.*

3.1.4 Torsional energy

Four aligned atoms will frequently rotate about a central bond, as shown in the figure 3.7.

Rotation about the bond is continuous, so when the bond rotates by 360^o the energy should return to the initial value, making torsional energy periodic. The potential is well represented by Fourier series.

$$E_{tors} = \sum \frac{1}{2} V_n \cos n\phi \tag{3.7}$$

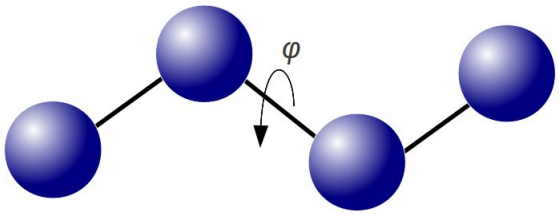

Figure 3.7: *Illustration of torsional angle, created by four linearly aligned atoms.*

where n is a periodicity term, depending on the allowed rotation it can be n=1 for full 360^o rotation, n=2 for 180^o, n=3 for 120^o etc. V_n is a constant determining the barrier for the rotation, V_n is not equal to zero for allowed periodic rotations, ϕ is the torsional angle (also called the dihedral angle), and is shown on Figure 3.7. Figure 3.8 shows a plot of the two torsional potentials with n=3, V_n = 4 (dashed line), n = 2, V_n = 3 (solid line) and the corresponding total torsional potential in red.

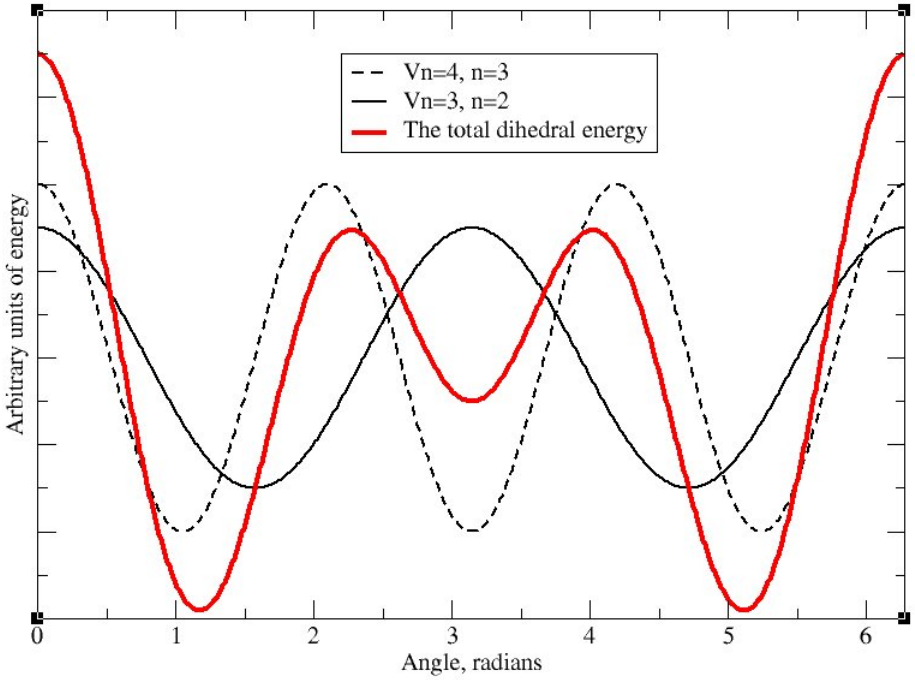

Figure 3.8: *Variation of torsional potentials for different values of n and V_n and the total potential (red).*

3.1.5 Van der Waals interactions

In addition to the bonded interactions described above,molecules also have non bonded interactions. These interactions appear between atoms in the same or neighbouring molecules and are normally described by two potentials, representing the Van der Waals energy and the electrostatic energy.

The Van der Waals energy describes the repulsion and attraction between non bonded atoms. At large interatomic distances the Van der Waals energy goes to zero, whereas at short distances it is positive and very repulsive. This mimics the overlap of the negatively charged electronic clouds of atoms. At intermediate distances there is a mild attraction between electronic clouds, due to *electron-electron correlation*. The attraction between two atoms arises because of an induced dipole moment created by the motion of electrons through the molecule, which affects the neighbouring molecule. The attraction between two fragments does not only depend on dipole–dipole interactions, but also on dipole–quadrupole, quadrupole–quadrupole etc. interactions. These interactions do not have a high contribution to the overall energy, so for simplicity they are often neglected in calculations.

In 1903 Gustav Mie proposed an intermolecular pair potential [68], comprising two parts to represent attractive and repulsive forces:

$$E_{pair}(r) = \left(\frac{n}{n-m}\right)\left(\frac{n}{m}\right)^{m/(n-m)} \epsilon \left[\left(\frac{\sigma}{r}\right)^{n} - \left(\frac{\sigma}{r}\right)^{m}\right] \tag{3.8}$$

where r is interatomic distance, ϵ is the depth of the well at σ, the interatomic separation at which repulsive and attractive terms balance out and m,n can be adjusted,

There have been a number of models suggested, where m and n take different values and show an accurate representation of experimentally known interactions [69, 70]. Nevertheless, the most popular one is the 12–6 Lennard-Jones potential [71]. The usage of 12 term reduces the amount of calculations needed, making it the lightest

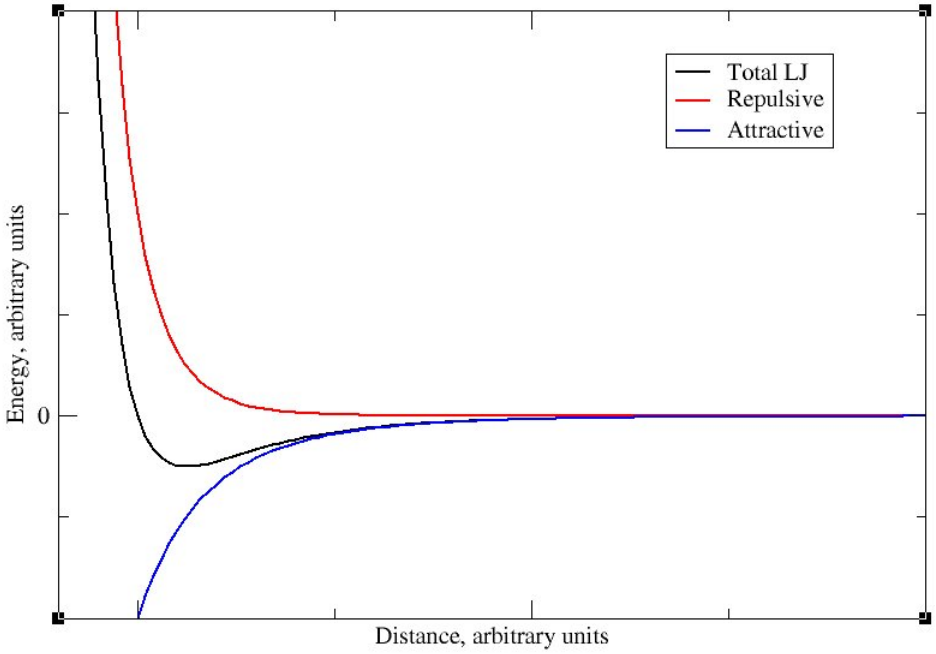

Figure 3.9: *Lennard-Jones potential (black) is a combination of attractive (blue) and repulsive (red) terms*

method available.

$$E_{VdW}^{LJ} = 4\epsilon^{AB}\left[\left(\frac{\sigma^{AB}}{r^{AB}}\right)^{12} - \left(\frac{\sigma^{AB}}{r^{AB}}\right)^{6}\right] \tag{3.9}$$

where σ is the interatomic separation at which repulsive and attractive terms balance out and ϵ is the depth of the well.

The 12–6 Lennard-Jones potential is shown on Figure 3.9. The repulsive term is shown in red, the attractive term in blue, and the overall potential in black. The positions of σ and ϵ are also shown on the graph.

It is possible to mix two Lennard-Jones potentials for single type atoms to obtain a potential describing interaction between two different atoms. There are three main approaches:

- Arithmetic or Lorentz-Berthelot rules [72]. The rules are for a hard sphere model, but are simple and therefore widely utilised.

$$\sigma_{ij} = \frac{\sigma_{ii} + \sigma_{jj}}{2} \tag{3.10}$$

$$\epsilon_{ij} = \sqrt{\epsilon_{ii}\epsilon_{jj}} \tag{3.11}$$

- Geometric rules [73].

$$\sigma_{ij} = \sqrt{\sigma_{ii}\sigma_{jj}} \tag{3.12}$$

  ϵ_{ij} is calculated, as given in the equation 3.11.

- Fender-Halsey rule [74].

$$\epsilon_{ij} = \frac{2\epsilon_i\epsilon_j}{\epsilon_i + \epsilon_j} \tag{3.13}$$

Additionally there are other more complex combining rules [75–77].

A slightly more accurate potential, but up to 4 times more computationally demanding, is the Buckingham or Hill potential [70]. Repulsive forces take the form of an exponential, since the repulsion arises due to electron correlation, and the electron density reduces exponentially with the distance.

$$E_{VdW}^{Hill} = A\exp(-Br_{AB}) - Cr_{AB}^{6} \tag{3.14}$$

where A, B and C are suitable constants.

3.1.6 Electrostatic energy

The electrostatic energy calculates non bonded interactions appearing due to an uneven internal distribution of electrons. This leads to positively and negatively charged parts in a molecule. The simplest way to model this behaviour is to place charges on atoms. The law of the interaction between two point charges was investigated by Charles Augustin Coulomb in 1780s, and can be expressed by the Coulomb potential:

$$E_{el} = \frac{1}{4\pi\epsilon_0}\frac{Q^A Q^B}{r^{AB}} \tag{3.15}$$

where ϵ_0 is the dielectric constant, Q^A and Q^B and are partial electronic charges on atoms A and B, and r is a distance between them. The atomic charges are mainly taken from electrostatic potential calculations obtained from quantum mechanical calculations. An alternative method to obtain partial charges is from assignment of bond dipole moments. These two methods produce similar results, results will however be identical only for interactions at larger distances.

3.1.7 Cross terms

As mentioned above, there are also cross terms available for some force fields. These can cover the coupling between the fundamental stretching, bending and torsional interactions.

3.2 Molecular Dynamics

Traditional simulation methods for many body systems are divided into molecular dynamics and Monte Carlo techniques. The latter one probes the conformational space of the system by using random numbers to generate states from a Boltzmann distribution. Molecular dynamic methods [78] not only probe conformational space, but also dynamical properties.

In molecular dynamics simulations, the classical equations of motion are solved step-by-step, by a procedure known as a *finite difference algorithm*. Newton's equations of motion for a simple system are given by:

$$\begin{aligned} m_i \frac{\partial^2 r_i}{\partial t^2} &= \boldsymbol{F}_i \\ \boldsymbol{F}_i &= -\frac{\partial E}{\partial r_i} \end{aligned} \tag{3.16}$$

where $\boldsymbol{F}_i$ is a force acting on the atom i, m_i is the mass of i, t is time, E is the potential energy (discussed in the section 3.1) and r_i represent the atomic coordinates of i. Integration of a set of particles, modelled by equation 3.16 allows one to find the trajectory describing positions and velocities. Knowing positions and velocities allows one to predict the state of the system at any time.

3.2.1 Integration algorithms

The coupled differential equation 3.16 cannot be solved analytically, but can be solved numerically. A number of algorithms have been developed to integrate the equation of motion, the most widely used ones are discussed below.

Verlet algorithm

The algorithm was developed by Loup Verlet in 1967 [79] and became a base for algorithms used in modern calculations. The algorithm calculates positions forward and backward in time. This is done via a third order Taylor expansion:

$$\begin{aligned} r(t+\delta t) &= r(t) + v(t)\delta t + \frac{1}{2}a(t)\delta t^2 \\ r(t-\delta t) &= r(t) - v(t)\delta t + \frac{1}{2}a(t)\delta t^2 \end{aligned} \tag{3.17}$$

where r is the position, v is velocity and a is acceleration.

By adding the two above expressions one gets:

$$r(t+\delta t) = 2r(t) - t(t-\delta t) + a(t)\delta t^2 \tag{3.18}$$

The main problem with this algorithm is that the velocities are not directly generated. However, this makes the algorithm computationally cheaper, as lower data storage is required. On the base of this algorithm, several improvements have been proposed.

The leap-frog algorithm

The leap frog algorithm is a modification of the classical Verlet algorithm discussed above. This calculates velocities, v, at a half time $\frac{\delta t}{2}$ step in advance of the reference time, t:

$$v(t+\frac{\delta t}{2}) = v(t-\frac{\delta t}{2}) + a(t)\delta t \tag{3.19}$$

These are then used to calculate the position at the full time step, δt:

$$r(t+\delta t) = r(t) - v(t+\frac{\delta t}{2})\delta t \tag{3.20}$$

In this method the velocities leap over positions, which in turn leap over velocities. The advantage of this method is that velocities are calculated accurately. However, they are not calculated at the same time as positions. So if velocities at a given time, t, are required they must be averaged as:

$$v(t) = \frac{1}{2}\left[v(t-\frac{\delta t}{2}) + v(t+\frac{\delta t}{2})\right] \tag{3.21}$$

This algorithm is easily applied to complex molecules. It may also be combined with constraint algorithms, such as the SHAKE procedure (see section 3.2.2). Its speed and simplicity often makes it a first choice for molecular simulation.

The velocity Verlet algorithm

This is another modification of the Verlet algorithm, allowing for the calculation of positions, velocities and accelerations at a given time. This results in more accurate trajectories and less drift of the total energy. However, the increase in precision also comes with increase in computational cost.

Beeman's algorithm

Beeman's algorithm is also related to Verlet algorithm. Beeman's algorithm [80] uses more accurate expressions, that allows for more accurate velocities and provides better energy conservation. This method is computationally more expensive and is only used when high accuracy is required.

3.2.2 Constraints

To be able to calculate a realistic molecular model, many degrees of freedom need to be accounted for[1]. Internal degrees of freedom in the molecule vary in their frequencies, from under 10^{12} to 10^{14} Hz, with the slowest being torsional motion and fastest bond stretching. The latter limits the size of the time step, by such making the calculation more expensive. It is a common practice to constrain bond length and occasionally bond angles within the molecule.

There are algorithms available to implement these constraints, the most popular ones are SHAKE [81], and LINCS [82]. SHAKE is the first constraint algorithm developed, and can be implemented as a modification of the Verlet and leap-frog algorithms, see 3.2.1, where the calculated velocities, $v(r)$, are then modified to agree with the constraints and preserve bond (and rarely angle) lengths. There are further extensions of SHAKE algorithm, such as RATTLE (for the use with velocity Verlet algorithms) [80] and SETTLE [83].

LINCS (Linear Constraint Solver) is a newer algorithm, based on the EEM (Edberg, Evans and Morriss) [84] algorithm, developed in 1986. LINCS has shown to be faster and more stable then SHAKE. Additionally, a parallel version of LINCS has recently become available [85].

System sizes accessible to atomistic simulations are of the order of thousands of atoms. These are typically enclosed in a simulation box. The molecules on the surface of the box will experience different forces to the ones in the centre. By imposing periodic boundary conditions, i.e. by surrounding the simulation box with 'pseudo' simulation boxes, which are clone of the original one, results in a simulation with bulk properties across the whole of the original box. When a molecule leaves the box on one side, as shown on the figure 3.10, it will enter the neighbouring 'pseudo' box, and by such re-enter the initial box from the opposite side.

To be able to perform calculations at a reasonable speed, the interaction of the

[1] A molecule with N atoms has $3N-6$ normal modes of vibration.

molecule is only calculated with its direct neighbours. The standard way is to use a Verlet list [79] that, for every particle, defines a surrounding shell at a distance slightly larger than a predefined cut-off radius. The cut-off distance should be less or equal to half of the box size.

3.2.3 Thermodynamic ensemble

Computational studies are performed in microscopic simulations, but they attempt to mimic the behaviour of macroscopic systems. To be able to do so effectively, a thermodynamic ensemble is required. A thermodynamic ensemble is a collection of systems having different microscopic states but have an identical macroscopic or thermodynamic state. There are different ensembles typically used in simulation:

- **Microcanonical**: The thermodynamic state with fixed number of atoms, N, a fixed volume, V, and a fixed energy, E. This ensemble describes an isolated system.
- **Canonical**: The collection of systems with fixed number of atoms, N, a fixed volume, V, and a fixed temperature, T.
- **Isothermal-isobaric**: In this ensemble the number of atoms, N, the pressure, P, and the temperature, T, are fixed.
- **Isoenthalpic-isobaric**: This ensemble is characterised by a constant number of atoms, N, the pressure, P, and the enthalpy, H.
- **Grand canonical**: Volume, V, temperature, T, and chemical potential, μ, are all fixed.

Molecular dynamics calculations can be performed in a number ensembles. The default ensemble for many calculation is the microcanonical, with constant number of particles, volume and energy. Sometimes it is in our interest to perform calculations at constant temperature or pressure.

Temperature coupling

Temperature coupling is used to control the temperature of the system. The temperature of the system is related to the average kinetic energy, so the temperature can be controlled by scaling velocities. There are a number of methods developed for this purpose, one of which is the **Berendsen thermostat** [86]. This algorithm mimics a weak coupling of the system to an external heat bath at a given temperature, T_0. A deviation of the system temperature from the T_0 is given by

$$\frac{dT}{dt} = \frac{T_0 - T}{\tau} \tag{3.22}$$

where τ is a time constant. This method does not generate a proper canonical ensemble, as it suppresses the fluctuation of the kinetic energy. This will affect the results only for very small systems or when calculating the kinetic energy itself. The velocities are rescaled by a scaling factor, λ

$$\lambda = \left[1 + \frac{\Delta t}{\tau_t}\left(\frac{T_0}{T\left(t - \frac{\Delta t}{2}\right)} - 1\right)\right]^{\frac{1}{2}} \tag{3.23}$$

where τ_T is close to but not equal to τ, the time constant. In practice the scaling factor is limited to avoid too large scaling at an individual time step, which can lead to failure of the calculation.

The **velocity rescaling thermostat** [87] is similar to Berendsen thermostat, but it allows one to produce the correct ensemble by addition of a random force.

The two algorithms discussed above are weak coupling and are used for relaxing systems to a desired temperature. To probe the correct canonical ensemble the **Nosé-Hoover** temperature coupling [88, 89] is frequently used. In this method, a thermal reservoir and a friction coefficient are introduced into the equation of motion, thereby allowing for kinetic energy changes in the system.

Pressure coupling

Similarly to temperature coupling, the system can be coupled to a pressure bath. The simplest procedure is the **Berendsen algorithm** for pressure coupling. This rescales the coordinates and box vectors at every step towards a given reference pressure, P_0. So that

$$\frac{dP}{dt} = \frac{P_0 - P}{\tau_P} \tag{3.24}$$

Rescaling is performed by applying the scaling matrix, μ,

$$\mu = \delta_{ij} - \frac{\Delta t}{3\tau_P}\beta_{ij}\left[P_{0ij} - P_{ij}(t)\right] \tag{3.25}$$

where β is the isothermal compressibility of the system.

In cases where fluctuations in pressure are important, the exact thermodynamic ensemble should be generated. As discussed above, this is not feasible using weak coupling. This can be done using the **Parrinello-Rahman** pressure coupling method [90]. This approach is similar to the Nose- Hoover for temperature coupling, where the equation of motion for particles is updated at every step.

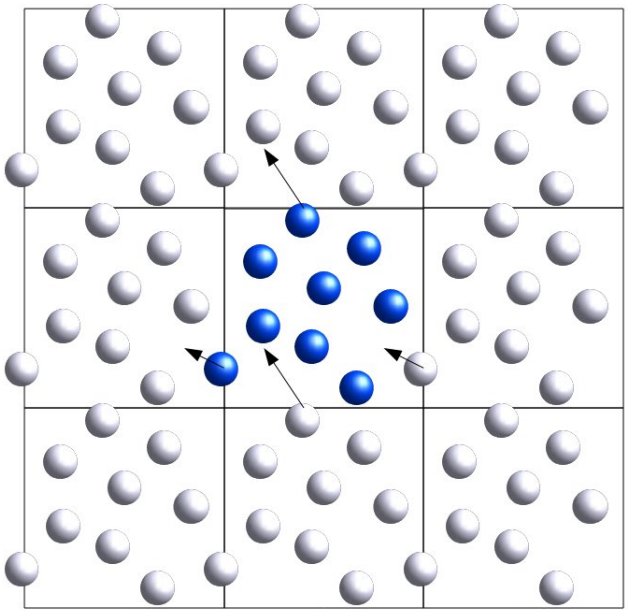

Figure 3.10: *The two dimensional illustration of periodic boundary condition: the box containing blue atoms is the simulation box, while the boxes containing grey atoms are 'pseudo' boxes, that mimic the behaviour of the main simulation box.*

3.3 The force field

The correct choice of force field is essential for performing accurate simulations. A large number of force fields have been developed through the last decades. In this section we overview and compare the available force fields.

A force field consists of two parts, the mathematical functional form (equation 3.1) and a set of parameters depending on the nature of atoms involved in a specific interaction. The combination of a functional form and and appropriate set of parameters, describes the potential energy of the system.

Ideally, force fields are designed to be transferable between a number of molecular systems. Nevertheless, some are more suitable for particular systems and states than others. Any comparison of force field performance should be done with a specific study in mind. Typical tests consist of comparisons with experimental physical properties such as density, boiling and melting temperatures, protein secondary structure (for amino acids parameter sets), as well as agreement with vapour-liquid coexistence data and reproduction of thermodynamic properties.

Most force fields represent all atom systems, with a few describing united atom systems, i.e. having hydrogens united to the neighbouring heavy atoms. United atom representation have less interaction sites, by such speeding up the calculations. Not every system can be accurately represented with united atoms. For example, systems having hydrogen bonding, benzene rings, polar and charged systems require an all atom representation.

Further reduction of atoms leads to coarse grained models. The general problem of a coarse grained force field is that the loss of fine information caused by grouping atoms limits its transferability [91–93]. Coarse graining is discussed independently in section 7. The following overview is aimed at finding the most suitable available force field, transferable over a range of temperatures and capable of reproducing crystallisation phenomena.

3.3.1 Overview of available force fields

Our study is aimed at the simulation of long chain *n*-alkane molecules, aliphatic and aromatic solvents as well as additives containing hydroxyl, carboxyl and phenyl groups. The systems are studied at a variety of temperatures, including the crystallisation temperature. The main requirement for our force field of choice is a good reproduction of these structural and physical properties. These characteristics will be highlighted, for every force field, in the discussion below.

The force fields selected for this overview fall into two categories, all atom and united atom.

All atom force fields:

- OPLS-AA (Optimised Potentials for Liquid Simulations)
- CHARMM (Chemistry at HARvard Macromolecular Mechanics)
- AMBER (Assisted Model Building with Energy Refinement)
- UFF (Universal Force Field)

United atom force fields:

- OPLS
- CHARMM
- GROMOS (GROningen MOlecular Simulation)
- TraPPE (Transferable Potentials for Phase Equilibria)

Universal Force Field

UFF [94] was developed by Rappe *et al.* in 1992. It is an unusual force field, unlike others it covers the full periodic table, from hydrogen to lawrencium. The parameters are estimated by using given general rules, converting values associated to an individual element into the intermolecular and intramolecular parameters required for calculations.

Table 3.1 shows the performance of the force field with respect to experimental results [95]. Since there is no consistency within simulation and experiment, this force field is not suitable for the condensed state calculations necessary in our work. This force field could be an interesting choice for calculations involving exotic molecules.

Assisted Model Building with Energy Refinement

AMBER is both a molecular dynamics package and a set of force fields [96, 97]. The force field uses 12-6 Lennard-Jones (equation 7.8) with parameters computed by Lorentz-Berthelot mixing rules (equations 3.10 and 3.11). 1-4 interactions are scaled by $\frac{1}{2}$ and Columbic interactions are represented by point charges and scaled by $\frac{5}{6}$. Bond and angle interactions are expressed as harmonic potentials and torsional interactions as cosine series.

AMBER force fields are all atom only, parameterised for biomolecular simulations, and contain 20 common amino acids as functional groups. More recently, there have been some works put in to extend the AMBER force field to a wider range of systems through the development of the general AMBER force field (GAFF) [98].

Chemistry at HARvard Molecular Mechanics

CHARMM is also molecular dynamics program [99], as well as a set of force fields. CHARMM22, [100, 101] CHARMM27 and [102] CgenFF [103] are all atom force fields, whereas CHARMM19 [104] is united atom. The potential function used by all these force fields is of the same form as AMBER, while non bonded parameters are not scaled.

All of these force fields, apart from more recent CgenFF, are parameterised for biomolecular simulations, similarly to AMBER, contains 20 common amino acid groups. CgenFF was created as a general force field for drug-type molecules, to accompany the rest of the force fields.

Optimised Potentials for Liquid Simulations

OPLS force field was developed by the group of William L. Jorgensen. This contains several sets of parameters, for both all atom and united atom calculations, that can also be mixed [105, 106]. The potential functions are the same as in AMBER, Lennard-Jones is computed by geometrical mean mixing rules (equation 3.12). Both Lennard-Jones and Coulombic parameters are scaled by a factor of $\frac{1}{2}$.

OPLS was initially parameterised not only for biomolecular systems, but also for organic liquids. The parameters were optimized to fit experimental densities and heats of vaporisation of liquids, as well as gas-phase torsional profiles. The force field is being constantly updated, and many independent modifications have been developed [107, 108]. OPLS is, arguably, the most widely parameterised force field available.

GROningen MOlecular Simulation

GROMOS is also both a molecular dynamics package [109] and the complementary force field. The first was also the base for the GROMACS package [110] used in this work. GROMOS is a united atom force field, with ongoing improvements being produced on regular basis. The current most widely used version of the force field are GROMOS-96 [111] and its latest update GROMOS-05 [109]. This force field is also aimed at biomolecular calculations, and is parameterised for proteins.

Unlike AMBER, the Lennard-Jones parameters for heteroatomic interactions are readily provided by the force field and should not be calculated via mixing rules. The force field uses a quartic expression for the bond length, a harmonic cosine potential for angle bending and a single cosine series for torsional angle potential.

Transferable Potentials for Phase Equilibria

The TraPPE force field evolved from a previous force field, SKS (Smit-Karaborni-Siepmann) [112]. SKS was developed in Shell laboratories in the 1990s, and is the first force field aimed at reproducing the properties of the main components in fuels,

n-alkanes. The TraPPE force field contains parameters for alkanes and aromatics, as well as some oxygen, sulphur and nitrogen containing compounds.

Figure 3.11 shows the comparison between OPLS and SKS force field for a range of alkanes [113]. SKS has a better agreement for longer *n*-alkanes than OPLS, however, it overestimates the properties of shorter chains.

TraPPE is mainly a united atom force field [114–120], with two explicit hydrogen models [121, 122]. Unlike most of united atom force fields, in TraPPE hydrogen atoms are also united in aromatic interactions.

TraPPE's functional form is the same as in AMBER, including mixing rules. Coulombic terms are scaled by $\frac{1}{2}$. Since the force field was developed with Monte Carlo calculations, there is no improper torsional angle term that can lead to incorrect conformations when performing molecular dynamics.

The force field is parameterised to fit the vapour-liquid coexistence curve for small organic molecules. This type of force field looks very promising for the research in this thesis, so the following section is dedicated to the the evaluation of TraPPE with respect to the other discussed ones.

3.3.2 Force fields evaluation

Table 3.2 shows a comparison between OPLS, SKS and TraPPE force fields for *n*-octane [114]. With TraPPE, two systems of 200 and 1600 molecules are tested. Interestingly,TraPPE performance is lower for the bigger system, making the force field system size dependent. Nonetheless, TraPPE shows the best agreement for both boiling and critical temperatures.

Nuno *et al.* [123] performed a comparative study for 1-octanol at different temperatures for a wide variety of united atom force fields, as well as an all atom force field, OPLS-AA. The production times were also evaluated for every method. Results are summarised in Table 3.3.

Table 3.1: *Comparison of calculated and experimental liquid densities at 101 kPa for propanamide (383 K) and ethanethiol (298 K) and crystallisation temperatures of isopropanol and pentane [95]*

	Density, g/ml		Crystallisation Temperature, K	
	propanamide	ethanethiol	isopropanol	pentane
UFF	0.678	0.824	497	627
exp	0.926	0.833	508	470

Table 3.2: *Comparison of normal boiling points and critical properties (β = 0.32) obtained with OPLS-UA, SKS, and TraPPE force fields with the experimental ones for n-octane [114].*

Method	T_B, K	T_C, K	ρ_C, g/mL	p_C, MPa
OPLS	442	656	0.235	2.8
SKS	417	607	0.228	3.0
TraPPE-200	388	568	0.240	2.7
TraPPE-1600	386	570	0.239	2.6
expt	399	569	0.232	2.5

Table 3.3: *Comparison of heat of vaporisation and densities (at 1 bar) of 1-octanol, produced by a range of force fields, to experimental measurements [123].*

T, K	280		400		298		time
Method	$\rho, \frac{kg}{m^3}$	$dev, \%$	$\rho, \frac{kg}{m^3}$	$dev, \%$	$\Delta_v H, \frac{kJ}{mol}$	$dev, \%$	hr/ns
G43A2	864.4	3.4	779.7	5.0	64.4	-10.5	1.09
G53A5	867.9	3.8	785.3	5.7	59.5	-17.3	1.09
OPLS-UA	859.5	2.8	773.5	4.1	72.3	0.4	1.19
OPLS-AA	841.8	0.7	719.5	-3.1	70.7	-1.8	8.00
TraPPE	837.0	0.08	744.5	0.2	67.0	-6.9	1.15
expt	836.26		742.75		71.98		–

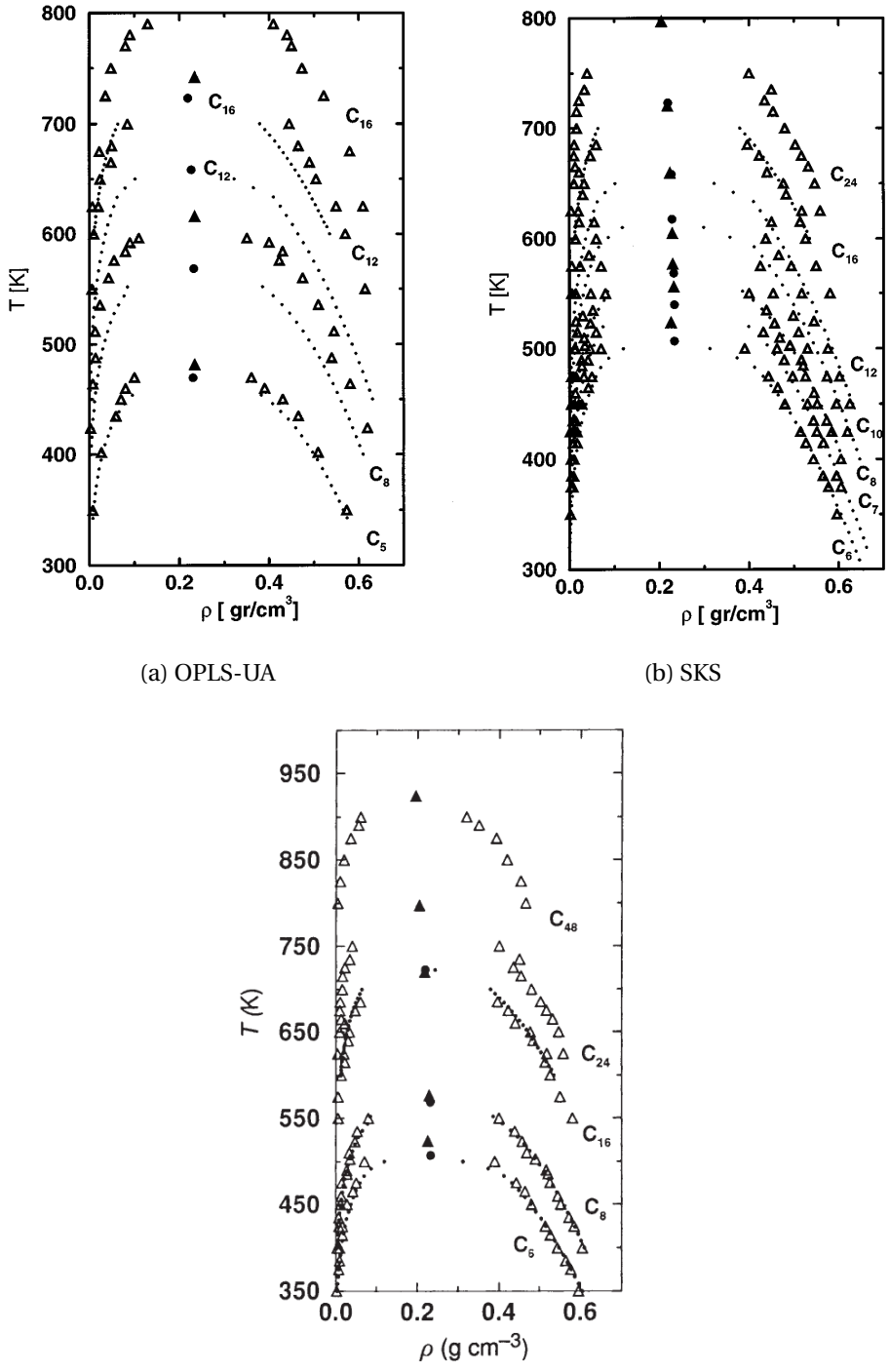

(a) OPLS-UA

(b) SKS

(c) SKS-longer alkanes

Figure 3.11: *Vapour-Liquid equilibria of various alkanes: open triangles - calculations with with OPLS (a) and SKS (b)(c), small dots - experimental data. The filled triangle is an estimate of critical point using the simulation and large dots are experimental critical points [113].*

Table 3.3 shows that OPLS-AA and TraPPE provide the best overall agreement with experimental data. All atom calculations are always more computationally demanding than united atom ones, due to the presence of the hydrogens. In this case OPLS-AA required eight hours of calculations per each nanosecond of simulation, while united atom ones only needed just over one hour.

From the comparative studies presented above, one may conclude that TraPPE force field is the most suitable for the problem in mind. The only limitation is that TraPPE contains only a very small number of parameters, and does not account for improper torsional angles.

3.3.3 Force field parameters used in this work

For our calculations, we adopted the TraPPE united atom force field. As mentioned earlier (section 3.3.1), the force field does not include improper dihedral angles. For this reason, we tested the effect of the addition of improper dihedrals in the force field on a 1,2-dimethylbenzene [2] system. The xylene molecule was built with the TraPPE force field parameters as given in literature [116]. A periodic box of 250 molecules was simulated at 1 bar and 300 K for 10 ns. Figure 3.12 illustrates the geometry of an equilibrated xylene molecule.

Figure 3.12 shows that dihedral interactions alone are not sufficient to preserve planar geometry of the molecule. To prevent incorrect molecular conformations, one should treat benzene rings as rigid units, or include a term for improper dihedral angles. The first solution is implemented by imposing a value for the angle and a permitted fluctuation around it. The parameters for improper torsions will differ depending on the formulation of the force field and can either be borrowed from other force fields or calculated. All GROMOS force fields include improper torsions as a constrained angle. Using the GROMOS formulation is a straightforward input, when only the angle needs to be defined.

[2] 1,2-dimethylbenzene is a systematic name for o-xylene. In the following it will be abbreviated to xylene, as no other isomers are investigated in this work

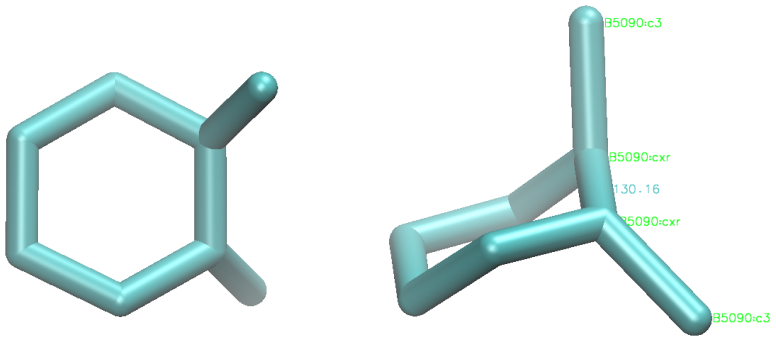

Figure 3.12: *Geometrical conformation of o-xylene molecule calculated without improper dihedral angles. Top view (a) and side view (b), showing a measured dihedral angle along the* $CH_3 - CH_2 - CH_2 - CH_3$ *bond.*

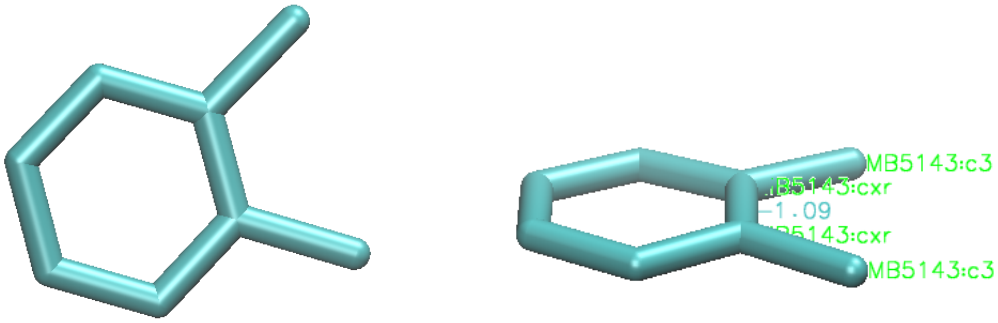

Figure 3.13: *Geometrical conformation of o-xylene molecule calculated with improper dihedral angles. Top view (a) and side view (b), showing a measured dihedral angle along the* $CH_3 - CH_2 - CH_2 - CH_3$ *bond.*

The Automated Topology Builder (ATB) of Malde *et al.* [124] was used to evaluate the necessary improper torsions. ATB is an online tool assisting the development of a force field. The force field is obtained via a few steps, starting from calculating the molecular geometry quantum mechanically. The improper torsion angles obtained in such manner are included into a molecular dynamic calculation and verified through the simulation. Figure 3.13 shows the geometry of the resulting xylene molecule. By comparing the two xylene structures, the importance of correct inclusion of improper dihedral is obvious.

Tables 3.4 and 3.5 provide non bonded and bonded parameters used in our calculations. A small number of parameters (marked in the table) were borrowed from OPLS-UA [105], and improper torsions for aromatics have been calculated using ATB [124].

Table 3.4: *Non bonded force field parameters used in further calculations, given in the units used in GROMACS.*

Atom type	$\epsilon, \frac{kJ}{mol}$	σ, nm	charge
C3	0.1852	0.375	0
C2	0.3827	0.395	0
C1	0.0833	0.468	0
C	0.1662	0.385	0
CH_2 (aromatic)	0.42035	0.3695	0
CH(aro link)	0.1746	0.388	0
C(ether)	0.0833	0.433	0.25
CH_2(ether)	0.0801	0.395	0.25
CH_3(ether)	0.8152	0.375	0.25
-O-(ether)	0.4572	0.28	-0.5
C=(ketone)	0.33285	0.382	0.67*
=O	0.6573	0.305	-0.42
O(alcohol)	0.657	0.305	-0.7
H(alcohol)	0.00	0.00	0.435
CH(aro link to alco)	0.1746	0.388	0.265

* The charge in the literature on carbon is 0.42, in this model charge has to be rebalanced since the group is adjacent to ether oxygen.

Table 3.5: *Bonded parameters used in further calculations, given in units for GROMACS.*

stretch	r_0, nm*
$CH_x - CH_y$	0.154
$C - O$	0.141
$C = O$	0.123
$CH_3 - C$ (carbonyl)	0.152
$CH_x - CH_y$ (aromatics)	0.14
$CH_x - O$(aromatics)	0.143
$O - H$ (alcohol)	0.0945

* Bonds in TraPPE force field are rigid, so no stretching force constant is given.

[Continued]

bend	θ, deg	$k_\theta, \frac{kJ}{molrad^2}$
$CH_x - CH_2 - CH_y$	114	520
$CH_x - CH - CH_y$	112	520
$CH_x - C - CH_y$	109.47	520
$CH_3 - CH_y - O$	112*	418.5
$CH_x - O - CH_y$	112*	502.5
$CH_x - C - CH_y$ (carbonyl)	117.2	520
$CH_x - C - O$ (carbonyl)	117.2*	520*
$CH_x - C = O$	121.4*	520
$O - C = O$**	121.4*	520
$CH_x - CH_y - CH_z$	120	1488.8***
$CH_x - CH_y - CH_3$	120	1488.8

* In the later publication [125] slight improvements to these parameters were made. The work in this thesis began by the use of older parameters, that were preserved to maintain consistency of results.
** The original TraPPE force field did not include parameters for interaction, the interaction was assumed to be equivalent to the $CH_x - C - O$.
*** TraPPE force field states this angle as *rigid*, the value from OPLS-UA is used.

torsion	$C_1, \frac{kJ}{mol}$	$C_2, \frac{kJ}{mol}$	$C_3, \frac{kJ}{mol}$
$CH_x - CH_2 - CH_2 - CH_y$	5.9075	-1.3462	13.1675
$CH_x - CH_2 - CH - CH_y$	7.1343	-1.861	7.3428
$CH_x - CH - CH - CH_y$	7.1343	-1.861	7.3428
$CH_x - CH_2 - C - CH_y$	0.0	0.0	7.676
$CH_x - CH_y - O - CH_z$	12.0697	-2.7248	9.288
$CH_x - CH_y - CH_z - O-$	2.9391	-0.8876	12.8116
$CH_x - CH_y - CH_z = O$	-12.2623	0.9625	-4.8793
$CH_x - O - C = O*$	2.9391	-0.8876	12.8116
$CH_x - CH_2 - CH_2 - CH_y$	5.9075	-1.3462	13.1675

improper torsion	$\phi, degrees$
$CH_w - CH_x - CH_y - CH_z$(aromatic)**	167.36

* The parameter was obtained from OPLS-UA. In the later TraPPE publication [125] the parameter became available, but the initial model was preserved through the work of this thesis to maintain consistency of results.
** Obtained through ATB, only the constraint angle is given.

Bibliography

[1] Online Etymology Dictionary. *http://dictionary.reference.com/browse/paraffin*, December 2011.

[2] G. Totten. The timeline of highlights from the histories of ASTM committee D02 and the petroleum industry. *ASTM standardisation News*, pages 18–27, 2004.

[3] NationMaster: Energy statistics. *http://www.nationmaster.com/statistics*, 2011.

[4] S. Aoshima. *Wax crystal control, nanocomposites, stimuli-responsive polymers*, volume 210 of *Advances in polymer science*. Springer, 2008.

[5] G. Yu-hui and S. Ben-xian. QSAR research of the activity of span surfactants as wax antisettling additives for diesel. *Energy & fuels*, 20(4):1579–1583, 2006.

[6] E. Marie, Y. Chevalier, S. Brunel, F. Eydoux, L. Germanaud, and P. Flores. Settling of paraffin crystals in cooled middle distillate fuels. *Journal of Colloid and Interface Science*, 269(1):117 – 125, 2004.

[7] Kristofer Paso, M. Senra, Y. Yi, A. M. Sastry, and H. Scott Fogler. Paraffin polydispersity facilitates mechanical gelation. *Industrial & Engineering Chemistry Research*, 44(18):7242–7254, 2005.

[8] D.L. Dorset. The bridged lamellar structure of synthetic waxes determined by electron crystallographic analysis. *The Journal of Physical Chemistry B*, 104(19):4613–4617, 2000.

[9] A. Aiyejina, D.P. Chakrabarti, A. Pilgrim, and M.K.S. Sastry. Wax formation in oil pipelines: A critical review. *International Journal of Multiphase Flow*, 37(7):671 – 694, 2011.

[10] S.R. Craig, G.P. Hastie, K.J. Roberts, and J.N. Sherwood. Investigation into the structures of some normal alkanes within the homologous series $C_{13}H_{28}$ to $C_{60}H_{122}$ using high-resolution synchrotron X-ray powder diffraction. *Jornal of Materials Chemistry*, 4:977–981, 1994.

[11] S. C. Nyburg and J. A. Potworowski. Prediction of unit cells and atomic coordinates for the n-alkanes. *Acta Crystallographica Section B: Structural Crystallography and Crystal Chemistry*, 29(2):347–352, 1973.

[12] H. M. M. Shearer and V. Vand. The crystal structure of the monoclinic form of n-hexatriacontant. *Acta Crystallographica*, 9(4):379–384, 1956.

[13] A. E. Smith. The crystal structure of the normal paraffin hydrocarbons. *The Journal of Chemical Physics*, 21(12):2229–2231, 1953.

[14] A.K. Winkel, J.K. Hobbs, and M.J. Miles. Annealing and melting of long-chain alkane single crystals observed by atomic force microscopy. *Polymer*, 41(25):8791–8800, 2000.

[15] G. Ungar, J. Stejny, A. Keller, I. Bidd, and M.C. Whiting. The crystallization of ultralong normal paraffins: the onset of chain folding. *Science*, 229(4711):386, 1985.

[16] SJ Organ, A. Keller, M. Hikosaka, and G. Ungar. Growth and nucleation rate minima in long n-alkanes. *Polymer*, 37(12):2517–2524, 1996.

[17] M. Dirand, M. Bouroukba, V. Chevallier, D. Petitjean, E. Behar, and V. Ruffier-Meray. Normal alkanes, multialkane synthetic model mixtures, and real petroleum waxes: Crystallographic structures, thermodynamic properties, and crystallization. *Journal of Chemical & Engineering Data*, 47(2):115–143, 2002.

[18] P. G. Vekilov. Nucleation. *Crystal growth & design*, 10(12):5007, 2010.

[19] I. J. Ford. Nucleation theorems, the statistical mechanics of molecular clusters, and a revision of classical nucleation theory. *Physical Review E*, 56(5):5615, 1997.

[20] Y.V. Mnyukh. The structure of normal paraffins and of their solid solutions. *Journal of Structural Chemistry*, 1:346–365, 1960.

[21] J. J. Retief, D. W. Engel, and E. G. Boonstra. X-ray powder diffractometric procedure for lattice parameter determination for long-chain molecules. *Journal of Applied Crystallography*, 18(3):150–155, 1985.

[22] S.R. Craig, G.P. Hastie, K.J. Roberts, A.R. Gerson, J.N. Sherwood, and R.D. Tack. Investigation into the structures of binary-, tertiary- and quinternary-mixtures of n-alkanes and real diesel waxes using high-resolution synchrotron X-ray powder diffraction. *Jornal of Materials Chemistry*, 8(4):859–869, 1998.

[23] A. M. Taggart, F. Voogt, G. Clydesdale, and K. J. Roberts. An examination of the nucleation kinetics of n-alkanes in the homologous series $C_{13}H_{28}$ to $C_{32}H_{66}$, and their relationship to structural type, associated with crystallization from stagnant melts. *Langmuir*, 12(23):5722–5728, 1996.

[24] D.L. Dorset and R. G. Snyder. Phase separation of a metastable three-component n-paraffin solid solution. *The Journal of Physical Chemistry B*, 103(16):3282–3286, 1999.

[25] A. Muller. The crystal structure of the normal paraffins at temperatures ranging from that of liquid air to the melting points. *Proceedings of the Royal Society of London. Series A*, 127(805):417–430, 1930.

[26] I. Denicolò, J. Doucet, and A. F. Craievich. X-ray study of the rotator phase of paraffins (III): Even-numbered paraffins $C_{18}H_{38}$, $C_{20}H_{42}$, $C_{22}H_{46}$, $C_{24}H_{50}$, and $C_{26}H_{54}$. *The Journal of Chemical Physics*, 78(3):1465–1469, 1983.

[27] J. Doucet, I. Denicolò, and A. Craievich. X-ray study of the rotator phase of the odd-numbered paraffins $C_{17}H_{36}$, $C_{19}H_{40}$, and $C_{21}H_{44}$. *The Journal of Chemical Physics*, 75(3):1523–1529, 1981.

[28] E.B. Sirota, H.E. King Jr, D.M. Singer, and H.H. Shao. Rotator phases of the normal alkanes: An X-ray scattering study. *The Journal of Chemical Physics*, 98:5809, 1993.

[29] E.B. Sirota and D.M. Singer. Phase transitions among the rotator phases of the normal alkanes. *The Journal of Chemical Physics*, 101:10873, 1994.

[30] E.B. Sirota, H.E.J. King, H.H. Shao, and D.M. Singer. Rotator phases in mixtures of n-alkanes. *The Journal of Physical Chemistry*, 99(2):798–804, 1995.

[31] A.J. Briard, M. Bouroukba, D. Petitjean, and M. Dirand. Models for estimation of pure n-alkanes' thermodynamic properties as a function of carbon chain length. *Journal of Chemical & Engineering Data*, 48(6):1508–1516, 2003.

[32] L.I. Rossemyr. Cold flow properties and response to cold flow improver of some typical fuel oils. *Industrial & Engineering Chemistry Product Research and Development*, 18(3):227–230, 1979.

[33] A. Heraud and B. Pouligny. How does a "cloud point" diesel fuel additive work? *Journal of Colloid and Interface Science*, 153(2):378 – 391, 1992.

[34] D. Merino-Garcia, M. Margarone, and S. Correra. Kinetics of waxy gel formation from batch experiments. *Energy & Fuels*, 21(3):1287–1295, 2007.

[35] P. Claudy, J.M. Létoffé, B. Neff, and B. Damin. Diesel fuels: determination of onset crystallization temperature, pour point and filter plugging point by differential scanning calorimetry. Correlation with standard test methods. *Fuel*, 65(6):861 – 864, 1986.

[36] J.L. Hutter, S. Hudson, C. Smith, A. Tetervak, and J. Zhang. Banded crystallization of tricosane in the presence of kinetic inhibitors during directional solidification. *Journal of Crystal Growth*, 273(1-2):292 – 302, 2004.

[37] E. Marie, Y. Chevalier, F. Eydoux, L. Germanaud, and P. Flores. Control of n-alkanes crystallization by ethylene–vinyl acetate copolymers. *Journal of Colloid and Interface Science*, 290(2):406 – 418, 2005.

[38] M.J. Mandell, J.P. McTague, and A. Rahman. Crystal nucleation in a three-dimensional lennard-jones system: A molecular dynamics study. *The Journal of Chemical Physics*, 64(9):3699–3702, 1976.

[39] K.W. Won. Thermodynamics for solid solution-liquid-vapor equilibria: wax phase formation from heavy hydrocarbon mixtures. *Fluid Phase Equilibria*, 30(0):265 – 279, 1986.

[40] K. Schou Pedersen, P. Skovborg, and H.P. Roenningsen. Wax precipitation from North Sea crude oils. 4. Thermodynamic modeling. *Energy & Fuels*, 5(6):924–932, 1991.

[41] K. Esselink, P.A.J. Hilbers, and B.W.H. Van Beest. Molecular dynamics study of nucleation and melting of n-alkanes. *The Journal of Chemical Physics*, 101(10):9033–9041, 1994.

[42] N. Waheed, M.S. Lavine, and G.C. Rutledge. Molecular simulation of crystal growth in n-eicosane. *The Journal of Chemical Physics*, 116(5):2301–2309, 2002.

[43] J.P. Ryckaert, I.R. McDonald, and M.L. Klein. Disorder in the pseudohexagonal rotator phase of n-alkanes: molecular-dynamics calculations for tricosane. *Molecular Physics*, 67(5):957–979, 1989.

[44] J.P. Ryckaert, M.L. Klein, and I.R. McDonald. Disorder at the bilayer interface in the pseudohexagonal rotator phase of solid n-alkanes. *Physical review letters*, 58(7):698–701, 1987.

[45] J.P. Ryckaert, M.L. Klein, and I.R. McDonald. Computer simulations and the interpretation of incoherent neutron scattering experiments on the solid rotator phases of long-chain alkanes. *Molecular Physics*, 83(3):439–458, 1994.

[46] A. Marbeuf and R. Brown. Molecular dynamics in n-alkanes: Premelting phenomena and rotator phases. *The Journal of Chemical Physics*, 124(5):054901, 2006.

[47] M. Cao, A.P. Malanoski, J.W. Schroer, and P.A. Monson. Solid–fluid equilibrium for organic molecules: understanding the link between molecular structure and phase diagrams. *Fluid Phase Equilibria*, 228-229(0):75 – 82, 2005.

[48] N. Wentzel and S.T. Milner. Crystal and rotator phases of n-alkanes: A molecular dynamics study. *The Journal of Chemical Physics*, 132(4):044901, 2010.

[49] Y. Tsuchiya, H. Hasegawa, and T. Iwatsubo. Prediction of the melting point of n-alkanes using the molecular dynamics method. *The Journal of Chemical Physics*, 114(5):2484–2488, 2001.

[50] D. M. Duffy and P. M. Rodger. The structure of liquid heptane at wax surfaces. *Physical Chemistry Chemical Physics*, 3:3580–3585, 2001.

[51] D.M. Duffy, C. Moon, and P. M. Rodger. Computer-assisted design of oil additives: Hydrate and wax inhibitors. *Molecular Physics*, 102(2):203–210, 2004.

[52] D. M. Duffy and P. M. Rodger. Wax inhibition with poly(octadecyl acrylate). *Physical Chemistry Chemical Physics*, 4:328–334, 2002.

[53] Y.H. Jang, M. Blanco, J. Creek, Y. Tang, and W. A. Goddard. Wax inhibition by comb-like polymers:âĂĽ Support of the incorporationâĹŠperturbation mechanism from molecular dynamics simulations. *The Journal of Physical Chemistry B*, 111(46):13173–13179, 2007. PMID: 17975910.

[54] J. Zhang, C. Wu, W. Li, Y. Wang, and H. Cao. DFT and MM calculation: the performance mechanism of pour point depressants study. *Fuel*, 83(3):315 – 326, 2004.

[55] J. Zhang, M. Zhang, J. Wan, and W. Li. Theoretical study of the prohibited mechanism for ethylene/vinyl acetate co-polymers to the wax crystal growth. *The Journal of Physical Chemistry B*, 112(1):36–43, 2008.

[56] C. Wu, J. Zhang, W. Li, and N. Wu. Molecular dynamics simulation guiding the improvement of EVA-type pour point depressant. *Fuel*, 84(16):2039 – 2047, 2005.

[57] W.C. Hollyday. Fuel oil with improved flow properties, 1971. US Patent 3,620,696.

[58] N. Feldman. Combination of ethylene polymer, polymer having alkyl side chains, and nitrogen containing compound to improve cold flow properties of distillate fuel oils, July 8 1980. US Patent 4,211,534.

[59] R.D. Tack, S.L. Pearce, and A. Rossi. Middle distillate compositions with improved cold flow properties, November 27 1991. EP Patent 0,153,176.

[60] R. Tack. Additives for fuel oils, June 23 2010. EP Patent 2,199,377.

[61] D.C. Young. *Computational chemistry: a practical guide for applying techniques to real world problems*. Wiley-Interscience, 2001.

[62] F. Jensen. *Introduction to computational chemistry*. John Wiley & Sons, 2007.

[63] D.C. Rapaport. *The art of molecular dynamics simulation*. Cambridge University Press, 2004.

[64] CECAM - Centre Européen de Calcul Atomique et Moléculaire. *http://www.cecam.org/*, 2012.

[65] G.A. Voth. *Coarse-graining of condensed phase and biomolecular systems*. CRC Press, 2009.

[66] S.O. Nielsen, R.E. Bulo, P.B. Moore, and B. Ensing. Recent progress in adaptive multiscale molecular dynamics simulations of soft matter. *Physical Chemistry Chemical Physics*, 12(39):12401–12414, 2010.

[67] P.M. Morse. Diatomic molecules according to the wave mechanics. II. Vibrational levels. *Physical Review*, 34:57–64, 1929.

[68] G. Mie. Zur kinetischen Theorie der einatomigen Körper. *Annalen der Physik*, 316(8):657–697, 1903.

[69] A. Warshel and S. Lifson. Consistent force field calculations. II. Crystal structures, sublimation energies, molecular and lattice vibrations, molecular conformations, and enthalpies of alkanes. *The Journal of Chemical Physics*, 53:582, 1970.

[70] D.N.J. White. A computationally efficient alternative to the Buckingham potential for molecular mechanics calculations. *Journal of Computer-Aided Molecular Design*, 11(5):517–521, 1997.

[71] J. E. Jones. On the determination of molecular fields. I. From the variation of the viscosity of a gas with temperature. *Proceedings of the Royal Society of London. Series A*, 106(738):441–462, 1924.

[72] H. A. Lorentz. Über die Anwendung des Satzes vom Virial in der kinetischen Theorie der Gase. *Annalen der Physik*, 248(1):127–136, 1881.

[73] R.J. Good and C.J. Hope. New combining rule for intermolecular distances in intermolecular potential functions. *The Journal of Chemical Physics*, 53(2):540–543, 1970.

[74] B. E. F. Fender and Jr. G. D. Halsey. Second virial coefficients of Argon, Krypton, and Argon-Krypton mixtures at low temperatures. *The Journal of Chemical Physics*, 36(7):1881–1888, 1962.

[75] H.J. Böhm and R. Ahlrichs. A study of short-range repulsions. *The Journal of Chemical Physics*, 77(4):2028–2034, 1982.

[76] M.D. Pena, C. Pando, and J.A.R. Renuncio. Combination rules for intermolecular potential parameters. II. Rules based on approximations for the long-range dispersion energy and an atomic distortion model for the repulsive interactions. *The Journal of Chemical Physics*, 76(1):333–339, 1982.

[77] C.L. Kong. Combining rules for intermolecular potential parameters. II. Rules for the Lennard-Jones (12–6) potential and the Morse potential. *The Journal of Chemical Physics*, 59(5):2464–2467, 1973.

[78] B. J. Alder and T. E. Wainwright. Studies in Molecular Dynamics. I. General Method. *The Journal of Chemical Physics*, 31(2):459–466, 1959.

[79] L. Verlet. Computer "Experiments" on classical fluids. I. Thermodynamical properties of Lennard-Jones molecules. *Physical Review*, 159:98–103, Jul 1967.

[80] D. Beeman. Some multistep methods for use in molecular dynamics calculations. *Journal of Computational Physics*, 20(2):130 – 139, 1976.

[81] J.P. Ryckaert, G. Ciccotti, and H.J.C. Berendsen. Numerical integration of the cartesian equations of motion of a system with constraints: molecular dynamics of n-alkanes. *Journal of Computational Physics*, 23(3):327 – 341, 1977.

[82] B. Hess, H. Bekker, H.J.C. Berendsen, and J.G.E.M. Fraaije. LINCS: A linear constraint solver for molecular simulations. *Journal of Computational Chemistry*, 18(12):1463–1472, 1997.

[83] S. Miyamoto and P.A. Kollman. SETTLE: An analytical version of the SHAKE and RATTLE algorithm for rigid water models. *Journal of Computational Chemistry*, 13(8):952–962, 1992.

[84] R. Edberg, D.J. Evans, and G.P. Morriss. Constrained molecular dynamics: Simulations of liquid alkanes with a new algorithm. *The Journal of Chemical Physics*, 84(12):6933–6939, 1986.

[85] B. Hess. P-LINCS: A parallel linear constraint solver for molecular simulation. *Journal of Chemical Theory and Computation*, 4(1):116–122, 2008.

[86] H.J.C. Berendsen, J.P.M. Postma, W.F. Van Gunsteren, A. DiNola, and J.R. Haak. Molecular dynamics with coupling to an external bath. *The Journal of Chemical Physics*, 81(8):3684–3690, 1984.

[87] G. Bussi, D. Donadio, and M. Parrinello. Canonical sampling through velocity rescaling. *The Journal of Chemical Physics*, 126(1):014101, 2007.

[88] S. Nosé and M.L. Klein. Constant pressure molecular dynamics for molecular systems. *Molecular Physics*, 50(5):1055–1076, 1983.

[89] S. Nosé. A unified formulation of the constant temperature molecular dynamics methods. *The Journal of Chemical Physics*, 81(1):511–519, 1984.

[90] M. Parrinello and A. Rahman. Polymorphic transitions in single crystals: A new molecular dynamics method. *Journal of Applied Physics*, 52(12):7182–7190, 1981.

[91] P. Carbone, H.A.K. Varzaneh, X. Chen, and F. Müller-Plathe. Transferability of coarse-grained force fields: The polymer case. *The Journal of Chemical Physics*, 128(6):064904, 2008.

[92] H. Fukunaga, J. Takimoto, and M. Doi. A coarse-graining procedure for flexible polymer chains with bonded and nonbonded interactions. *The Journal of Chemical Physics*, 116(18):8183–8190, 2002.

[93] T. Vettorel and H. Meyer. Coarse graining of short polythylene chains for studying polymer crystallization. *Journal of Chemical Theory and Computation*, 2(3):616–629, 2006.

[94] A. K. Rappe, C. J. Casewit, K. S. Colwell, W. A. Goddard, and W. M. Skiff. UFF, a full periodic table force field for molecular mechanics and molecular dynamics simulations. *Journal of the American Chemical Society*, 114(25):10024–10035, 1992.

[95] M.G. Martin. Comparison of the AMBER, CHARMM, COMPASS, GROMOS, OPLS, TraPPE and UFF force fields for prediction of vapor–liquid coexistence curves and liquid densities. *Fluid Phase Equilibria*, 248(1):50 – 55, 2006.

[96] W.D. Cornell, P. Cieplak, C.I. Bayly, I.R. Gould, K.M. Merz, D.M. Ferguson, D.C. Spellmeyer, T. Fox, J.W. Caldwell, and P.A. Kollman. A second generation force field for the simulation of proteins, nucleic acids, and organic molecules. *Journal of the American Chemical Society*, 117(19):5179–5197, 1995.

[97] Y. Duan, C. Wu, S. Chowdhury, M.C. Lee, G. Xiong, W. Zhang, R. Yang, P. Cieplak, R. Luo, T. Lee, J. Caldwell, J. Wang, and P. Kollman. A point-charge force field for molecular mechanics simulations of proteins based on condensed-phase quantum mechanical calculations. *Journal of Computational Chemistry*, 24(16):1999–2012, 2003.

[98] J. Wang, R.M. Wolf, J.W. Caldwell, P.A. Kollman, and D.A. Case. Development and testing of a general amber force field. *Journal of Computational Chemistry*, 25(9):1157–1174, 2004.

[99] B. R. Brooks, C. L. Brooks, A. D. Mackerell, L. Nilsson, R. J. Petrella, B. Roux, Y. Won, G. Archontis, C. Bartels, S. Boresch, A. Caflisch, L. Caves, Q. Cui, A. R. Dinner, M. Feig, S. Fischer, J. Gao, M. Hodoscek, W. Im, K. Kuczera, T. Lazaridis, J. Ma, V. Ovchinnikov, E. Paci, R. W. Pastor, C. B. Post, J. Z. Pu, M. Schaefer, B. Tidor, R. M. Venable, H. L. Woodcock, X. Wu, W. Yang, D. M. York, and M. Karplus. CHARMM: The biomolecular simulation program. *Journal of Computational Chemistry*, 30(10):1545–1614, 2009.

[100] A. D. MacKerell Jr, D. Bashford, M. Bellott, R. L. Dunbrack Jr, J. D. Evanseck, M. J. Field, S. Fischer, J. Gao, H. Guo, S. Ha, D. Joseph-McCarthy, L. Kuchnir, K. Kuczera, F. T. K. Lau, C. Mattos, S. Michnick, T. Ngo, D. T. Nguyen, B. Prodhom, W. E. Reiher, B. Roux, M. Schlenkrich, J. C. Smith, R. Stote, J. Straub, M. Watanabe, J. Wiorkiewicz-Kuczera, D. Yin, and M. Karplus. All-atom empirical potential for molecular modeling and dynamics studies of proteins. *The Journal of Physical Chemistry B*, 102(18):3586–3616, 1998.

[101] A.D. Mackerell Jr, M. Feig, and C.L. Brooks III. Extending the treatment of backbone energetics in protein force fields: Limitations of gas-phase quantum

mechanics in reproducing protein conformational distributions in molecular dynamics simulations. *Journal of computational chemistry*, 25(11):1400–1415, 2004.

[102] A.D. MacKerell Jr, N. Banavali, and N. Foloppe. Development and current status of the CHARMM force field for nucleic acids. *Biopolymers*, 56(4):257–265, 2000.

[103] K. Vanommeslaeghe, E. Hatcher, C. Acharya, S. Kundu, S. Zhong, J. Shim, E. Darian, O. Guvench, P. Lopes, I. Vorobyov, et al. CHARMM general force field: A force field for drug-like molecules compatible with the CHARMM all-atom additive biological force fields. *Journal of Computational Chemistry*, 31(4):671–690, 2010.

[104] W. E. Reiher. *Theoretical studies of hydrogen bonding*. PhD thesis, Harvard University, 1985.

[105] W.L. Jorgensen and J. Tirado-Rives. The OPLS [optimized potentials for liquid simulations] potential functions for proteins, energy minimizations for crystals of cyclic peptides and crambin. *Journal of the American Chemical Society*, 110(6):1657–1666, 1988.

[106] W.L. Jorgensen, D.S. Maxwell, and J. Tirado-Rives. Development and testing of the OPLS all-atom force field on conformational energetics and properties of organic liquids. *Journal of the American Chemical Society*, 118(45):11225–11236, 1996.

[107] S.V. Sambasivarao and O. Acevedo. Development of OPLS-AA force field parameters for 68 unique ionic liquids. *Journal of Chemical Theory and Computation*, 5(4):1038–1050, 2009.

[108] Z. Xu, H.H. Luo, and D.P. Tieleman. Modifying the OPLS-AA force field to improve hydration free energies for several amino acid side chains using new atomic charges and an off-plane charge model for aromatic residues. *Journal of Computational Chemistry*, 28(3):689–697, 2007.

[109] M. Christen, P.H. Hünenberger, D. Bakowies, R. Baron, R. Bürgi, D.P. Geerke, T.N. Heinz, M.A. Kastenholz, V. Kräutler, C. Oostenbrink, , C. Peter, D. Trzesniak, and W.F. F. Van Gunsteren. The GROMOS software for biomolecular simulation: GROMOS05. *Journal of Computational Chemistry*, 26(16):1719–1751, 2005.

[110] B. Hess, C. Kutzner, D. Van Der Spoel, and E. Lindahl. GROMACS 4: Algorithms for highly efficient, load-balanced, and scalable molecular simulation. *Journal of Chemical Theory and Computation*, 4(3):435–447, 2008.

[111] W.F. van Gunsteren, SR Billeter, AA Eising, P.H. Hünenberger, P. Krüger, A.E. Mark, WRP Scott, and I.G. Tironi. *Biomolecular simulation: The GROMOS96 manual and user guide*. 1996.

[112] J.I.I. Siepmann, S. Karaborni, and B. Smit. Simulating the critical behaviour of complex fluids. *Nature*, 1993.

[113] B. Smit, S. Karaborni, and J.I. Siepmann. Computer simulations of vapor–liquid phase equilibria of n-alkanes. *The Journal of Chemical Physics*, 102(5):2126–2140, 1995.

[114] M.G. Martin and J.I. Siepmann. Transferable potentials for phase equilibria. 1. United-atom description of n-alkanes. *The Journal of Physical Chemistry B*, 102(14):2569–2577, 1998.

[115] M.G. Martin and J.I. Siepmann. Novel configurational-bias Monte Carlo method for branched molecules. Transferable potentials for phase equilibria. 2. United-atom description of branched alkanes. *The Journal of Physical Chemistry B*, 103(21):4508–4517, 1999.

[116] C.D. Wick, M.G. Martin, and J.I. Siepmann. Transferable potentials for phase equilibria. 4. United-atom description of linear and branched alkenes and alkylbenzenes. *The Journal of Physical Chemistry B*, 104(33):8008–8016, 2000.

[117] B. Chen, J.J. Potoff, and J.I. Siepmann. Monte Carlo calculations for alcohols and their mixtures with alkanes. Transferable potentials for phase equilibria. 5. United-atom description of primary, secondary, and tertiary alcohols. *The Journal of Physical Chemistry B*, 105(15):3093–3104, 2001.

[118] J.M. Stubbs, J.J. Potoff, and J.I. Siepmann. Transferable potentials for phase equilibria. 6. United-atom description for ethers, glycols, ketones, and aldehydes. *The Journal of Physical Chemistry B*, 108(45):17596–17605, 2004.

[119] C.D. Wick, J.M. Stubbs, N. Rai, and J.I. Siepmann. Transferable potentials for phase equilibria. 7. Primary, secondary, and tertiary amines, nitroalkanes and nitrobenzene, nitriles, amides, pyridine, and pyrimidine. *The Journal of Physical Chemistry B*, 109(40):18974–18982, 2005.

[120] N. Lubna, G. Kamath, J.J. Potoff, N. Rai, and J.I. Siepmann. Transferable potentials for phase equilibria. 8. United-atom description for thiols, sulfides, disulfides, and thiophene. *The Journal of Physical Chemistry B*, 109(50):24100–24107, 2005.

[121] B. Chen and J.I. Siepmann. Transferable potentials for phase equilibria. 3. Explicit-hydrogen description of normal alkanes. *The Journal of Physical Chemistry B*, 103(25):5370–5379, 1999.

[122] N. Rai and J.I. Siepmann. Transferable potentials for phase equilibria. 9. Explicit hydrogen description of benzene and five-membered and six-membered heterocyclic aromatic compounds. *The Journal of Physical Chemistry B*, 111(36):10790–10799, 2007.

[123] N.M. Garrido, A.J. Queimada, M. Jorge, E.A. Macedo, and I.G. Economou. 1-Octanol/Water partition coefficients of n-alkanes from molecular simulations of absolute solvation free energies. *Journal of Chemical Theory and Computation*, 5(9):2436–2446, 2009.

[124] A. K. Malde, L. Zuo, M. Breeze, M. Stroet, D. Poger, P.C. Nair, C. Oostenbrink, and A.E. Mark. An Automated force field Topology Builder (ATB) and Repository: Version 1.0. *Journal of Chemical Theory and Computation*, 7(12):4026–4037, 2011.

[125] K.A. Maerzke, N.E. Schultz, R.B. Ross, and J.I. Siepmann. TraPPE-UA force field for acrylates and Monte Carlo simulations for their mixtures with alkanes and alcohols. *The Journal of Physical Chemistry B*, 113(18):6415–6425, 2009. PMID: 19358558.

Part II

Molecular dynamics studies of diesel and diesel additives at an atomistic level

4 Paraffins

4.1 Introduction

This chapter aims to study the formation of wax crystals from diesel fuel, using a direct molecular dynamics approach to cool the fuel to the point at which crystallisation occurs. The first part of the chapter describes the creation of a simple paraffin model for diesel fuel and the establishment of an effective cooling procedure from homogeneous melt to crystal. Our paraffin model is then used to study the effect of a nucleation centre and the effects of four common solvents upon crystallisation. Additionally, the crystallisation of mixtures of paraffins of similar lengths is investigated.

4.2 A model of diesel fuel

In a typical fuel, wax crystals are formed by the heaviest fraction, i.e. longest *n*-alkanes. The composition of a wax crystal is temperature dependent. Under normal conditions these are composed of paraffins having chains over 20 carbon long[1]. The crystals formed from a mixture of *n*-alkanes will be orthorhombic. Notably, this structure is also shown by single odd-length *n*-alkane systems. Additionally, both mixtures and odd-alkanes will exhibit the same structural transitions [2–4].

Tricosane is one of the shortest molecules producing an orthorhombic packing and tricosane is commonly present in fuel waxes. For this reason, we adopted tricosane as

[1] Melting temperature of icosane at 1 bar pressure is 310 K [1].

a basic model for diesel fuel in our simulations.

4.3 Building a tricosane model

United atom representations merge hydrogen atoms with adjacent heavy atoms, by such reducing the computational cost of calculations. However, using this representation is only possible when hydrogen atoms are not essential in modelling molecular interactions. For example, Table 3.3 shows that for the calculation of an octanol system a speedup of nearly eight times was obtained using the OPLS united atom model, compared to its all atom counterpart [5]. The choice of force fields was discussed in the section 3.3.1. The most suitable one for this work was found to be the TraPPE-UA force field [6–13]. The TraPPE-UA parameters used in this study are given in Tables 3.4 and 3.5.

A single tricosane molecule was built using the Maestro modelling software [14] and written as a Protein Data Bank (PDB) file containing coordinates, atom types and connectivity. This file was converted into a suitable GROMACS input [15] comprising coordinate and topology files. The latter contains all of the required force field parameters for the model. Even though GROMACS includes a program for such conversion, it is only capable of assigning parameters included in the package by amino acid residue name. Therefore, a conversion program capable of assigning a user specified force field was developed.

A simulation box comprising 1000 molecules was created by multiplying the coordinate file of the initial molecule. A grid of $10\times10\times10$ boxes of the initial molecule was built, occupying $50.00\times50.00\times50.00$ nm^3. This box does not represent a realistic system, and so it was relaxed in the NPT ensemble to obtain a liquid phase system.

The initial volume is very large, increasing temperature and pressure will result in a faster exploration of phase space by molecules, and so speed up the relaxation process. If the pressure is not sufficiently high, paraffin droplets surrounded by vacuum may form. These would take too long to come into contact with each other. If temperature

is too low, formation of crystal units in the vacuum may occur. Nevertheless, both temperature and pressure should not be increased dramatically, as this would lead to instabilities due to atoms moving at high speed. A temperature range of 350 K to 500 K and a pressure range of 5 to 50 bar were found to be reasonable to provide optimal compression to a liquid state. Berendsen thermostat and barostat were chosen, as they provide stable simulations for systems which are initially a long way from equilibrium. The simulation parameters used for the initial simulation are given in Table 4.1.

Table 4.1: *Parameters for pre-equilibration simulation of the tricosane system*

Integration	Leap frog
System size	1000 molecules
Step size	2 fs
Length of calculation	5 ns + 5 ns
Periodic boundary	xyz
Ensemble	*NPT*
Temperature	500 K + 520 K
Thermostat	Berendsen
Pressure	50 bar & 1 bar
Barostat	Berendsen
Compressibility [16]	9×10^{-5} bar^{-1}

Figure 4.1 shows the initial simulation box, and the resulting system after relaxation. The first 5 ns were performed at 500 K and 50 bar, and the following 5 ns at 520 K and 1 bar. The volume remains constant for the final 3 ns, indicating that a relaxed configuration is achieved.

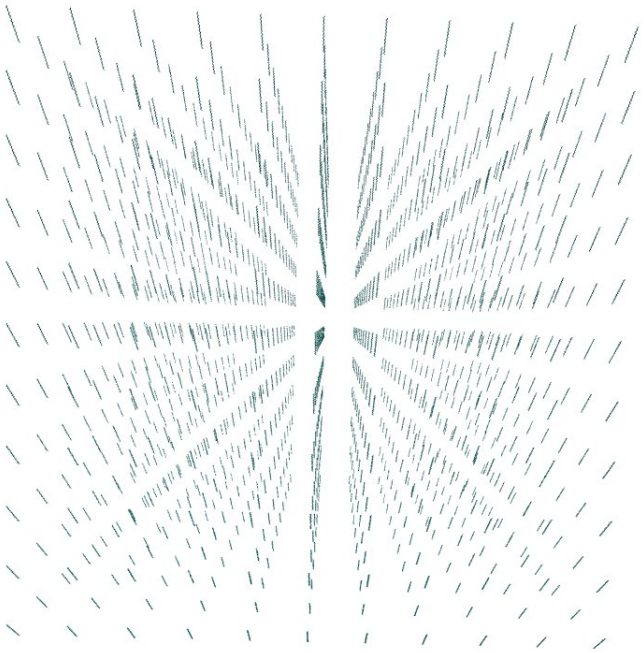

(a) Grid of 10×10×10 tricosane molecules

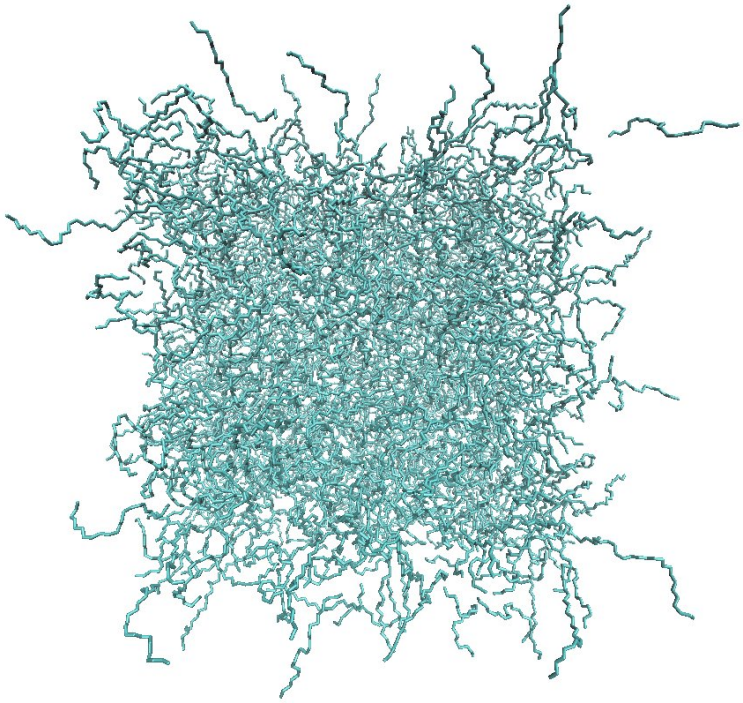

(b) Relaxed system of 1000 tricosane molecules

Figure 4.1: *Set up of the simulation box: initial low density grid (a) and the resulting pre-equilibrated system (b)*

4.4 Temperature annealing of tricosane system

The simulation box, assembled and relaxed as described in section 4.3, was used as a starting model in this study. Our aim was to mimic the natural behaviour of diesel upon cooling. The pressure was kept atmospheric (1 bar) through all subsequent simulations, while the temperature was gradually decreased. The slowest cooling affordable by our simulation is in the order of tens degrees per nanosecond. Clearly, this is extremely rapid cooling compared to the real life conditions and experiments.

When the temperature is decreased steadily, a glass structure initially forms. Further cooling, below 260 K, leads to the formation of nano-crystalline domains. This is an indication of over cooling. To manage this problem, we devised a stepwise temperature decrease protocol. Such a protocol is subject to two constraints. First, the system must come to equilibrium before the next temperature drop. Second, the total length of simulation must be available within current computational resources.

To assess the simulation time needed for the system to re-equilibrate, the changes in the structure through the simulation were quantified by computing the system's root mean square deviation (RMSD) [17, 18]. Figure 4.2 shows the RMSD for simulation of liquid tricosane at 520 K and tricosane crystal at 260 K. In the case of a liquid (a), the system stabilises within 1 ns from the start of the simulation, while it takes over 20 ns for the RMSD to level out for the crystal (b).

Based on these observations a scheme for stepwise annealing was developed. The simulation times for each temperature are given in the Table 4.2.

The control parameters for the simulated annealing studies are given in Table 4.3. Unlike earlier pre-equilibration runs (Table 4.1), where Berendsen coupling was used for temperature and pressure control, these calculations used the more advanced Nosé-Hoover thermostat and the Parrinello-Rahman barostat. Use of extended ensembles allows for a better energy conservation and are beneficial when predicting fine changes of the structure. The extended ensembles are sensitive to large changes, making simulations unstable when large fluctuations in temperature and/or pressure

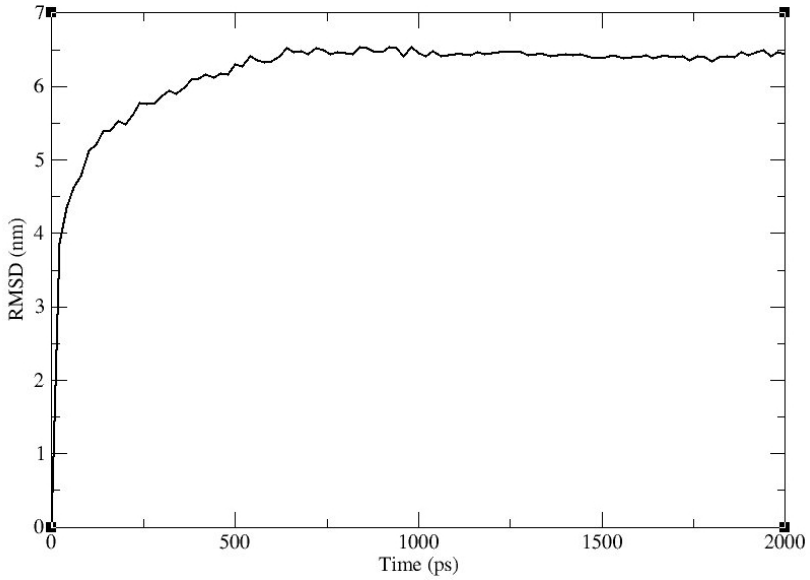

(a) RMSD for 2 ns simulation of tricosane liquid at 520 K

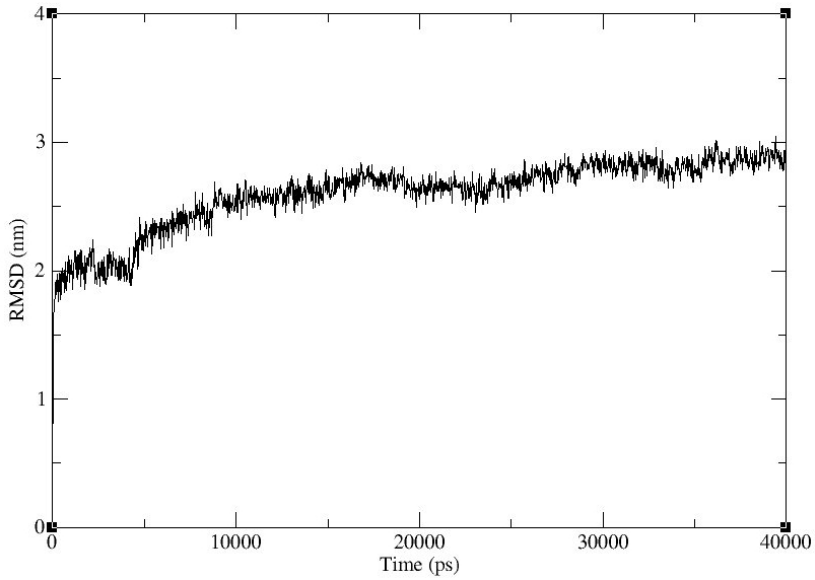

(b) RMSD for 40 ns simulation of tricosane crystal at 260 K

Figure 4.2: *Root mean square deviation through simulation of 1000 molecules of tricosane at 520 K (a) and 260 K (b)*

Table 4.2: *Simulation times and temperatures for stepwise annealing of tricosane*

Temperature, K	Time, ns
520	1
500	1
480	1
460	1
440	1
420	1
400	1
380	1
360	2
340	2
320	2
300	2
290	10
280	30
270	30
260	40
Total:	126

occur. It is therefore only possible to use them for a pre-equilibrated system.

Table 4.3: *Parameters for simulated annealing of tricosane system*

Integration	Leap frog
System size	1000 molecules
Step size	2 fs
Length of calculation	as given in the Table 4.2
Periodic boundary	xyz
Ensemble	*NPT*
Temperature	as given in the Table 4.2
Thermostat	Nosé-Hoover
Pressure	1 bar
Barostat	Parrinello-Rahman
Compressibility	9×10^{-5} bar^{-1}

Our simulated annealing runs are analysed to quantify the system changes upon temperature decrease. The next section describes in detail the analysis performed. These techniques will be also adopted in the following chapters.

4.4.1 Analysis of simulated annealing of tricosane system

Density

The density of the material varies with temperature and pressure, the change being small in liquids and solids. Nevertheless, a bigger change occurs when the material undergoes large rearrangements in the structure to increase the packing order, as for instance upon crystal formation. The partial density (density across the simulation box) can indicate the presence of changes in the structure and packing within the simulation box.

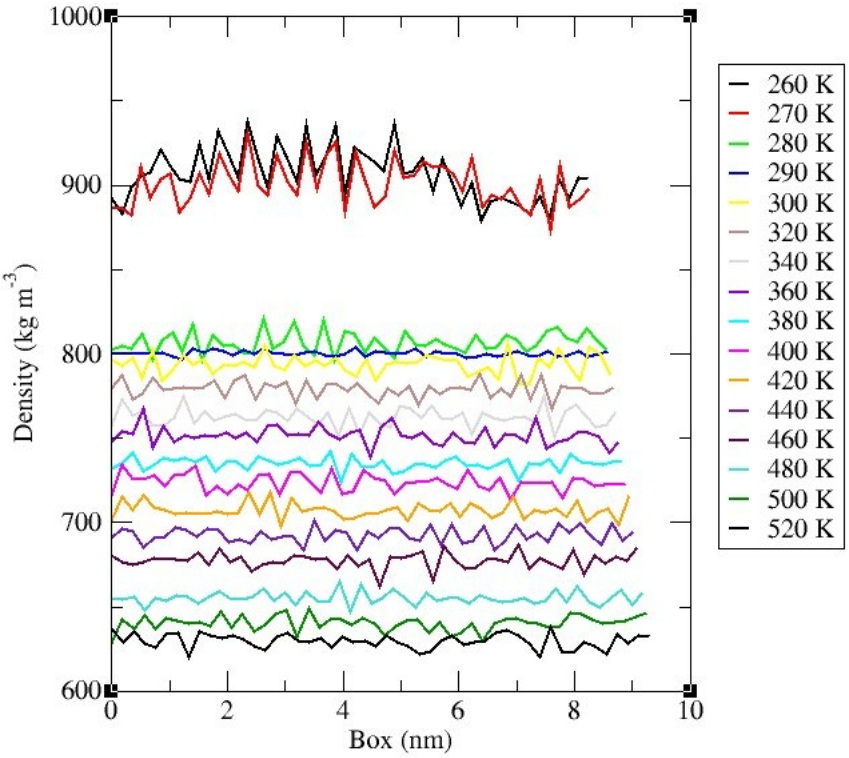

Figure 4.3: *Partial densities of tricosane through a range of temperatures from 520 K to 260 K*

Figure 4.3 shows the change of partial densities of the system with temperature. The system becomes monotonically denser while decreasing temperature down to 280

K, where a large change is observed. This indicates crystal formation between 280 K and 270 K. Experimentally, the measured crystallisation temperature of tricosane is 320 K [19], i.e. higher than in our observations. The main cause of such a difference arises from the parametrisation of TraPPE force field. The force field was originally formulated for liquid-vapour interface of shorter alkanes. Additionally, it was noted by Siepmann *et al.*, that the force field is system size dependent [6]. The calculated density at 280 K is 805 kg/m^3, comparable to the experimental value of 795 kg/m^3 (at 277.15 K and 1 bar) [20].

By comparing the shapes of partial density curves of liquid (above 280 K) and solid (below 270 K), it appears that the density profile across the simulation box is not uniform for the solid. The region between 1 and 6 nm shows an increased density, suggesting the formation of a crystal stack. Examining the configuration of a crystal, Figure 4.4, the formation of a number of crystal stacks can be seen. This arrangement can arise due to the restriction introduced by the use of the cubic box. A cubic box reduces in size isotropically, by such restricting the growth of the crystal. The best solution would be to increase the system's size, leading however to an increase in computational times, beyond the accessibility for the method and model.

Dihedral angle

Linear alkanes are chains of single bonded sp^3 hybridised carbon atoms. These are semi-flexible molecules that exhibit *trans* and *gauche* conformations in gas and liquid phases. In the crystal, the molecules are extended in all-*trans* arrangements, allowing a closer packing between molecules. The proportion of *gauche* dihedral angles can therefore be indicative of the level of disorder in the system.

Figure 4.5 shows the dihedral distribution for a tricosane system at a range of temperatures from 520 K down to 260 K. A significant drop in the number of *gauche* conformations (60^o and -60^o) occurs on cooling from 290 K to 280 K.

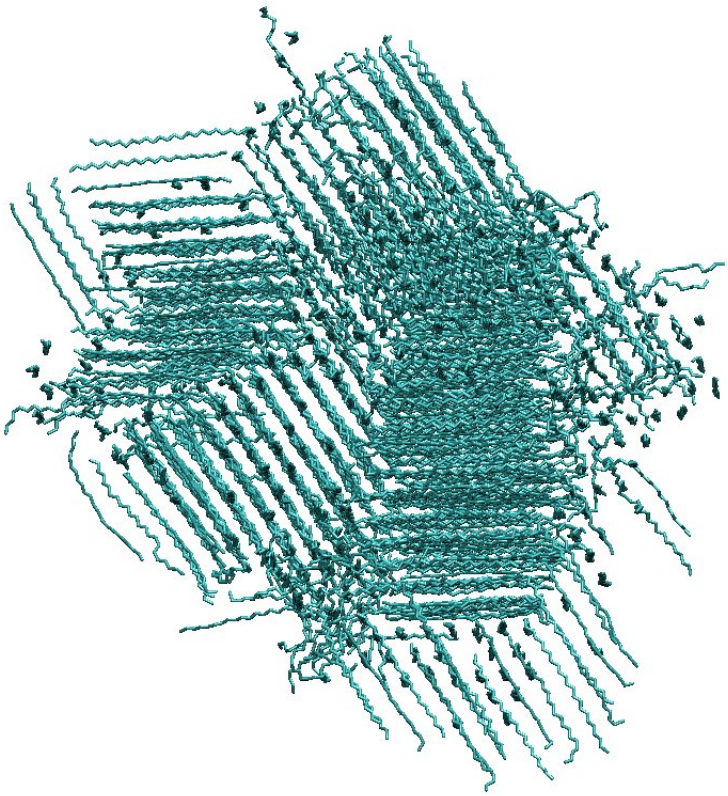

Figure 4.4: *Snapshot of tricosane system at 270 K*

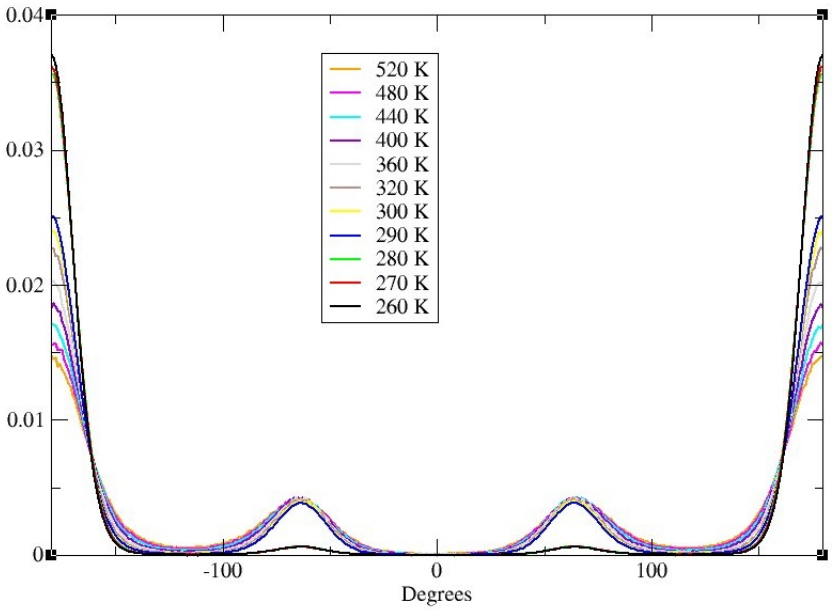

Figure 4.5: *Dihedral angles in a tricosane system over a range of temperatures from 520 K to 260 K*

Radius of gyration

The proportion of *trans* dihedral angles in the *n*-alkane is related to the extension of the chain. This can be quantified by computing the molecule's radius of gyration. This is calculated as the root mean square distance between the centre of mass and the furthest point in the molecule:

$$R_g^2 = \frac{1}{NM} \sum_{k=1}^{N} (r_k - r_{com})^2$$

where N is the number of atoms in the molecule, M the molecular weight, r_k is the mass weighted position of k-th atom of the system and r_{com} is the position of the centre of mass.

In the crystal, paraffin chains are fully extended, having therefore a maximum radius of gyration, while in the liquid the radius of gyration is smaller. The presence of *gauche* dihedral angles in the liquid leads to numerous interchanging conformations, the dynamics of which are dependant on the temperature. Figure 4.6 illustrates the evolution of the radius of gyration of tricosane over a 1 ns timescale at a range of temperatures. Fluctuations in the radius of gyration become smaller when decreasing the temperature. This is due to the *n*-alkane chains gradually becoming fully extended as the temperature decreases. Hence, a smaller variation in configurations are seen.

Figure 4.7 shows the distribution of the radius of gyration of tricosane for a set of temperatures. At temperatures below 280 K (long dashed lines) the distribution is narrow, with a peak corresponding to high values, indicative of fully straightened chains. At higher temperatures (dotted lines) the distribution is wider, and the average peak is lower, as chains exhibit numerous *gauche* conformations.

Figure 4.6 shows a comparison of the change in the mean radius of gyration and the density upon cooling. The two quantities are strongly correlated. A significant increase in density is observed between 280 K and 270 K, while an increase of radius of gyration is observed between 290 K and 280 K. We conclude that, upon approaching the phase transition, tricosane molecules first extend and then, upon further cooling, pack in a denser arrangement.

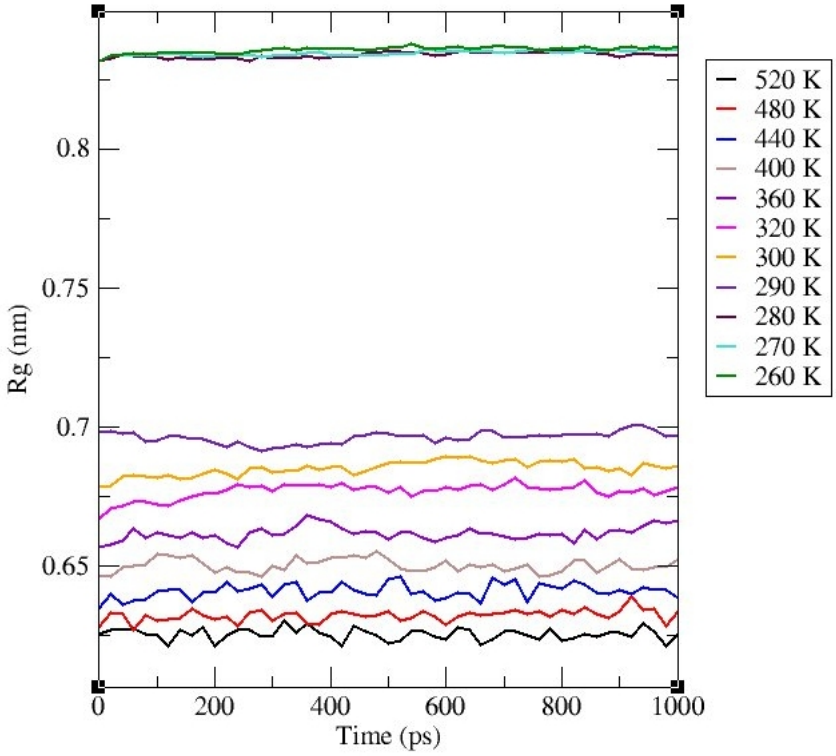

Figure 4.6: *Radius of gyration of a 1000 molecule tricosane system for the final 1 ns of simulations at a range of temperatures from 520 K to 260 K*

Radial distribution function

The radial distribution function (RDF) measures the variation of density of atoms as a function of distance from the reference atom. It is calculated as:

$$g(r) = \frac{n(r)}{4\pi r^2 \rho dr} \tag{4.1}$$

Where *n(r)* is the number of atoms in a spherical shell of width *dr* at a distance *r* and ρ is its number density.

RDF allows for the comparison of the order of the system to the X-ray or neutron scattering data. In the solid, molecules remain at a constant distance from one another, producing well defined peaks in the function. This will differ in a liquid, where no long range structural order is present, and in a gas, where molecules are dispersed through all the available volume.

Figure 4.9 shows the radial distribution function between carbon atoms in a tricosane system for a range of temperatures. Below 280 K the function shows ordering at much larger distances. This corresponds to the formation of an ordered structure.

Vectorial representation

A paraffin molecule is a single unbranched chain, and so can easily be represented as a set of vectors between atoms at 1-3 distance (see Figure 4.10).

When a molecule is randomly coiled, the vectors are also random. Conversely, when the molecule is crystallised, the preferred all-*trans* arrangement leads to parallel vectors. Hence, the vectors of co-crystallised molecules will be also parallel. For crystals of mixed alkanes, a vector representation can be readily used to quantify the alignment through a crystallisation mixture.

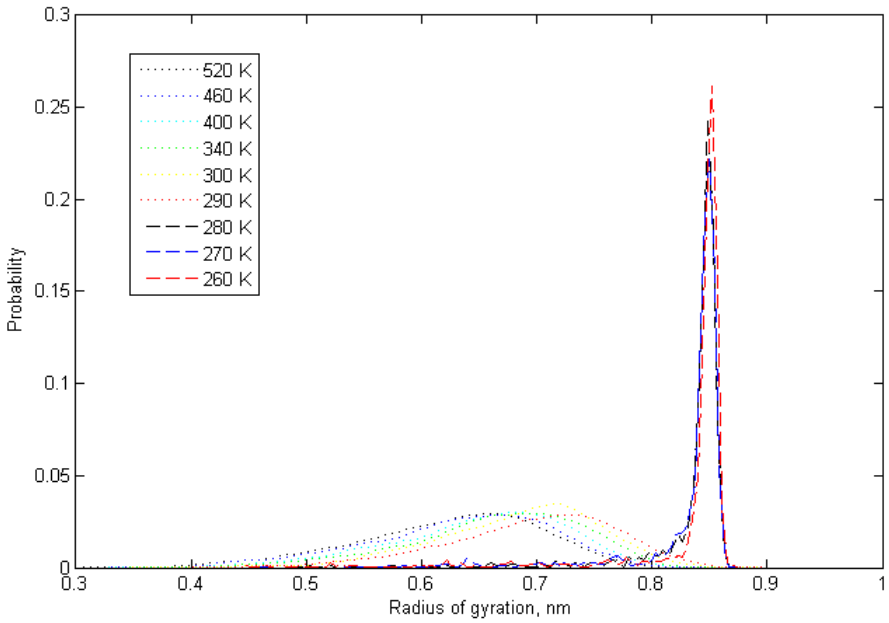

Figure 4.7: *Distribution of radius of gyration for tricosane molecules over a range of temperatures from 520 K to 260 K*

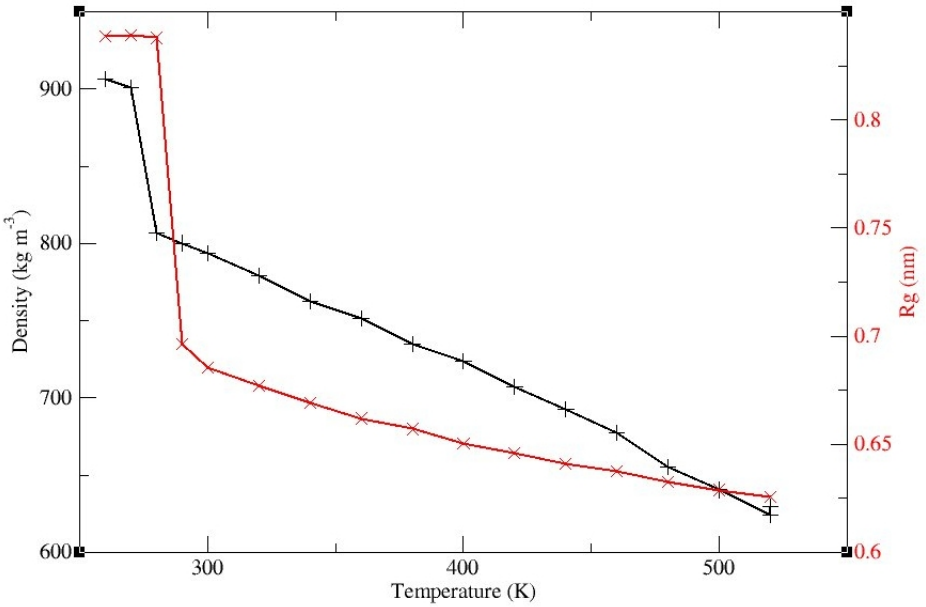

Figure 4.8: *Change of density (black) and mean radius of gyration (red) for a tricosane system at a range of temperatures from 520 K to 260 K*

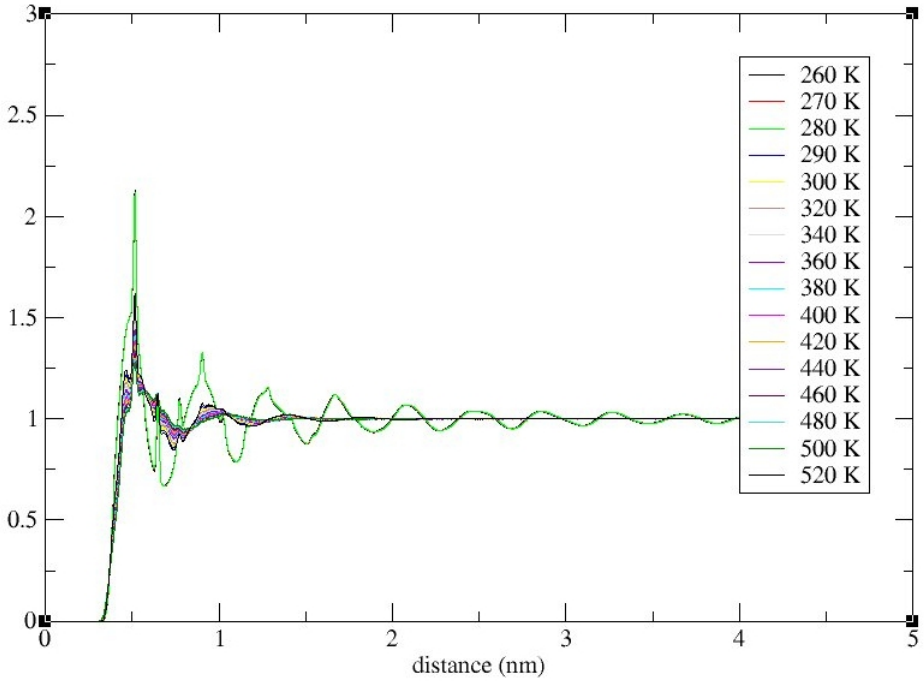

Figure 4.9: *Radial distribution function between carbon atoms in tricosane system in the temperature range from 520 K to 260 K*

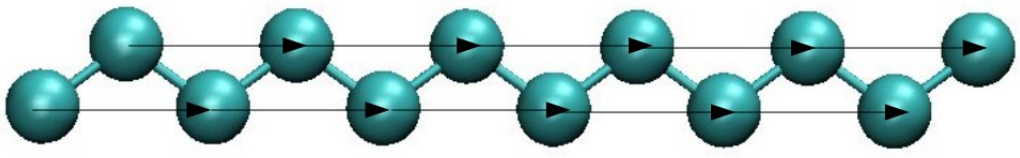

Figure 4.10: *Assigned vectors in a dodecane molecule for vector analysis*

The Cartesian coordinates (x, y, z) of every vector are extracted, normalised, and subsequently converted into spherical coordinates (r, θ, ϕ) using the equations:

$$r = \sqrt{x^2 + y^2 + z^2} \tag{4.2}$$

$$\theta = \arctan\left(\frac{\hat{y}}{\hat{x}}\right) \tag{4.3}$$

$$\phi = \arccos\left(\frac{\hat{z}}{r}\right) \tag{4.4}$$

Where $\hat{x}$, $\hat{y}$ and $\hat{z}$ are Cartesian components of the normalised vectors. Upon normalisation, r is equal to 1. Figure 4.11 shows the vectorial distribution for tricosane at 520 K and 270 K. The vectors are uniformly distributed in the melt (Figure 4.11 a), showing little variations in the probability density with angle. In the solid (Figure 4.11 b), a few peaks are present, each of them representing a stack of molecules corresponding to individually crystallised domains.

4.4.2 Analysis of the crystal structure

Crystal formation began at 280 K, and a stable well defined crystal was formed at 270 K. Figure 4.4 shows the equilibrated tricosane system at 270 K. The system contains numerous separate crystallites constituted of lamellar stacks. The stacks have nucleated and grown separately within the melt. Areas of disordered (glassy) frozen melt separate the meeting point of those domains. Alkane crystals grow with different rates, faster perpendicular to the lamellar layer (bc plane) rather than forming a new one (a plane) [21, 22].

For easier visualisation of the crystal structure, separate domains are selected from the bulk and presented individually. Figure 4.12(a) shows the projection of the bc plane. In the presented lamellar structure the molecules are shifted with respect of one another, causing a deformation of the stack alignment. These stacks pack in a herringbone arrangement with a 121^o to 125^o angle, as shown on Figure 4.12(c). This packing is due to the restriction in available space imposed by a cubic simulation box, changing volume isotropically with pressure. This set up will not be able to accommodate the crystal growing with unequal growth rates in different planes.

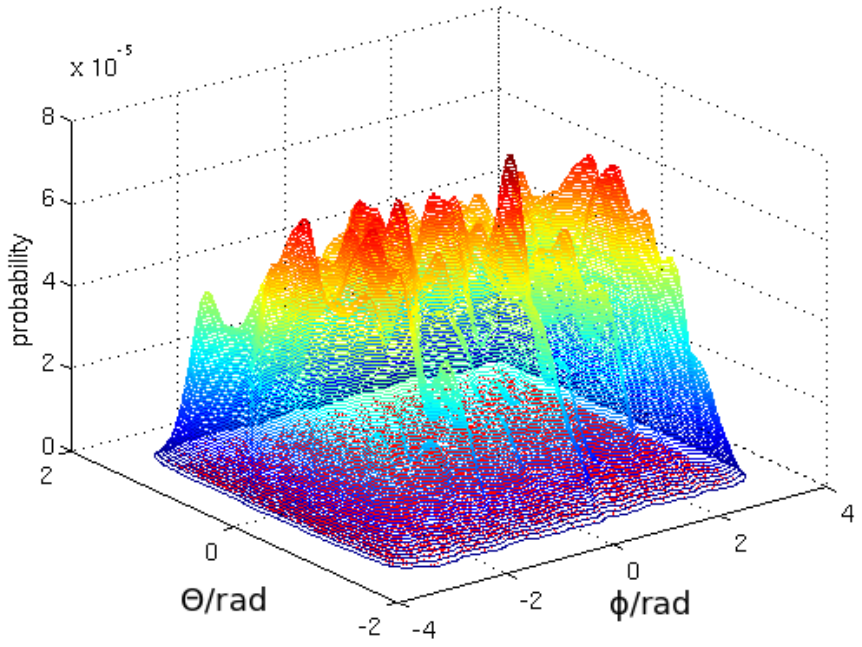

(a) Tricosane 520 K

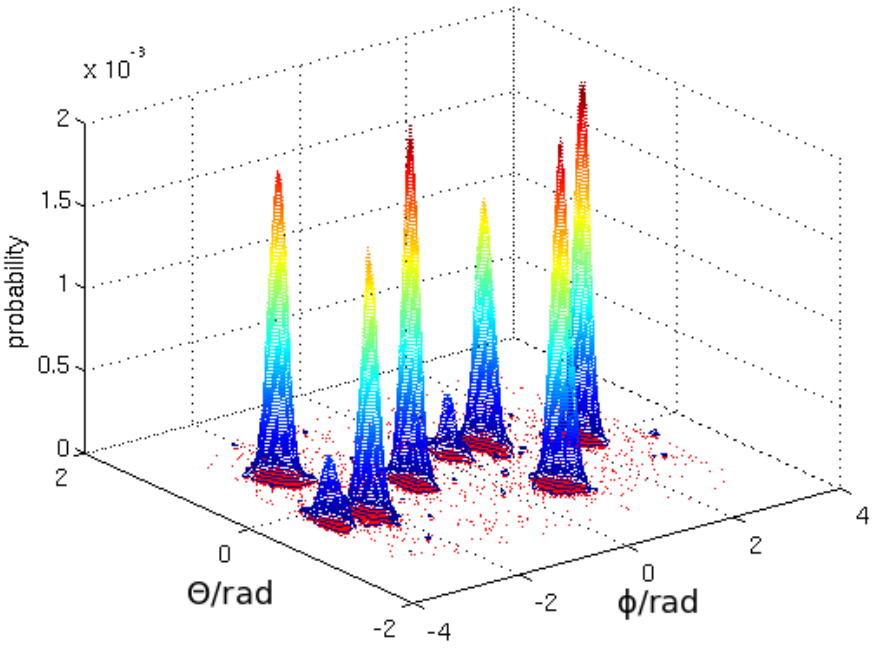

(b) Tricosane 270 K

Figure 4.11: *Normalised vector distribution for tricosane at 520 K (a) and 270 K (b)*

Figure 4.12 (b) shows the projection of the *ab* plane with molecular axes pointing outwards of the paper. A hexagonal packing arrangement is observed, however molecules rotate freely around the molecular axis. Additionally, *gauche* defects are present in few molecules. The observed phase at 270 K is a rotator phase, see Chapter 2.2.4. This phase is expected at temperatures slightly below the melting point.

Table 4.4 lists the unit cell parameters of the experimental and computationally obtained crystal. The fluctuations within measures are due to the disorder in lamellae (Figure 4.12(a)) as well as rotation around the molecular axis, leading to a random orientation of the end CH_3 groups (Figure 4.12(b)). Since the crystal is stacked in a herringbone alignment (Figure 4.12(c)), it is not possible to determine realistic distances in the *c*-plane. Hence, measurements for the *c* parameter are not shown.

Table 4.4: *Unit cell parameters for tricosane crystal formed from a melt at 270 K*

	Experimental [3]	Measured sample	Average
a, nm	0.4967	0.4747 0.4599 0.4459 0.4697 0.5473	0.4795
b, nm	0.7441	0.7431 0.7773 0.7682 0.7982 0.8415	0.7856
c, nm	6.2189	-	-

The shape and dimensions of the simulation box play an important role in molecular modelling. A study of the effect of the simulation box on crystallisation of polymers was performed by Miura *et al.* [23]. The crystallisation behaviour was found to have significant differences between nanodomains and the bulk. Additionally, the shape of the domain (spherical or cubic) had an effect on crystallisation.

Using a larger simulation box would help in minimising the influence of box size on crystal formation. However it is not computationally affordable to increase the size of simulation box dramatically for united atom systems, and so a coarse grained approach would be required (see Chapter 6).

In order to avoid the formation of a herringbone structure, one could attempt to fix the simulation box size to the dimensions of a unit cell. However, this would require

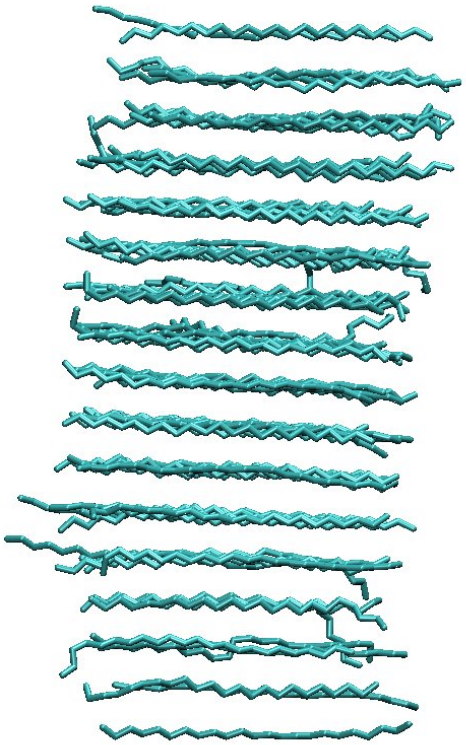

(a) Projection of the bc plane.

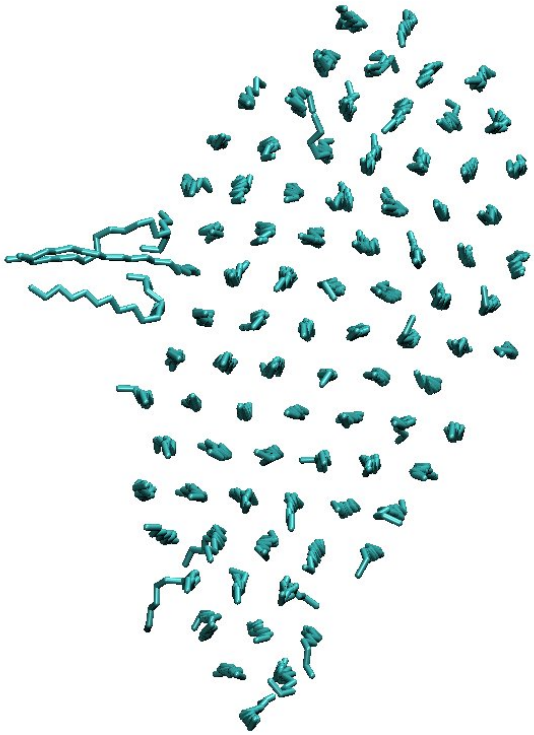

(b) Projection of the ab plane.

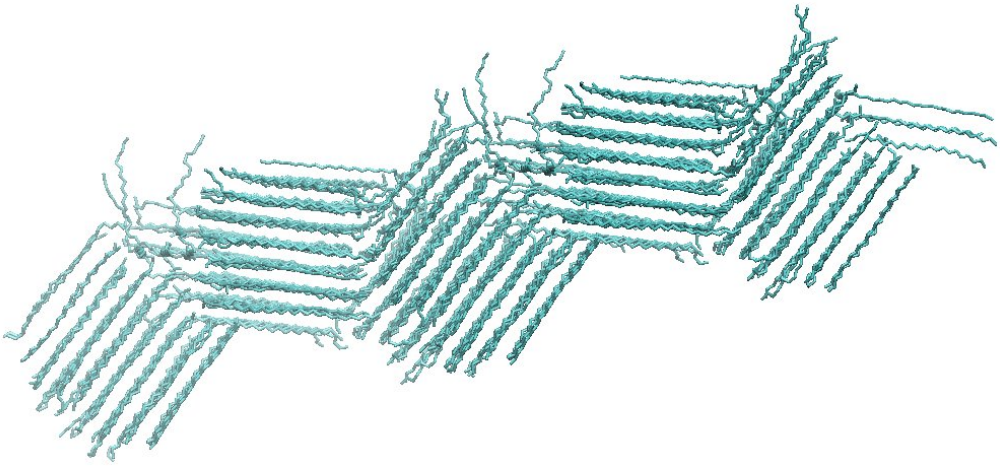

(c) Cross section along the z-axis of a double simulation box.

Figure 4.12: *Crystallised tricosane system at 270 K*

growth along the crystal unit cell axes to be commensurate with the direction of the simulation cell axis. This is very unlikely to happen as nucleation and growth from a melt can in principle lead to growth in any direction, and once growth of lamellae has started it is unlikely to be slow enough for the lamellae to re-align along the necessary simulation cell.

Alternatively, it is possible to use a nucleation centre to promote crystallisation. The nucleation centre should be composed of two lamellae stacks, that will drive further growth around themselves. This will prevent the initial compression of molecules into a herringbone pattern. This method is discussed in detail in chapter 4.6.

4.5 Paraffin mixtures

Wax precipitating from diesel fuel contains a range of paraffins of a similar molecular weight [24]. These alkanes co-crystallise, introducing defects into the crystal symmetry to accommodate different chain lengths. In this section binary and ternary mixtures of long *n*-alkanes are investigated.

In the previous section it was concluded that in order to avoid formation of an unwanted herringbone crystal and to speed up crystallisation a nucleation centre would be desirable. Use of such a nucleation centre (in the form of a seed crystal) is considered in section 4.6. However, prior to this, we first consider crystallisation from a melt without attempting to steer crystal growth by introducing a nucleation site. To attempt to minimise system size effects, the simulation box in this section is larger, which should reduce the effect of the box size upon crystallisation.

A mixture of tricosane and tetracosane was chosen as a binary mixture, due to the similar size, but different nature of homologous packing [3]. Pure tricosane (odd-number of carbon atoms) forms orthorhombic crystals, while tetracosane (even number of carbon atoms) forms triclinic ones. To form a tertiary mixture, heinecosane was added to the tricosane – tetracosane system. The heinecosane molecule is shorter than tricosane by two carbon atoms, and so introduces slightly larger differences in

molecular lengths into the mixture.

The systems were prepared following the procedure in section 4.3. The number of molecules of each kind was selected to fill the same volume. The resulting molecular composition for each simulation box is given in the Table 4.5. Calculations follow the earlier established annealing scheme in section 4.4. The input parameters for the simulation are given in the Table 4.6.

Table 4.5: *Type and number of alkane molecules in each of the two paraffin mixtures*

System:	Heinecosane	Tricosane	Tetracosane
Binary	–	1005	1000
Tertairy	1052	1005	1000

Table 4.6: *Parameters for simulated annealing of alkane mixtures*

Integration	Leap frog
System size	As given in the table 4.5
Step size	2 fs
Length of calculation	5 + 2 + 2 + 2 + 2 + 2 + 4 + 10 + 40 + 20 ns
Periodic boundary	xyz
Ensemble	*NPT*
Temperature	350 340 330 320 310 300 290 280 270 260 K
Thermostat	Nosé-Hoover
Pressure	1 bar
Barostat	Parrinello-Rahman
Compressibility	9×10^{-5} bar^{-1}

In the melt, both mixtures are completely miscible, showing a uniform distribution of each component across the simulation box. Upon cooling to 270 K a solid solution is formed as shown on Figure 4.13. Further temperature redution to 260 K over 20 ns, did not lead to rearrangements of the structure.

The density profile at 270 K, Figure 4.14, confirms the uniform distribution of components seen in the snapshots. The overall density is very similar for both binary and tertiary systems and the partial density profiles for each component are the same within statistical fluctuations.

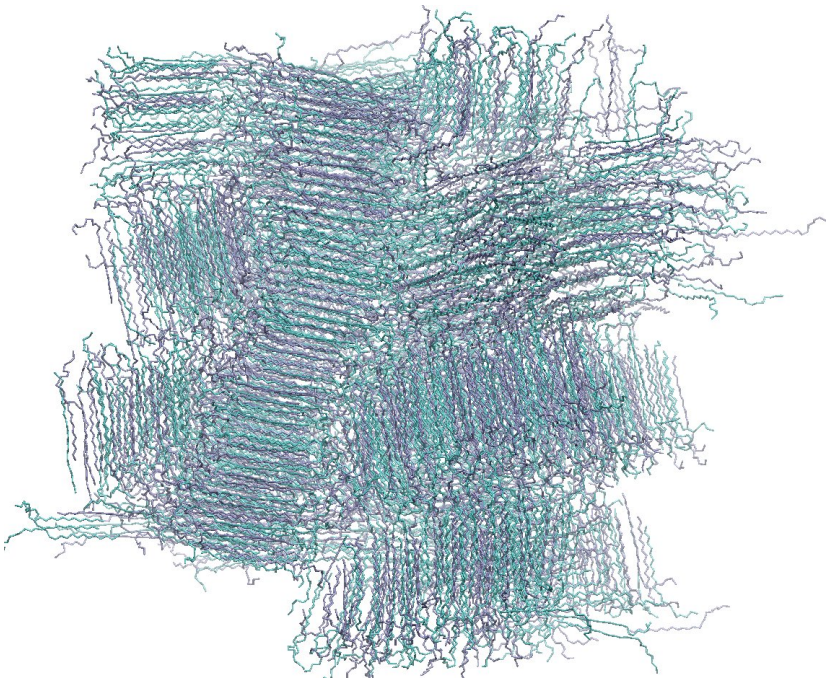

(a) binary alkane

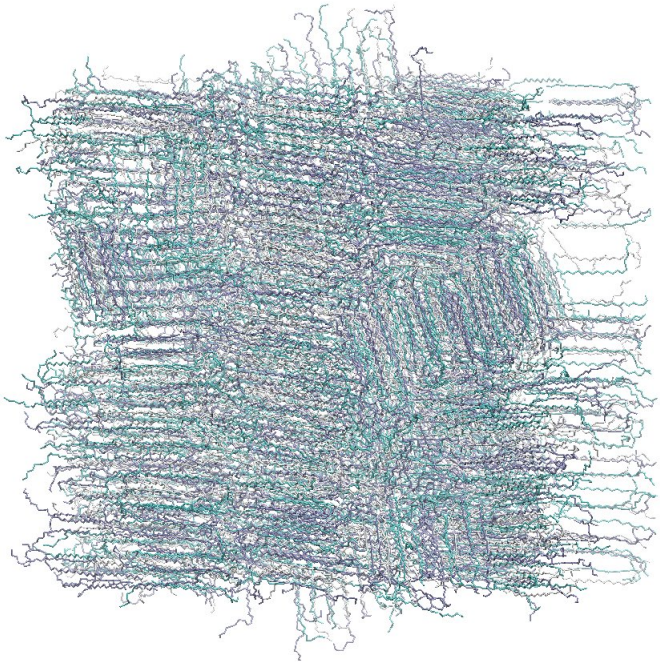

(b) tertiary alkane

Figure 4.13: *Binary (a) and tertiary (b) alkane mixtures at 270 K. Tricosane is shown in cyan, tetracosane in warm blue and heinecosane in light grey*

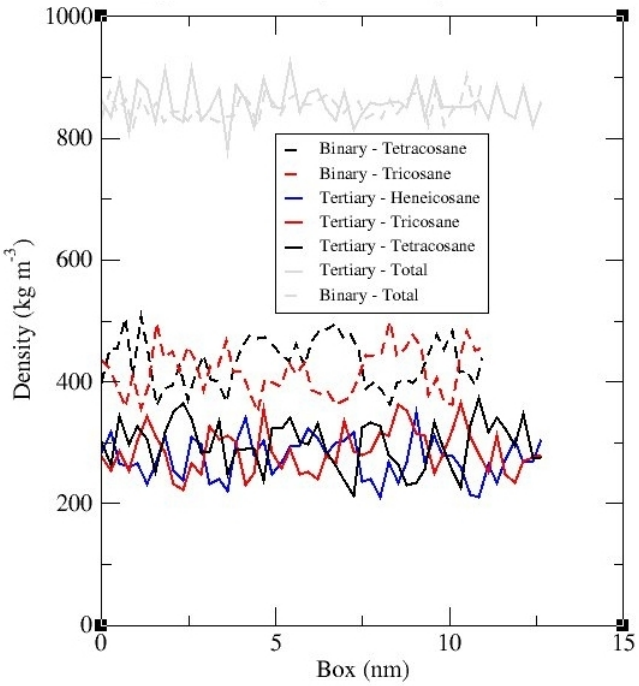

Figure 4.14: *Partial density of components and total for binary (dashed lines) and tertiary (solid lines) mixtures at 270 K*

A vector analysis, Figures 4.15 and 4.16, demonstrates that for both the binary and the tertiary mixtures a small number of well-formed domains are grown. Here the different components show almost identical alignment, confirming that co-crystals have been formed.

A selected crystal from the tertiary mixture is shown on Figure 4.17. The image shows that molecules pack in a hexagonal arrangement with the central part of the lamellae stack well ordered while edges show a disorder. Shorter, heneicosane molecules (grey) are fully incorporated into the co-crystals. Typically, heneicosane molecules show *gauche* defects only at one end of the molecule, with the other end of the molecule being well-ordered and remaining within the body of the lamellae. In comparison to pure tricosane the presence of molecules of unequal length within the crystals significantly increases the number of *gauche* defects at both ends of the molecule.

The distribution function for the radius of gyration of chains is plotted in Figure 4.18. Tetracosane (bright blue) and tricosane (dark blue) show wide Gaussian distributions

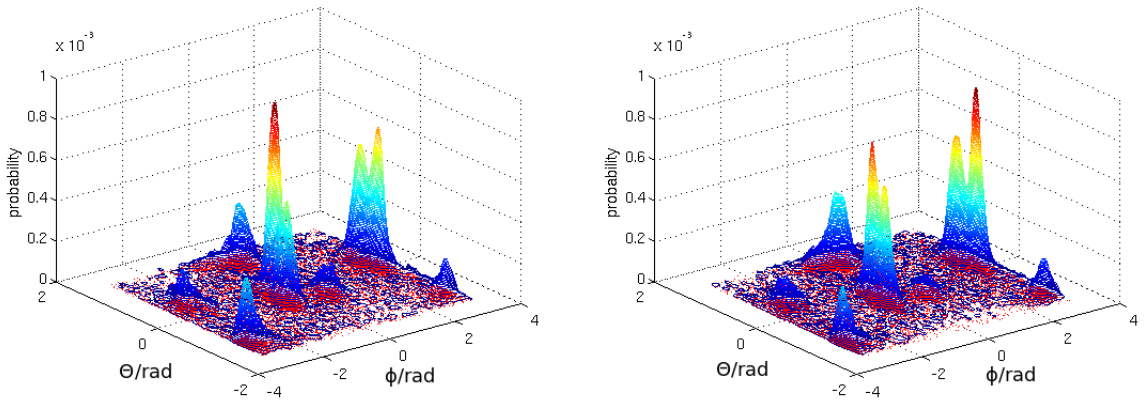

(a) Tricosane vector distribution

(b) Tetracosane vector distribution

Figure 4.15: *Normalised vector distribution for tricosane (a) and tetracosane (b) in a binary alkane mixture at 270 K*

in the binary mixture. In the tertiary mixture those peaks are further widened with respect to binary mixture. This is caused by the arrangements induced by the presence of heneicosane. Heneicosane molecules exhibit disorder to a smaller extent than longer chains. This results in a slightly narrower distribution, with the peak shifted towards its highest value. The reference system for comparison purposes is pure tricosane simulated earlier at 270 K, which showed a narrow distribution with a peak at its maximum value, corresponding to fully extended chains. The average radius of gyration is given in Table 4.7.

Table 4.7: *Average radius of gyration of each of the components of paraffin mixtures*

	Radius of gyration, nm		
System	Heneicosane	Tricosane	Tetracosane
Binary	-	0.7364	0.7831
Tertairy	0.7035	0.7585	0.7802
Reference	-	0.8336	-

From the above observations we can conclude that alkanes of a similar weight crystallise in a solid solution. The differences in length lead to structural defects. This disordered state is found to be stable between 270 K and 260 K. Similar results have been obtained experimentally, where binary mixtures have shown a stable rotator phase over a 10 degrees temperature range [25].

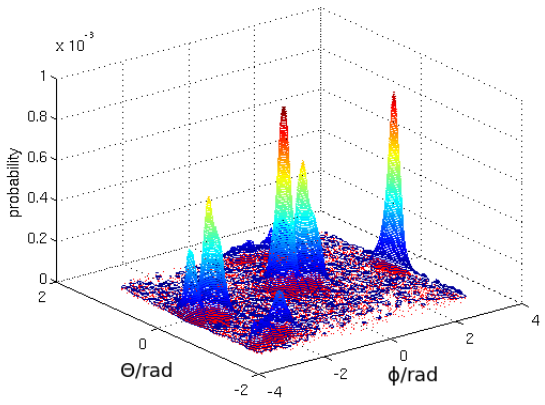

(a) Tricosane vector distribution

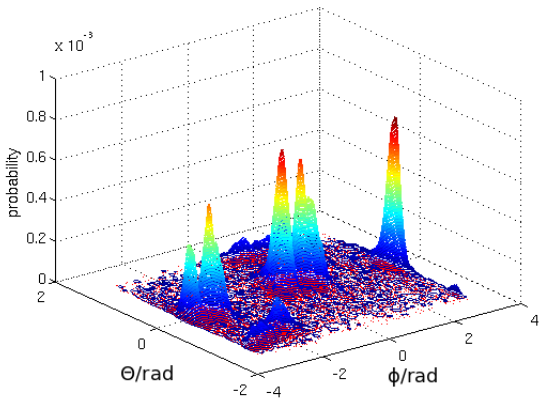

(b) Tetracosane vector distribution

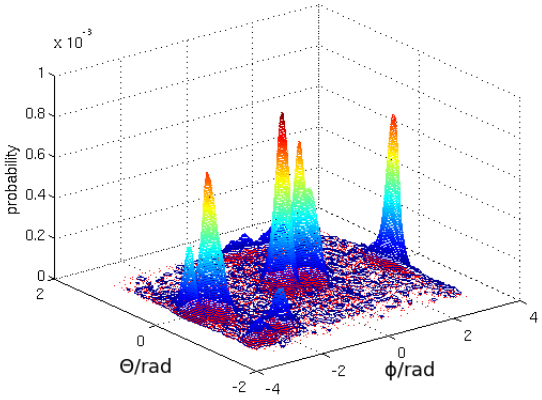

(c) Henecosane vector distribution

Figure 4.16: *Normalised vector distribution for tricosane (a), tetracosane (b) and heinecosane (c) in a tertiary mixture at 270 K*

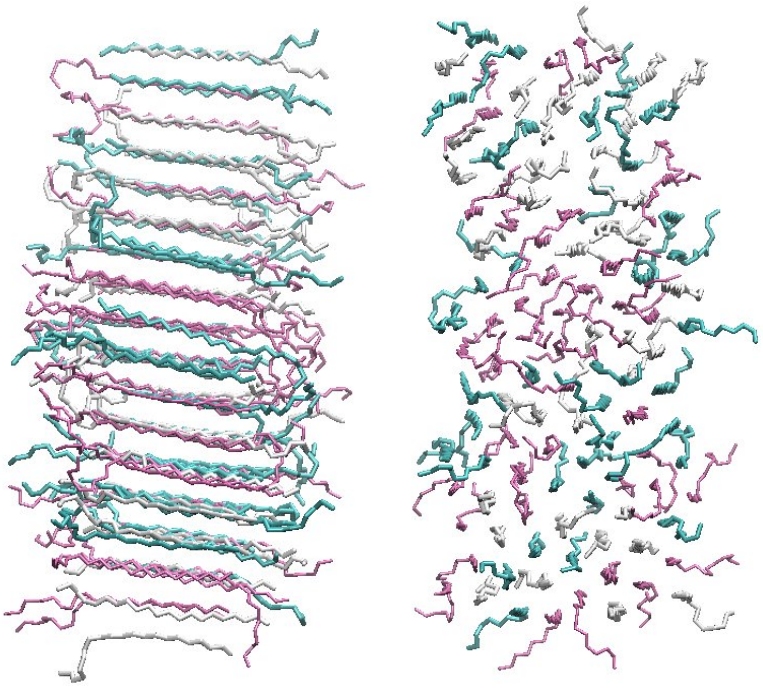

(a) view on the bc plane (b) view on the ac plane

Figure 4.17: *Crystal fragment from a tertiary alkane mixture at 270 K. Heneicosane is shown in light grey, tricosane in cyane, tetracosane in mauve*

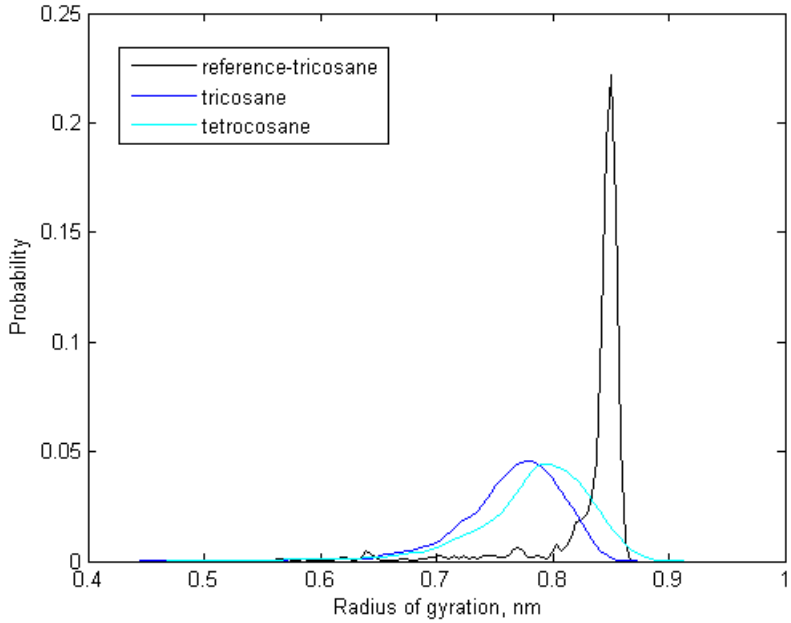

(a) Binary mixture

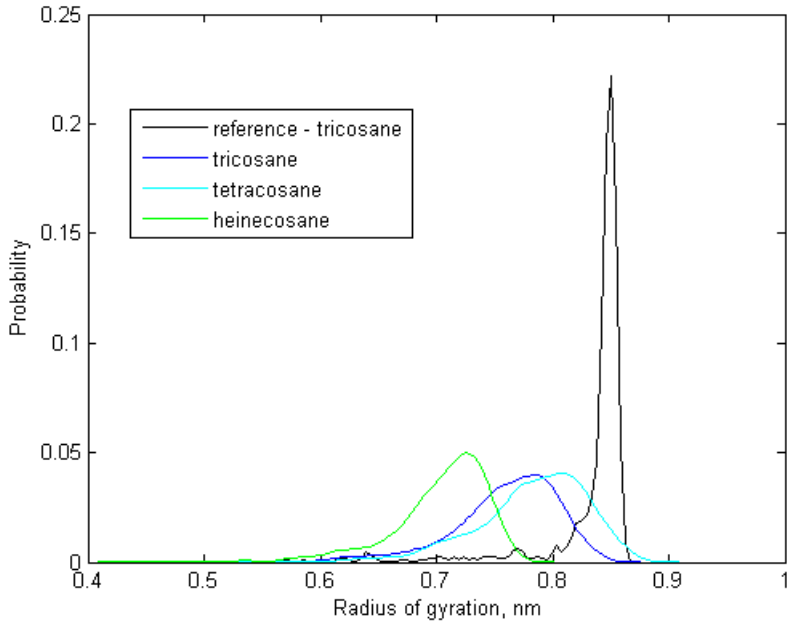

(b) Tertiary mixture

Figure 4.18: *Distribution of radius of gyration of alkanes in binary (a) and tertiary (b) mixtures at 270 K*

In the previous section 4.4 we observed that, upon crystallisation, pure tricosane formed a herringbone structure. We hypothesised that this arrangement can be caused by the usage of a too small simulation box. In this section we modelled a larger system and consistently with our hypothesis, no herringbone structure was found.

Nevertheless, there larger system presents a second important difference - it's composition. While in section 4.4 we simulated a pure tricosane system, here a mixture of molecules having different chain lengths has been studied. We have shown that this mixture forms crystal stacks having *gauche* defects at their edges, causing the lamellar layers to be less rigid. This increased flexibility allows growing crystals to accommodate into less space, fitting in fact even in box length not commensurating to molecules chain lengths.

4.6 Studies of heterogeneous nucleation

The presence of a nucleation centre can speed up the crystallisation process, and allow for the direction of crystal growth to be controlled, to minimise the problems associated with a finite size simulation box. A positionally restrained tricosane crystal was introduced into the tricosane melt. The crystal was originally build by Matteo Nasi [26] using cell parameters measured by Steven Craig [3, 4], given in Table 4.8. The crystal is orthorhombic with a P_{bcm} space group and is composed of 64 tricosane molecules, as shown on Figure 4.19

Table 4.8: *Unit cell parameters for an orthorhombic tricosane crystal with P_{bcm} space group*

Unit cell parameters	
a, nm	0.4967
b, nm	0.7441
c, nm	6.2189
α, deg	90.00
β, deg	90.00
γ, deg	90.00

The stability of the crystal was initially tested by Nasi via 2 ns molecular dynamics

calculations at 100 K using the TraPPE force field. Apart from initial minor adjustments to the lowest energy of the force field, the crystal remained stable over the course of the simulation.

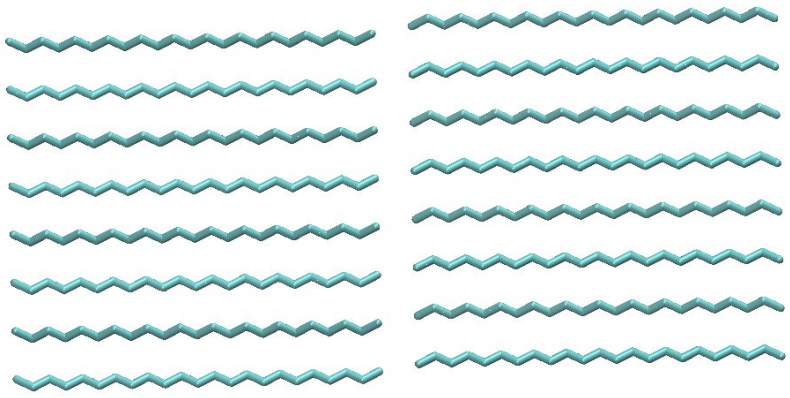

(a) view on the bc plane

(b) view on the ab plane

Figure 4.19: *An orthorhombic crystal of 64 molecules of tricosane, view from bc and ab planes. The molecules further away are shown in the dusk shade*

To serve as a nucleation centre, the crystal must not melt in the initial preparation of a system. The crystal is initially built from tricosane molecules and so has exactly the same properties as the rest of the system. Positional restrains are therefore needed to prevent molecules from moving from their positions and hence to prevent the crystal from distorting. There are a few approaches to implementing the necessary restrains:

- Introducing energy penalties for movement of atoms.

- Lowering the temperature (or freezing) of a selected group of atoms and hence significantly slowing their movements.

- Increasing the mass of the atoms, by such requiring higher energy for them to move.

In this work, positional restraints were applied by increasing the mass of atoms in the crystal. For CH_3 united atoms masses were increased to 300 g/mol and CH_2 to 250 g/mol. This gave a moderate restraint, that holds at 280 K, but for higher temperatures is less effective.

The positionally restrained crystal was surrounded by 1000 tricosane molecules in the melt. The calculations were performed at temperatures around the crystallisation point. Simulation parameters are shown in Table 5.4.

Table 4.9: *Parameters for simulated annealing of tricosane system with a nucleation centre*

Integration	Leap frog
System size	Tricosane: 1000 molecules
	Crystal: 64 molecules
Step size	2 fs
Length of calculation	30 + 30 + 40 ns
Periodic boundary	xyz
Ensemble	*NPT*
Temperature	280 K, 270 K, 260 K
Thermostat	Nosé-Hoover
Pressure	1 bar
Barostat	Parrinello-Rahman
Compressibility	9×10^{-5} bar^{-1}

Figure 4.20 shows the final conformation at 270 K resulted from hererogeneus nucleation simulation. Tricosane molecules have formed a crystal around the nucleation centre (dark blue). Lowering the temperature further to 260 K did not lead to significant changes.

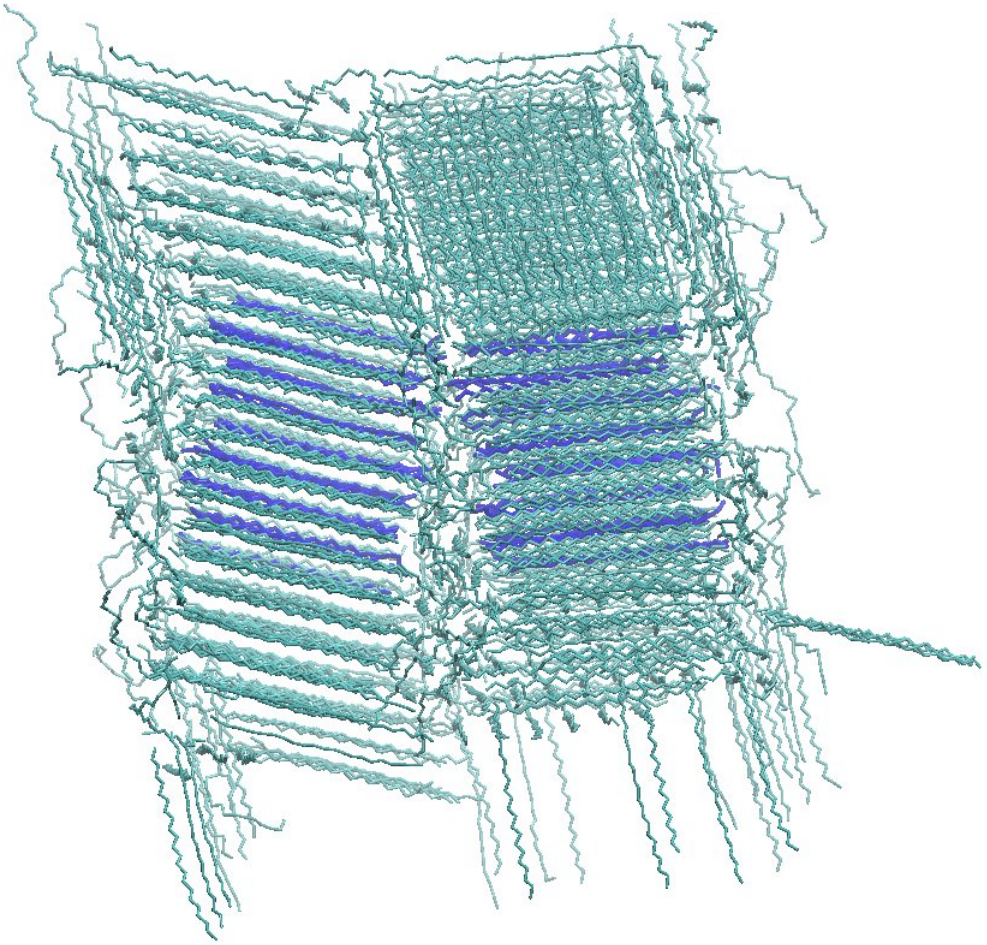

Figure 4.20: *Snapshot of tricosane system with positionally restrained tricosane crystal, acting as nucleation centre (dark blue) at 270 K*

The nucleation centre triggers the formation of two stacks, that no longer collapse into a herringbone alignment. Instead, chains from the melt grow around the nucleation site. Remaining chains either pack perpendicularly to the main stacks or get forced between lamella layers.

The vector analysis of the system was performed using the procedure described in section 4.4.1. The vector orientations of simulations of tricosane with (Figure 4.21) and without (Figure 4.11(b)) the presence of a nucleation centre can now be compared. We observe that the latter produces a finer aligned but much larger number of peaks, corresponding to formation of nano-domains. The system with the nucleation centre shows peaks associated with the main crystal and a few small ones. These corresponds to the formation of a dominant stack (started from the nucleation crystal) and a few smaller surrounding crystals.

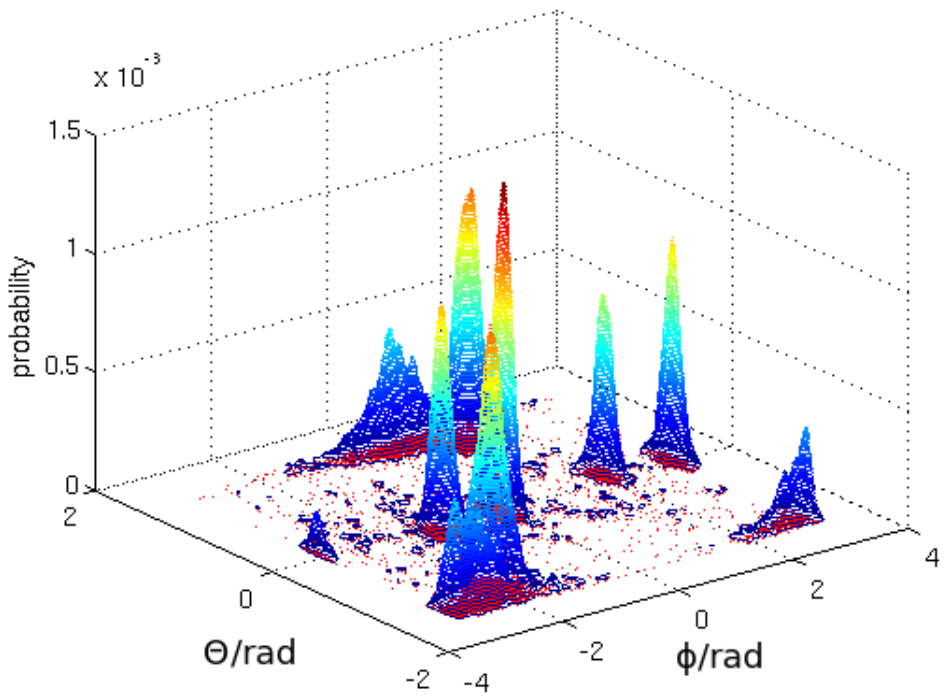

Figure 4.21: *Normalised vector distribution of tricosane crystal formed around the nucleation centre at 270 K*

The unit cell parameters for the crystal is given in Table 4.10. The unit cell parameters

Table 4.10: *Unit cell parameters for tricosane crystal formed around nucleation crystal at 270 K*

	Experimental [3]	Measured sample	Average
a, nm	0.4967	0.4770 0.5500 0.4378 0.4482 0.4665	0.4759
b, nm	0.7441	0.7311 0.7620 0.7971 0.8162 0.8333	0.7963
c, nm	6.2189	6.3616 6.4881 6.3943 6.2190 5.9193	6.2765

of homogeneous (Table 4.4) and heterogeneous (Table 4.10) crystals are very close in values, and agree well with the experimentally measured ones. The introduction of the nucleation centre prevented the collapse of new forming crystal stacks into a herringbone pattern.

4.7 Fuel solvents

In this section we investigate the interaction between common solvents and paraffin molecules at crystallisation. There are two main types of solvent in diesel fuel: aromatic and aliphatic. Toluene and ortho-xylene are commonly found in diesel fuel and are also used in the experimental crystallisation studies of paraffins. Aliphatic solvents are a wide range of linear, branched and cyclic molecules. In this work dodecane and isododecane are chosen as representatives of the first two classes.

In typical commercial diesel mixtures a large proportion of solvent is present. To obtain such concentrations for 500 tricosane molecules 90 000 molecules of solvent would be necessary. This cannot currently be achieved by simulation at a molecular level. Fo this reason we will use 1:1 ratio.

Solvent molecules are modelled by united atoms using the TraPPE force field. The procedure described in section 4.3 was followed to create four systems of 1000 solvent molecules of each type. The solvent and 1000 molecules of tricosane were randomly placed into a simulation box, providing even dispersions of both. Obtained systems were allowed to mix at 500 K and 1 bar, where the solvent is in the gas phase. Subsequently, the temperature was brought down to 350 K, where both solute and the solvent are in the liquid phase.

4.7.1 Solvent and tricosane

Each system of solvent and tricosane was simulated, decreasing temperature stepwise from 350 K to 260 K. Parameters describing the simulations are given in Table 5.6.

Table 4.11: *Parameters for simulated annealing of tricosane – solvent mixtures*

Integration	Leap frog
System size	Tricosane 1000 molecules, Solvent 1000 molecules
Step size	2 fs
Length of calculation	5 + 2 + 2 + 2 + 2 + 2 + 4 + 4 + 10 + 30 ns
Periodic boundary	xyz
Ensemble	*NPT*
Temperature	350 340 330 320 310 300 290 280 270 260 K
Thermostat	Nosé-Hoover
Pressure	1 bar
Barostat	Parrinello-Rahman
Compressibility	9×10^{-5} bar^{-1}

We observe that the formation of crystals in the presence of solvent occurs at 260 K, that is 10 K lower than pure tricosane. This is due to a decrease of the chemical potential in the liquid, arising from mixing, leading to a freezing point depression.

The level of mixing of tricosane and solvent is assessed at 300 K and 260 K. Calculating the partial density distribution for each component of the mixture across the simulation box is indicative of their dispersion level, Figure 4.22. All four mixtures are liquid at 300 K. The closely uniform distribution (dotted line) of densities of both components indicates a high level of mixing and a uniform distribution, as also observed experimentally at this temperature [27].

At 260 K, when crystallisation occurs, the distribution of densities (solid line) shows variation throughout the simulation box. The peaks in density of the tricosane (black line) indicate the position of crystals, while the solvent (red line) is displaced to other regions of the simulation box.

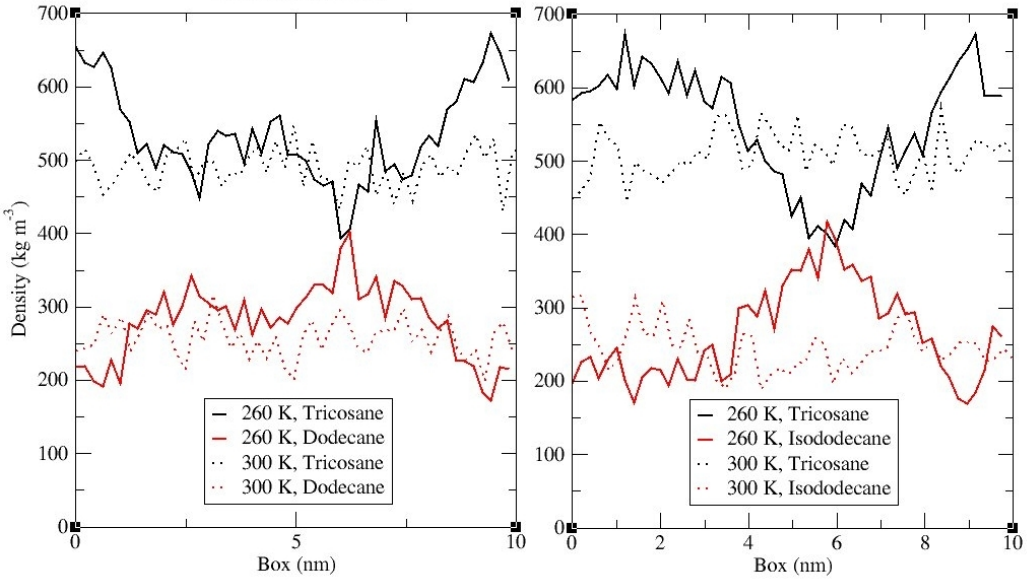

(a) tricosane + dodecane

(b) tricosane + isododecane

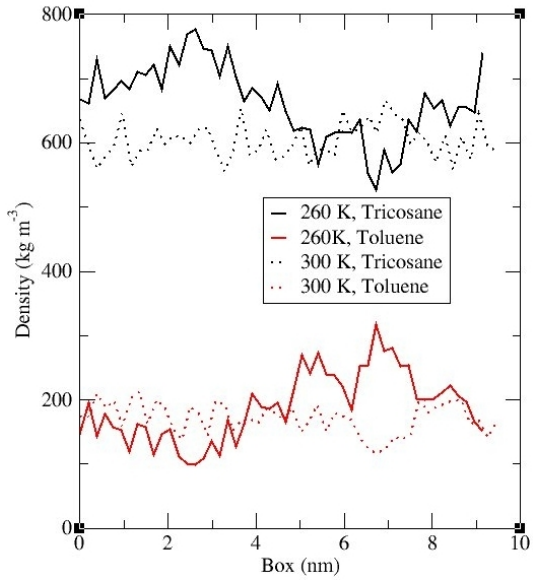

(c) tricosane + toluene

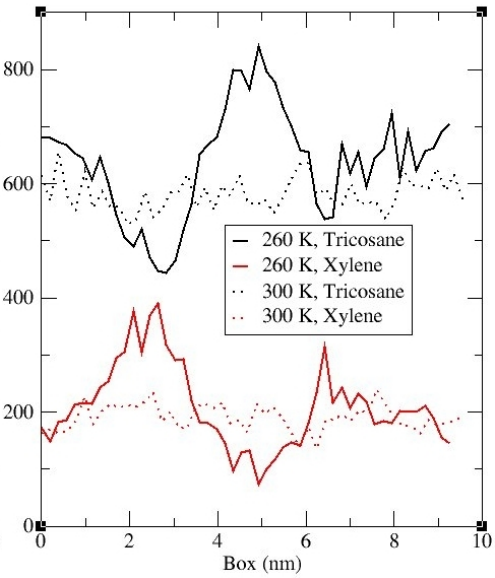

(d) tricosane + xylene

Figure 4.22: *Partial densities of tricosane (black) and solvent (red) at 300 K (dotted line) and 260 K (solid line)*

We note that the crystallisation from the solvent is very slow. To promote a faster crystallisation, we have introduced a nucleation centre to the simulation box. Heterogeneous nucleation in the presence of the solvent is discussed in the following section.

4.7.2 Solvent, tricosane and crystal

It was shown earlier (Section 4.6) that the presence of a nucleation centre induces crystallisation. The tricosane – solvent system is larger in volume than the previously studied tricosane (Section 4.6) and so will benefit from a larger nucleation crystal surface. The new nucleation centre was created by a larger crystal comprised of 256 tricosane molecules, as shown in Figure 4.23.

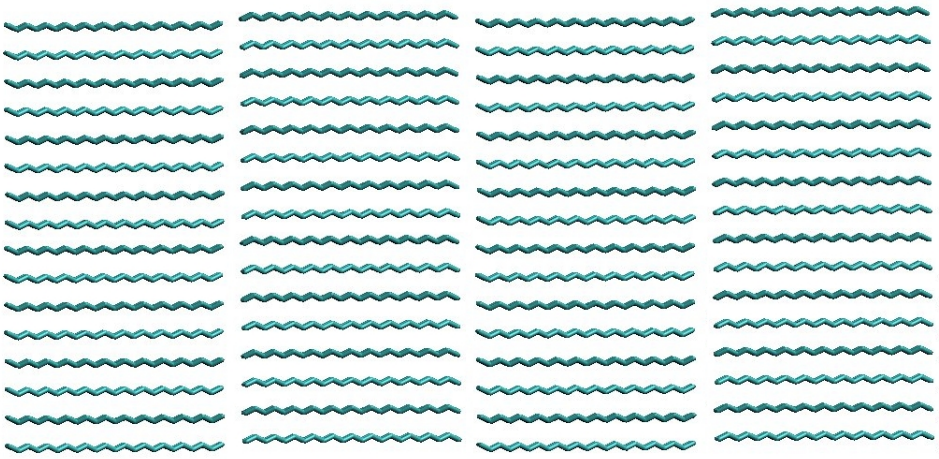

Figure 4.23: *Positionally restrained tricosane crystal, used as nucleation centre*

The crystal was then surrounded by a tricosane melt and solvent mixture to fill a cubic box of $15\times15\times15$ nm^3. The number of molecules for each simulation setup is given in Table 4.12 and the the simulation parameters are given in Table 4.13.

The resulting crystal configurations for each system are shown in Figure 4.24. Their corresponding density profiles at 260 K are given on Figure 4.26. The crystal, acting as a nucleation centre, is positionally restrained by increasing its weight and so has

Table 4.12: *Number of molecules of nucleation centre crystal, tricosane and solvent in each system*

Solvent type:	Crystal	Tricosane	Solvent
Dodecane	256	2207	2520
Isododecane	256	2156	3006
Toluene	256	2646	3465
Xylene	256	2515	3635

Table 4.13: *Parameters for simulation of tricosane – solvent systems with nucleation crystal*

Calculation parameters:	
Integration	Leap frog
System size	As given in the table 4.12
Step size	2 fs
Length of calculation	65 ns
Periodic boundary	xyz
Ensemble	*NPT*
Temperature	260 K
Thermostat	Nosé-Hoover
Pressure	1 bar
Barostat	Parrinello-Rahman
Compressibility	9×10^{-5} bar^{-1}

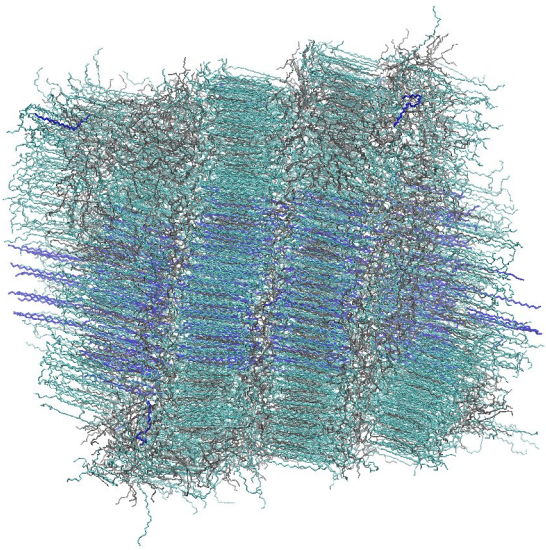

(a) tricosane + dodecane + crystal

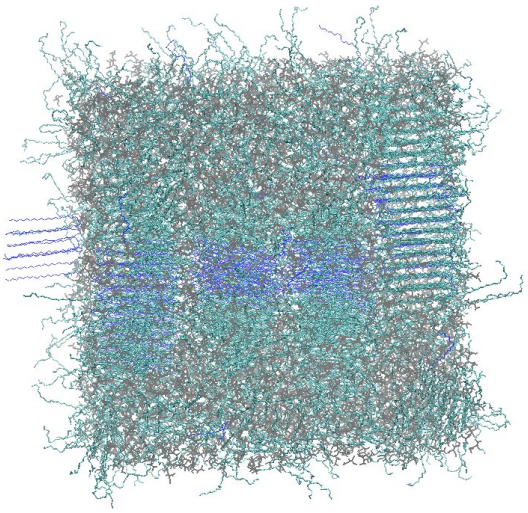

(b) tricosane + isododecane + crystal

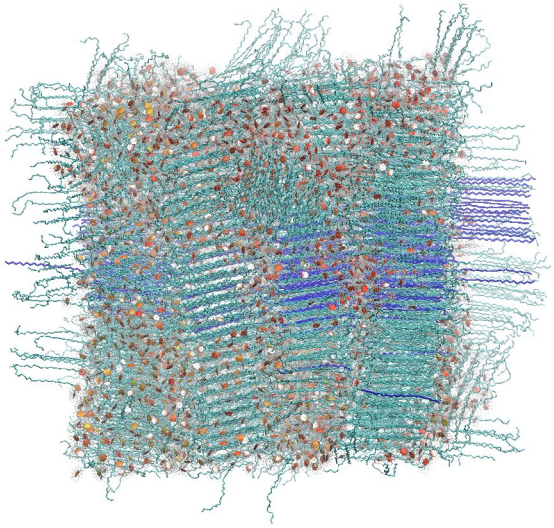

(c) tricosane + toluene + crystal

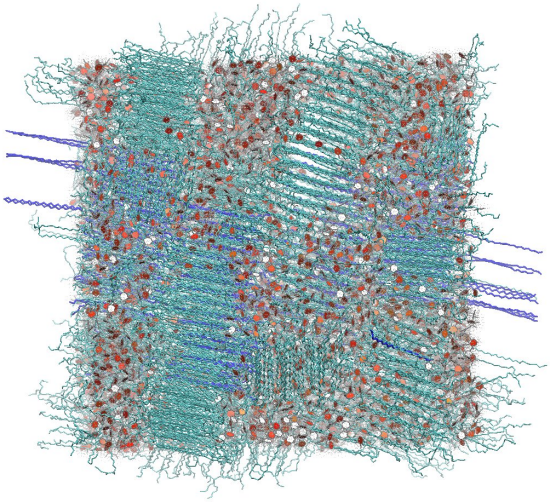

(d) tricosane + xylene + crystal

Figure 4.24: *Tricosane (cyan) in four solvents (dark grey) from heterogenious crystallisation calculations at 260 K: dodecane (a), isododecane (b), toluene (c) and xylene (d). The original nucleation crystal is shown in blue*

higher density than tricosane, as seen on the density profiles. The increase in the density (grey - positionally restrained crystal, black - tricosane) corresponds to the formation of a crystal stack. In all four systems, tricosane crystallises from the surface of the nucleation centre. Most of the solvent is expelled from the crystal and surrounds the crystal stacks, while part of it is trapped within crystal stacks. The level of inclusion of solvent in the crystal strongly depends on the nature of the solvent. Both aromatic solvents are almost entirely expelled from the crystal, unlike aliphatic ones. Dodecane is a linear molecule, strongly interacting with longer *n*-alkanes. Additionally it can be accommodated within the crystal stack with only small distortion of the overall structure. This is not the case for isododecane. Isododecane has similar interactions to dodecane and longer paraffins, but due to its branched structure cannot be easily embedded into the crystal. Isododecane is also expelled, but not to such a high extent as the aromatic solvents.

In all four solvents crystallized paraffin molecules show *gauche* defects at the ends. The level of distortion varies between systems. Since paraffin chains are linear and normally in an extended all-*trans* configuration within a crystal, and so the radius of gyration is related to its dihedral angles. Figure 4.25 shows the distribution function for the radius of gyration of tricosane in four solvents with the pure tricosane system given as a reference. In the presence of solvents, the shape of the distribution curve shows a large variation of conformations (wide distribution). This is not the case for pure tricosane system (black line). When compared to a melt (Figure 4.7, dotted lines) it appears that the average radius of gyration is larger and the distribution is not as broad. The average radius of gyration of tricosane in four systems and a reference is given in Table 4.14.

Table 4.14: *Average radius of gyration of tricosane in four solvents and of a pure tricosane system at 260 K*

System solvent	Radius of gyration, nm
Dodecane	0.749
Isododecane	0.730
Toluene	0.766
Xylene	0.761
Pure tricosane	0.834

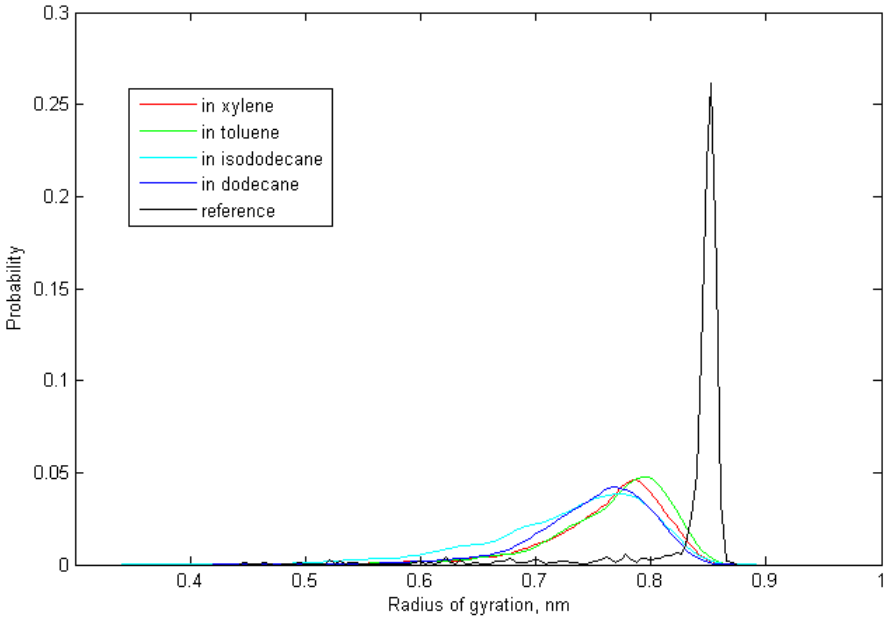

Figure 4.25: *Probability distribution of the radius of gyration of tricosane molecules (tricosane in the nucleation crystal is not included) from heterogeneous nucleation at 260 K in four model solvents. The reference (black line) is taken from the earlier study of pure tricosane at 260 K.*

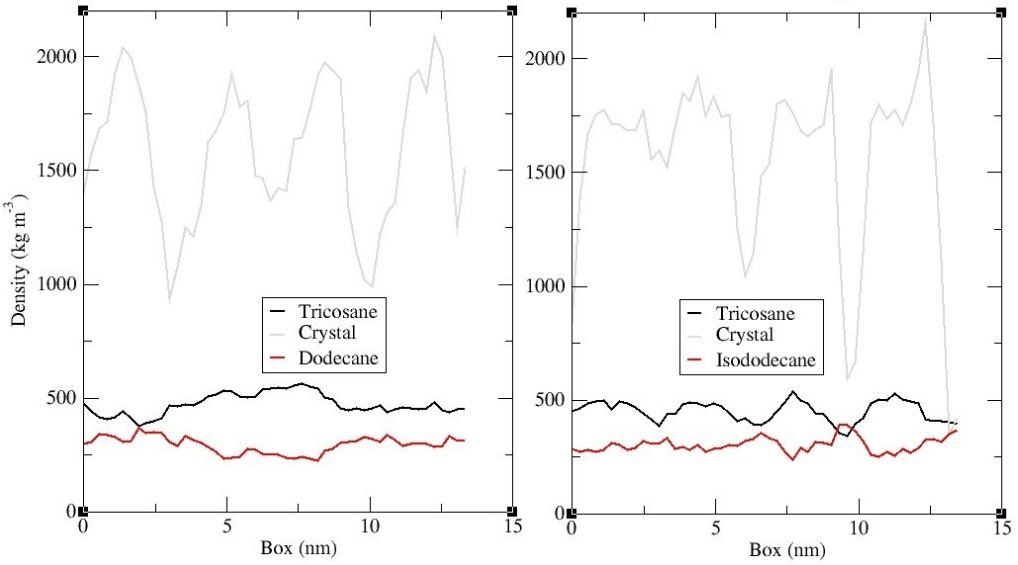

(a) tricosane + dodecane + crystal

(b) tricosane + isododecane + crystal

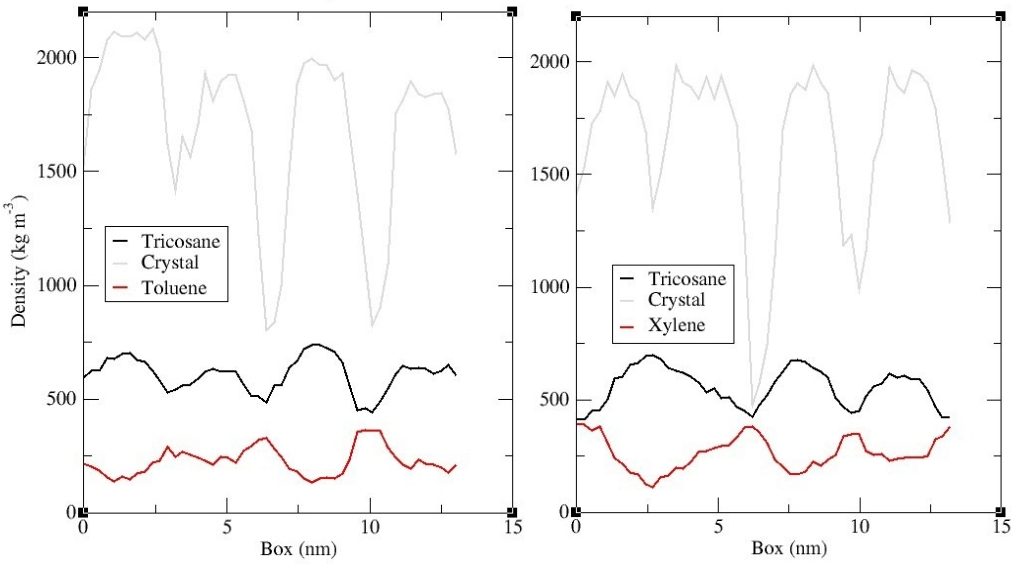

(c) tricosane + toluene + crystal

(d) tricosane + xylene+ crystal

Figure 4.26: *Partial densities of tricosane (black) and solvent (red) and positionally restrained crystal (grey) at 260 K. Note that initial seed crystal is heavier and so appears at a much higher density*

The vectorial analysis described in Section 4.4.1, highlights the level of alignment in the crystal formed from the various solutions. We exclude the positionally restrained crystal from the analysis, as in all four cases it is very well aligned and will mask the results of the crystal grown from the solvent.

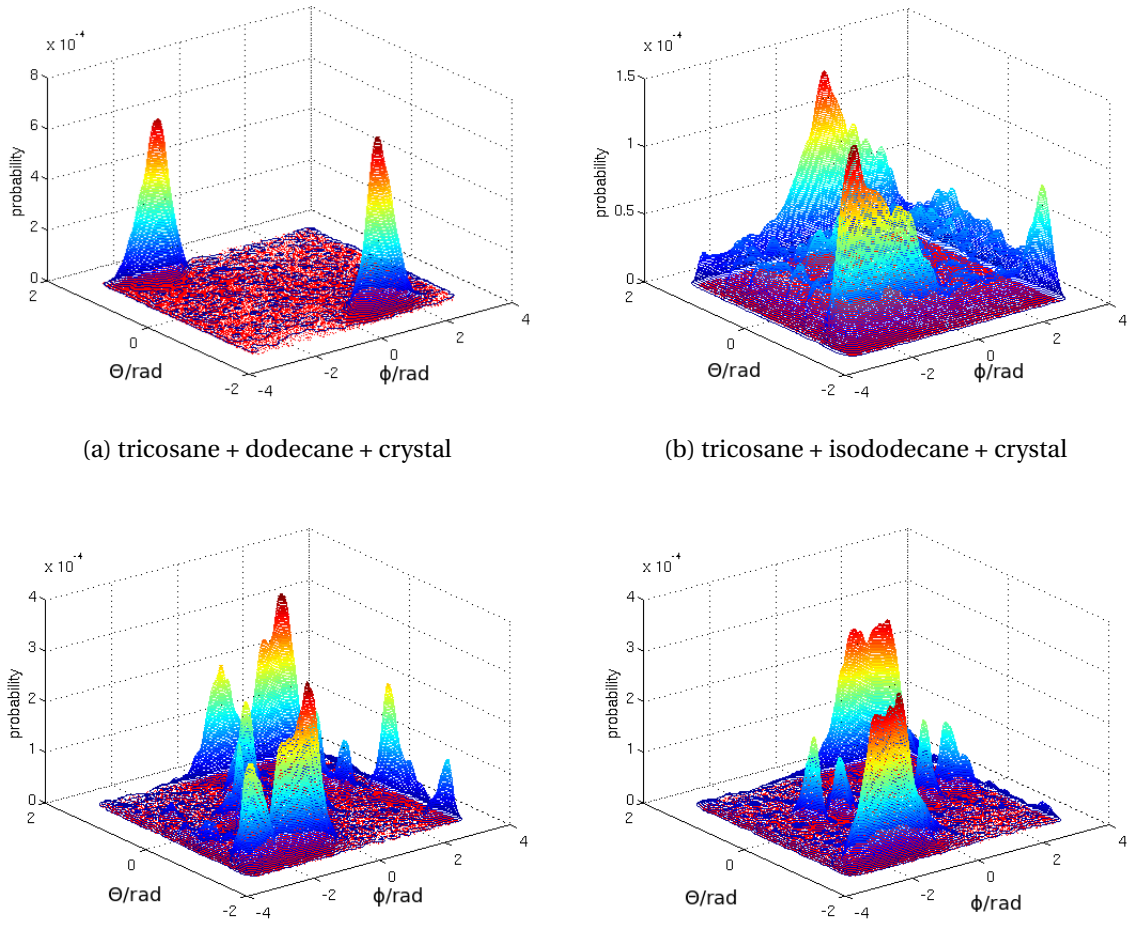

(a) tricosane + dodecane + crystal

(b) tricosane + isododecane + crystal

(c) tricosane + toluene + crystal

(d) tricosane + xylene + crystal

Figure 4.27: *Normalised vector distribution of tricosane crystallised from four solvents: dodecane (a), isododecane (b), toluene (c) and xylene (d) at 260 K*

Figure 4.27 shows the vectorial distributions from tricosane molecules in four solvents. Both aromatic solvents produce a well ordered crystal. This is due to the higher level of displacement of the solvent from the crystal, as demonstrated by the density distribution (Figure 4.26c and d). The tricosane crystals grown from these solvents has a larger radius of gyration, due to the better aligned central part of the molecule.

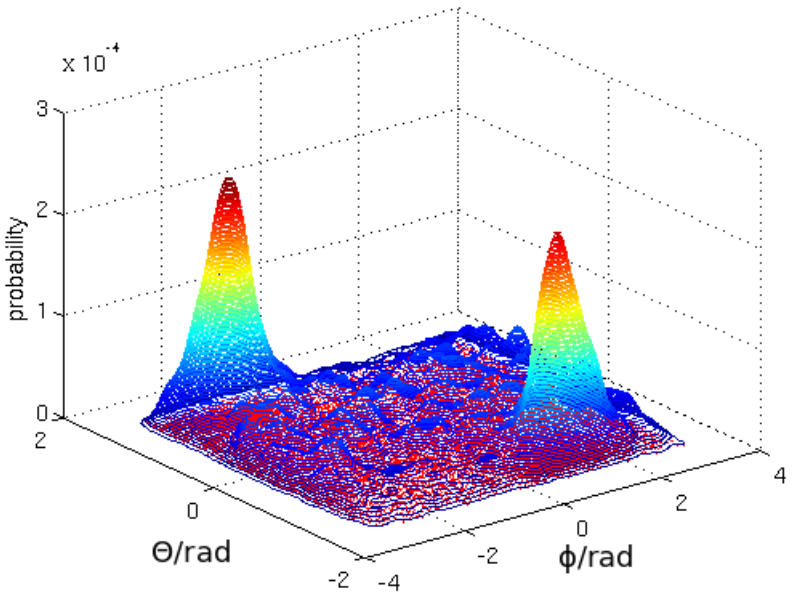

Figure 4.28: *Normalised vector distribution of dodecane from tricosane, dodecane and the nucleation centre system at 260 K*

Toluene and xylene are common aromatic solvents used for growing single paraffin crystal [28–30].

The vectorial analysis suggests a very good alignment of the tricosane crystal formed from the dodecane solvent, Figure 4.27 (a). The dodecane solvent has also the same alignment of vectors as tricosane, Figure 4.28. This can indicate either the co-crystallisation of dodecane solvent or the formation of a separate stack of solvent parallel to tricosane crystal. The density distribution, Figure 4.26 (a), shows a very small dodecane (red line) density decrease at the point of formation of the tricosane stack (black and grey lines). This is indicative of co-crystallisation of both species. This can also be confirmed by visual inspection of the snapshots, Figure 4.24 (a).

By observing a selected crystal from the simulation, Figure 4.29, it is noticeable how the tricosane molecules are well aligned in their central section while being disordered at their ends. Most dodecane molecules (grey) are incorporated into the tricosane crystal (cyan), while the remaining form a non-crystalline layer between crystalline stacks. Tricosane chains create defects to accommodate the void space introduced

by the incorporation of shorter dodecane molecules. Due to the randomly oriented ends of tricosane molecule, the width of the stacks was reduced from 6.2 nm [3] to approximately 4 nm. The unit cell parameters could not be measured accurately due to these large structural distortions.

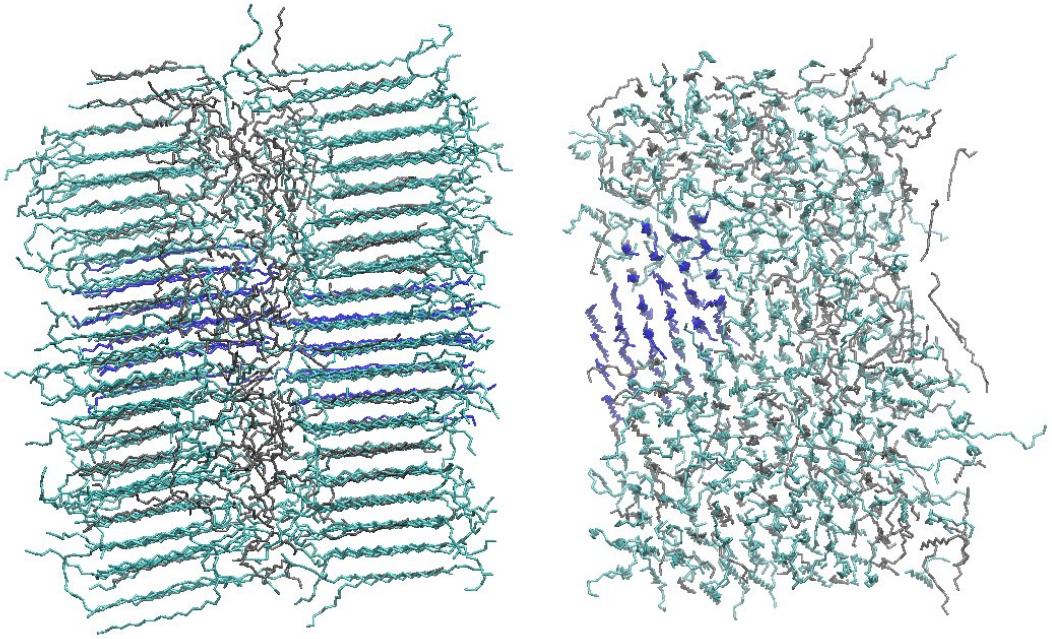

(a) view on the bc plane

(b) view on the ab plane

Figure 4.29: *Tricosane crystal (cyan), formed in the presence of dodecane solvent (dark grey) and a nucleation centre (blue) at 270 K*

In similar way to dodecane, isododecane molecules are integrated between crystal stacks. The branched nature of the solvent causes greater distortion of the ends of the crystallised tricosane. Unlike dodecane, there is no evidence for strong incorporation of solvent into the crystal.

Experimental studies show that a pure tricosane crystal forms from a binary mixture of paraffins, when the difference in length between the solvent is 10 or more carbon atoms shorter [31]. When the difference of chain lengths is smaller, a solid solution forms. The formed solution separates over time into micro-domains of pure paraffin crystals. The extent of this rearrangement is dependent on the differences in paraffin chain lengths [32, 33].

4.8 Conclusions

In this chapter we studied a range of alkane systems and developed approaches for investigation of the crystallisation process.

As a base for further studies, a tricosane model was developed. A simulated annealing procedure leading from melt to crystallisation was established, accounting for the increased equilibration time required for lower temperatures. A nucleation centre was created by applying positional restraints on a tricosane crystal. The use of a nucleation centre reduces the creation of small crystal domains due to supercooling without the need for a substantial increase of the simulation box size.

The crystallisation of binary and tertiary mixtures of paraffins having similar length has been modelled. Such systems are found to co-crystallise into hexagonally arranged lamellae. The presence of different length alkanes creates disorder in a crystal and promotes the formation of *gauche* defects.

Crystallisation from four common solvents, present in the diesel fuel, was modelled. General behaviour trends were characterised for the solvent types. Aromatic solvents are shown to separate from the crystal, leading to the formation of a well aligned crystal structure. Aliphatic solvents, with similar interactions to tricosane, show a lower expulsion rate from a forming crystal, and can therefore co-crystallise with tricosane.

All simulations were subject to the two common limitations of computational studies: a relative small system size and a relative short timescale. Additionally, cooling rates are rapid in comparison to real experiments. The inclusion of a nucleation centre made the study of crystallisation more effective. Nevertheless, these studies would benefit from an additional coarse grained study. A coarse grained model of alkanes, capable of reproducing crystallisation is developed in Chapters 6 and 7.

A knowledge of tricosane crystallisation, the effect of a nucleation centre and the approach to annealing developed here, form the base for the investigation of the effect of additives on wax formation presented in the next chapter.

5 Fuel additives

5.1 Introduction

In the last decades, the use of fuel additives has been steadily growing [34–36]. Additives are constantly adapted in order to increase their performance in specific conditions [37–39]. However, the current lack of understanding about their mechanism of action has limited these improvements.

In this chapter we study pour point depressants for diesel fuel, and more specifically wax crystal modifiers. For this purpose, we model the interactions between paraffin systems and additives during crystal growth. Four common additives and a modification of each are investigated. Generally, additives can be separated into two types – linear and comb structured. Ethylene vinyl acetate (EVA) is a typical example of a linear additive. There have been numerous efforts aimed at improving EVA and currently a few modifications of it are available [40, 41]. By varying the length and proportion of side chains it is possible to adjust this additive for use over a wider temperature range. It is not uncommon to use a combination of different EVAs in fuel.

Within comb type additives there are a few variations. Polyalphaolefin (PAO) is a stereotypical comb polymer consisting of a backbone with alkane side chains of various lengths. Other side chains, such as acrylates, are also used in comb-type polymers, as in polymethylmethacrylate (PMA) [42]. PMA is typically of a comparable size to PAO, but has methacrylate groups linking alkane side chains and the backbone [43].

Alkylphenol formaldehyde condensates (APFC) consist of a few phenol rings, forming the core of the molecule, and alkane side chains. The lengths of side chains are known to be responsible for the effectiveness of the additive. To date there are a few modifications of APFC having different bridges between phenol rings and containing other elements, such as sulphur and nitrogen [44–46].

In this work we use pure tricosane to model the fuel. Due to the large size of additives the simulation box has to become larger than in previous chapters. To make the simulation of such systems computationally affordable, we have to narrow the range of studied temperatures. To minimise simulation times for crystallisation to start, a nucleation centre, created by a positionally restrained tricosane crystal, is used.

5.2 Ethylene vinyl acetate additive

Ethylene vinyl acetate (EVA) exists in a variety of sizes. Generally, the longer the backbone, the higher the temperatures at which EVA is effective. Additionally, variations in the frequency of side chains and vinyl acetate (VA) groups affects the properties of an additive.

In the following, two model EVA additives are investigated. The first one, EVA1, is relatively short with only a few side chains and VA groups. The second, EVA2, is longer with fewer VA groups but a higher proportion of side chains. The experimental and model characteristics are given in the Table 5.1 and extended structures are shown in Figure 5.1.

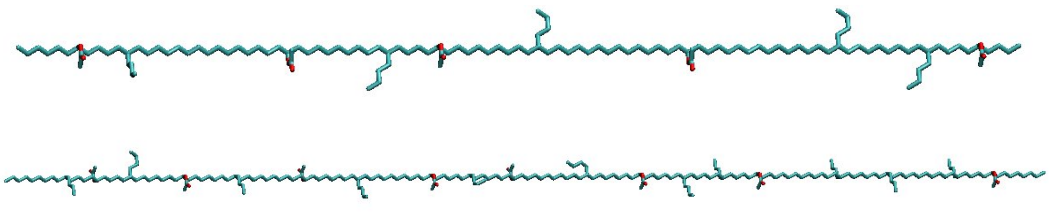

Figure 5.1: *Two extended models of ethylene vinyl acetate additives used in the study: EVA1 - top, EVA2 - bottom*

Table 5.1: *The molecular composition of two models of ethylene vinyl acetate additives used in this study*

		EVA1	EVA2
experim	Vinyl acetate, mol %	15	5
	Side chain, per 100 C atoms	10	8
	Number average molecular weight, g/mol	3000	5000
model	Number of vinyl acetate	5	8
	Number of side chains	5	11
	Backbone length, atoms	105	160
	Molecular weight, g/mol	2435	3245

Ideally, the length of the simulation box should be twice as large as the longest molecule in it. However, since we can assume that the polymer will relax into a coiled conformation, the simulation box can be smaller than a fully extended polymer. Nevertheless, the box size is still dependent on the length of EVA. For this reason both additives are slightly scaled down in size.

Initially each molecule is simulated in vacuum. This allows the molecule to relax from its initial conformation. The details of the simulation parameters are given in Table 5.2.

Table 5.2: *Parameters for simulation of a single molecule in vacuum*

Calculation parameters:	
Integration	Leap frog
System size	1 molecule
Step size	2 fs
Length of calculation	1 ns
Periodic boundary	no
Ensemble	NVT
Temperature	300 K
Thermostat	V-rescale

The initial extended conformation is rapidly lost within the first calculation steps. Both molecules rapidly collapse into a spherical conformation. The radius of gyration fluctuates with an average of 0.78 nm for EVA1 and 0.97 nm for the longer EVA2.

5.2.1 Ethylene vinyl acetate - type 1

In order to investigate the behaviour of EVA1 in the melt during crystallisation, we performed a set of annealing simulations. For the very first simulation, one fully extended EVA1 (radius of gyration 3.5 nm) was placed into a tricosane melt at 500 K and allowed to relax for 2 ns. The system was subsequently cooled to 280 K over 20 ns with 2 ns time step after each 20 K temperature drop. Simulation parameters are given in Table 5.4.

Table 5.3: *Parameters for simulated annealing of EVA1 additive in tricosane*

Calculation parameters:	
Integration	Leap frog
System size	1 molecule EVA1
	1000 molecules tricosane
Step size	2 fs
Length of calculation	24 ns in 2 ns steps
Periodic boundary	xyz
Ensemble	*NVT*
Temperature	500 K – 260 K with 20 K step
Thermostat	Nosé-Hoover
Pressure	1 bar
Barostat	Parrinello-Rahman
Compressibility	9×10^{-5} bar^{-1}

In the melt EVA1 is mixed with tricosane. The radius of gyration of EVA1 fluctuates between 1.6 nm and 1.0 nm, that is larger than when the molecule is interacting only with itself in a vacuum (approx. 0.78 nm), and indicates favourable interactions with the tricosane solvent (polymer swelling). Consistent with our earlier study of crystallisation from a pure tricosane (Section 4.4), obtaining a well-ordered crystal was found to be difficult and micro-domains and glassy structures were formed. For this reason a new system containing a nucleation centre was set up.

EVA1 was added to the earlier investigated tricosane system containing a positionally restrained crystal (Section 4.6). The seed crystal remains undisrupted for temperatures under 280 K. So the system was initially simulated at 280 K for 40 ns and the temperature was then reduced to 270 K for a further 40 ns. We found that the system containing EVA1 crystallises at 280 K. So a further simulation was carried out cooling

from 300 K to 290 K, where it proved possible to study a slower crystallization process in the presence of EVA1. A higher temperature simulation at 400 K was also carried out to provide a comparison structure for EVA1 within liquid tricosane. Simulation parameters are given in Table 5.4.

Table 5.4: *Parameters for simulations of EVA1 additive in tricosane in the presence of a nucleation crystal*

Calculation parameters:	
Intergration	Leap frog
System size	Additive: 1 molecule EVA
	Tricosane: 1017 tricosane
	Crystal: 64 molecules
Step size	2 fs
Length of calculation	10 ns
	10 + 40 ns
	40 + 40 ns
Periodic boundary	xyz
Ensemble	*NPT*
Temperature	400 K
	300 + 290 K
	280 + 270 K
Thermostat	Nosé-Hoover
Pressure	1 bar
Barostat	Parrinello-Rahman
Compressibility	9×10^{-5} bar^{-1}

On cooling to 290 K, a large crystalline domain grows across the whole simulation box, and the EVA1 molecule is found to be incorporated between two crystal stacks, as shown in Figure 5.2. Here, the EVA1 backbone creates a turn of a backbone at every position of a side chain. The extended parts of the backbone between each turn are incorporated between tricosane molecules in the crystal stack. In the process EVA1 causes distortions from a perfect crystal structure. This is consistent with one of the proposed hypotheses for the experimental role of EVA additives, which are believed to lead to a change in crystal structure of longer chain alkanes. The incorporation of EVA1 into the crystal stacks is also observed on a partial density profile, Figure 5.3.

It is quite instructive to view the change in EVA1 structure from the higher temper-

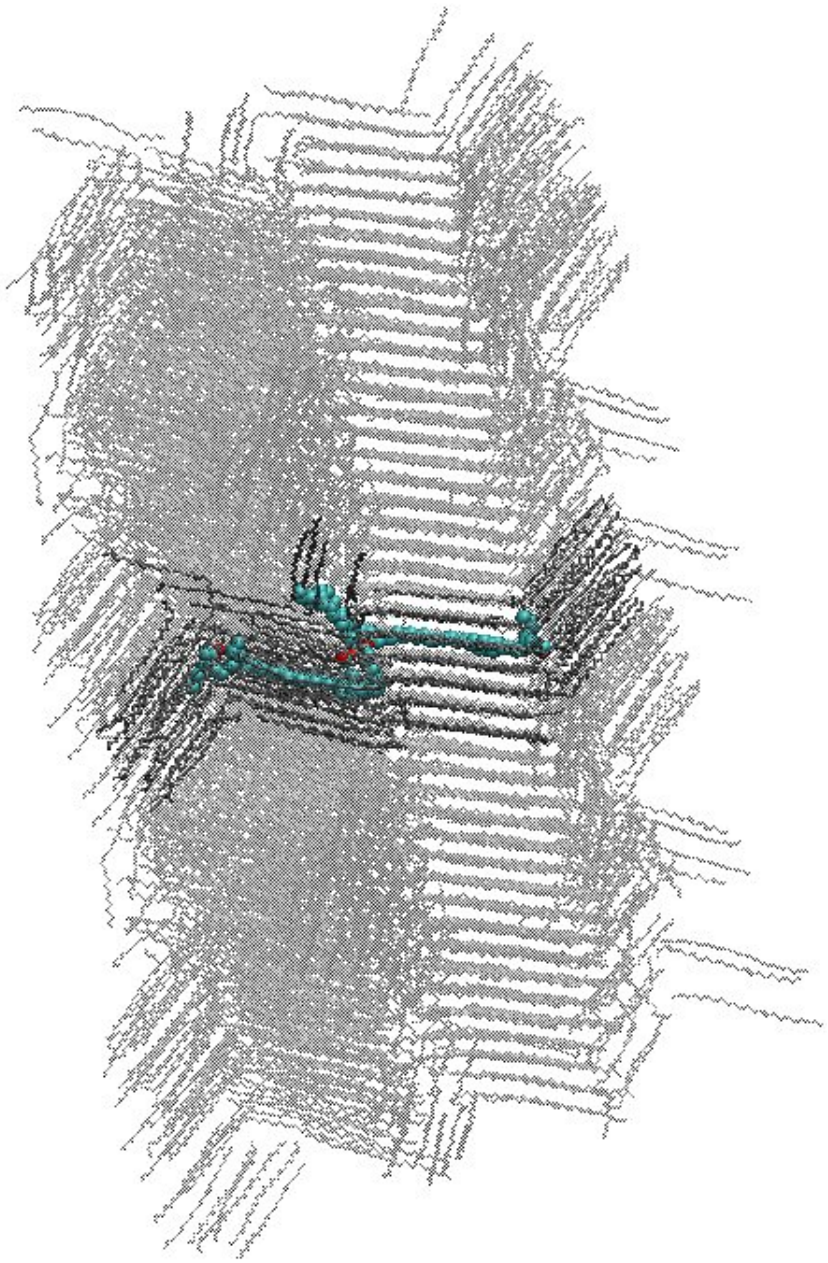

Figure 5.2: *EVA1 additive in tricosane system at 280 K. EVA1 is shown in cyan and tricosane in transparent grey and dark grey for the molecules within 1 nm of EVA1.*

ature liquid simulation at 400 K, to the lower temperature simulations. Figure 5.4 shows typical snapshots of EVA1 structures taken from the simulations. At 400 K, EVA behaves as a typical polymer "sphere" with a radius of gyration of between 1.2 and 0.98 nm. On cooling the chains stretch out with an overall increase in radius of gyration to 1.98 nm at 280 K, accompanied by a considerable increase in anisotropy.

In previous simulations of pure tricosane, analysis of dihedral angle distributions and radius of gyration indicated that, prior crystallization, the number of *trans* conformations increases, Figure 4.8. A similar effect is also observed for a system of tricosane mixed with EVA1. Where a large increase in radius of gyration prior crystallization is observed, Figure 5.5. The sharp peak in radius of gyration at 300 K indicates the presence of chains having a large proportion of *trans* conformations.

The important difference between crystallisation of pure tricosane, and a system of tricosane mixed with EVA1 is the crystallisation temperature. Pure tricosane was found to crystallise at 270 K, and at 280K when nucleated by a positionally restrained crystal. Pure tricosane system was found to crystallise at 270 K, when nucleated with positionally restrained crystal the crystallisation occurred at 280 K. In the presence of EVA1 the crystallisation was observed at 290 K. This suggests that, while EVA1's extended backbone at 300 K contributes to nucleation, its side-chains distorts its linearity, and therefore arrangements of growing lamellar stacks.

A well formed crystal can be observed at 290 K. This allows us to measure the unit cell parameters, Table 5.5. It is not possible to measure the unit cell in the *c*-direction, as the crystal is not sufficiently well aligned. In *a* and *b* directions, the measured tricosane crystal does not show a large change with respect to the pure paraffin system.

In these studies we have observed the behaviour of a small EVA molecule in tricosane at different temperatures. The additive mixes well with the paraffin melt and upon cooling co-crystallises between the stacks. Side-chains create turns in the backbone, backbone co-crystallises with the lamellar layers by such EVA disturbs the growing crystal. For the sizes of system we are able to simulate, we are not able to detect significant change in growth speed along *a,b,c* crystal directions. However, it seems reasonable to hypothesize that the ready incorporation of EVA1 into a growing crystal,

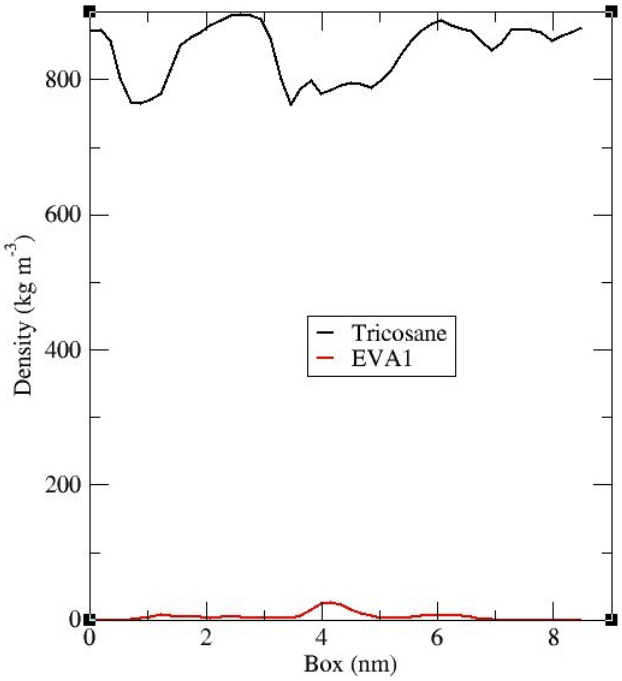

Figure 5.3: *Partial density of tricosane and EVA1 additive in the mixed system at 280 K. The nucleation centre is included as part of the tricosane (with corrected mass)*

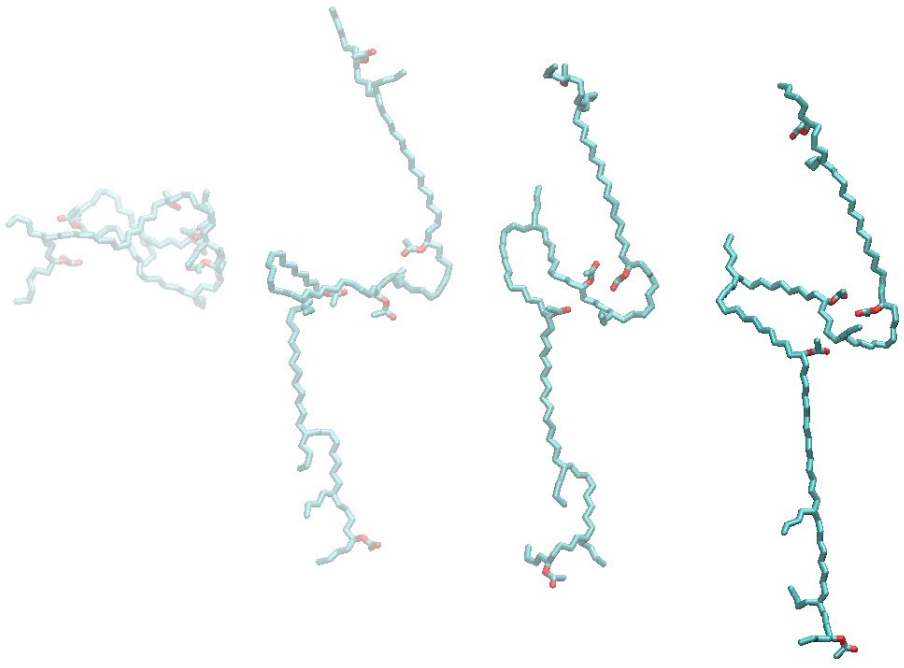

Figure 5.4: *Evolution of EVA1 additive with reduction of temperature from 400 K (furthest left) to 300 K, 290 K and 280 K (furthest right)*

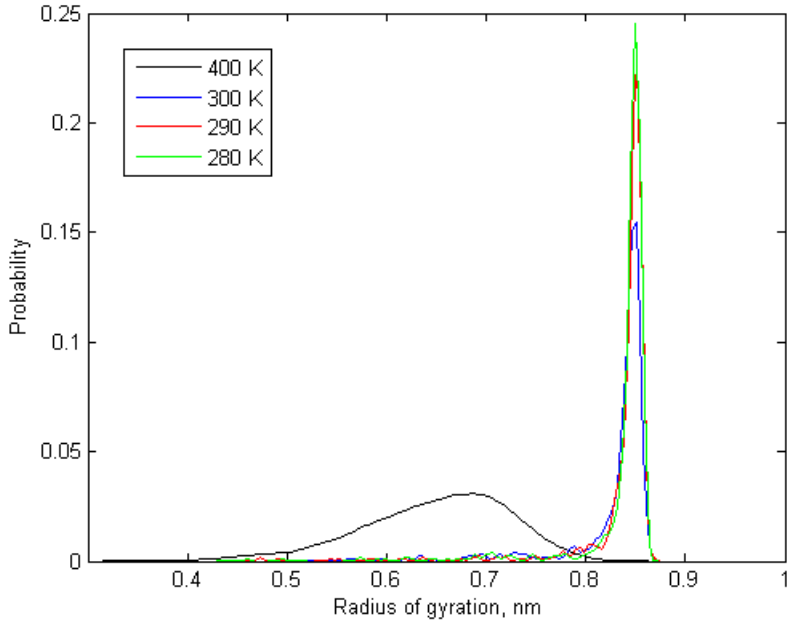

Figure 5.5: *Radius of gyration distribution of tricosane in the presence of EVA1 additive over temperature between 400 K and 260 K*

Table 5.5: *The unit cell parameters of modelled tricosane crystal formed in the presence of EVA1 additive at 280 K, compared to the model of pure tricosane crystal and experimental measures*

	Experimental	Computational	
	Pure tricosane [3]	Pure tricosane	with EVA1
a/ nm	0.4967	0.4759	0.4747
b/ nm	0.7441	0.7963	0.8132
c/ nm	6.2189	6.2765	-

as seen in this study, provides the underlying mechanism for paraffin crystal modification by the distortion of the growing crystal.

5.2.2 Ethylene vinyl acetate - type 2

EVA2's backbone is longer than EVA1, and requires therefore a larger simulation box. For this reason, the EVA2 system was designed to be three times larger and so only a limited range of temperatures can be simulated. Table 5.6 summarises the system size and parameters for the calculation.

Table 5.6: *Parameters for simulated annealing of the EVA2 additive in tricosane in the presence of a nucleation crystal*

Calculation parameters:	
Integration	Leap frog
System size	Additive: 1 molecule EVA
	Tricosane: 3526 tricosane
	Crystal: 256 molecules
Step size	2 fs
Length of calculation	60 ns and 40 ns
Periodic boundary	xyz
Ensemble	*NPT*
Temperature	280 K and 270 K
Thermostat	Nosé-Hoover
Pressure	1 bar
Barostat	Parrinello-Rahman
Compressibility	9×10^{-5} bar^{-1}

Similarly to the shorter EVA1, at crystallisation the EVA2 unfolds (radius of gyration changes from 1.25 nm to 1.75 nm) and co-crystallises with tricosane, Figure 5.6. The longer EVA2 chain does not unfold to quite the same extent as the shorter EVA1. This is likely to be a combined effect of both relatively rapid cooling of a long chain and a higher frequency of side chains, that create more turning points in the backbone.

EVA additives contain extended regions of a backbone, that trigger crystallisation around themselves. Notably, the length of these regions is just under a half of the length of the alkane chains. This distorts long range lamellar structure of the crystals

forming around the additive.

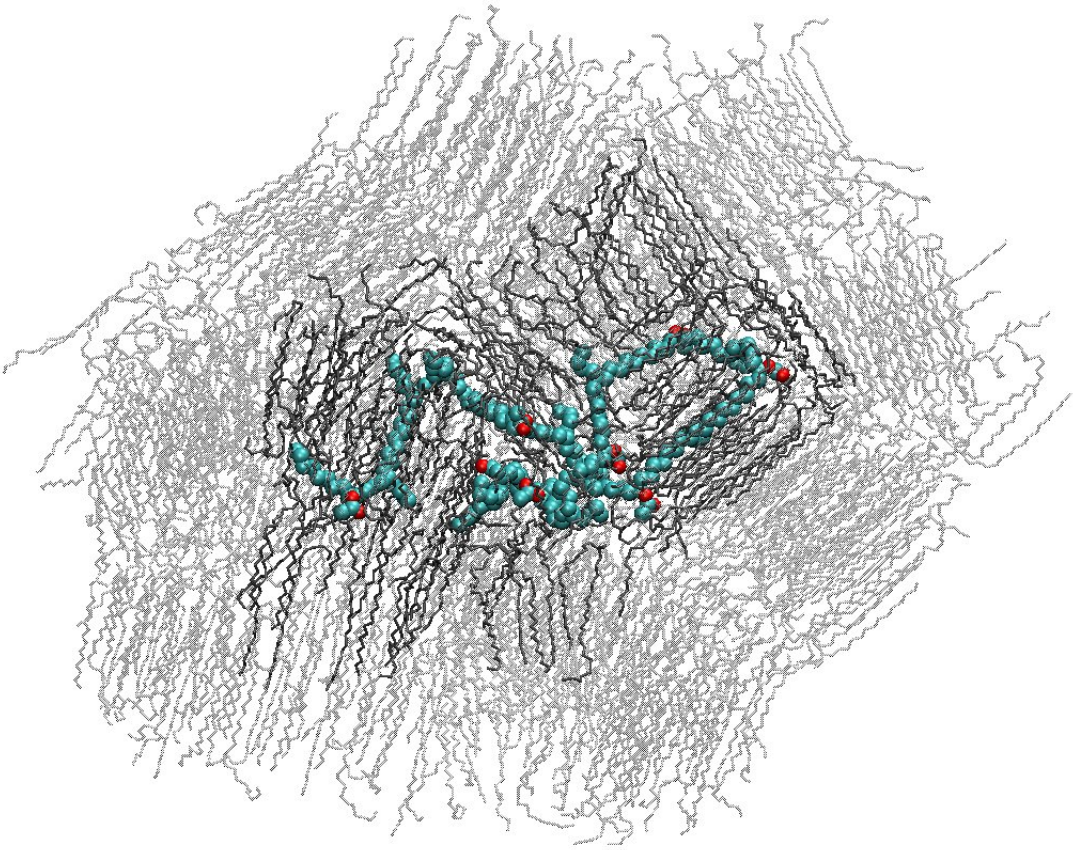

Figure 5.6: *EVA2 additive (shown in bold cyan) and surrounding tricosane system (transparent grey) at 270 K. Tricosane molecules within 5 nm from the additive are shown in dark grey*

To further investigate this hypothesis, longer simulations with slower cooling rates should be performed. This is not currently achievable by atomistic methods and a future coarse grained model will be useful for such studies.

Experimental studies have shown that EVA changes the shape of the crystal from plate-like to needle-like [47]. This is due to changes in growth rates of crystal planes caused by the additive. In our work a relatively small cubic simulation box is used. This does not allow to observe the variation in crystallisation rates. This is a very interesting side of crystallisation and it may be that future coarse-grained methods will allow this effect to be studied.

5.3 Polyalphaolefin additive

Polyalphaolefins (PAO) are comb-type molecules, where shorter and longer linear alkyl side chains alternate. Typically, there is one short side chain for every four long ones. The short chain is three to five carbon atoms and the long chain is fourteen to sixteen carbon atoms. The number average molecular weight is 5000 g/mol.

The backbone of the model additive used in this study is fifty-carbon long, with 20 $C_{14}H_{25}-$ and 5 C_3H_5- side chains and an overall weight of 4752 g/mol. This polymer can be isotactic, syndiotactic or atactic. In this work isotactic and atactic models are compared. The extended atactic molecule is shown of Figure 5.7.

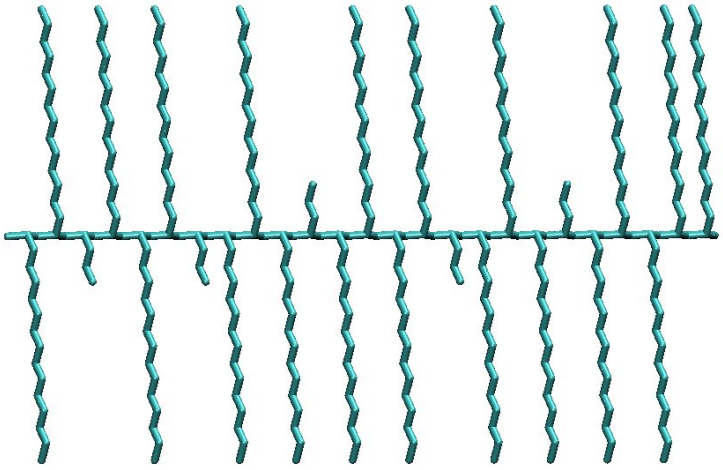

Figure 5.7: *Extended structure of atactic polyalphaolefin additive*

The first step involves relaxing the additive in vacuum. Simulation parameters are the same as for EVA additives, Table 5.2. Both PAO atactic (PAOa) and isotactic (PAOis) form a globular structure in vacuum, Figure 5.8. The average radius of gyration is 1.08 nm for both molecules. Notably, the backbone of the atactic polymer is smoother, straighter and adopts a spiral alignment. The backbone of the isotactic polymer is compressed in order to accommodate all of the side chains on one side.

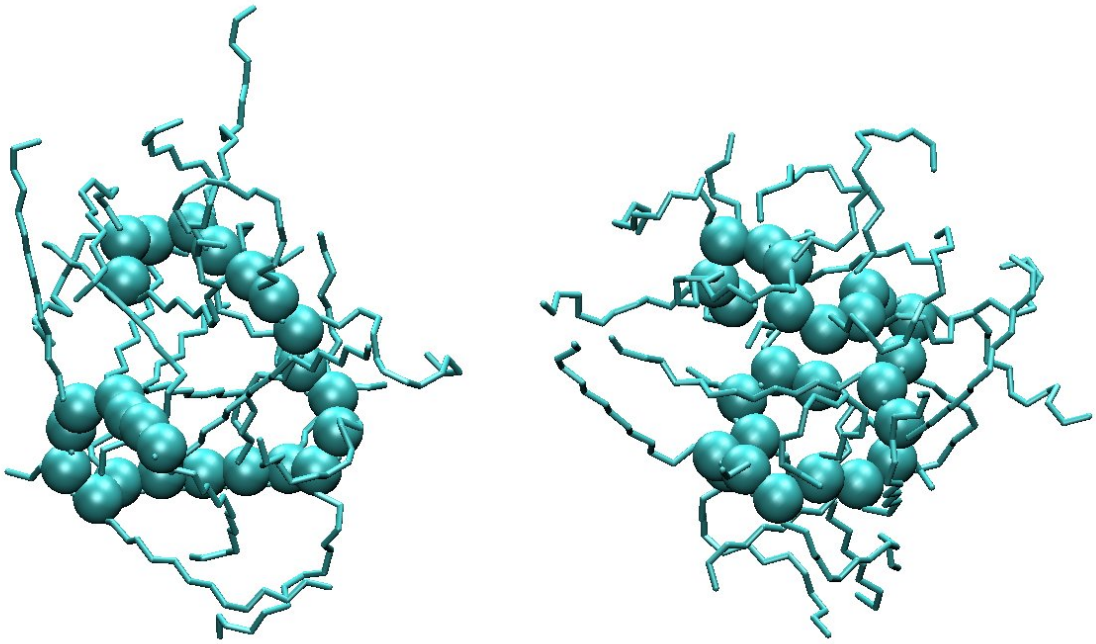

(a) atactic PAO additive

(b) isotactic PAO additive

Figure 5.8: *Atactic PAO (a) and isotactic PAO (b) additives in vacuum at 300 K. The backbone is indicated by large spheres.*

5.3.1 Crystallisation in the presence of PAO additive

PAO is large and so requires a simulation box larger than the EVA1. For this reason the system is studied in the presence of a nucleation centre and at only two temperatures, 270 K and 260 K. The simulation parameters for these studies are given in Table 5.7.

Table 5.7: *Parameters for simulated annealing of PAO additives in tricosane in the presence of a nucleation crystal*

Calculation parameters:	
Integration	Leap frog
System size	Additive: 1 molecule PAO
	Tricosane: 3501 tricosane
	Crystal: 1024 molecules
Step size	2 fs
Length of calculation	220 ns and 100 ns
Periodic boundary	xyz
Ensemble	*NPT*
Temperature	270 K and 260 K
Thermostat	Nosé-Hoover
Pressure	1 bar
Barostat	Parrinello-Rahman
Compressibility	9×10^{-5} bar^{-1}

The crystal stacks nucleate at the seed crystal and grow outwards, trapping the additive. Figure 5.9 shows PAO surrounded by a tricosane crystal within a 2 nm radius. PAOa arranges with a spiral alignment of the backbone, triggering the formation of three non-parallel crystal stacks. In contrast, PAOis lays between the two parallel crystal stacks and does not distort crystal growth to such a high extent. Interestingly, it also appears that some long side chains extend and co-crystallise with paraffin.

The radius of gyration of long, $C_{14}H_{25}-$, side chains shows the level of their extension and is given in Figure 5.10. In Figure 5.7, the colour code is assigned from blue for the first chain to brown for the twentieth chain, as counted right to left. Both PAOa and PAOis show the presence of both fully extended and curled side chains. In the case of PAOa there is a group of fully extended chains (radius of gyration of 0.475 nm) and a second group of relaxed chains with shorter radius of gyration (0.385 nm).

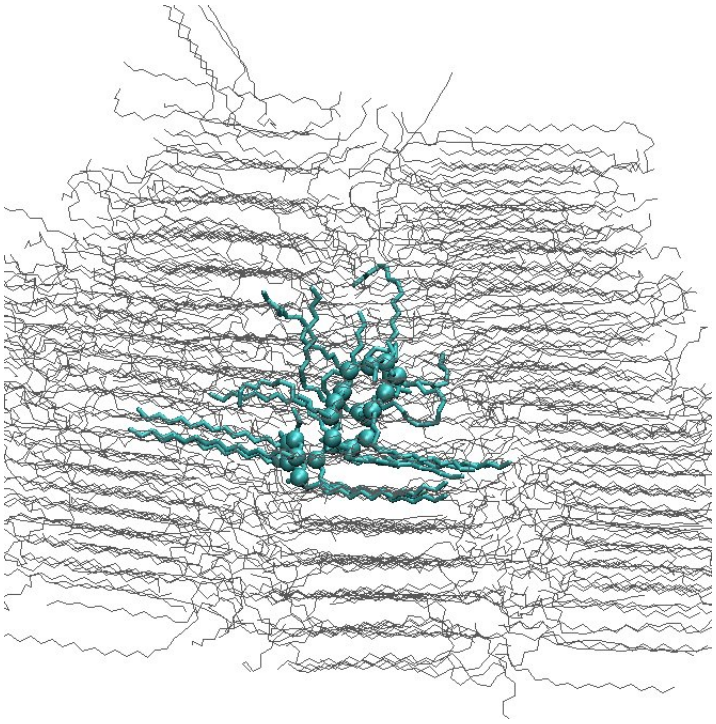

(a) atactic PAO additive

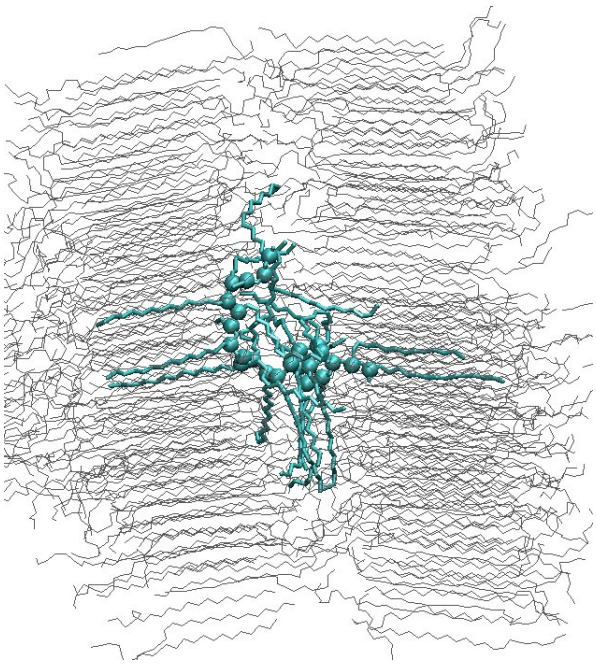

(b) isotactic PAO additive

Figure 5.9: *Atactic (a) and isotactic (b) PAO additives (cyan) surrounded by tricosane molecules (grey) within a 2 nm radius from the additive at 270 K. The backbone of PAO additives is indicated with spheres*

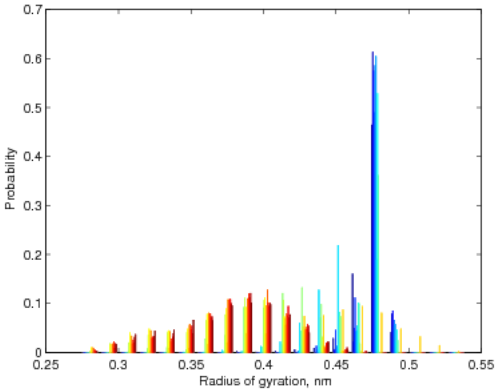

(a) Atactic PAO additive at 270 K

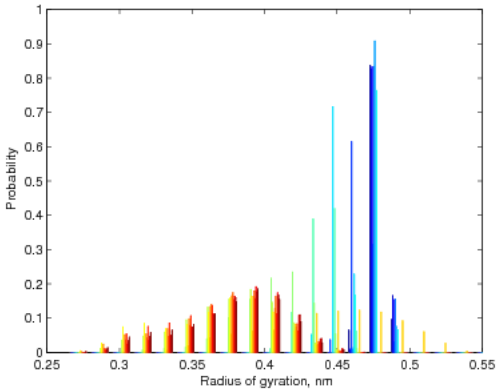

(b) Atactic PAO additive at 260 K

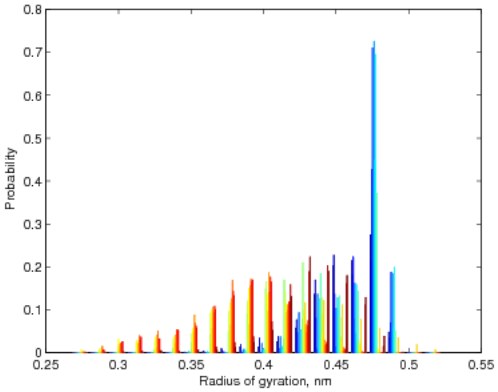

(c) Isoatactic PAO additive at 270 K

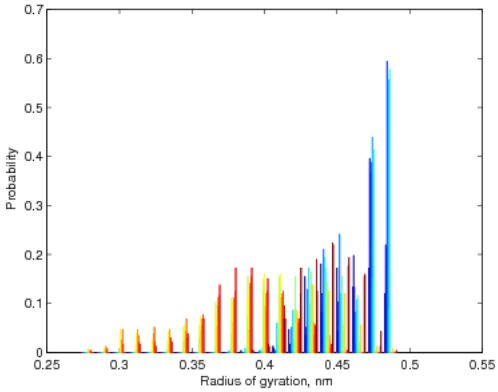

(d) Isotactic PAO additive at 260 K

Figure 5.10: *Radius of gyration of individual long side chains of PAO atactic (a, b) and PAO isotactic (c,d) additives at 270 K (a,c) and 260 K (b,d). The chains are coloured by the number from blue (no. 1) to brown (no. 20), following Figure 5.7 from right to left.*

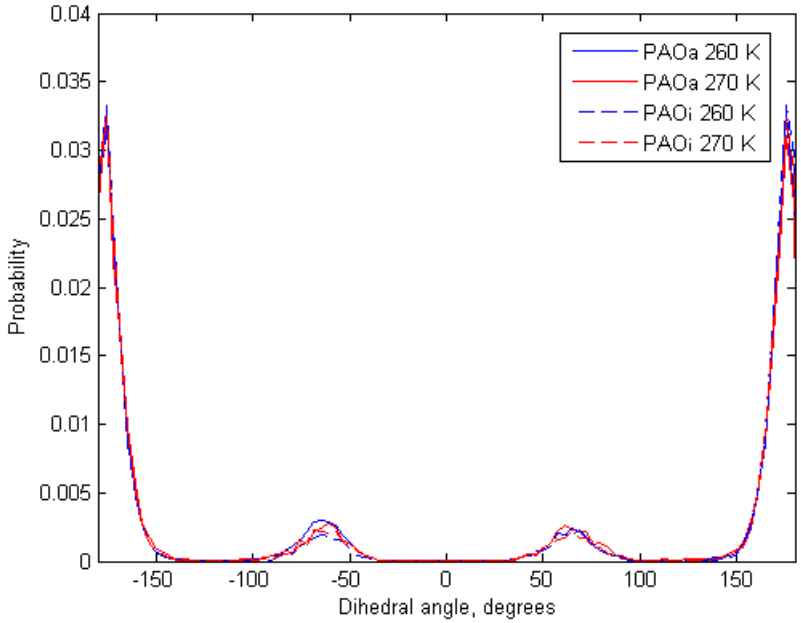

Figure 5.11: *Dihedral angle distribution in long side chains in atactic and isotactic PAO additives at 260 K and 270 K*

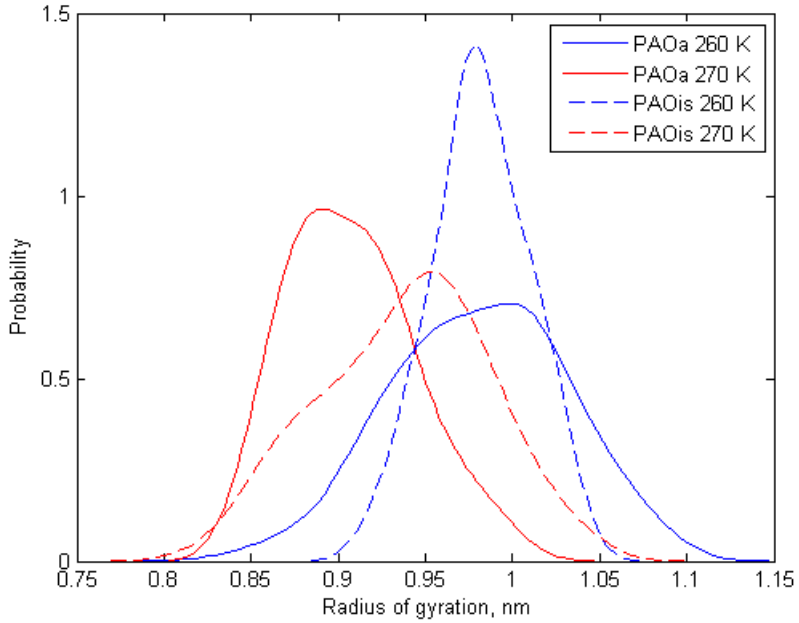

Figure 5.12: *Radius of gyration of backbone in atactic and isotactic PAO additives at 260 K and 270 K*

Notably, the fully extended chains are the first five from one side. PAOis shows a similar behaviour but has a smaller number of fully extended chains, and has a third group with intermediary values at radius of gyration of 0.45 nm. With decreasing of temperature the intensities of radius of gyration peaks increase, while their position and number of the chains per group remains the same.

Figure 5.11 shows the distribution of dihedral angles in the long side chains of PAO additives. The majority of angles are *trans* with dihedral angles of approximately 180^o. The overall proportion of *gauche* dihedral angles at 60^o and -60^o is very low, indicating the presence of well-extended chains, with only a few kinks.

The fully extended chains appear to create an anchor, by co-crystallising with paraffin stacks, as observed in Figure 5.9. The remaining chains are not incorporated into the crystal stacks, leading to distortion of the crystal lamellae. The distortion is largest for PAOa, as the side chains are randomly oriented on the backbone.

The radius of gyration of the backbone for the two PAO additives is shown in Figure 5.12. The mean radius of gyration changes slightly upon cooling of both additives: PAOa is 0.9 nm at 270 K and 1 nm at 260 K; PAOis is 0.95 nm at 270 K and 0.98 nm at 260 K. This small difference indicates that the backbone remains curled with respect to the full extension at 1.85 nm.

5.4 Polymethylmethacrylate additive

Polymethylmethacrylate (PMA) is another comb-type molecule with methyl methacrylate side chains of identical length. The PMA molecule is slightly smaller than PAO with number average molecular weight of 3000 g/mol.

Figure 5.13 shows the extended atactic model of PMA additive we used. The backbone of the model PMA is twentyone carbons long, the side chains are fourteen carbons long and the molecular weight is 2876 g/mol. As with PAO, both isotactic (PMAis) and atactic (PMAa) additives are modelled.

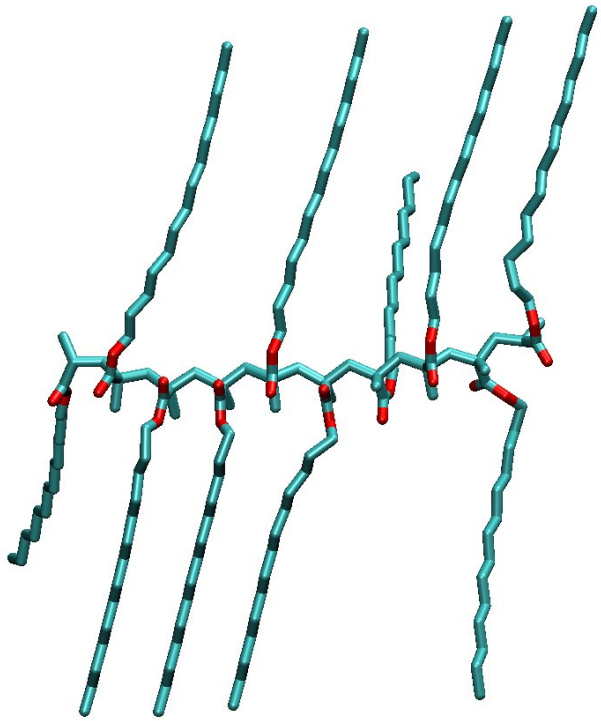

Figure 5.13: *Extended structure of atactic polymethylmethacrylate additive*

As with previous studies, both additives were initially simulated in vacuum, to provide starting structures for subsequent simulations in tricosane. Their simulation parameters are given in the Table 5.2. The average radius of gyration of PMAa in vacuum is 0.89 nm, similar to 0.84 nm for PMAis. Nevertheless, the configurations of the relaxed molecules are very different, as given in Figure 5.14. The backbone of PMAa is extended and has side chains surrounding it. The backbone of PMAis is coiled, with all ester groups and alkyl chains on the same side.

5.4.1 Crystallisation in the presence of PMA additive

The systems containing PMA were simulated at 270 K and 260 K in the presence of a nucleation centre, to facilitate crystal growth. Parameters for calculation are the same as for PAO and given in Table 5.7. The number of tricosane molecules slightly varies – 3526 tricosane molecules were necessary to fill the box with PMAa and 3529 molecules were required for PMAis.

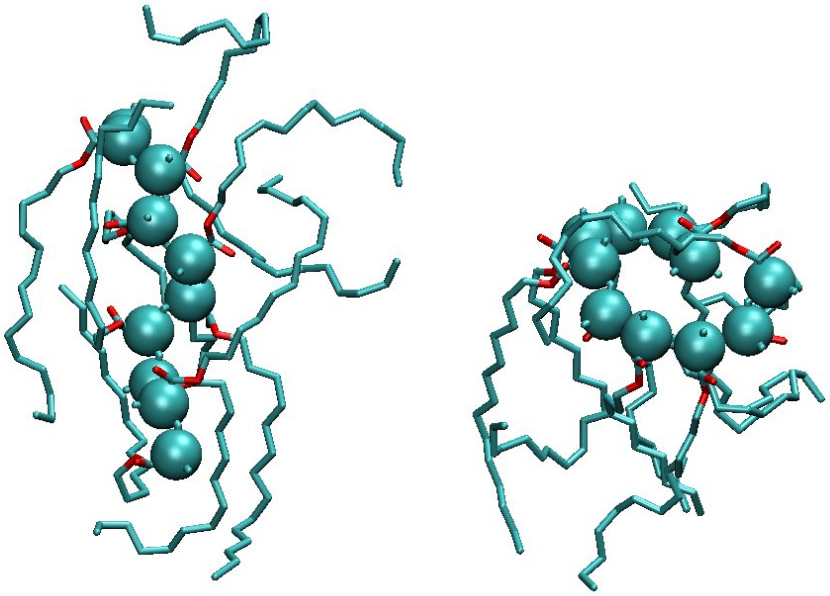

(a) atactic PMA additive (b) isotactic PMA additive

Figure 5.14: *Atactic (a) and isotactic (b) PMA additives in vacuum at 300 K. The backbone is indicated by large spheres*

Figure 5.15 shows tricosane molecules within 2 nm of the PMA in the simulation box at 270 K. Both PMA show similar configurations to the ones observed in the vacuum. The distributions of radius of gyration for their backbone is given in Figure 5.16. The backbone of PMAa is partially extended at 0.6 nm (a complete extension of the backbone is 0.73 nm) and side chains lay on both sides of the backbone. Upon temperature decrease, the backbone arrangement remains stable. In the case of PMAis the side chains are on one side and therefore backbone remains in a coiled arrangement. At lower temperature the radius of gyration becomes more pronounced at 0.43 nm, indicating that the backbone remains coiled.

The distribution of the radius of gyration of side chains for PMA, Figure 5.18, is similar to the ones in PAO, Figure 5.10. Consequently, the dihedral angle distribution shows a dominance for *trans* dihedrals, Figure 5.17. The side chains of PMA and the longer side chains of PAO are of the same length, so are expected to behave similarly under the same conditions.

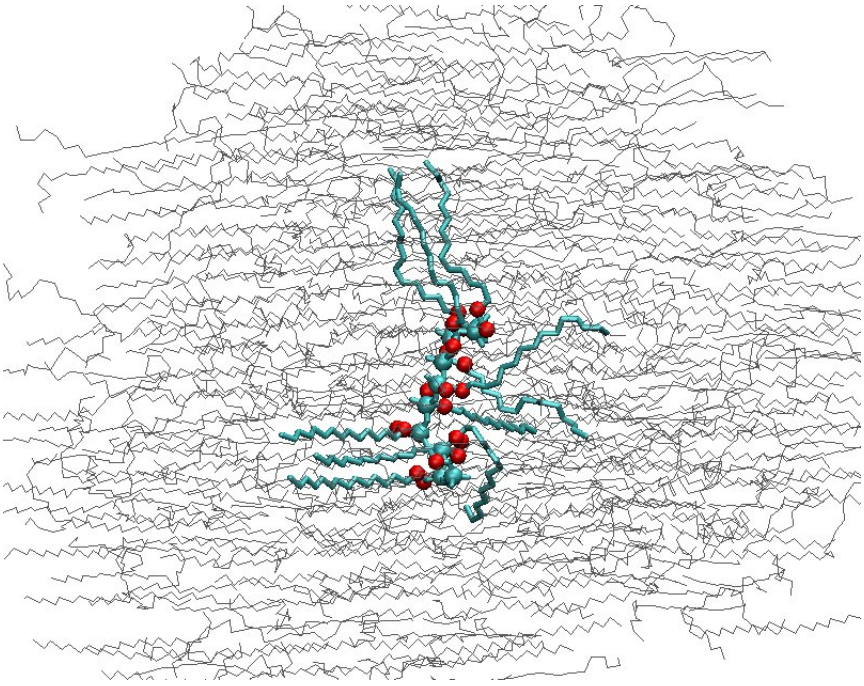

(a) atactic PMA additive

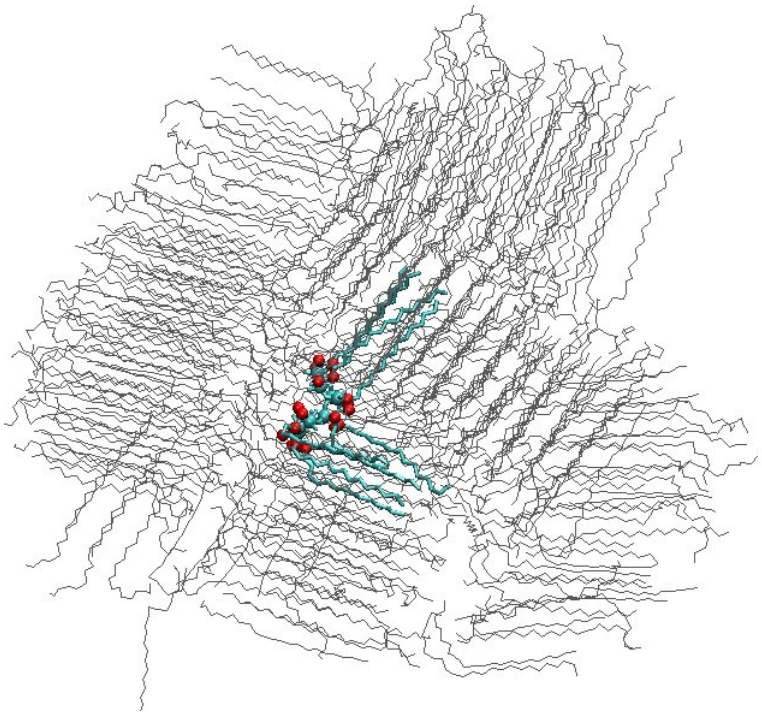

(b) isotactic PMA additive

Figure 5.15: *Interaction between tactic (a) and isotactic (b) PMA additives (cyan and red) and tricosane (grey) within 2 nm radius from additive at 270 K. The backbone of the PMA additives is indicated with spheres*

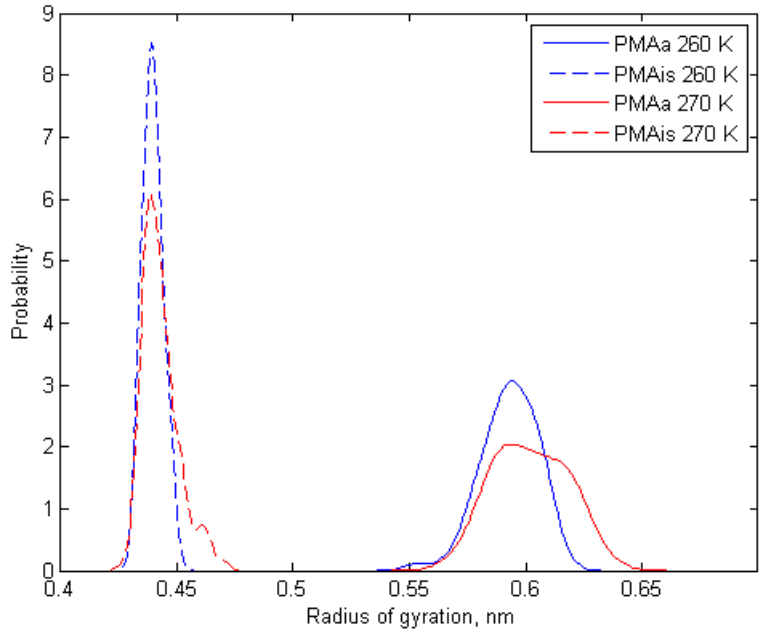

Figure 5.16: *Radius of gyration of backbone in atactic and isotactic PMA additive at 260 K and 270 K*

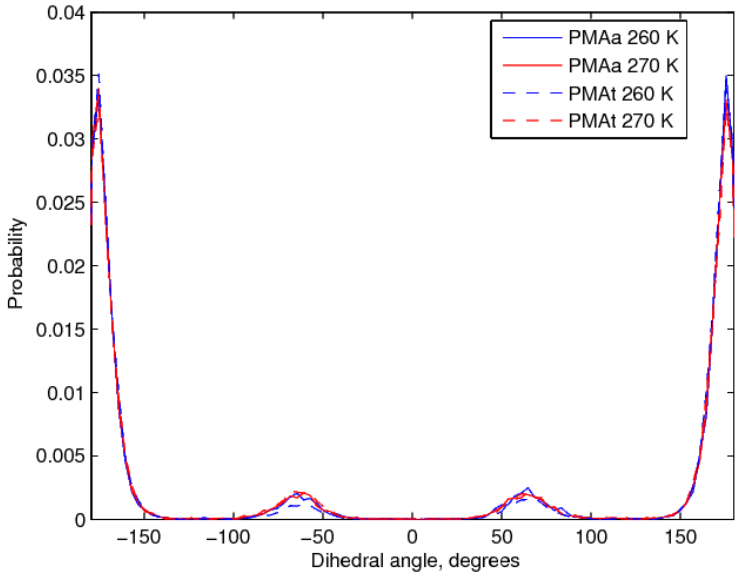

Figure 5.17: *Dihedral angle distribution function for side chains of atactic and isotactic PMA additive at 260 K and 270 K*

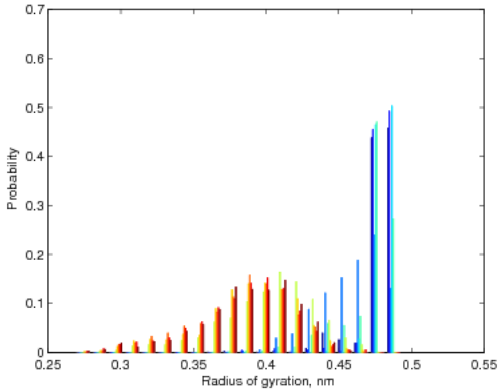

(a) Atactic PMA additive at 270 K

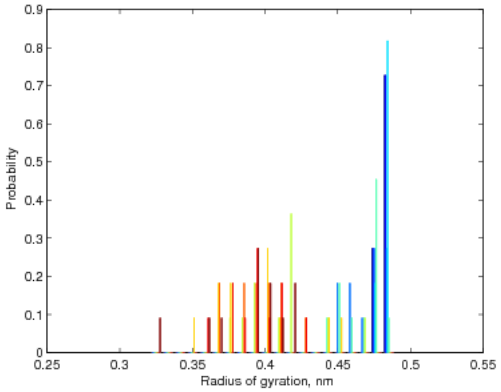

(b) Atactic PMA additive at 260 K

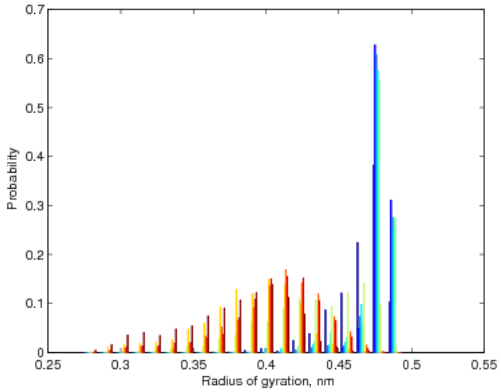

(c) Isoatactic PMA additive at 270 K

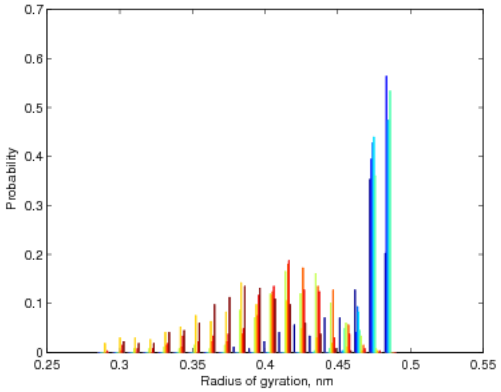

(d) Isotactic PMA additive at 260 K

Figure 5.18: *Radius of gyration of individual side chains of PMA atactic (a, b) and PMA isotactic (c, d) additives at 270 K (a,c) and 260 K (b,d). Chains are coloured by number from blue (1) to brown (10)*

In PMAa, some of the side chains co-crystallise with tricosane, while the rest are randomly oriented, creating disorder between two stacks of the crystal. The anchoring behaviour of this additive is similar to the one observed in both PAO molecules. PMAis behaves differently, placing nearly all side chains into one stack of the tricosane crystal. This leads to only local distortions, that do not affect the longer range crystal growth.

To date, not many studies of the mechanism of action of the comb-type additives have been performed. A set of theoretical investigations have been carried out by Duffy *et al.*, where an extended polyoctadecyl acrylate molecule (an additive similar to the PMA) was deposited on a paraffin wax surface [48–50]. The study shows, that due to the difference in spacing between paraffin chains of the crystal and the side chains in the additive, further crystal growth is hindered. The study is based on the assumption that the additive is fully extended prior to the interaction with growing wax crystals. In our work, a decrease in temperature revealed a similar trend in extension of side chains. However, this was not the case for the molecule's backbone. The side chains of additives extend and partially integrate into the crystal, which is likely to restrict the extension of the backbone. Similar observations were obtained by Jang *et al.*, where four hypothetical mechanisms of interaction of polyacrylate and paraffin crystal were compared [51].

Experimental observations of the interaction between comb-type polymers and wax do not provide unique conclusions. There are observations suggesting that comb-type molecules create steric hindrance [52], and that the additives disperse crystals from one another [42]. In our work we have observed distinct behaviour for PMA and PAO. While the backbone of PMAis is extended, the backbone of PAOis is coiled. The latter is likely to be an effect caused by the few short side chains in PAO, that are not present in PMA.

5.5 Alkylphenol formaldehyde condensate additive

Alkylphenol formaldehyde condensates (APFC) form yet another group of additives. The model of APFC used in this study contains six phenol ring repeat units with alkyl substituents. Similar to previous additives, the length of the side chains is essential

for the additive to act effectively. In this work eight (APFC-8) and eleven (APFC-11) carbon long alkyl chains are studied.

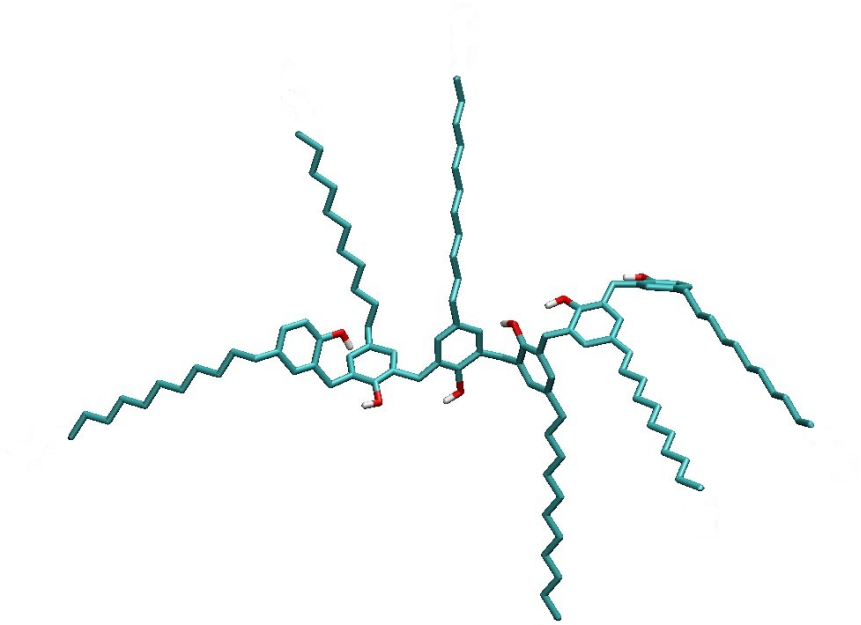

Figure 5.19: *Extended structure of an atactic model of an alkylphenolformaldehyde condensate additive*

Both additives were initially simulated in vacuum, parameters for calculation are given in Table 5.2. For the first steps of the simulation the additive wraps round on itself to form a cone with hydroxyl groups at the top and alkyl chains moving freely at the bottom. The additive then flattens out and extends. In the case of APFC-8 the OH groups remain together in a zip-like alignment, while APFC-11 forms a crescent. These conformational rearrangements also correspond to changes in radius of gyration. Figure 5.20 shows the radius of gyration over time and the associated conformations.

5.5.1 Crystallisation in the presence of APFC additive

Similarly to earlier additive studies, APFC-11 was simulated at 270 K and 260 K, while APFC-8 was simulated only at 260 K. The additives were modelled in tricosane with

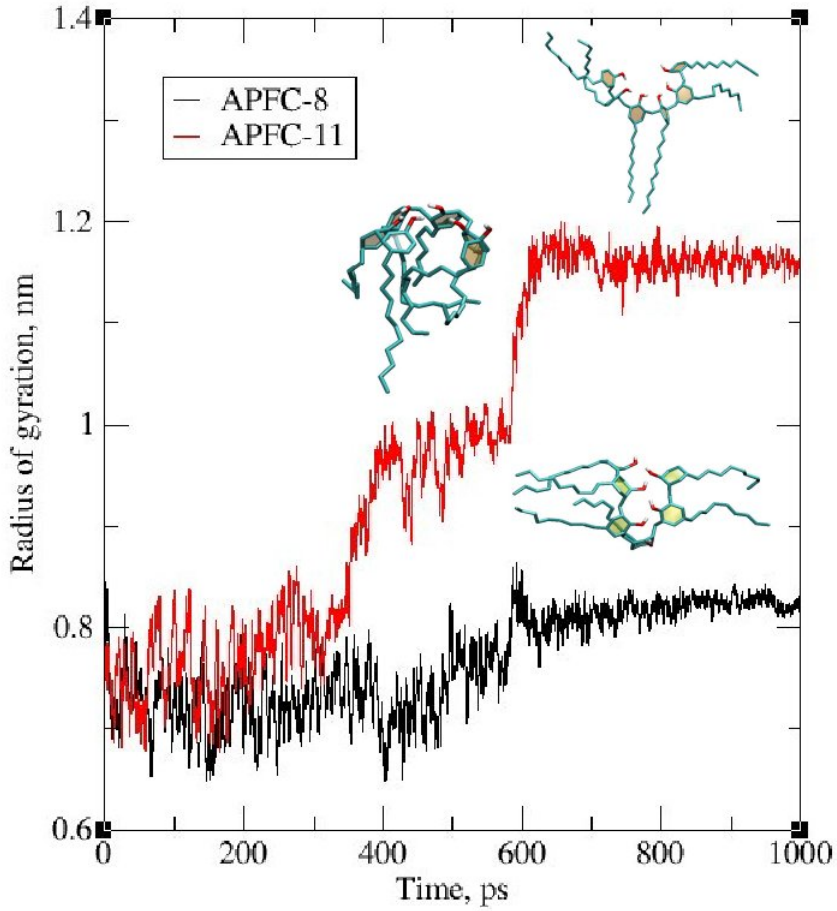

Figure 5.20: *Changes of radius of gyration of APFC-11 and APFC-8 in a vacuum at 300 K with corresponding structures. Phenyl rings are coloured for visualisation purposes*

2955 molecules for the APFC-8 system and 2933 molecules for the APFC-11 one. In both systems a nucleation centre was used. The remaining simulation parameters are the same as for earlier studies and are given in Table 5.7.

Figure 5.21 shows a fragment of the simulation box at 260 K, containing APFC additives and tricosane molecules within 1.5 nm from the additive. It can be seen that the phenol rings in the additive arrange in a disk-like structure, while the side chains extended outwards. Tricosane crystallises parallel to APFC side chains, by such creating small but randomly oriented crystal stacks. The crystal is less well-defined in the case of APFC-8, as the total simulation time was shorter.

Figure 5.22 shows APFC in tricosane at 260 K. Tricosane molecules are shown in grey as a background only. Phenol rings are coloured with changing intensity according to the tilt. The tilt is similar for all six rings with hydroxyl groups pointing towards each other, so that the phenyl rings form a near planar disk. All hydroxyl groups point to the centre of the molecule, forming hydrogen bonds of 1.7 – 2.2 Å. The side chains are stretched out sideways. The behaviour of the core of these additives and the side chains are analysed separately below.

The radius of gyration of the core of the molecules, measured by the positions of hydroxyl groups, is given on Figure 5.23. For APFC-8 the average radius of gyration is greater than for APFC-11. This is due to one of the hydroxyl groups falling out from the central alignment and no longer participating in the hydrogen bonding, as shown on Figure 5.22. APFC-11 core does not undergo any further conformational change upon temperature decrease. It is nevertheless possible that, as in the gas phase study, the core of the molecule can adopt several conformations, and that just one was explored in our simulation.

Figure 5.24 shows the dihedral angle distribution of side chains in APFC-8 and APFC-11 additives. Side chains of both APFC show the presence of *gauche* conformations. Longer chains in APFC-11 show higher amounts of *trans* conformations than shorter ones in APFC-8. The radius of gyration of individual chains in APFC-11, Figure 5.25, also suggests that chains do not extend further upon cooling. This effect is possibly

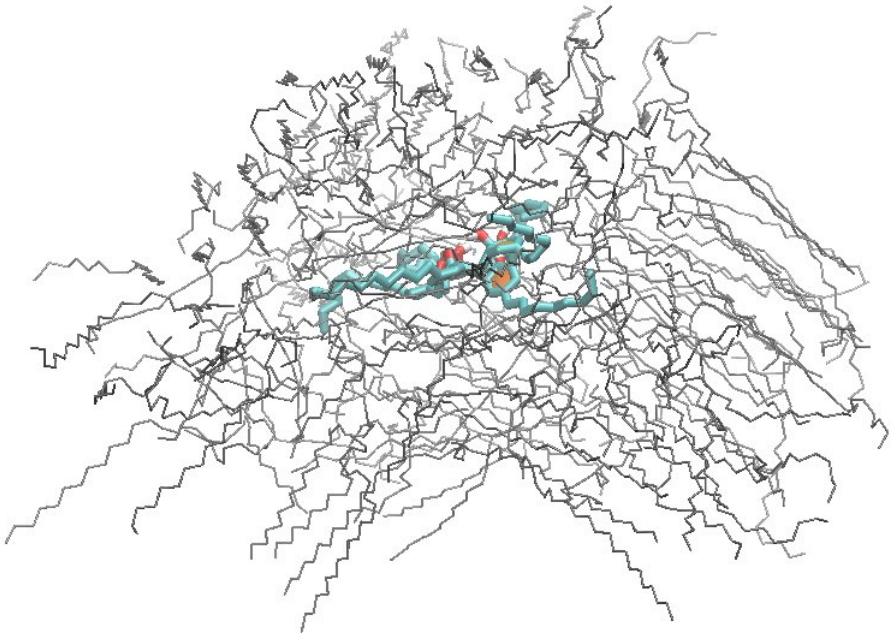

(a) APFC-8 in tricosane

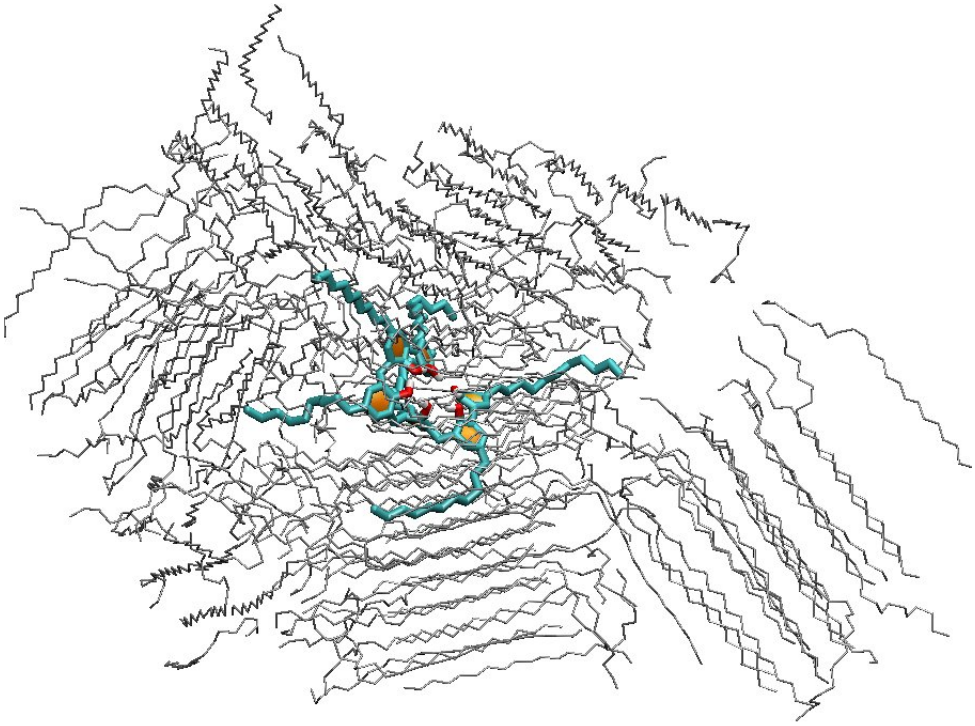

(b) APFC-11 in tricosane

Figure 5.21: *Interaction between APFC-8 (a) and APFC-11 (b) additives (shown in cyan) and tricosane (grey) within 1.5 nm radius at 260 K. The phenol rings are coloured for visualisation purposes*

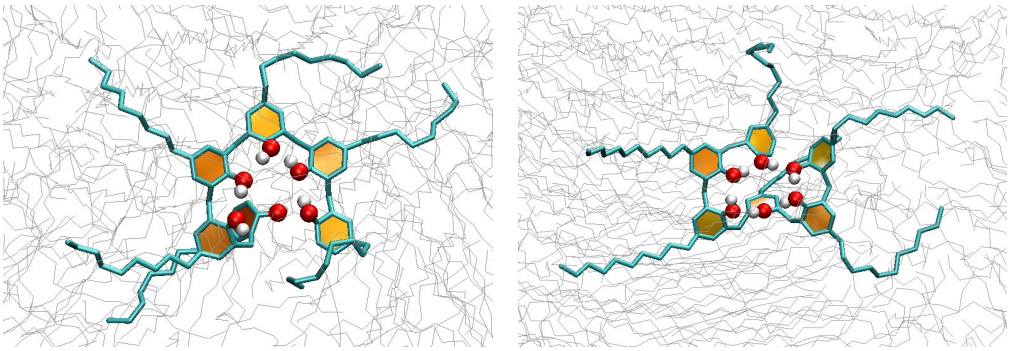

(a) APFC-8 in tricosane (b) APFC-11 in tricosane

Figure 5.22: *Top view on the APFC-8 (a) and APFC-11(b) additives in tricosane (grey) at 260 K. For visualisation purposes phenol rings are coloured with intensity changing with the tilt, oxygen and hydrogen atoms are shown as spheres*

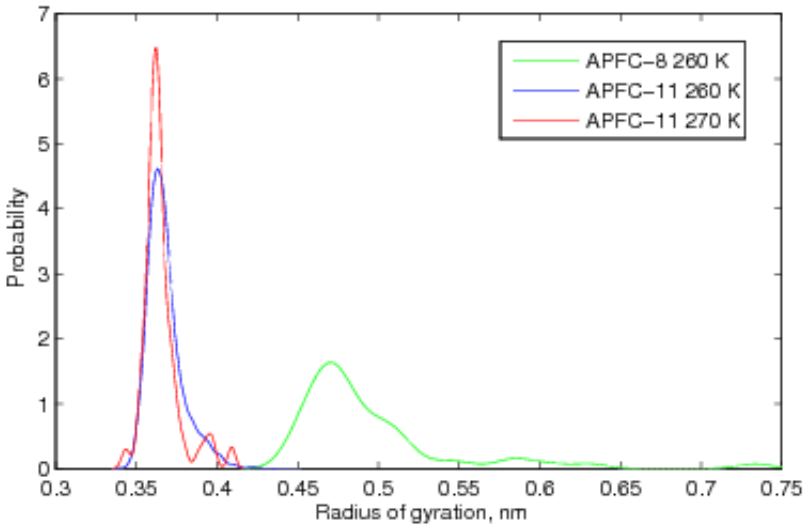

Figure 5.23: *Radius of gyration of the core of APFC-11 at 260 K and 270 K and the core of APFC-8 at 260 K*

caused by chains being trapped in a certain conformation by a surrounding growing crystal.

It is known from personal conversations with *Infineum*, that for APFC the length of side chains is critical for the effectiveness of the molecule. Ten to fourteen carbons-long side chains show the best results in a standard diesel fuel. In additives, side chains influence a large number of properties, including crystallisation temperature. While it was shown to be hard to predict the exact crystallisation temperature of simple alkanes by molecular dynamics studies, the mechanism of action can be well modelled. Clearly, for an additives to be effective, side chains have to be long enough to be able to co-crystallise with the paraffin. Both APFC-8 and APFC-11 co-crystallise with tricosane to create crystal micro-domains around each side chain. Following this observation, it would be interesting to study whether side chains act as a nucleation centre, thereby promoting the growth of a small disordered crystal over a larger plate crystal.

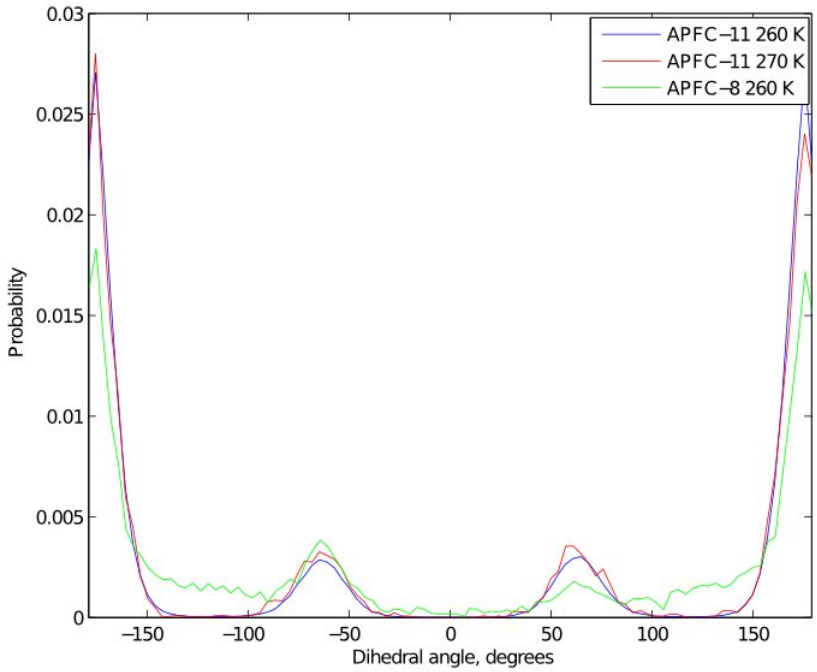

Figure 5.24: *Dihedral angle distribution of side chains of APFC-11 at 260 K and 270 K and APFC-8 at 260 K*

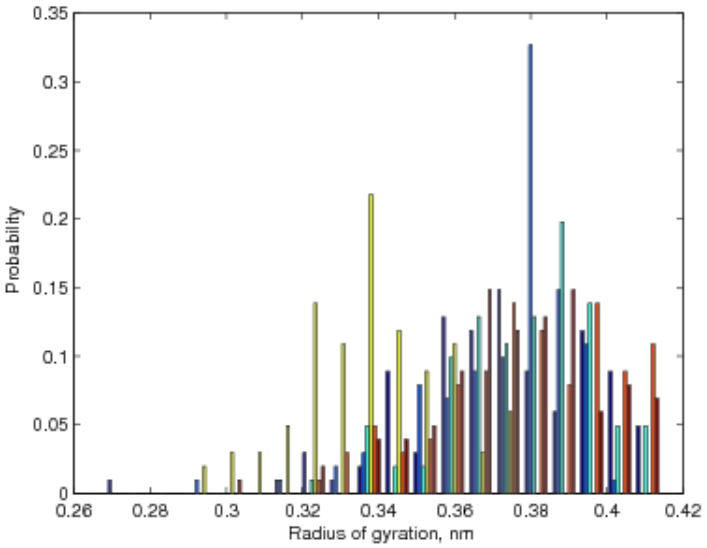

(a) Atactic APFC-11 additive at 270 K

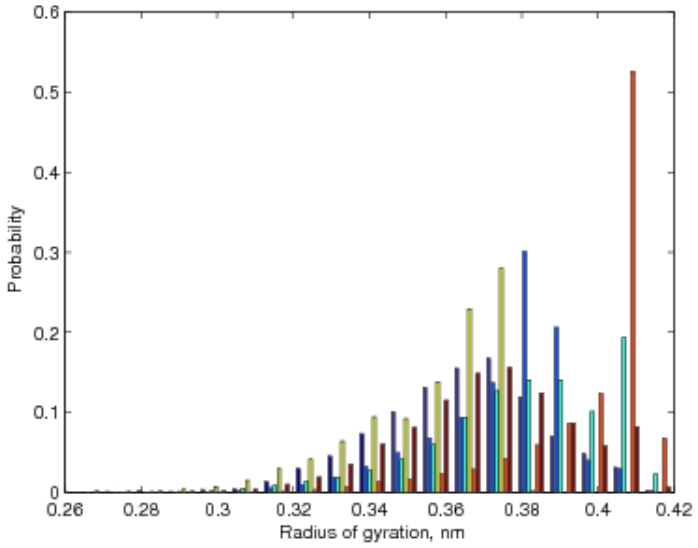

(b) Atactic APFC-11 additive at 260 K

Figure 5.25: *Radius of gyration of individual side chains of APFC-11 at 260 K and 270 K. Chains are coloured blue (1) to brown (6)*

5.6 Conclusions

In this chapter we have studied the behaviour of four types of additives during paraffin crystallisation. Even though distinct mechanisms have been observed, the action of each of the additives is based upon partial co-crystallisation with the paraffin molecules and distortion of the alignment of forming crystal domains.

In the case of EVA, the backbone co-crystallises with the alkanes. Side chains of EVA create turns in the backbone and vinyl acetate groups further distort the alignment of co-crystallising paraffins. The forming wax nanodomains can no longer organise into lamellar layers. For the additive to be effective, the longest linear fragment of the backbone must be shorter than the targeted *n*-alkanes. The distance between side chains in EVA used in this work is under a half of the length of the targeted alkanes. Additionally, the length of EVA determines the temperature of straightening of the backbone, and should be similar to the targeted paraffins, by such allowing the two to co-crystallise.

In comb-type additives, such as PMA and PAO, side chains are approximately half the length of the paraffin. Upon temperature decrease, the side chains straighten and crystallise with the *n*-alkanes. The behaviour of the backbone is different between the two additives. Similarly to EVA, PMA has a few short side chains, which generate kinks in the backbone. Consequently, the backbone remains tangled even at lower temperatures. On the other hand, side chains of PAO are all of the same length. Atactic PAO will extend its backbone at lower temperatures. In isotactic PAO the side chains are on one side of the molecule, therefore the backbone creates a circular arrangement in order to accommodate them.

APFC has side chains of similar length as well. The main difference to previously discussed additives is the core, which is comprised of six phenol rings. The core strongly interacts with itself through hydrogen bonding and so does not rearrange, while side chains do extend. In a similar way to the other additives, paraffin molecules co-crystallise around its side chains.

In this work a set of commonly used additives have been studied. This allowed us to observe similarities and differences between their mechanism of action. Based on our observations further, more detailed studies have to be performed. The additives in this study are composed of a linear aliphatic chains of approximately half of the length of the paraffin. It would be interesting to observe how crystallisation is affected by changing the length of this fragment. Additional simulations aimed at observing the behaviour of the additive prior to crystal formation, as well as during the crystal growth, should be also performed.

It is known experimentally, that combinations of several additives can lead to more effective crystal modification. This suggests that additives may interact with each other. This has not been studied in neither this work nor in any previously published works and so would be an interesting future project.

Bibliography

[1] A. Genovese, G. Amarasinghe, M. Glewis, D. Mainwaring, and R.A. Shanks. Crystallisation, melting, recrystallisation and polymorphism of n-eicosane for application as a phase change material. *Thermochimica acta*, 443(2):235–244, 2006.

[2] J. J. Retief, D. W. Engel, and E. G. Boonstra. X-ray powder diffractometric procedure for lattice parameter determination for long-chain molecules. *Journal of Applied Crystallography*, 18(3):150–155, 1985.

[3] S.R. Craig, G.P. Hastie, K.J. Roberts, and J.N. Sherwood. Investigation into the structures of some normal alkanes within the homologous series $C_{13}H_{28}$ to $C_{60}H_{122}$ using high-resolution synchrotron X-ray powder diffraction. *Jornal of Materials Chemistry*, 4:977–981, 1994.

[4] S.R. Craig, G.P. Hastie, K.J. Roberts, A.R. Gerson, J.N. Sherwood, and R.D. Tack. Investigation into the structures of binary-, tertiary- and quinternary-mixtures of n-alkanes and real diesel waxes using high-resolution synchrotron X-ray powder diffraction. *Jornal of Materials Chemistry*, 8(4):859–869, 1998.

[5] N.M. Garrido, A.J. Queimada, M. Jorge, E.A. Macedo, and I.G. Economou. 1-Octanol/Water partition coefficients of n-alkanes from molecular simulations of absolute solvation free energies. *Journal of Chemical Theory and Computation*, 5(9):2436–2446, 2009.

[6] M.G. Martin and J.I. Siepmann. Transferable potentials for phase equilibria. 1. United-atom description of n-alkanes. *The Journal of Physical Chemistry B*, 102(14):2569–2577, 1998.

[7] M.G. Martin and J.I. Siepmann. Novel configurational-bias Monte Carlo method for branched molecules. Transferable potentials for phase equilibria. 2. United-atom description of branched alkanes. *The Journal of Physical Chemistry B*, 103(21):4508–4517, 1999.

[8] C.D. Wick, M.G. Martin, and J.I. Siepmann. Transferable potentials for phase equilibria. 4. United-atom description of linear and branched alkenes and alkylbenzenes. *The Journal of Physical Chemistry B*, 104(33):8008–8016, 2000.

[9] B. Chen, J.J. Potoff, and J.I. Siepmann. Monte Carlo calculations for alcohols and their mixtures with alkanes. Transferable potentials for phase equilibria. 5. United-atom description of primary, secondary, and tertiary alcohols. *The Journal of Physical Chemistry B*, 105(15):3093–3104, 2001.

[10] J.M. Stubbs, J.J. Potoff, and J.I. Siepmann. Transferable potentials for phase equilibria. 6. United-atom description for ethers, glycols, ketones, and aldehydes. *The Journal of Physical Chemistry B*, 108(45):17596–17605, 2004.

[11] C.D. Wick, J.M. Stubbs, N. Rai, and J.I. Siepmann. Transferable potentials for phase equilibria. 7. Primary, secondary, and tertiary amines, nitroalkanes and nitrobenzene, nitriles, amides, pyridine, and pyrimidine. *The Journal of Physical Chemistry B*, 109(40):18974–18982, 2005.

[12] N. Lubna, G. Kamath, J.J. Potoff, N. Rai, and J.I. Siepmann. Transferable potentials for phase equilibria. 8. United-atom description for thiols, sulfides, disulfides, and thiophene. *The Journal of Physical Chemistry B*, 109(50):24100–24107, 2005.

[13] K.A. Maerzke, N.E. Schultz, R.B. Ross, and J.I. Siepmann. TraPPE-UA force field for acrylates and Monte Carlo simulations for their mixtures with alkanes and alcohols. *The Journal of Physical Chemistry B*, 113(18):6415–6425, 2009. PMID: 19358558.

[14] Maestro, version 9.2, Schreodinger, 2011.

[15] B. Hess, C. Kutzner, D. Van Der Spoel, and E. Lindahl. GROMACS 4: Algorithms for highly efficient, load-balanced, and scalable molecular simulation. *Journal of Chemical Theory and Computation*, 4(3):435–447, 2008.

[16] C.A. Cerdeiriña, C.A. Tovar, D. González-Salgado, E. Carballo, and L. Romaní. Isobaric thermal expansivity and thermophysical characterization of liquids and liquid mixtures. *Physical Chemistry Chemical Physics*, 3(23):5230–5236, 2001.

[17] V. N. Maiorov and G. M. Crippen. Size-independent comparison of protein three-dimensional structures. *Proteins: Structure, Function, and Bioinformatics*, 22(3):273–283, 1995.

[18] F.E. Cohen and M.J.E. Sternberg. On the prediction of protein structure: the significance of the root-mean-square deviation. *Journal of molecular biology*, 138(2):321–333, 1980.

[19] J. Moos and T. Haas. Removal of paraffin from hydrocarbon oils as a problem of solubility. *Erdoel und Kohle*, 1:29–38, 1948.

[20] Advanced Chemistry Development (ACD/Labs) Software V11.02, 1994–2012.

[21] J.W. Mullin. *Crystallization*. Chemical, Petrochemical & Process. Butterworth-Heinemann, 2001.

[22] J. P. Eerden and O. S. L. Bruinsma. *Science and technology of crystal growth*. Kluwer Academic Publishers, 1995.

[23] M. Miura, T.and Mikami. Molecular dynamics study of crystallization of polymer systems confined in small nanodomains. *Physical Review E*, 75(3):031804, 2007.

[24] D.L. Dorset. Crystal structure of lamellar paraffin eutectics. *Macromolecules*, 19(12):2965–2973, 1986.

[25] I. Denicolo, A. F. Craievich, and J. Doucet. X-ray diffraction and calorimetric phase study of a binary paraffin: $C_{23}H_{48}$–$C_{24}H_{50}$. *The Journal of Chemical Physics*, 80(12):6200–6203, 1984.

[26] Matteo Nasi. Computer simulation of diesel and diesel additives. Master's thesis, Durham Univesity, 2007.

[27] E. Provost, V. Chevallier, M. Bouroukba, D. Petitjean, and M. Dirand. Solubility of some n-alkanes (c23, c25, c26, c28) in heptane, methylcyclohexane, and toluene. *Journal of Chemical & Engineering Data*, 43(5):745–749, 1998.

[28] A. A. Schaerer, C. J. Busso, A. E. Smith, and L. B. Skinner. Properties of pure normal alkanes in the c17 to c36 range. *Journal of the American Chemical Society*, 77(7):2017–2019, 1955.

[29] R. G. Alamo, L. Mandelkern, G. M. Stack, C. Krohnke, and G. Wegner. Crystallization kinetics of long-chain n-alkanes from the melt and from solution. *Macromolecules*, 27(1):147–156, 1994.

[30] D.H.M. Beiny and J.W. Mullin. Solubilities of higher normal alkanes in m-xylene. *Journal of Chemical & Engineering Data*, 32(1):9–10, 1987.

[31] E. Sloutskin, E. B. Sirota, H. Kraack, B. M. Ocko, and M. Deutsch. Surface freezing in *n*-alkane solutions: The relation to bulk phases. *Phys. Rev. E*, 64(3):031708, 2001.

[32] E.P. Gilbert. The stability of binary alkane blends. *Physical Chemistry Chemical Physics*, 1(7):1517–1529, 1999.

[33] J. Cousty and L.P. Van. Formation of partially demixed two-dimensional solid solutions from binary mixtures of n-alkanes with very different lengths. *Physical Chemistry Chemical Physics*, 5:599–603, 2003.

[34] D. Chanda, A. Sarmah, A. Borthakur, K.V. Rao, B. Subrahmanyam, and H.C. Das. Combined effect of asphaltenes and flow improvers on the rheological behaviour of indian waxy crude oil. *Fuel*, 77(11):1163–1167, 1998.

[35] K.A. Frost Jr. Pour point depressants, October 31 1978. US Patent 4,123,232.

[36] J. Zhang, C. Wu, W. Li, Y. Wang, and Z. Han. Study on performance mechanism of pour point depressants with differential scanning calorimeter and X-ray diffraction method. *Fuel*, 82(11):1419–1426, 2003.

[37] R. Tack. Additives for fuel oils, June 23 2010. EP Patent 2,199,377.

[38] R. Tack and D. Riano-gordo. Method of improving oil compositions, June 16 2010. EP Patent 2,196,520.

[39] R.D. Tack. Additives for fuel oils, December 4 2009. US Patent App. 12/630,863.

[40] C.X. da Silva, D.R.S. Álvares, and E.F. Lucas. New additives for the pour point reduction of petroleum middle distillates. *Energy & Fuels*, 18(3):599–604, 2004.

[41] E. Marie, Y. Chevalier, F. Eydoux, L. Germanaud, and P. Flores. Control of n-alkanes crystallization by ethylene–vinyl acetate copolymers. *Journal of Colloid and Interface Science*, 290(2):406 – 418, 2005.

[42] C. Jiang, M. Xu, X. Xi, P. Qi, and H. Shang. Poly-acrylic acid derivatives as diesel flow improver for paraffin-based daqing diesel. *Journal of Natural Gas Chemistry*, 15(3):217–222, 2006.

[43] H. J. Oschmann M. Feustel, M. Krull. Additives for improving the cold flow properties and the storage stability of cude oil, December 23 2004.

[44] D.J. Martella, J.J. Jaruzelski, and F.J. Chen. Process for preparing alkyl phenol-sulfur condensate lubricating oil additives, November 16 1993. US Patent 5,262,508.

[45] D.J. Martella and J.J. Jaruzelski. Alkyl phenol-formaldehyde condensates as fuel and lubricating oil additives, March 24 1993. EP Patent 0,311,452.

[46] T.P. Traise. Lubricating oil additives, May 6 1969. US Patent 3,442,808.

[47] H.S. Ashbaugh, X. Guo, D. Schwahn, R.K. Prud'homme, D. Richter, and L.J. Fetters. Interaction of paraffin wax gels with ethylene/vinyl acetate co-polymers. *Energy & Fuels*, 19(1):138–144, 2005.

[48] D. M. Duffy and P. M. Rodger. Wax inhibition with poly(octadecyl acrylate). *Physical Chemistry Chemical Physics*, 4:328–334, 2002.

[49] D.M. Duffy, C. Moon, and P. M. Rodger. Computer-assisted design of oil additives: hydrate and wax inhibitors. *Molecular Physics*, 102(2):203–210, 2004.

[50] D.M. Duffy and P. M. Rodger. Modeling the activity of wax inhibitors: A case study of poly (octadecyl acrylate). *The Journal of Physical Chemistry B*, 106(43):11210–11217, 2002.

[51] Y.H. Jang, M. Blanco, J. Creek, Y. Tang, and W. A. Goddard. Wax inhibition by comb-like polymers:support of the incorporation-perturbation mechanism from molecular dynamics simulations. *The Journal of Physical Chemistry B*, 111(46):13173–13179, 2007. PMID: 17975910.

[52] H.S. Ashbaugh, A. Radulescu, R.K. Prud'Homme, D. Schwahn, D. Richter, and L.J. Fetters. Interaction of paraffin wax gels with random crystalline/amorphous hydrocarbon copolymers. *Macromolecules*, 35(18):7044–7053, 2002.

Part III

Development of coarse grained force field for paraffin crystallisation

6 Theoretical background of coarse graining

6.1 Introduction

Computational power is rapidly increasing, with hardware performance doubling every two years [1]. Coupled to these improvements, considerable effort is being made towards the development of ever more efficient algorithms to deliver faster and more accurate calculations. Despite these advances, there is a pressing need to simulate chemical systems over time scales that go far beyond those currently obtainable with atomistic systems.

This chapter aims to increase the time scales accessible to computation through a reduction of the number of sites necessary to represent the system. The method is known as coarse graining. The chapter provides a summary of the theory of this technique, a brief discussion regarding the application of the method to crystallisation, and the development of appropriate coarse grained models for paraffin chains and hence model diesel.

6.2 Theory of coarse graining

The basic concept of coarse graining involves a reduction of the number of sites in a system. While this technique allows for smaller computational load, it also leads to a loss of fine detail in the system. There is a delicate balance between these two factors, ideally leading to a considerable speed up of the calculation while still preserving the

necessary chemical and physical information.

Computational time can scale up to N^2 (N is a number of interaction sites) for pairwise potentials. Therefore decreasing the number of interaction sites in the model will lead to a significant speed up of the calculation. A second advantage of coarse graining is the loss of some intermolecular movements that allow the system to explore phase space faster. A third source of speed up is the increase in timestep. Longer timesteps can typically be made in coarse grained simulations because the vibrational frequency of larger particles is slower.

In chemistry, a coarse grained system will typically still be represented at the molecular level, as prediction of local properties of the system is usually dependent on the presence of molecules. A common type of coarse grained model represents a group of atoms with a single interaction centre, a so called "super atom". These super atoms are then assigned interaction parameters. The parameters are derived from a smaller scale, higher resolution model of the system. Additionally, they may be fitted to known experimental values.

Currently there is only one readily available coarse grained force field, MARTINI [2]. It was developed by the research group lead by Marrink. The force field is designed to be used in biomolecular simulations of lipids, proteins and carbohydrates [3–5]. The model uses a shifted Lennard-Jones 12-6 potential with parameters fitted to free energies of vaporisation, hydration and separation between water and organic solvents at room temperature (300 K) only. There are criticisms of water in this model due to its inability to remain in the liquid state in or around membrane pores [6, 7]. Recently a more sophisticated, polarisable water model was developed by the same group [8]. Water is proving to be one of the most difficult systems to coarse grain, as finding potentials capable of exhibiting the correct behaviour is difficult. Many efforts have been made recently [9, 10], and notably another promising polarisable water model was developed by van Gusteren *et al.* [11].

Polymers have initially been the main focus of coarse grained modelling [12–14]. Earlier models are often revisited [15, 16]. An example relevant to this thesis is a model for

n-alkanes [17] developed by the research group of Klein, which expresses non bonded potentials in Lennard-Jones form and is later extended to produce a surfactant coarse grained model [16].

Recently a slightly different approach was carried out by Chiu *et al.*[18] for deriving potentials of water and *n*-alkanes. The developers used the Morse potential and fitted the results to experimental bulk densities, thermodynamic data and surface tensions. In their following work the force field was modified by creating better interaction potentials between water and *n*-alkanes by fitting to interfacial tensions and solvation free energies [19]. The authors have shown that the Morse potential allows for bigger timesteps than the Lennard-Jones. Authors have obtained very good agreements with experimental results at room temperature.

The Minnesota group, led by Siepmann (well known for their united atom TraPPE force field [20–25]) have recently developed a coarse grained model for linear alkanes [26]. The resulting force field was shown to accurately represent vapour and liquid densities and transfer free energies. It is a very new force field, so it has not yet been tested outside of the developers' own work.

The main constraint of coarse grained potentials is the limited transferability between different systems and between thermodynamic conditions. Recently, Carbone *et al.* have performed a study to investigate this problem [27]. The conclusions are that transferability is highly dependent on the system parametrized, and is generally better for finer grained models and for superatoms representing approximately spherically symmeteric groups of atoms. For polymer systems it was also shown that transferability is not affected greatly by a change of the length of the polymer chain.

Transferability over a range of temperatures was well demonstrated for the coarse grained force field developed by Siepmann [26]. Nevertheless, the parameters were developed for the liquid–gas interface and would not be optimal for modelling a liquid to crystal transition.

To derive a suitable coarse grained potential, one would normally follow the general

procedure shown in Figure 6.1. A smaller scale, higher resolution atomistic (sometimes united atom) model is sampled using molecular dynamics or Monte Carlo simulations. When setting up the initial calculation it is important to consider which properties are needed and at which time and length scales. The system is then mapped onto a coarse grained representation. The trajectories from high resolution calculations are then analysed and the starting potentials for the coarse grained model are obtained. In most cases the obtained coarse grained potential has to be refined in order to produce results consistent with its higher resolution counterpart.

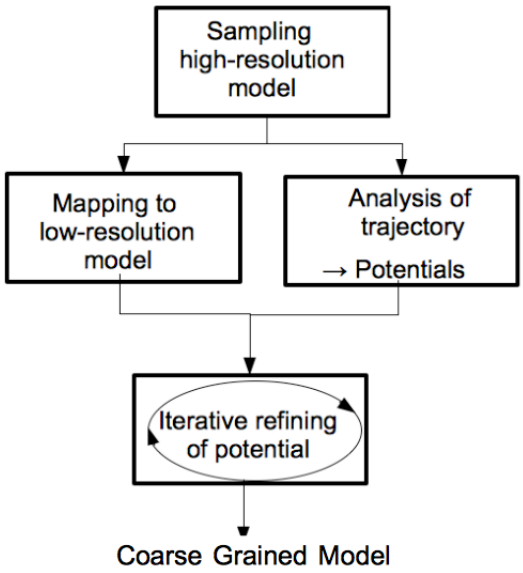

Figure 6.1: *Illustration of the coarse graining procedure: sampling of a high resolution model, analysis of the trajectory, mapping to low resolution, iterative refining of the potential*

In the next section I will discuss mapping, followed by sections on the derivation of coarse grained potentials and their refinements. The following chapter is focused on developing and testing paraffin models capable of reproducing the crystallisation process.

6.2.1 Mapping

In the mapping procedure, one represents a group of atoms with a single interaction centre. This centre is called a super atom, and is commonly positioned at the centre

of mass of the group of initial atoms. Super atoms, as in atomistic calculations, are interlinked with springs and follow the same rules of Newtonian mechanics, discussed in Chapter 3. The choice of atoms to group into a bead is typically done by geometrical examination of the molecule and this leads to a coarse grained molecule still resembling the general shape of the initial molecule. This procedure allows a better agreement with non bonded properties. Additionally, one should choose a potential having simplest possible form, ideally a single well. This will be beneficial when refining the system in further iterative steps [28]. The parts of the molecule that are geometrically mobile (eg. undergoing *gauche* - *trans* conformational changes) will typically lead to potentials with more then one well.

6.2.2 Potentials

When the mapping is chosen, the next step is to evaluate the optimal parameters to describe the interactions between the coarse grained sites. Over the last few years a number of approaches have been developed. Within these are force matching, inverse Monte Carlo and iterative Boltzmann inversion.

In force matching a multibody potential of mean force of a high resolution system is matched by a low resolution one [29]. This approach looks at individual configurations, rather than the average properties of the system as encompassed by radial distribution functions. This method has been widely used by Voth and co-workers [30, 31].

The other two methods are based on fitting potentials to the average properties of the system. The potentials are derived from distributions: bond length, angle, dihedral angle and radial distribution functions (RDF). The fitting is often done iteratively, allowing a better match [32, 33]. As the name suggests, in the inverse Monte Carlo approach [33, 34] new parameters are fitted using Monte Carlo calculations. In the case of iterative Boltzmann inversion, the procedure is performed by fitting with the aid of molecular dynamics calculations. These calculations are dependent on a single coordinate, making this method computationally inexpensive.

Our work aims at investigating crystallisation phenomena and therefore we are interested in matching the physical properties, rather than forces action on the system. Additionally, during state transitions the algebraic formulation is likely to limit the transferability, see section **??**. For the above reasons force matching is not the ideal technique for problem in mind. For our preliminary calculations were have been using molecular dynamics and so changing to Monte Carlo would require additional computational expenses. Therefore, in this work iterative Boltzmann inversion is used and discussed in greater detail below.

6.2.3 Iterative Boltzmann Inversion

Iterative Boltzmann Inversion (IBI) is a structure-based method aimed at matching distribution functions of a new coarse grained model to a higher resolution calculation or experiment. Bonded interactions (bond, angle and dihedral) incorporate neglected degrees of freedom and temperature effects. Non bonded interactions (RDF) are calculated separately, creating physically sensible interactions between molecules.

Generally, bonded potentials are deeper than non bonded ones. Typically, the deepest potentials are bond potentials, followed by angle and dihedral (if the latter are used). The fitting of these potentials should start with the deepest one, as these will change the least during fitting of the others, hence the order:

$$P_{bond} \longrightarrow P_{angle} \longrightarrow P_{dihedral} \longrightarrow P_{nonbonded}$$

Figure 6.2 illustrates the procedure for deriving an effective potential *V(x)* from a known probability distribution, $P_{ref}(x)$. In Figure 6.2, and in the following discussion, *P(x)* is a general term for the distribution, that could be a RDF *g(r)*, bond length *b(r)*, angle $a(\theta)$ or dihedral angle $d(\phi)$ distribution.

In the first iteration, a reasonable guess of an effective potential should be obtained. This can be derived from a reference probability, $P_{ref}(x)$, of a high resolution simula-

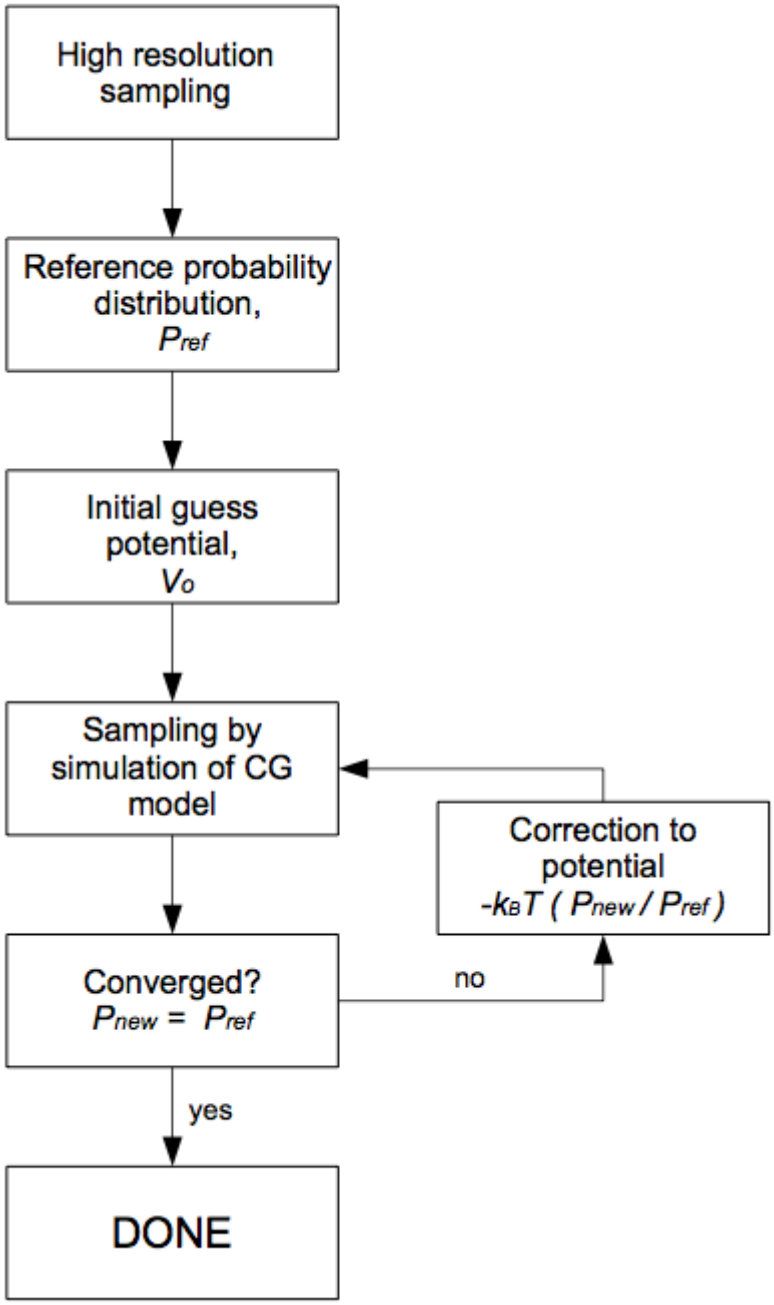

Figure 6.2: *Illustrated procedure for deriving effective potentials by the iterative Boltzmann inversion (IBI) method*

tion of a pure system,

$$V_0(x) = -k_B T \ln P_{ref}(x) \tag{6.1}$$

It should be mentioned that V_0 is not a potential energy, but rather a free energy, dependant on temperature and pressure. V_0 is a reasonable guess for the first coarse grained potential. A coarse grained simulation is performed and new probability distributions $P_i(x)$ evaluated. The new distribution will differ from $P_{ref}(x)$ and so the new potential should include a correction, in order to provide a better representation of the system.

$$V_{i+1}(x) = V_i(x) - \lambda k_B T \ln \frac{P_i(x)}{P_{ref}(x)} \tag{6.2}$$

where $\lambda \in (0,1]$ is a numerical scaling factor.

The new calculation will again result in a probability distribution, P_{i+1}. The iterative procedure should be repeated until P_{i+n} is sufficiently close to P_{ref}.

It has been shown that it can take up to 200 iterations to obtain a potential capable of representing aggregate distributions [35], and over 1000 iterations to recover correct potential functions [36].

6.3 Software

In this work both high and low resolution systems are simulated and analysed using GROMACS (GROningen MAchine for Chemical Simulations) [37]. The derivation of guessed potentials and the management of the iterative workflow is assisted by VOTCA - Versatile Object-oriented Toolkit for Coarse Graining [38] and some assisting scripts developed within the Durham research group.

7 Development and testing of the coarse grained model for linear alkanes

7.1 Choice of the model

The research topic of this thesis is focused on the study of diesel fuel behaviour at low temperatures. The objective here is therefore to develop a coarse grained model capable of reproducing crystallisation. It has been shown in an investigation of transferability done by Carbone *et al.* [27] that the length of the chain does not have a large effect on transferability of the potential. As converging to the final potential can take hundreds of steps, choosing a short chain will speed the process of coarse graining.

As described in section 6.2 and shown in Figure 6.1, the first step includes creating a high resolution model of a simple system. A linear alkane dodecane molecule is chosen to model the basic alkane interactions. Dodecane is a twelve carbon atom chain and so can be represented by four beads of three carbon atoms each, as shown in Figure 7.1(a). A three-to-one mapping limits the transferability between different lengths of alkanes. For this reason, additional interactions between terminal united atom, CH_3, and a linear coarse grained bead are calculated, Figure 7.1(b).

Ideally, the bonded interactions should be independent of non bonded potentials, and so derived from single molecule canonical sampling in vacuum [13]. However, this approach will not provide correct bonded distributions for the crystallisation process of alkanes, as the intermolecular changes are also affected by intramolecular interactions. Polymer chains in a melt tend to be randomly coiled, Figure 7.2 (a). Upon a temperature decrease the chains unfold, Figure 7.2 (b), and align parallel to each

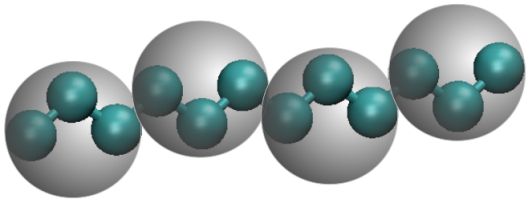

(a) 3:1 mapping of dodecane

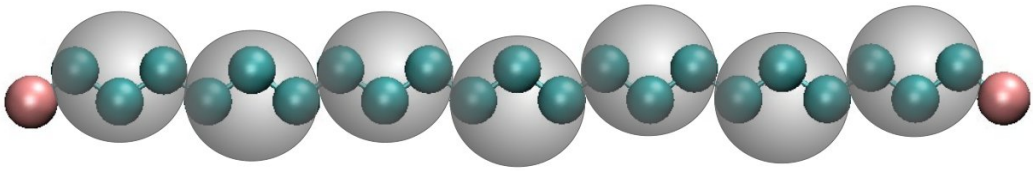

(b) mixed mapping of both coarse grained (grey) and united atom (pink) sites of tricosane

Figure 7.1: *Illustrated mapping of dodecane and tricosane*

other, forming a lamellar structure. Figure 7.3 shows a mixture of paraffin chains in a melt (a) and crystal (b).

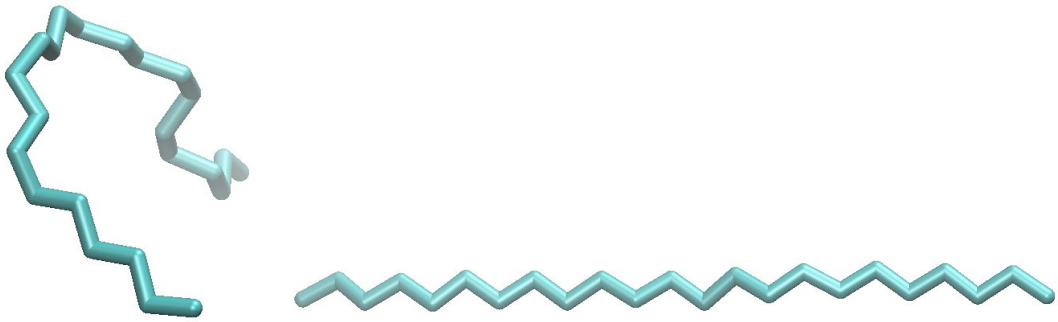

(a) Tricosane at 500 K (b) Tricosane at 260 K

Figure 7.2: *Tricosane chain in a melt at 500 K (a) and in a crystalline at 270 K (b)*

As chains straighten out, the number of *trans* (180°) dihedral angles increases, Figure 7.4. This affects the bonded distributions in the reference system and consequently the coarse grained potentials. Figures 7.5 and 7.6 show the change in bond and angle distribution between coarse grained beads and the corresponding effective potential over a range of temperatures. The two peaks in the bond and angle distributions for a coarse grained system correspond to *gauche* and *trans* conformations of the atomistically described molecule. The intensity of the peaks for bond length and bond angle distribution changes with the temperature, while their positions remain the same.

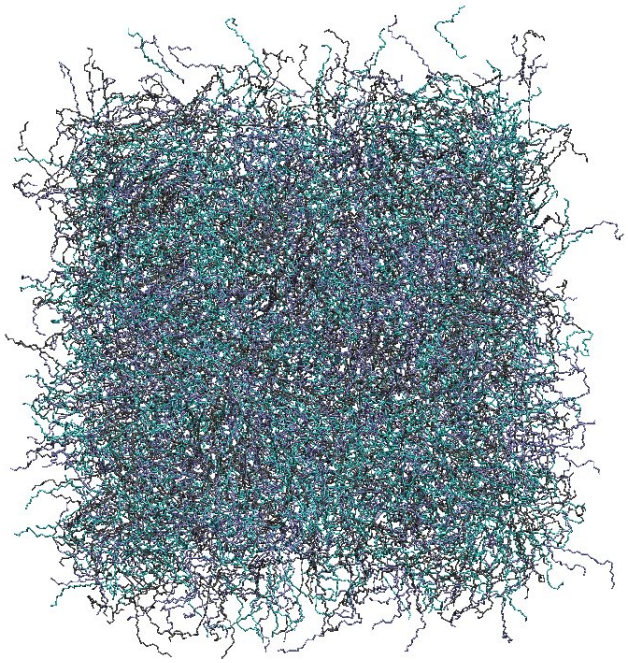

(a) Paraffin melt

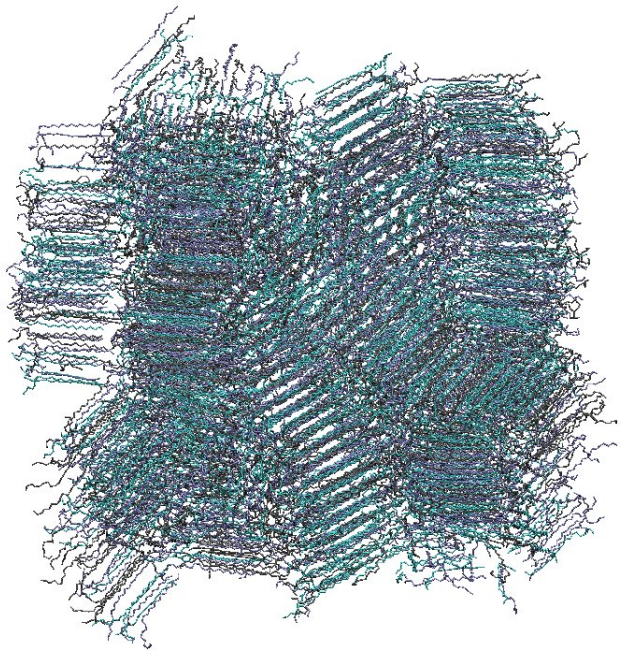

(b) Paraffin crystal

Figure 7.3: *Mixture of paraffins in the melt (a) and crystal (b): henicasane - cyan, tricosane - iceblue, tetracosane - grey*

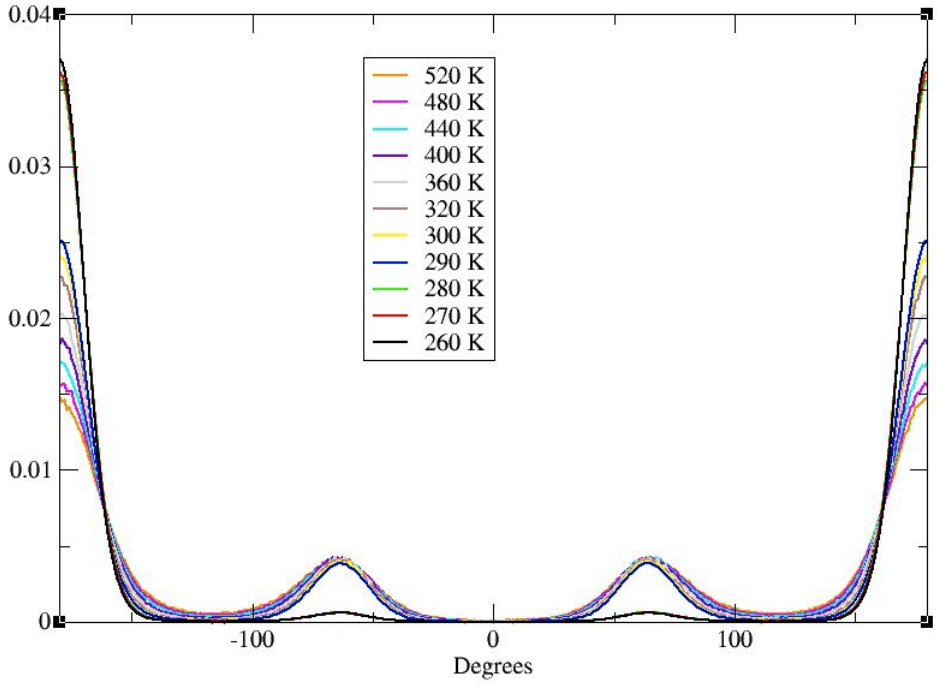

Figure 7.4: *Dihedral angle distribution for pure tricosane system upon cooling from 520 K to 260 K*

As the chains unfold it becomes possible for them to align, forming more ordered structures, Figure 7.3 (b). This will also affect radial distribution functions and consequently the non bonded potentials for coarse grained simulation.

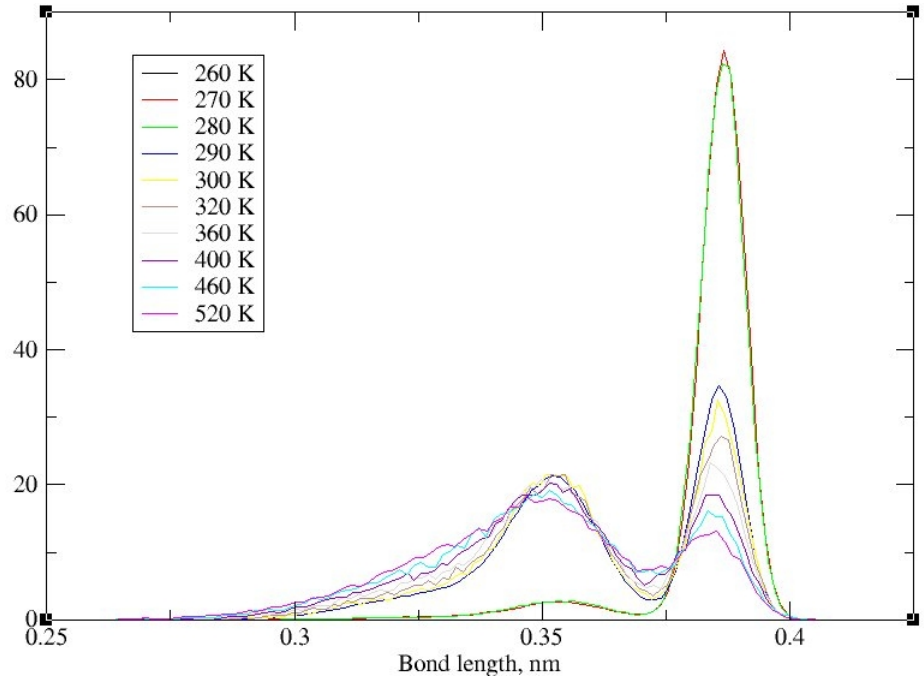

(a) Bond length distribution

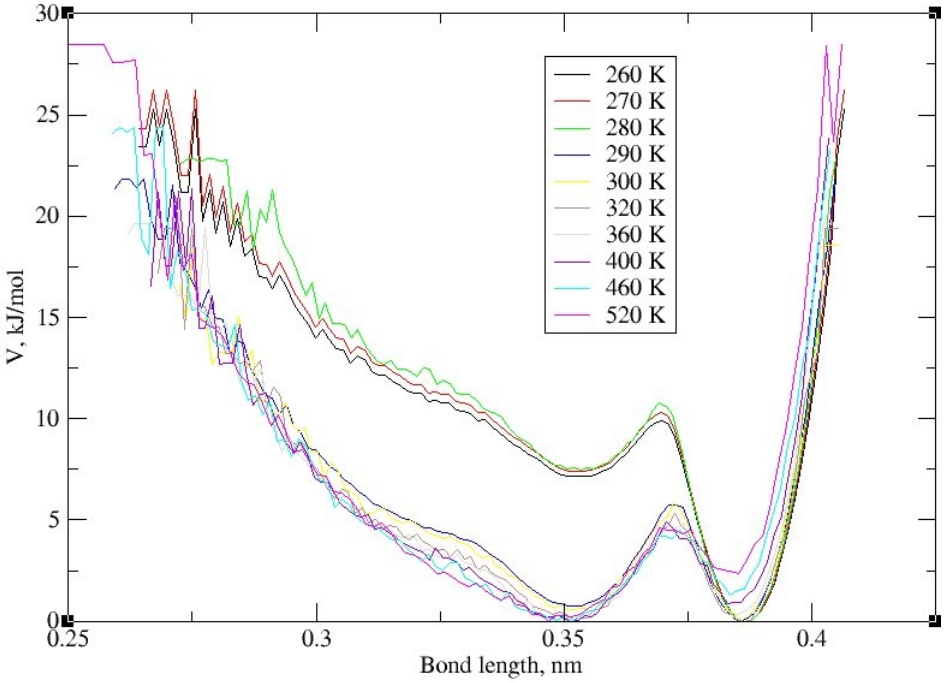

(b) Bond length potential

Figure 7.5: *The bond length distribution and corresponding effective potential for coarse grained beads in tricosane in the range of temperatures from 520 K to 260 K*

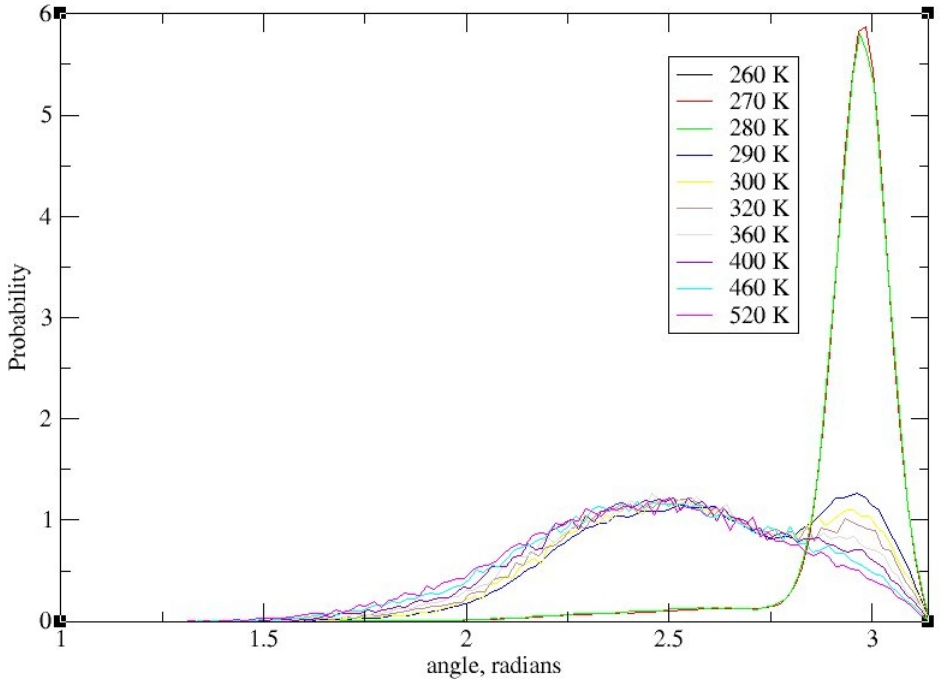

(a) Bond angle distribution

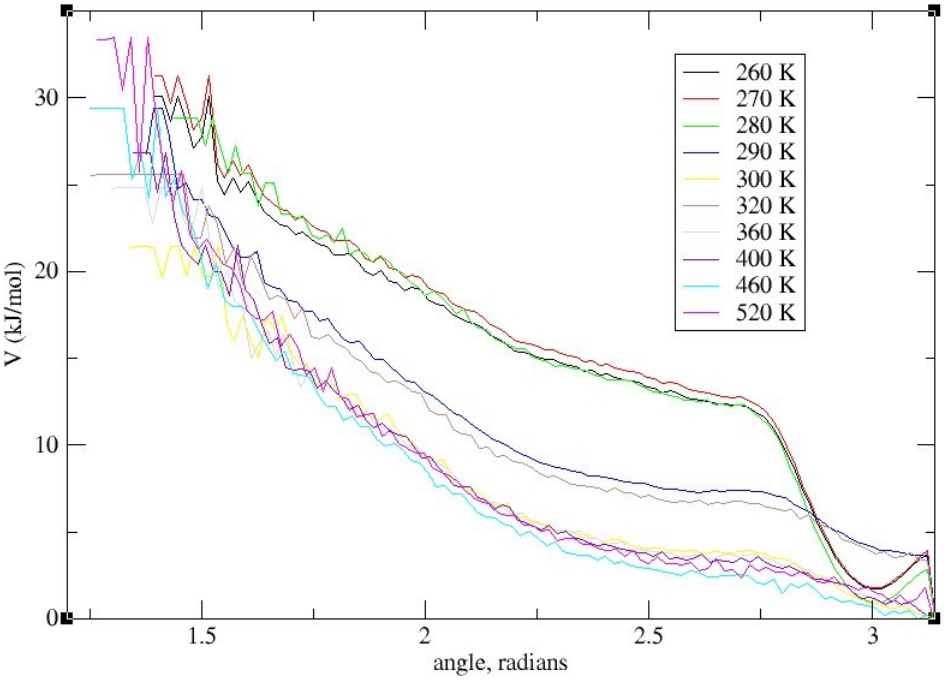

(b) Bond angle potential

Figure 7.6: *The angle distribution and corresponding effective potential for coarse grained beads in tricosane in the range of temperatures from 520 K to 260 K*

7.2 United atom reference systems

The fitting process discussed here is aimed at matching low resolution calculations to high resolution ones. For this reason the temperatures for coarse graining were identified computationally, rather then experimentally. For example, the shortest dodecane molecule was found to crystallise at 250 K.

The atomistic reference system was build with 1000 dodecane molecules, using the same procedure described in Section 4.3. The TraPPE united atom [20–25] force field was used. Since in this force field the fastest moving hydrogen atoms are not explicitly present, a larger time step than in all atom can be used. In all of the united atom calculations a time step of 2 fs is used.

The simulations were performed under the same conditions as in Section 4, and are summarised on Table 7.1 below.

Table 7.1: *Parameters for united atom calculation of the reference system*

Calculation parameters:	
System size	1000 molecules
Step size	2 fs
Length of calculation	10 ns
Integration	Leap frog
Periodic boundary	xyz
Ensemble	*NPT*
Temperature	250 K
Thermostat	Velocity rescale
Pressure	1 bar
Barostat	Parrinello-Rahman
Compressibility	9×10^{-5} bar^{-1}

The reference system was simulated with the isothermal-isobaric ensemble, which allows volume fluctuations. This approach guarantees that there is no restriction to the conformational changes, which are essential for studying crystallisation. Figure 7.7 shows the change of volume of the box through a simulation. The red line is the average volume of the system over the last 2 ns of calculation. Comparing the average (red line) to the volume of the simulation, one can see that the system converges to

a constant volume after an initial 3 ns. The last 5 ns, when the system is in equilibrium, are used to derive an initial guess for the potential in the coarse grained set up. Here, for a large enough system, a Boltzmann distribution of states should be obtained.

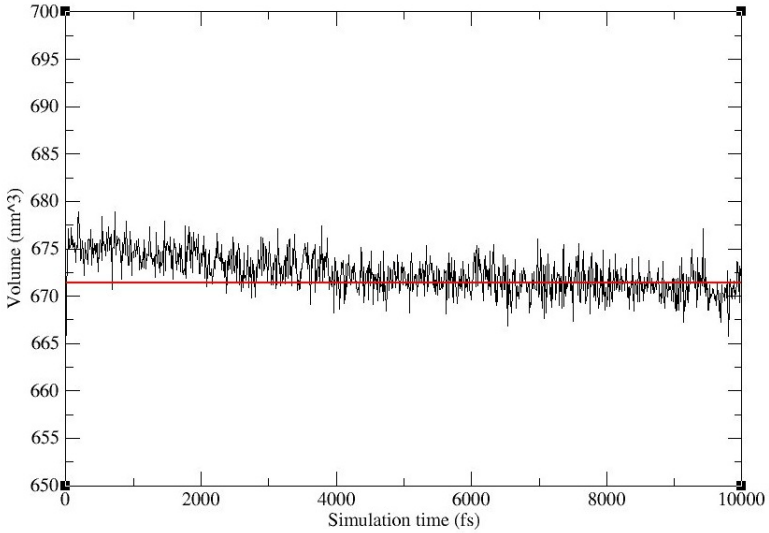

Figure 7.7: *Change in the volume of the box through the simulation. The red line is the average volume over the final 2 ns of calculation*

7.3 Development of a linear alkane coarse grained model

7.3.1 Bonded potentials

As discussed in Section 6.2.3, bond and angle distribution functions are evaluated from an atomistic trajectory and then converted into coarse grained potentials. To extract the necessary data from the atomistic reference calculation, the trajectory is analysed according to the mapping shown in Figure 7.1.

Figure 7.8 represents the mapping of a dodecane molecule. The central beads (C) are shown in blue and end beads (E) in red. The angle between coarse grained beads is shown by black lines. The centre of a bead is the centre of mass between the three united atoms. This is one of the major differences between the beads, as the bead E unites $CH_3 - CH_2 - CH_2$ while bead C unites all central carbons $CH_2 - CH_2 - CH_2$. The other difference is the non bonded interactions between types of beads, that

should define the correct crystal formation.

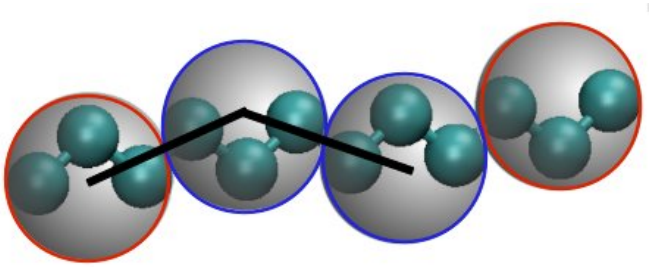

Figure 7.8: *The 3 to 1 mapping of the dodecane molecule, in red are the end beads, E, and in blue are the central beads, C. The angle E-C-C is also shown*

The bond and angle distributions are obtained from the united atom calculation at 250 K, shown in Figure 7.9 (a).

Due to the difference in volumes between atomistic and coarse grained beads, the distributions have to be normalised [13] by $1/4\pi r^2$ and then inverted following equation 7.1 to obtain the corresponding potential [1]

$$V(r) = -k_B T \ln b_{ref}(r) \tag{7.1}$$

To generate numerical input for GROMACS, the potential has to be extrapolated further than the cut off distance (1.5 nm for these calculations), the shape of the extrapolated part is not important, but should not be too steep, as this will create very high forces. The potential must be smoothed to provide a continuous force. An equally spaced table is created with *r, V(r), -V'(r)* , where *r* is the distance in nanometers, *V(r)* is the potential and *-V'(r)* is the force. A sampling of 0.002 nm was used in this work. Figure 7.9(b), shows the area of the well for the resulting bond potentials.

The angle potential is derived following the same procedure as the bond one. The distribution is normalised by $1/\sin(\theta)$, then inverted, smoothed and tabulated. The tabulated angle potential is of a similar form to the bonded and contains a list of three

[1] V_0 is a free energy, rather then potential, as there is a pressure contribution in the simulation.

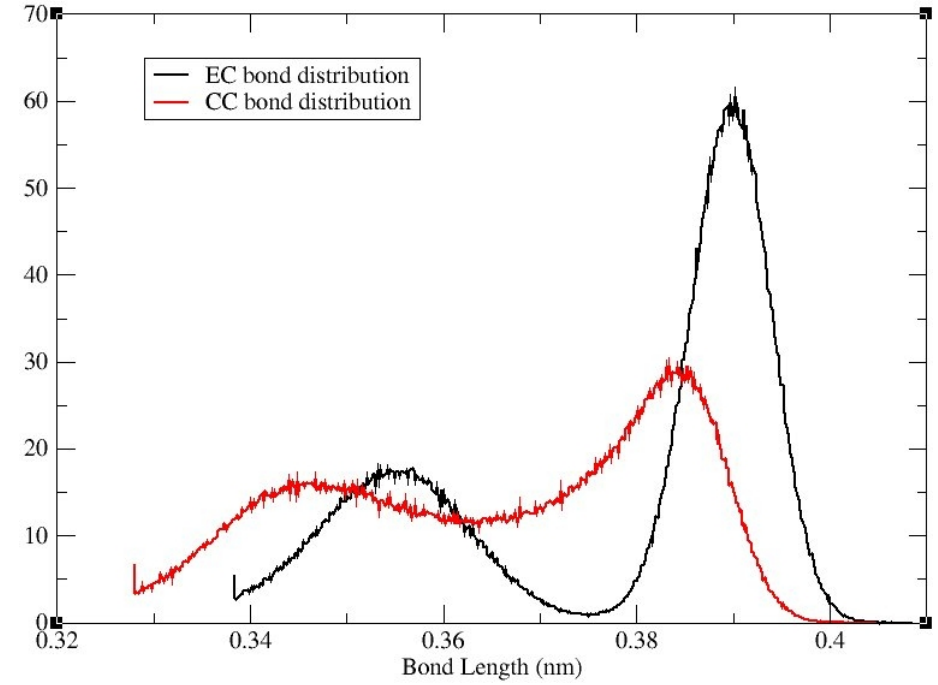

(a) Bond stretching distribution

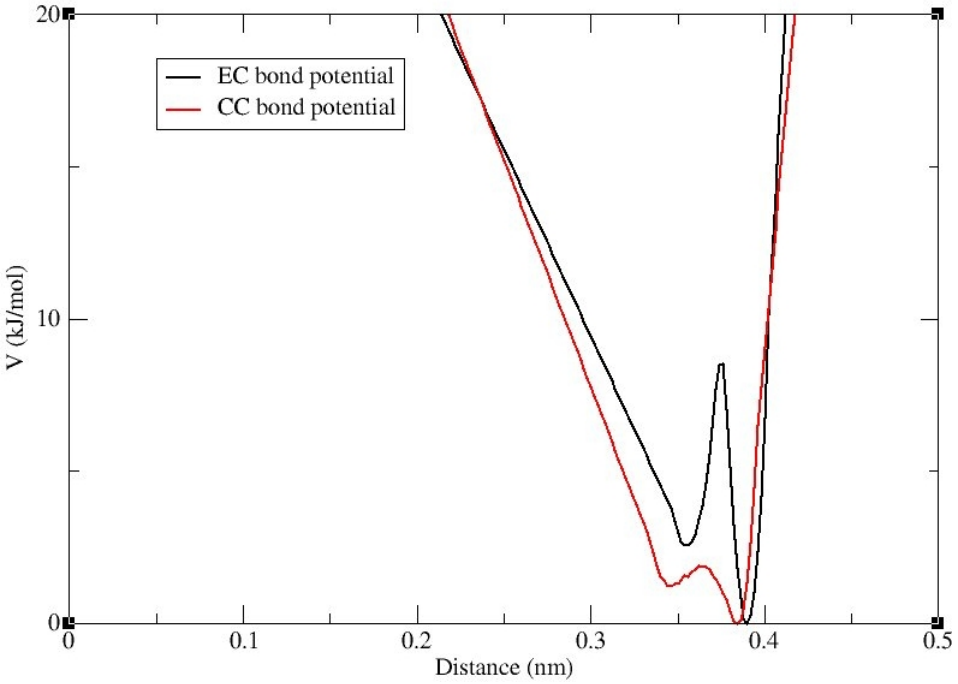

(b) Bond stretching potential

Figure 7.9: *Distribution of coarse grained bond lengths and the corresponding potential for dodecane at 250 K. The red line is the bond interaction between end (E) and central (C) beads and the black line is the interaction between central (C) beads*

values: $\theta, V(\theta), -V'(\theta)$ where θ is the angle in degrees from 0° to 180°, with sampling of 0.2°. The angle distribution and the well of the potential are given in Figure 7.10.

It is often assumed that coarse grained potentials derived for smaller molecules can be transferred to larger systems. This is done for example in the MARTINI force field for proteins [2, 4]. However, coarse grained potentials can also be very dependant on the state point, so transferability is not guaranteed. Figure 7.11 shows bond and angle distributions of dodecane, tricosane and tetracosane from united atom calculations at 250 K. From the comparison it can be seen that dodecane provides a good representation for angle distributions but not for bond distributions. Longer molecules show a wider distribution of *gauche* conformations (0.3 – 0.35 nm) and higher proportions of *trans* conformations (0.37 – 0.4 nm). This is likely due to the difference in crystallisation temperatures of dodecane (250 K), tricosane (275 K) and tetracosane (280 K). The higher peak in tricosane compared to tetracosane, corresponds to a higher proportion of *trans* dihedral angles in the first system. This is due to the restriction imposed by the simulation box on the tetracosane system. Tetracosane molecules are one carbon longer then tricosane, crystallise at slightly higher temperature and so require longer calculation times for the same number of molecules.

7.3.2 Non bonded potentials

In crystallisation of long chain paraffins the non bonded interactions play an important role. The difference in forces between central and end coarse grained beads defines the lamellar molecular alignment and directional growth speeds. These differences are subtle, even for high resolution calculations, and it is our aim to preserve them through coarse graining.

The radial distribution function (RDF) is calculated from united atom simulations and shown in Figure 7.12 (a). Similarly to bonded interactions, the RDF is inverted into the initial guess potential V_0, Figure 7.12(b).

The GROMACS input requires for the non bonded potential to be separated according

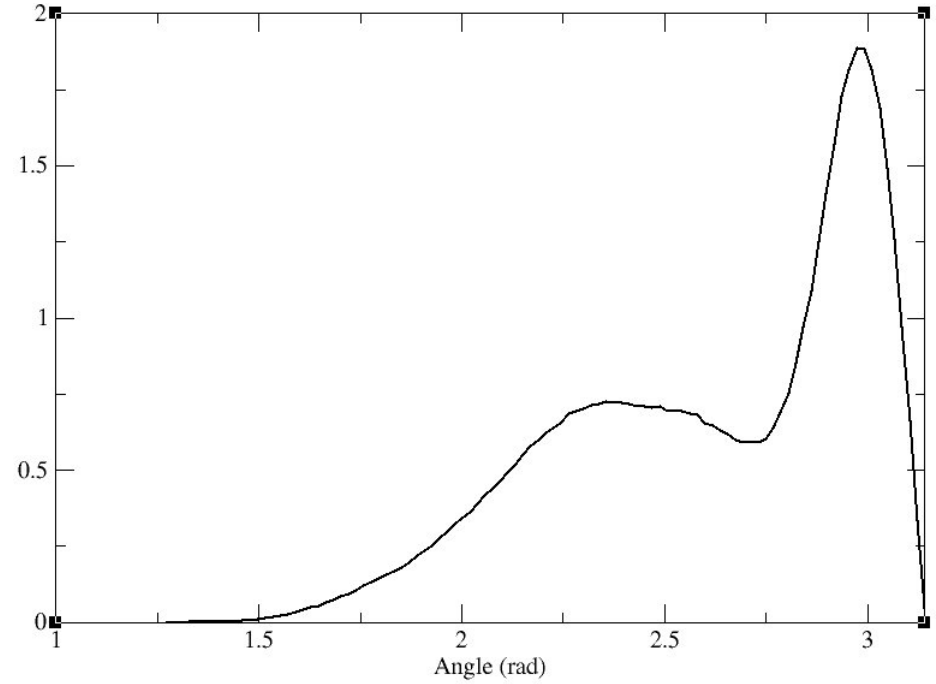

(a) Angle distribution

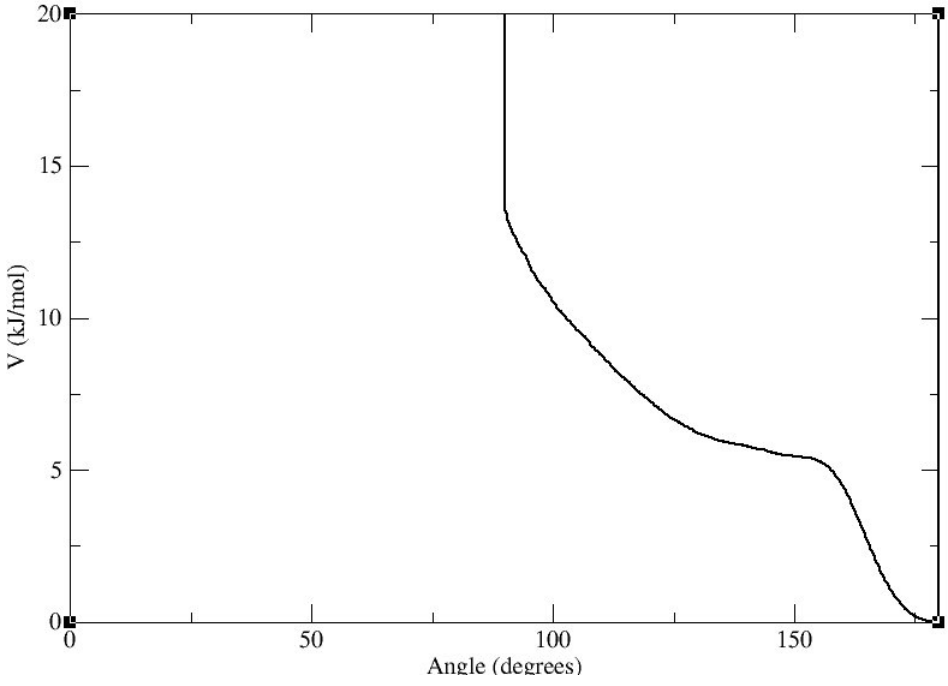

(b) Angle potential

Figure 7.10: *Distribution of a coarse grained ECC angle and the corresponding potential for dodecane at 250 K*

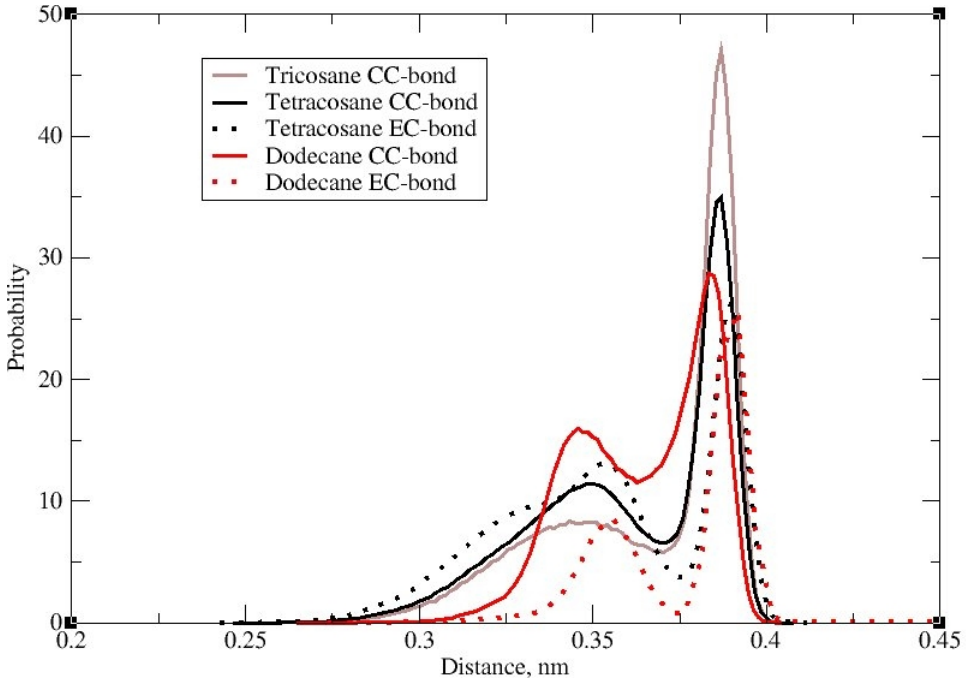

(a) Bond distribution

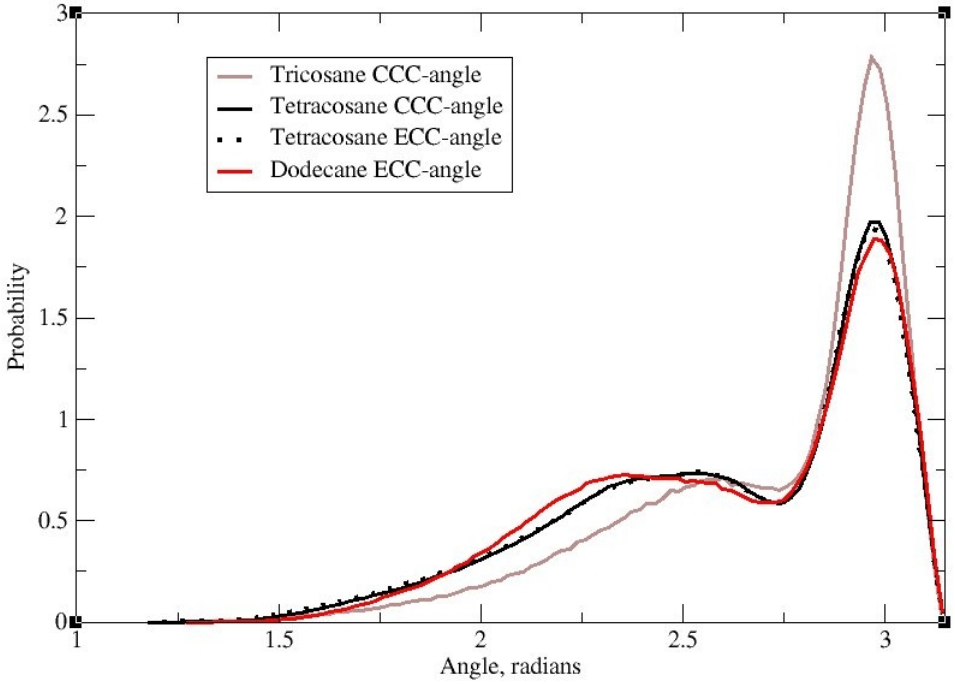

(b) Angle distribution

Figure 7.11: *Comparison of bond (a) and angle (b) distributions of beads in dodecane (red), tricosane (maroon) and tetracosane (black) at 250 K*

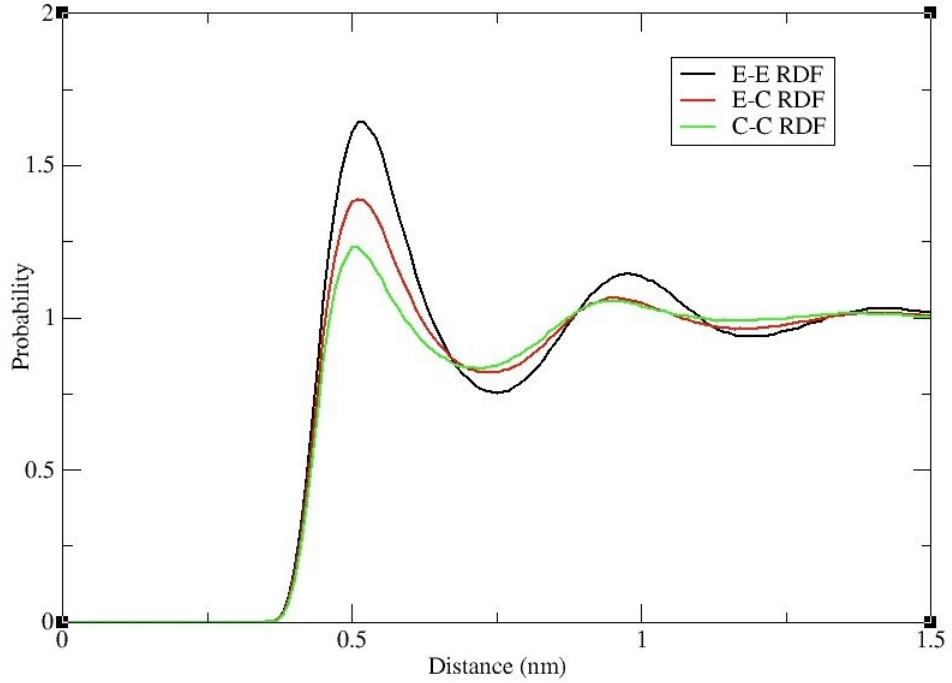

(a) Radial distribution funcliton

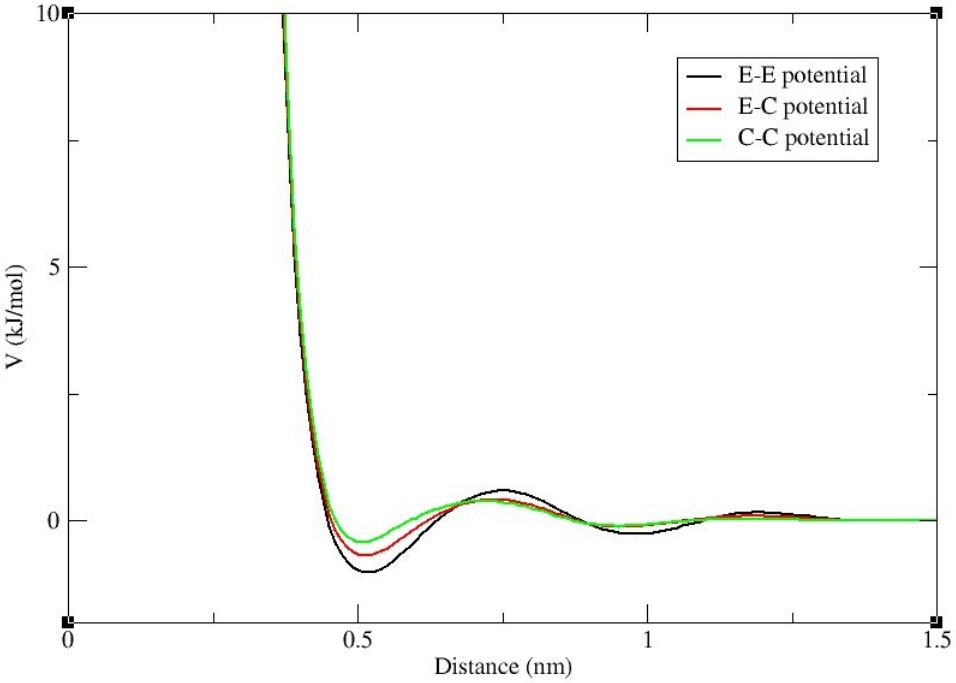

(b) Corresponding non bonded potential

Figure 7.12: *Radial distribution function (a) and corresponding non bonded potential (b) between coarse grained bead E and E (black), E and C (red) and C and C (green) of dodecane molecule at 250 K*

the following equation:

$$V(r_{ij}) = \frac{q_i q_j}{4\pi\epsilon_0} f(r_{ij}) + C_6 g(r_{ij}) + C_{12} h(r_{ij}) \tag{7.2}$$

where f, g, h are user defined functions, C_6 and C_{12} are coefficients and q_i, q_j are charges. The potential can then be represented as a seven-column table $r, f(r)$, $-f'(r), g(r), -g'(r), h(r), -h'(r)$ for inclusion as a numerical potential.

7.3.3 Iterative Boltzmann inversion

The initial coarse grained potentials previously derived were used to set up the first coarse grained calculations. These are further refined in a stepwise manner, starting at the bond potential and followed by the angle potential. When the bonded distributions are matched, non bonded potentials can also be refined. Table 7.2 summarises the parameters used for the coarse grained simulations.

Table 7.2: *Parameters for coarse grained iterative matching calculations*

Calculation parameters for coarse grain:	
System size	1000 molecules
Step size	4 fs
Length of calculation	2 ns
Integration	Leap frog
Periodic boundary	xyz
Ensemble	*NVT*
Temperature	250 K
Thermostat	Velocity rescale

The bond distributions obtained from the high resolution calculation provide the target, $b_{ref}(r)$, and are matched in an iterative process. After the first simulation a new bond distribution, $b_i(r)$ (i=1) is calculated and the new potential, V_{i+1} obtained,

by introducing a correction:

$$V_{i+1}(r) = V_i(r) - \lambda k_B T \ln \frac{b_i(r)}{b_{ref}(r)} \tag{7.3}$$

where $\lambda \in (0,1]$, depending on the amount of change required. λ is initially set to 1 and then reduced to 0.5.

The process is repeated until a good match between the high and low resolution distributions is obtained. Figure 7.13 shows the target bond distribution, the distribution from the first step and after 46 iterative steps, i.e. when the target is matched. The angle potential does not change through the process and represents well the target distribution without need for iterations.

Non bonded potential wells are not as deep as bonded ones, and so greater deviation through calculations is observed. After refining bonded potentials, the iterative process is performed on the non bonded potentials. The same calculation parameters, Table 7.2, are used through this refinement process.

Similarly to refining bonded potentials, the RDF obtained from a high resolution calculation are set as a target, $g_{ref}(r)$. After the first simulation a new RDF, $g_i(r)$, and hence a new potential, V_{i+1}, is obtained

$$V_{i+1}(r) = V_i(r) - \lambda k_B T \ln \frac{g_i(r)}{g_{ref}(r)} \tag{7.4}$$

where $\lambda \in (0,1]$, depending on the amount of change required. λ is set to 1 for the initial steps and then reduced to 0.5.

It was found that to match the RDF of dodecane, 50 iterative steps were sufficient. Figure 7.14 shows the change of RDF and the corresponding potential through iterative Boltzmann inversion.

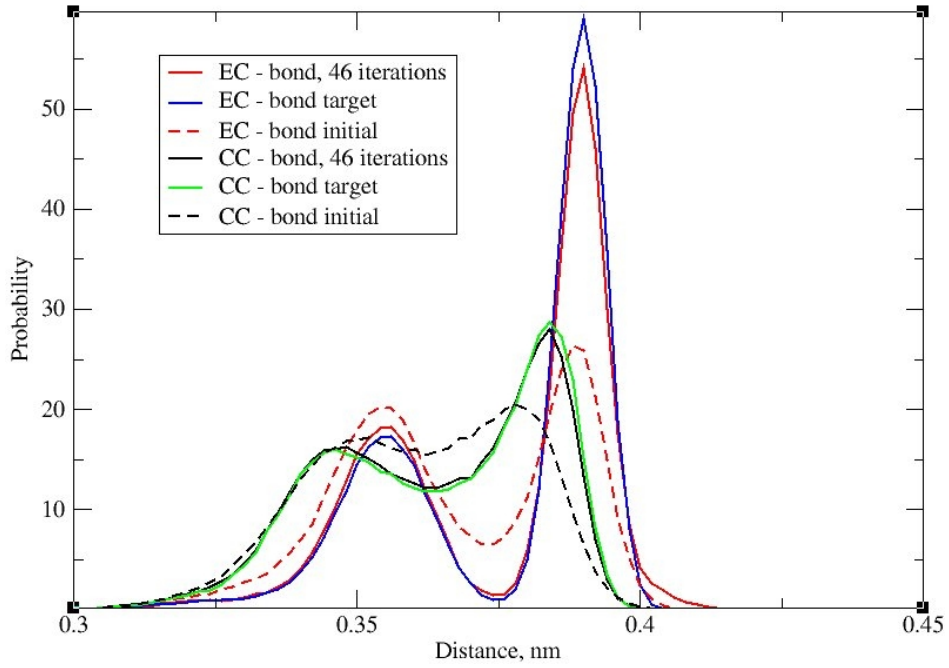

(a) Bond distribution

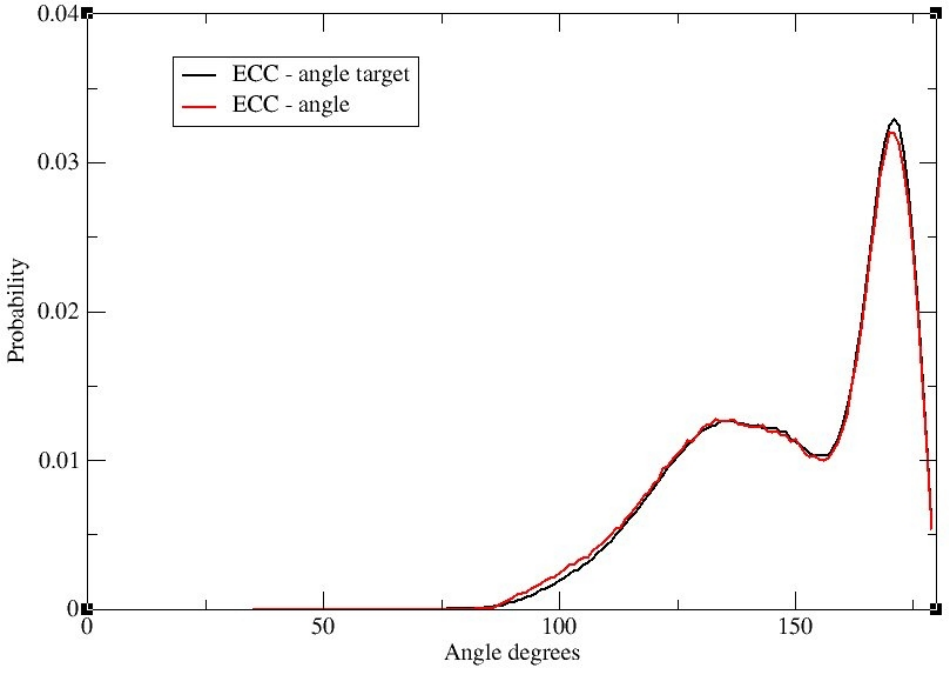

(b) Angle distribution

Figure 7.13: *Bond and angle distributions for coarse grained simulation of dodecane, matched through iterative Boltzmann inversion*

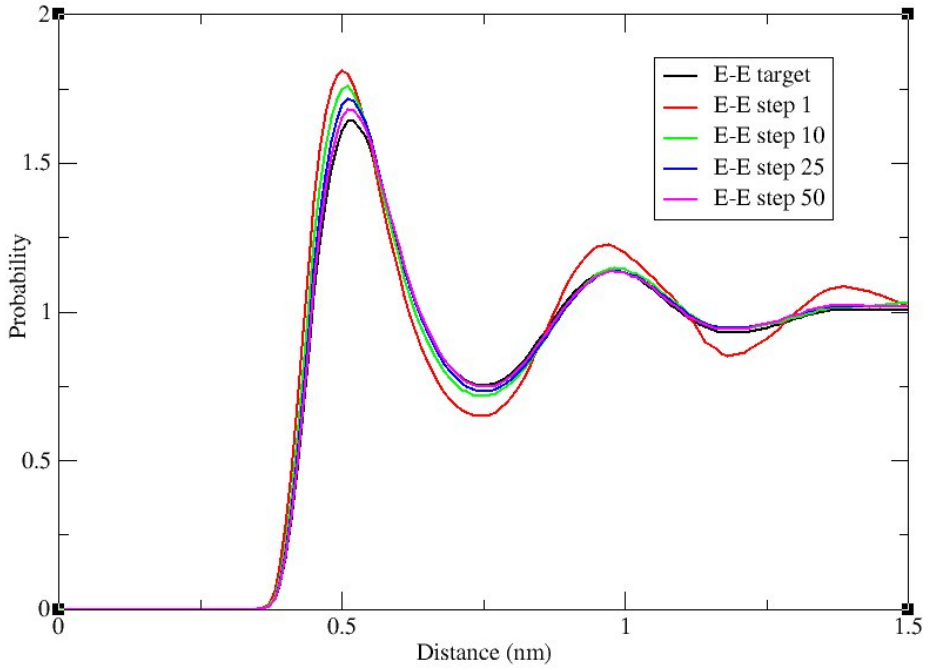

(a) RDF through iterative Boltzmann inversion

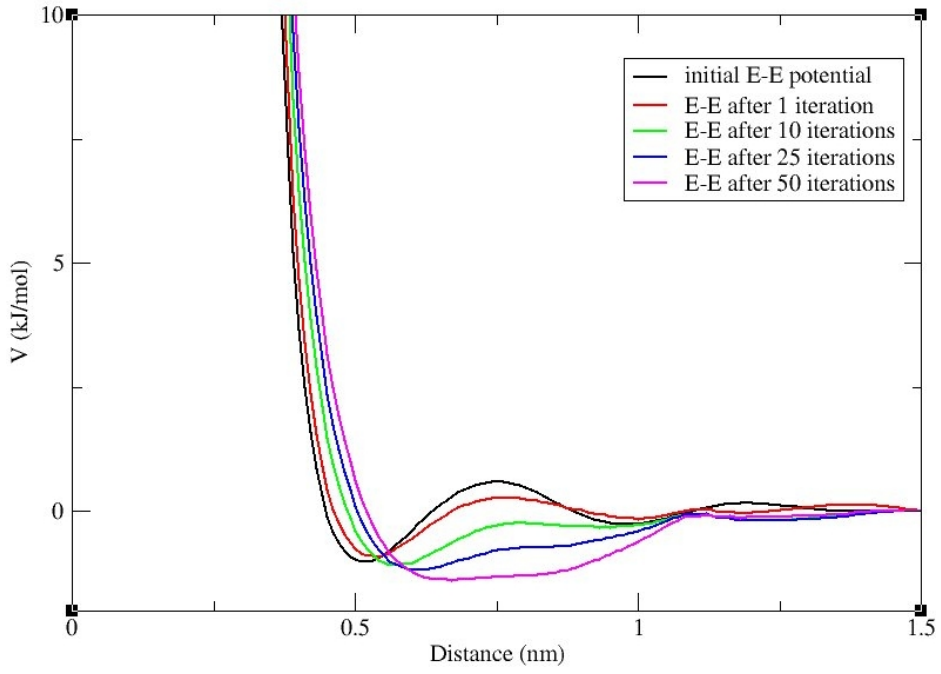

(b) Corresponding non bonded potential

Figure 7.14: *Change in the E-E RDF (a) and the corresponding potential (b) through the iterative process: Black line is the target RDF and the starting potential, red line – RDF and potential after first calculation, green line – after 10 steps of iteration, blue – after 25 steps of iteration, and magenta the final RDF and potential after 50 iterative steps*

7.4 Preliminary evaluation of the coarse grained model

In this section we test the performance of the coarse grained force field obtained in sections 7.3.1, 7.3.2 and 7.3.3. A simulation of 1000 coarse grained dodecane molecules at three temperatures was performed in the canonical ensemble (constant volume), using the parameters given in Table 7.3. The coarse grained force field was parameterised at 250 K. A lower temperature of 200 K and a higher temperature of 300 K were also assessed.

Table 7.3: *Parameters for coarse grained simulation of dodecane in the canonical ensemble*

Calculation parameters for coarse grained model:	
System size	1000 molecules
Step size	4 fs
Length of calculation	4 ns each
Integration	Leap frog
Periodic boundary	xyz
Ensemble	*NVT*
Temperature	200 K & 250 K & 300 K
Thermostat	Velocity rescale

The resulting bonded distributions, compared to the target ones, are shown in Figure 7.15 and 7.16. The matching with the target for the EC bonds is not as good as for the CC ones, but overall the bonded distributions are well represented and show temperature dependence. The highest probabilities of *trans* configuration are observed at 200 K.

The non bonded distributions show very good agreement with the united atom model. The density of both the coarse grained and united atom systems are 0.752 g/cm^3. The coarse grained simulations have to be performed at constant volume, due to the very high pressures arising through the calculations. The recorded pressures for these systems are over thousand bars. Pressure corrections should be applied for a successful development of temperature transferable potentials [39]. The next section discusses the approach in detail.

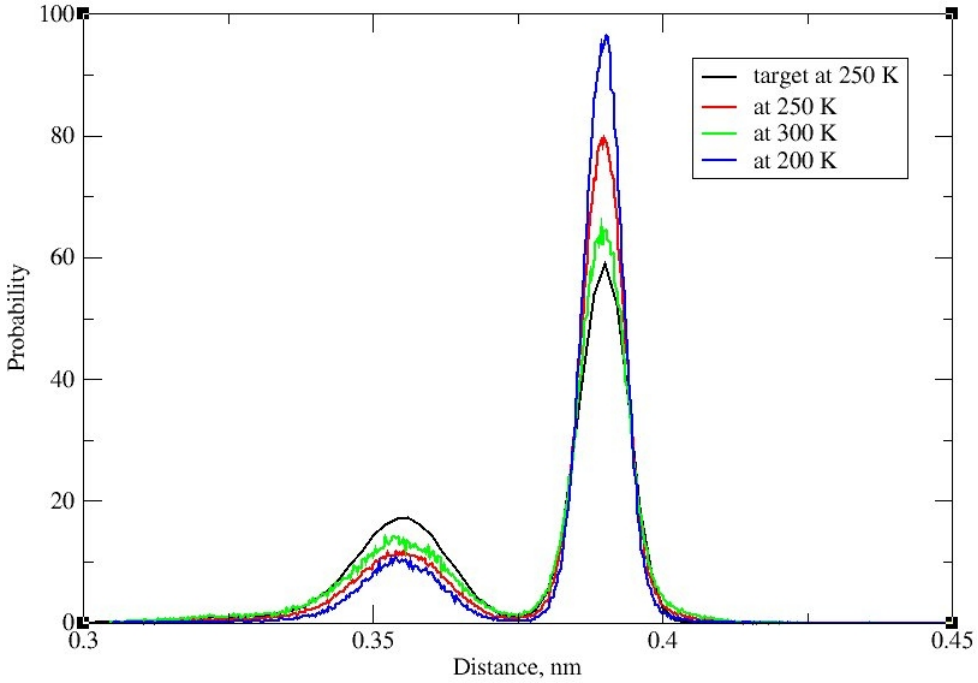

(a) Bond distribution between E-C beads

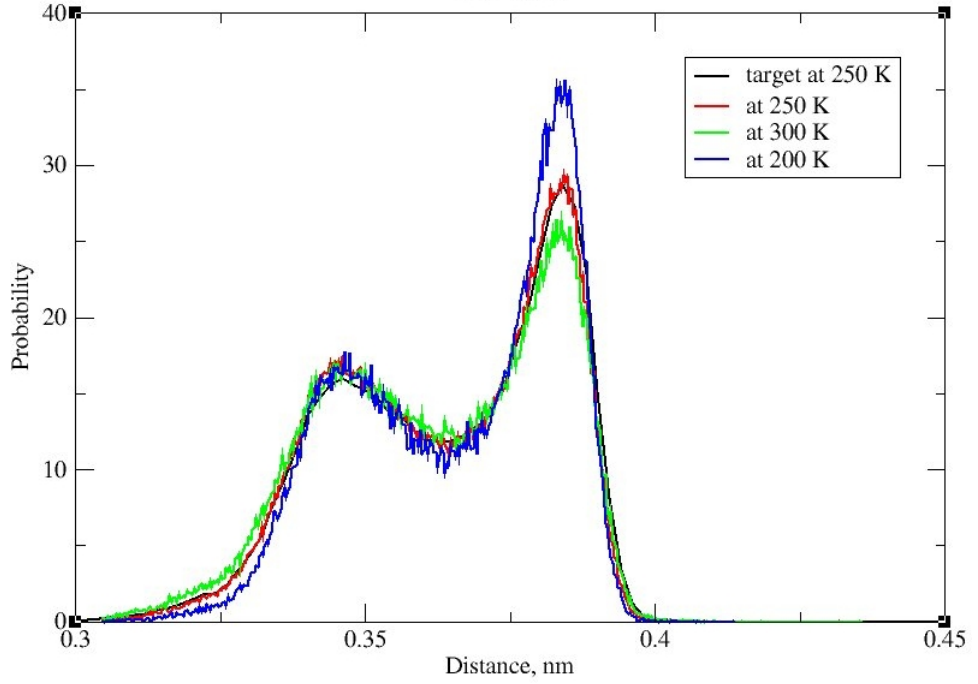

(b) Bond distribution between C-C beads

Figure 7.15: *Bond distributions for dodecane at 200 K , 250 K and 300 K , compared to the target atomistic distribution from united atom simulations at 250 K*

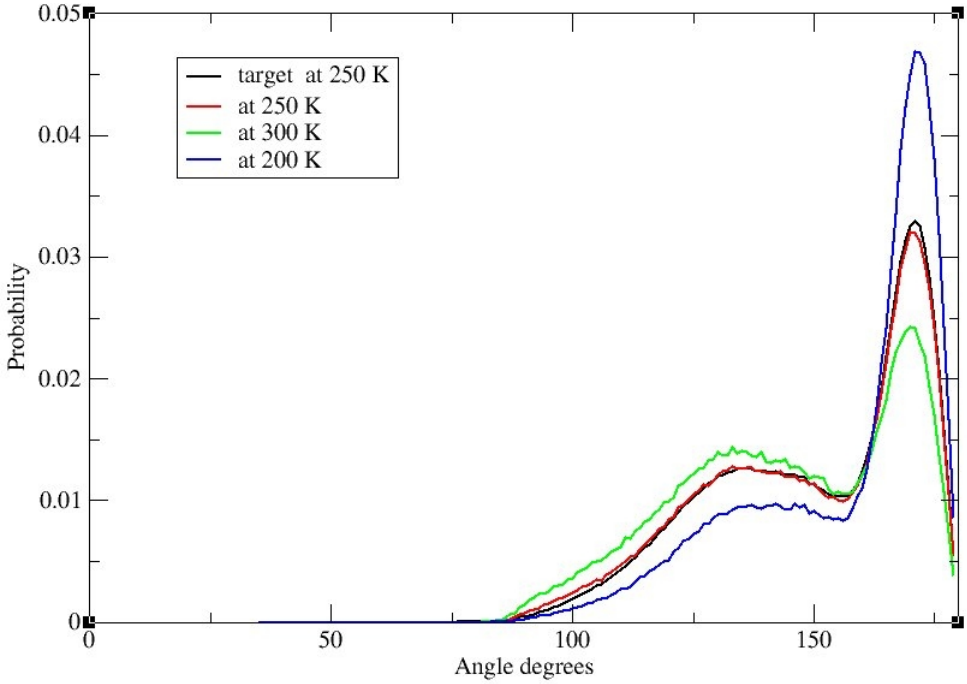

Figure 7.16: *Angle distributions for dodecane at 200 K , 250 K and 300 K , compared to the target atomistic distribution from united atom simulations at 250 K*

7.5 Pressure correction

A common problem in coarse graining bulk systems, is that even when good structural agreement is obtained, the pressure of the system is not necessarily well reproduced. There are two known ways to correct the pressure. Both of them are based on introducing a correcting potential to the RDF at long range [32],

$$V_{att} = A\left(1 - \frac{r}{r_{cutoff}}\right) \tag{7.5}$$

In the simplest method, A is a linear attractive potential

$$A = -0.1 k_B T \begin{cases} f\Delta P & |f\Delta P| < 1 \\ \dfrac{f\Delta P}{|f\Delta P|} & |f\Delta P| \geq 1 \end{cases} \tag{7.6}$$

$$\Delta P = P_i - P_{target}$$

where P_i is the pressure after iteration i, P_{target} is the target pressure (of 1 bar in this work) and f is a scaling factor, that is tuned during the pressure scaling.

Another method derives A from the virial expression [40]:

$$A = -\left[\frac{2\pi\rho^2}{3r_{cutoff}} \int_0^{r_{cutoff}} r^3 g_i(r) dr\right] A_i = [P_i - P_{target}] \tag{7.7}$$

where $g_i(r)$ is the RDF after iteration and ρ is the density.

The simplest approach was used in this work. Following equation 7.5 and using A as given by equation 7.6, the correction is applied to one potential per step, then the pressure of the system is evaluated and new potentials obtained. The pressure correction is followed by iterative matching of the potential.

After a few trials the scaling factor f was found to be best for values in the region between 0.0001 and 0.001. Smaller values led to insufficient corrections, while greater values caused overcorrection of the potential. It was observed that the best match for the RDF and the least deviation from the initial shape of the potential is obtained with a scaling factor allowing for the fastest converging to the target pressure. In the following work f was set to 0.0005.

Figure 7.17 shows the pressure for the dodecane system plotted through the pressure correction iteration process. The red dashed line shows the target pressure of 1 bar. The best pressure correction is -5.48 bar obtained after 24 steps and is marked with a red star. The corresponding non bonded potentials, as well as the initial ones are shown on Figure 7.18.

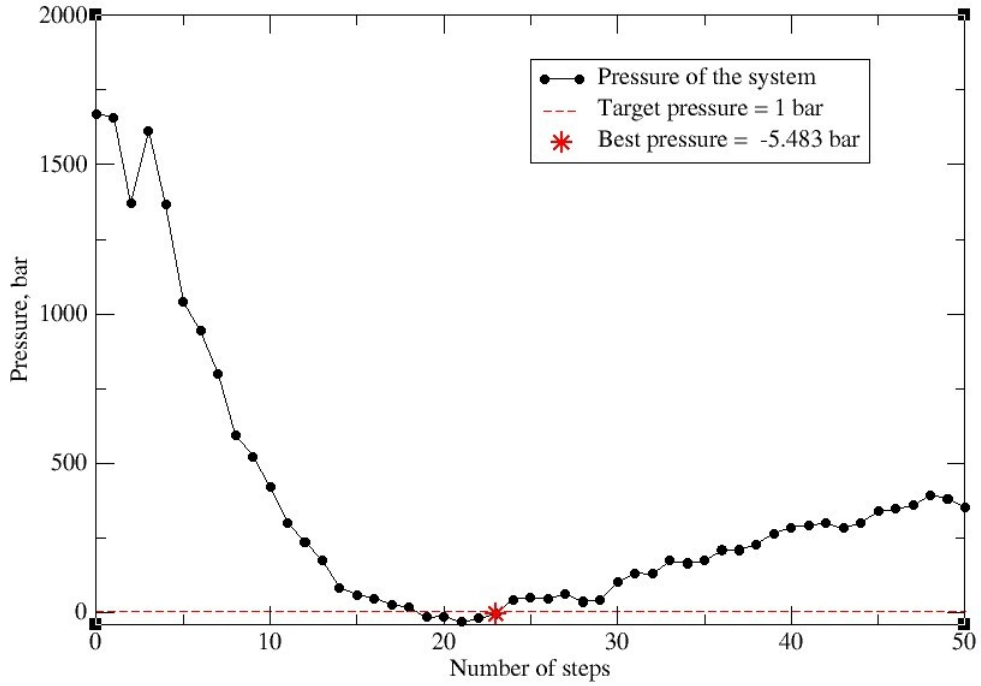

Figure 7.17: *Pressure of a coarse grained dodecane system during pressure correction simulations. Target value is shown by the dashed line, best match value is shown with a star*

As seen in Figure 7.17, after initial convergence, the pressure correction moves away from the desired pressure of 1 bar. This is a result of following the pressure correction step with fitting. It was found that the best fit potentials are obtained when pressure converges within few steps (larger scaling factor f may be required). In this study the best pressure correction is -5.48 bar (after 23 steps), the best positive pressure is 15.80 bar (after 19 steps). For coarse grained system, these values are very close to the desired pressure, given that typical pressure fluctuations in the *NPT* ensemble are around 30 bars. Below the two values are compared.

The pressure corrected systems are evaluated at an overall pressure of 1 bar, in the isothermal-isobaric ensemble. Parameters for the calculation are given in Table 7.4.

Figure 7.20 shows the bond and angle distributions and Figure 7.19 shows the RDF for two pressure corrected dodecane systems [2]. As may be expected, the bond and

[2] In the discussion and figures the system corrected to -5.48 bar is regarded as negative (-ve) pressure

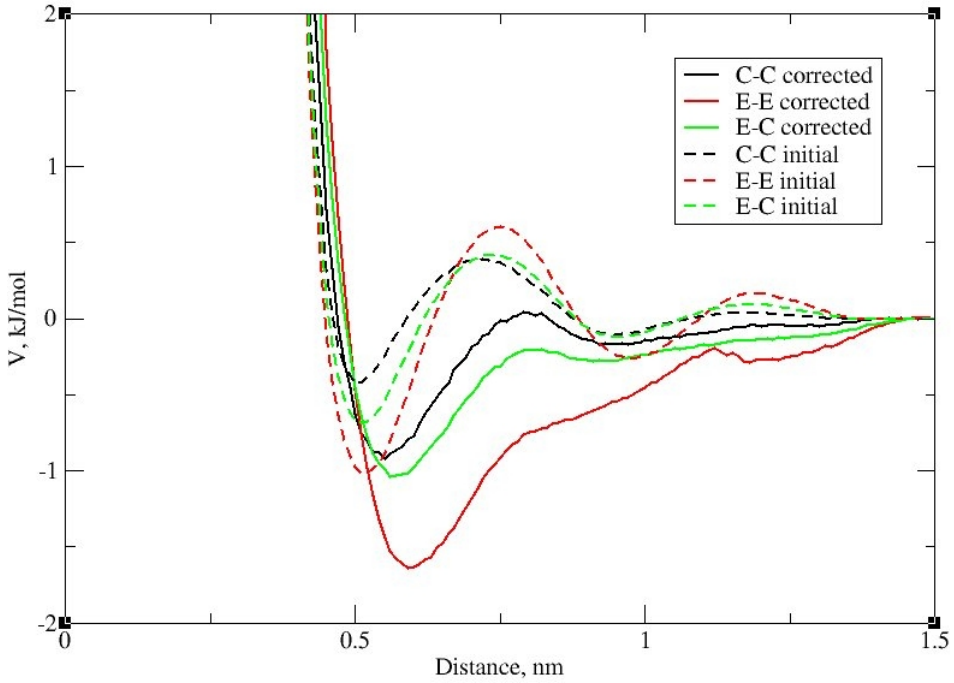

Figure 7.18: *Non bonded coarse grained potential for dodecane at 250 K before and after pressure correction*

Table 7.4: *Parameters for coarse grained simulation of dodecane in the isothermal-isobaric ensemble at 250 K*

Calculation parameters:	
System size	1000 molecules
Step size	4 fs
Length of calculation	6 ns
Intergration	Leap frog
Periodic boundary	xyz
Ensemble	*NPT*
Temperature	250 K
Thermostat	Velocity rescale
Pressure	1 bar
Barostat	Berendsen
Compressibility	9×10^{-5} bar^{-1}

angle distributions are not influenced by the pressure correction. The correction was only applied on the non bonded potential, that was then re-matched to fit the RDF. Applying a constant pressure allowed systems to relax and change the size of the simulation box, leading to a small change of density. The density of the system with corrected pressure down to -5.48 bar is 0.754 g/cm^3 while the density of the other system (15.80 bar) is 0.751 g/cm^3. The densities are in a good agreement with those from the united atom calculation, 0.752 g/cm^3 and comparable with the experimental density at 273 K of 0.763 g/cm^3 [41].

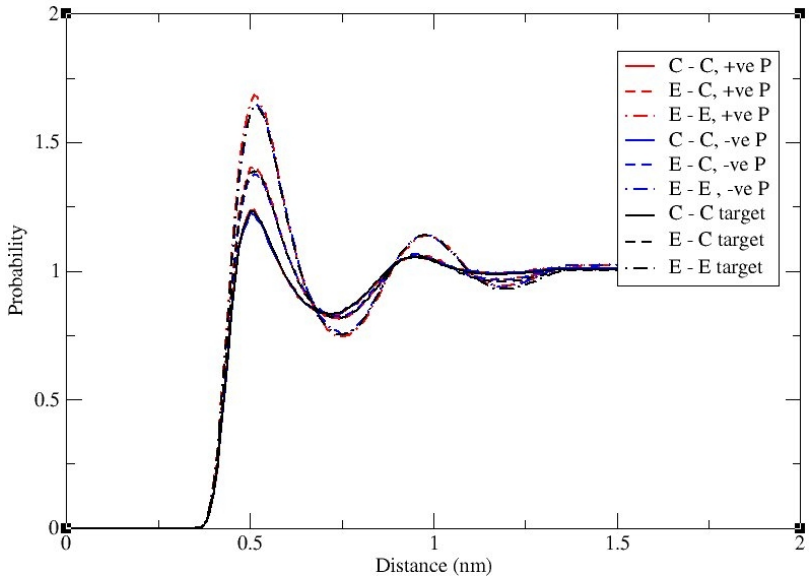

Figure 7.19: *RDFs for three interactions in dodecane after application of pressure correction. The target RDF is shown in black*

Additionally, the effect of changing the ensemble pressure to match the pressure correction (i.e -5.48 bar instead of 1 bar) was checked and no significant difference observed, as the deviation from the corrected pressure is very small from the target for such calculations.

The pressure correction is essential to allow coarse grained simulations to be performed in the isothermal-isobaric ensemble and so be transferable. No significant difference was found between two dodecane systems with different pressure corrections, when the correction is within half of the pressure fluctuations (i.e. 15 bar).

correction and the system corrected to 15.80 bar, as positive (+ve).

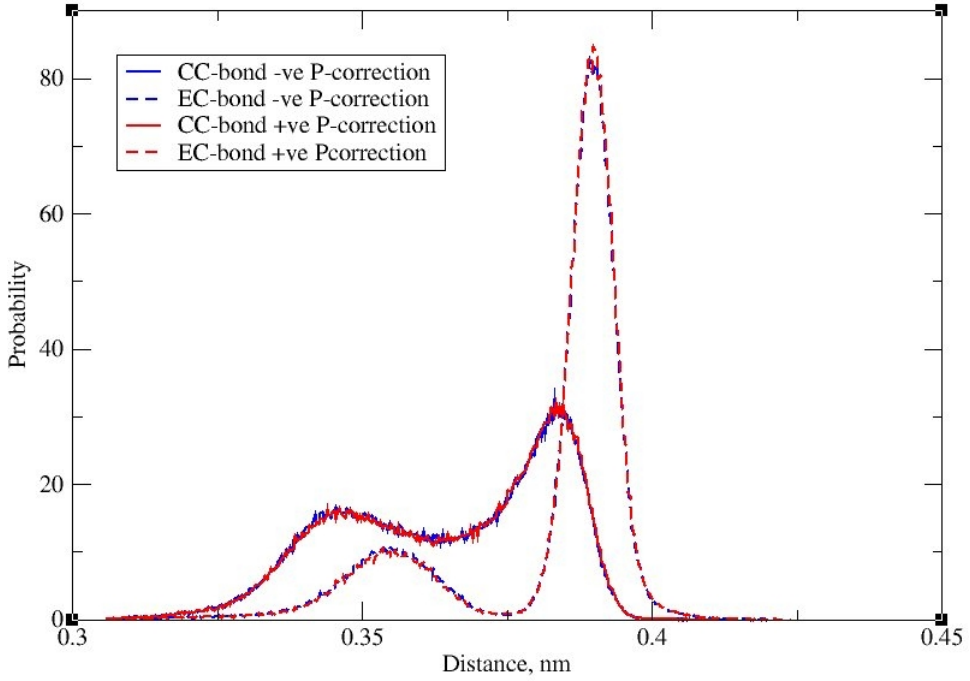

(a) Bond distribution after pressure correction

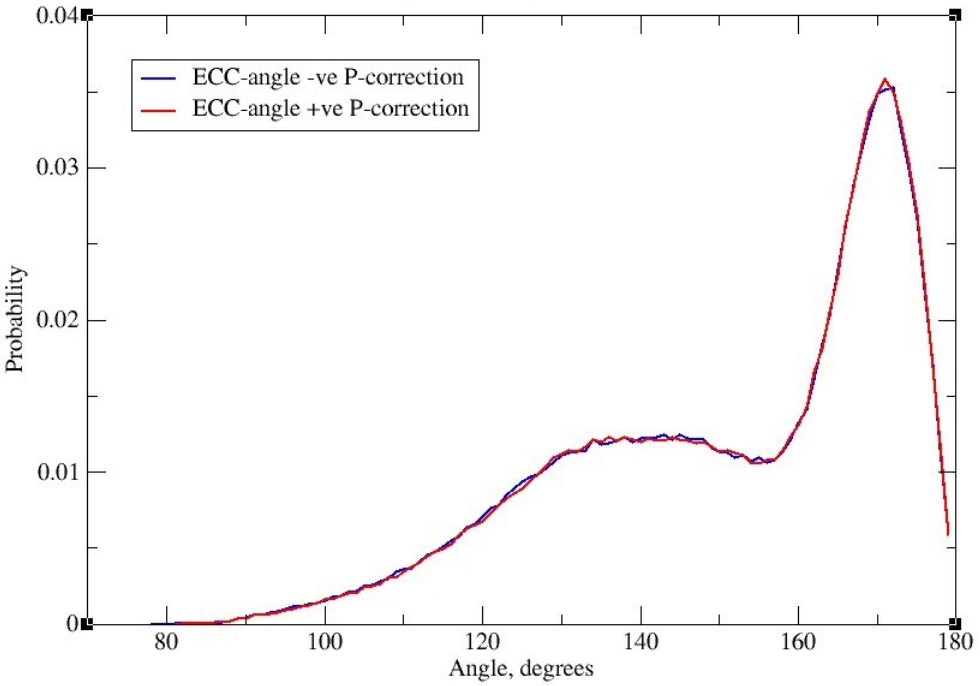

(b) Angle distribution after pressure correction

Figure 7.20: *Bond and angle distribution for the dodecane system at 250 K after pressure correction, leading to positive pressure (red line) and negative (blue line)*

7.6 Temperature transferability of coarse grained dodecane

Coarse grained simulations were performed at 320 K, 300 K, 250 K and 200 K in the isothermal-isobaric ensemble at 1 bar pressure, Table 7.5. Temperature and pressure couplings were applied with the simpler velocity rescaling thermostat and Berendsen barostat, as these are computationally faster and less sensitive to large fluctuations than the ones used in atomistic studies.

Table 7.5: *Parameters for coarse grained simulation of dodecane in the isothermal-isobaric ensemble at various temperatures*

Calculation parameters:	
System size	1000 molecules
Step size	4 fs
Length of calculation	8 ns each
Intergration	Leap frog
Periodic boundary	xyz
Ensemble	*NPT*
Temperature	200K & 250 K & 300 K & 320K
Thermostat	Velocity rescale
Pressure	1 bar
Barostat	Berendsen
Compressibility	9×10^{-5} bar^{-1}

The final conformations at lowest (200 K) and highest (320 K) temperatures are presented in Figure 7.21. A slight difference in the dodecane structure can be observed, with straighter chains at 200 K. The interchange between *trans* and *gauche* conformations of this model is defined by bond and angle distributions, which reflect the shape of the molecule, Figure 7.22. A steady shift towards *trans* conformations (longer bond, wider angle) upon decreasing the temperature is observed in both bond and angle distributions. This mirrors the trend observed in atomistic calculations, Figures 7.5 and 7.6.

The density of the coarse grained model, compared to experimental measurements[3],

[3]The data is taken from SciFinder, dodecane CAS Registry Number: 112-40-3, see scifinder.cas.org and references therein [41–43]

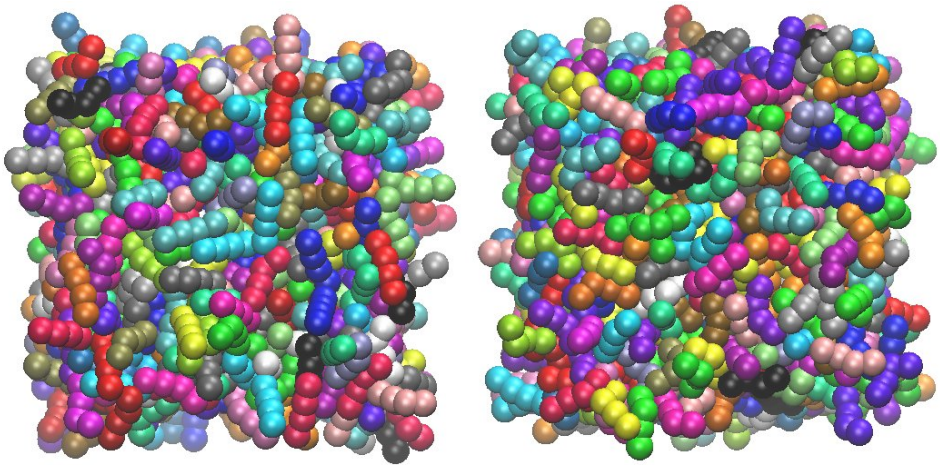

(a) 200 K (b) 320 K

Figure 7.21: *Snapshot of the final configuration of the coarse grained dodecane system with pressure correction at 200 K and 320 K*

is plotted in Figure 7.23. The density of our coarse grained model matched the density of the united atom model at 250 K, i.e. the temperature of parametrisation. This agreement also led to the same melting point. While the trend of the density change is well represented by the coarse grained model, this value is slightly lower than the experimental ones. As discussed above, this arises due to the initial slight mismatch of densities between united atom and experimental measures.

The developed coarse grained model represents the dodecane system well over a wide range of temperatures. In the next section this model is used to model longer tetracosane chains.

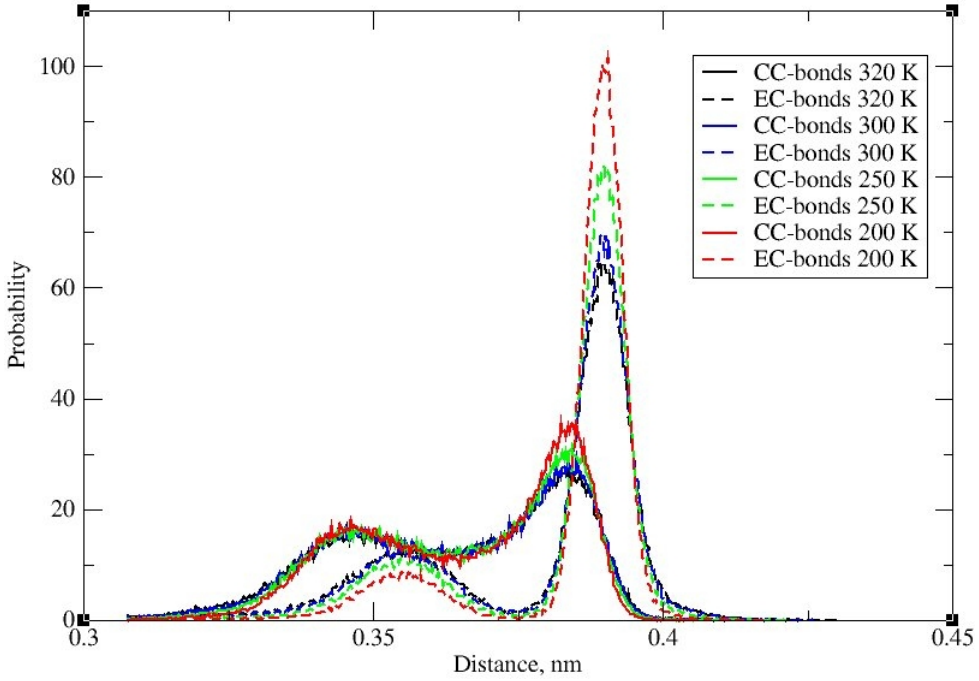

(a) Bond distribution

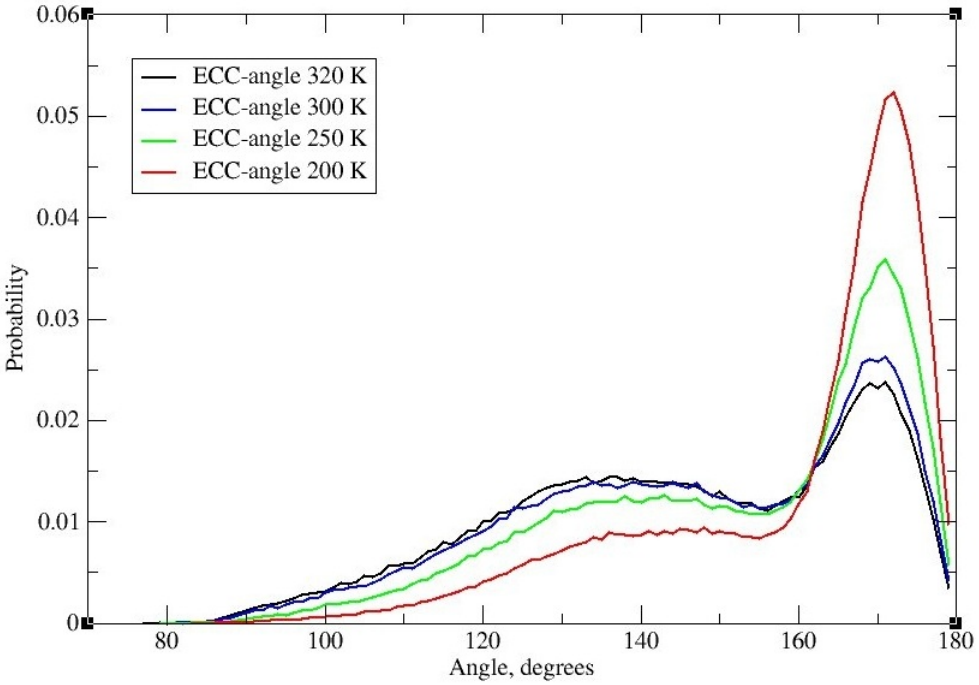

(b) Angle distribution

Figure 7.22: *Bond and angle distributions of coarse grained dodecane at 200 K (red), 250 K (green), 300 K (blue) and 320 K (black) at 1 bar*

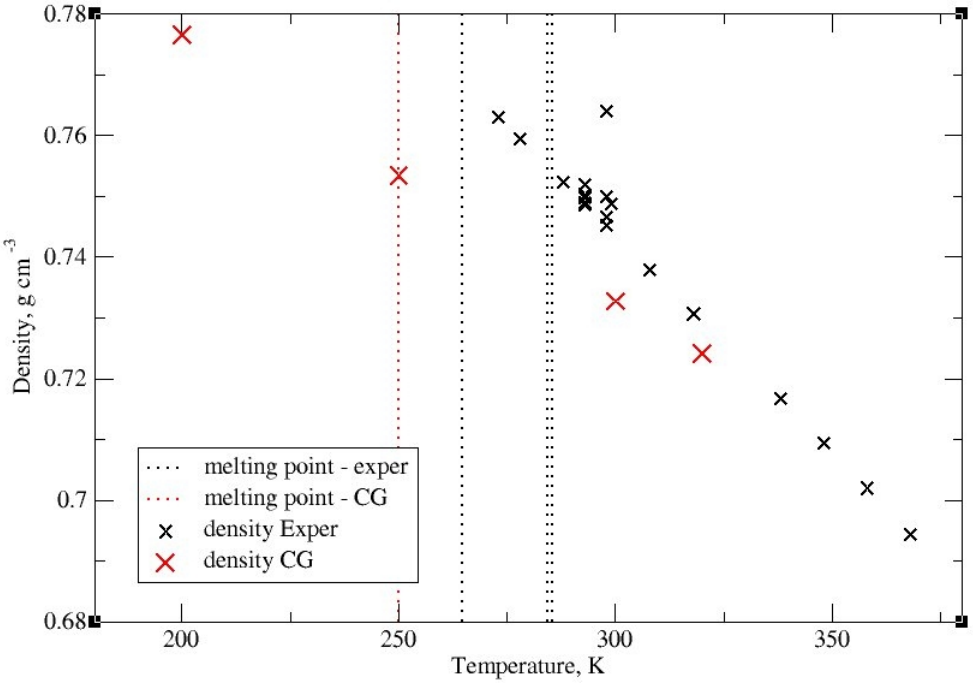

Figure 7.23: *Density and melting temperature of dodecane over a range of temperatures. The density calculated from the coarse grained model is marked with red crosses, experimentally measured density with black crosses. The melting point is shown as a vertical dotted line, red for the coarse grained model and black for experimental*

7.7 Coarse grained simulations of tetracosane

The main aim of this section is to develop potentials to be used on long chains and large systems. For this reason our coarse grained force field was tested on 8000 tetracosane molecules. The melting temperature of tetracosane (computationally evaluated to be 280 K) is higher than dodecane's. For the first test, the system was simulated at 250 K, i.e. the temperature of parametrisation of the force field. As expected, the formation of a crystal was observed. Since the mobility of molecules is very little at this state point, the system was left quenched, forming nano-crystal domains.

As shown in Section 4, stepwise annealing leads to a more equilibrated formation of a crystal. In order to characterise both crystallisation and melting, we performed two annealing sequences, both starting at 280 K. In the first sequence, the system was cooled to 270 K and then 250 K. In the second one, the system was heated stepwise to 290 K, 300 K and 320 K. The parameters for calculation are given in Table 7.6.

Table 7.6: *Parameters for coarse grained calculations of tetracosane over a range of temperatures*

Calculation parameters:	
System size	8000 molecules
Step size	4 fs
Length of calculation	4 ns at each temperature
Integration	Leap frog
Periodic boundary	xyz
Ensemble	*NPT*
Temperature	250 K
	280 K & 270 K & 250 K
	280 K & 290 & 300 K & 320 K
Thermostat	Velocity rescale
Pressure	1 bar
Barostat	Berendsen
Compressibility	9×10^{-5} bar^{-1}

The crystallisation temperature was found to be approximately 280 K, in agreement with the united atom model. It has to be noted that all high resolution studies we performed, consistently underestimate the crystallisation point, experimentally reported

to be 319 K [44].

Figure 7.24 shows the transition structure at 280 K, while the crystal at 250 K and a melt at 320 K are shown in Figure 7.25. There are two types of defects arising at the transition: *gauche* defects, displayed by the coarse grained model as curvature of the chain, and the disordered domains where molecules have shifted from their crystal positions. The *gauche* defects are commonly associated with a rotator phase in united atom calculations. Upon further cooling chains become straighter and, hence, more parallel, by such increasing the order and density. The disordered domains gradually minimise in size, giving better formed lamellar layers.

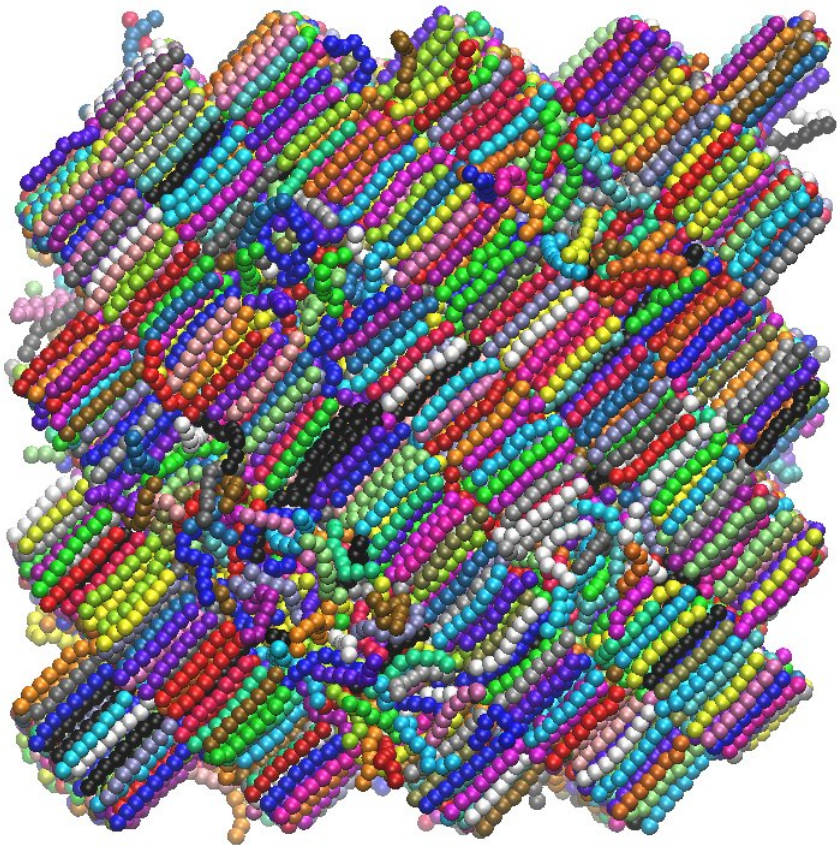

Figure 7.24: *A system of 8000 tetracosane molecules at 280 K, at the point of transition between crystal and the melt*

The change of densities with temperature, Table 7.7, are observed and plotted on Figure 7.26. The system exhibits a near linear increase in density upon cooling to 290

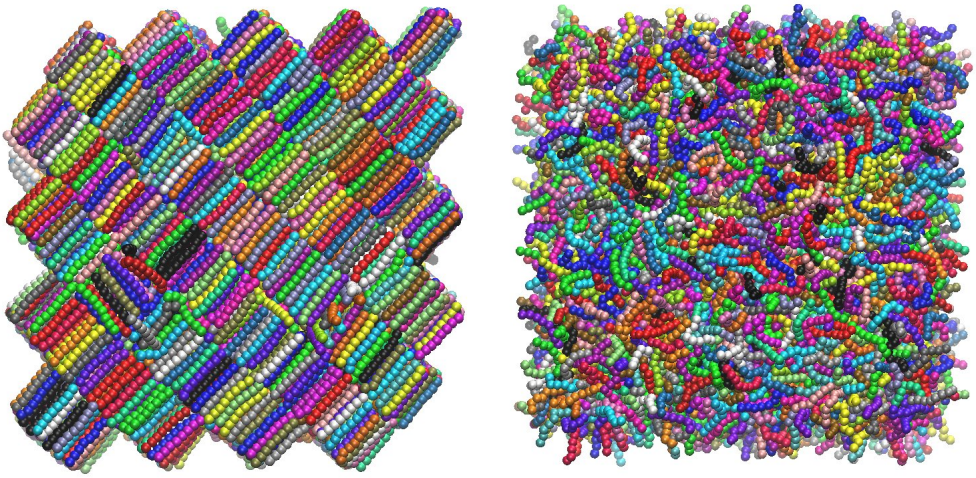

Figure 7.25: *System of 8000 tetracosane molecules in the crystal state at 250 K (left) and melt at 320 K (right)*

K, and then deviates from the trend between 290 K and 270 K, where reorganisation via a rotator phase is observed.

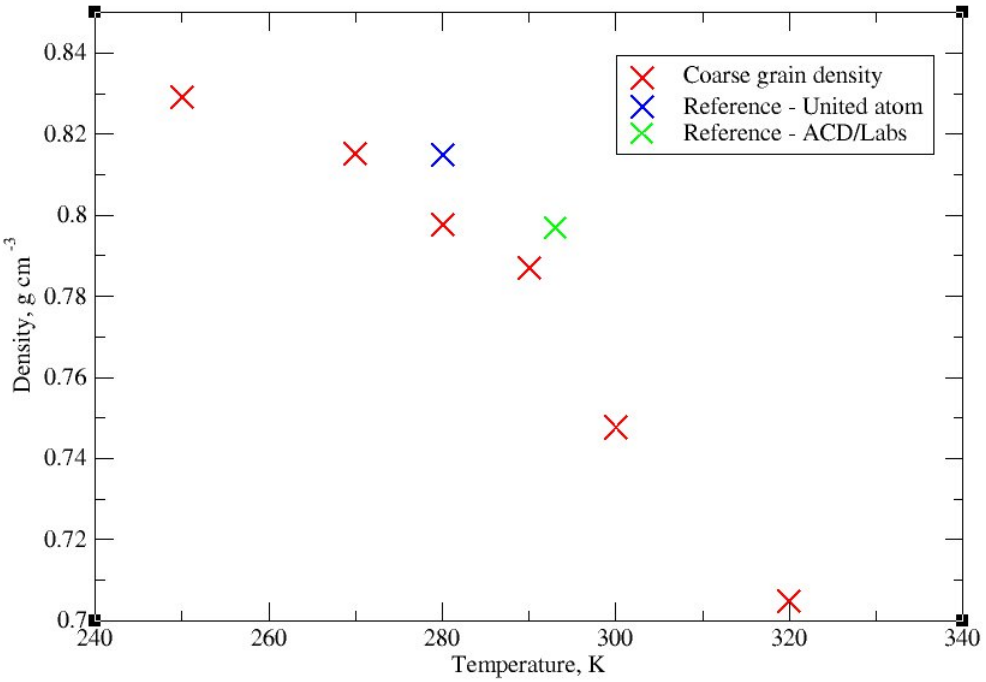

Figure 7.26: *Density of tetracosane over a range of temperatures, density from united atom simulations (blue) and ACD/Labs calculation (green) [45]*

Table 7.7: *Density of coarse grained tetracosane over the range of temperatures, reference united atom at 280 K and reference calculated by ACD-Labs at 293 K [45]*

Temperature, K	Density, g/cm^3
250	0.8292
270	0.8152
280	0.7977
290	0.7872
300	0.7470
320	0.70485
Reference:	
280	0.815 (UA)
293	0.797 [45]

Upon crystallisation the number of *trans* configurations increases, straightening the molecule. This phenomena is reflected in bond and angle distributions of the coarse grained model, Figure 7.27.

The angle distribution at 320 K has two peaks, allowing both *gauche* (less then 160^o degrees) and *trans* configurations. It gradually changes to only one peak, corresponding to fully extended configurations at 250 K. Thus, the bonded potentials are appearing to drive the crystallisation process.

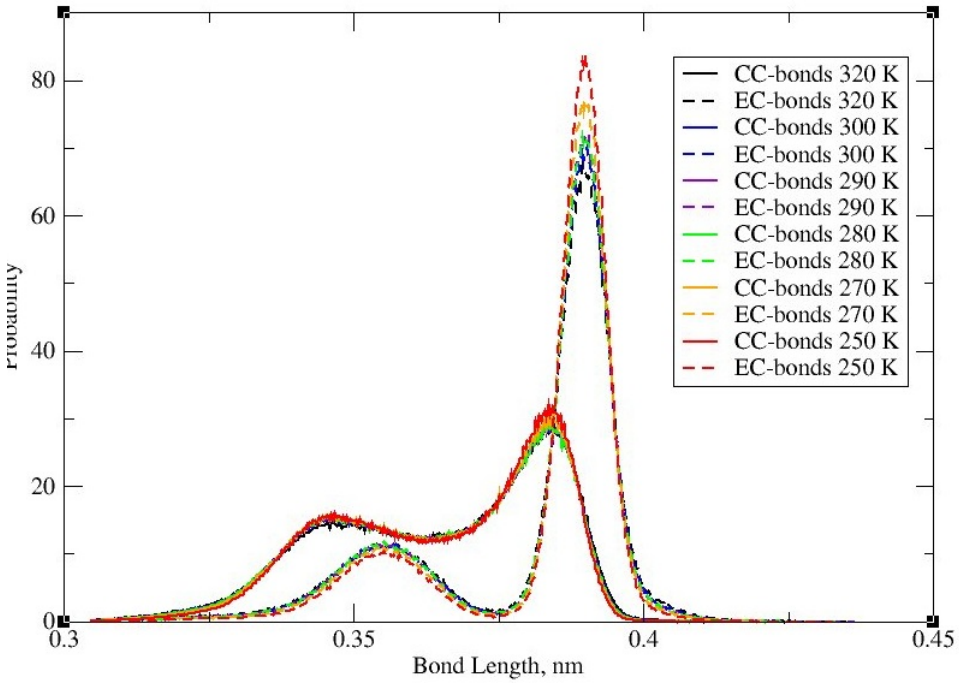

(a) Bond distribution

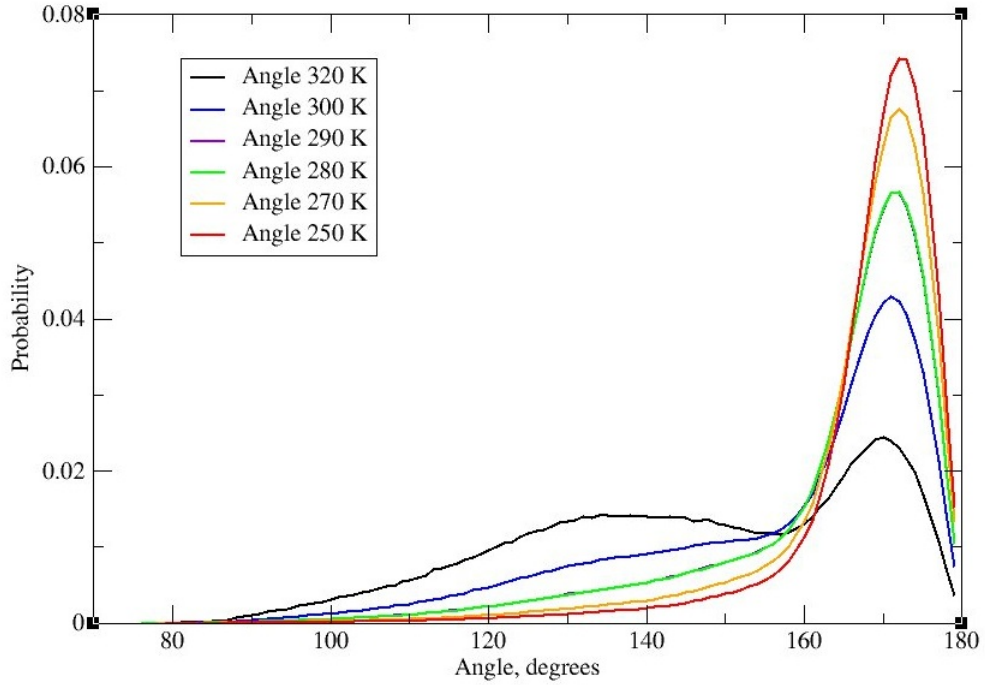

(b) Angle distribution

Figure 7.27: *Bond and angle distributions at a range of temperatures for the coarse grained model of tetracosane*

7.8 Lennard-Jones potentials for coarse grained non bonded interactions

It can be possible in coarse grained systems to use an analytical form for non bonded potentials [2, 4, 5, 14, 17]. The use of an analytical form can allow for easier handling of potentials and further extension of the force field. There is a number of analytical descriptions of non bonded interactions. The most commonly used one is the 12–6 Lennard-Jones potential [46]:

$$E^{LJ} = 4\epsilon \left[\left(\frac{\sigma}{r}\right)^{12} - \left(\frac{\sigma}{r}\right)^{6} \right] \tag{7.8}$$

where r is interatomic distance, ϵ is the depth of the well and σ is the distance where the potential is zero.

The 12–6 Lennard-Jones potential is historically chosen, as the most computationally efficient case of the Mie potential [47]:

$$E_{pair}(r) = \left(\frac{n}{n-m}\right)\left(\frac{n}{m}\right)^{m/(n-m)} \epsilon \left[\left(\frac{\sigma}{r}\right)^{n} - \left(\frac{\sigma}{r}\right)^{m} \right] \tag{7.9}$$

where n is a repulsive term and m is an attractive term.

In recent years n–6 potentials are becoming popular, as they have been shown to provide a better model for solid–liquid coexistence [48]. The value of n determines the hardness of the potential, $n = 12$ for a harder potential [49] and $n = 8$ for a softer one [50] :

$$E^{LJ} = \epsilon \left[2\left(\frac{r_m}{r}\right)^{9} - 3\left(\frac{r_m}{r}\right)^{6} \right] \tag{7.10}$$

$$E^{LJ} = \epsilon \left[3\left(\frac{r_m}{r}\right)^8 - 4\left(\frac{r_m}{r}\right)^6 \right] \tag{7.11}$$

where r_m is the distance of the potential minima.

The other variation is to preserve n=9, and reduce m to 3, as such creating a softer attraction. The 9-3 Lennard-Jones is frequently used to model an interaction between a continuous solid wall and a liquid [51]

$$E^{LJ} = \frac{3\sqrt{3}}{2}\epsilon \left[\left(\frac{\sigma}{r}\right)^9 - \left(\frac{\sigma}{r}\right)^3 \right] \tag{7.12}$$

It is possible to measure σ, ϵ and r_m from numerical potentials obtained in this work, Table 7.8.

Table 7.8: *Measured σ, ϵ and r_m from numerical non bonded potentials*

Interaction	σ, nm	ϵ, kJ/mol	r_m, nm
C-C	0.4686	0.92655	0.5494
E-E	0.48345	1.6810	0.5894
E-C	0.4813	1.0410	0.5720

The numerical non bonded coarse grained potentials, derived above were fitted with the four analytical potentials 12–6, 9–6, 8–6 and 9–3 (eqv. 7.8, 7.10, 7.11, 7.12), their fit is shown in Figure 7.28.

By inspecting the potentials in Figure 7.28, it can be seen that the repulsive part of 12–6 Lennard-Jones (magenta line) is too steep. This results in a shift of the well to a shorter distance. Both 9–6 and 8–6 Lennard-Jones (red and green lines respectively) provide a good representation of the potential well, but do not match the position of σ.

The numerical potential does not follow a shape of a typical Lennard-Jones, even presenting an additional local minimum. This is due to a higher order in the system,

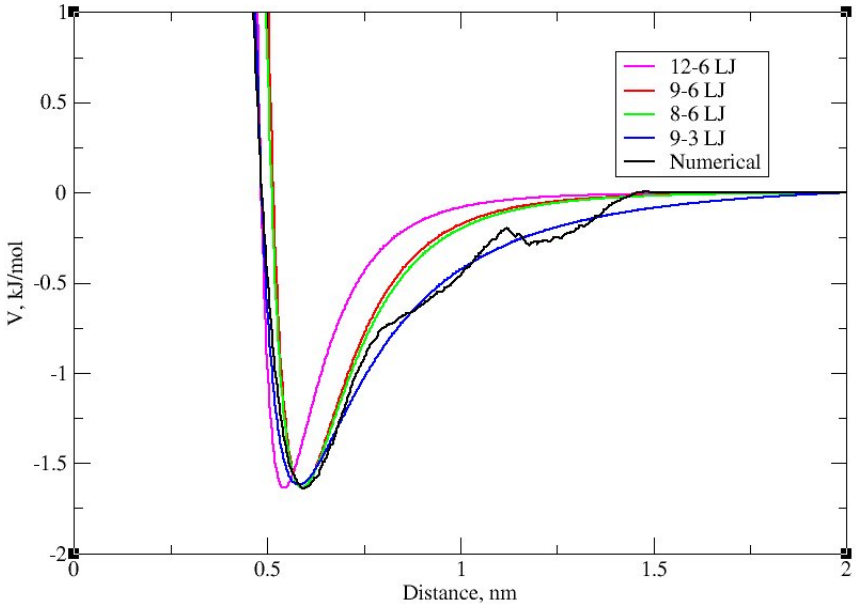

(a) Non bonded potential for E-E interaction: numerical (black) and analytical fit.

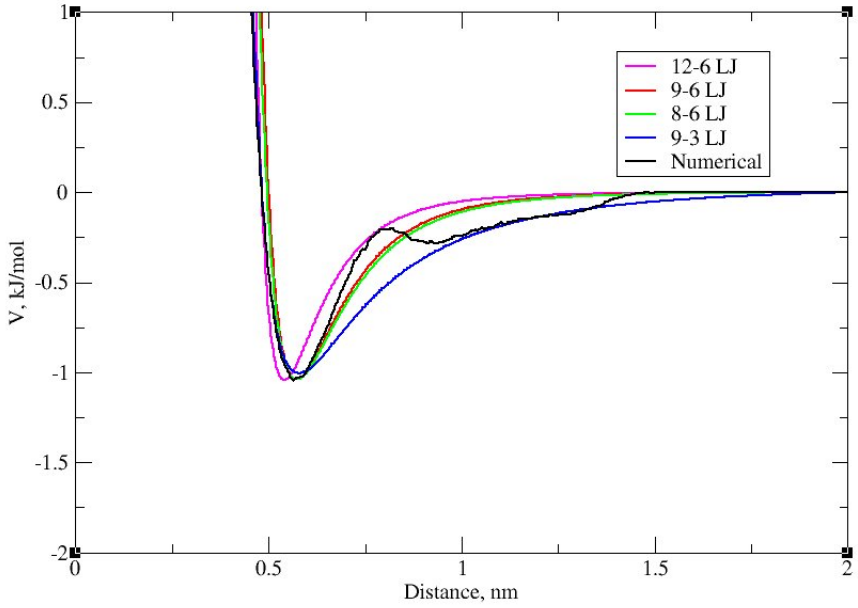

(b) Non bonded potential for E-C interaction: numerical (black) and analytical fit.

Figure 7.28: *Non bonded potentials for E-E (a), E-C (b) and C-C (c) interactions [Continued]*

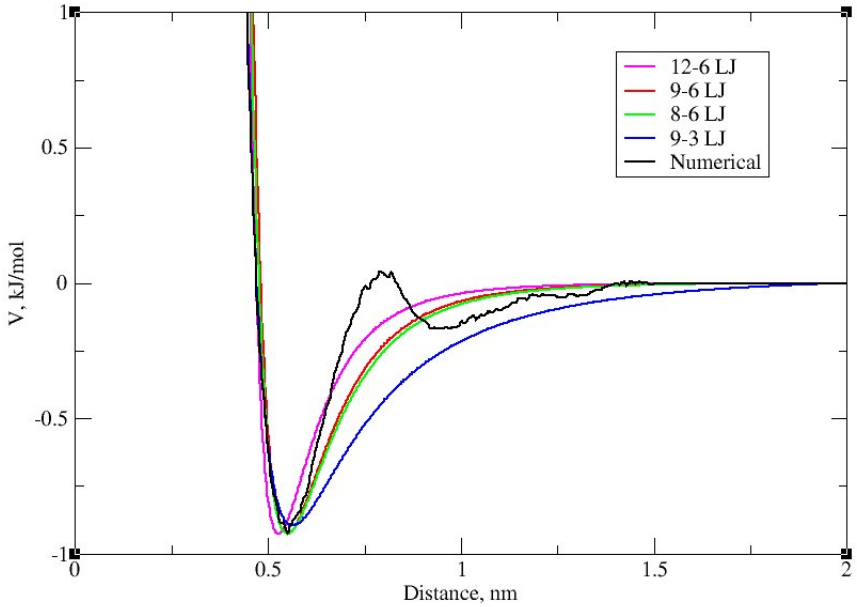

(c) Non bonded potential for C-C interaction: numerical (black) and analytical fit.

Figure 7.28: *[Continued] Non bonded potentials for E-E (a), E-C (b) and C-C (c) interactions*

as coarse graining is carried out at the crystal-liquid transition. The well is likely to be formed as a result of an area with no occupancy surrounding the first solvation shell, creating an artificial maxima on the potential. The interaction of a coarse grained beads is softer with respect to an all-atom model, as it averages over three atoms moving with respect to each other. The 9–3 model represents the potential better at longer range and matches the position of σ, unlike the 9–6 and 8–6 models. Using a softer, 9–3 Lennard -Jones potential, imposes a longer range cut off (2 nm instead of 1.5 nm) as such making calculations longer.

Combing σ, ϵ and r_m of E-E and C-C interactions it is possible to create a new representation of the E-C one. This mixing can be performed in number of ways, the most common ones discussed in Chapter 3.1.5.

By computing σ, ϵ and r_m of the E-C numerical potential, it is possible to evaluate the most suitable set of mixing rules. The calculated parameters with different mixing rules are given in Table 7.9.

Table 7.9: *Comparison of σ,ϵ and r_m obtained from the numerical potentials and calculated by the combination rules for the E-C non bonded potential*

Parameter	Numerical	Equation	Value
σ, nm	0.4813	3.10	0.4760 *
		3.12	0.47595
r_m, nm	0.5720	3.10	0.5694 *
		3.12	0.5691
ϵ, kJ/mol	1.0410	3.11	1.2480
		3.13	1.1946 *

From Table 7.9 it can be seen that all of the combination rules lead to a good result for σ, while slightly overestimating ϵ. The analytical potentials using the parameters calculated with mixing rules (marked with *) are given in Figure 7.29. The potentials have a deeper well with respect to Figure 7.28 (b), this is due to the overestimation of ϵ by combination rules. The overall shape of the potentials is preserved.

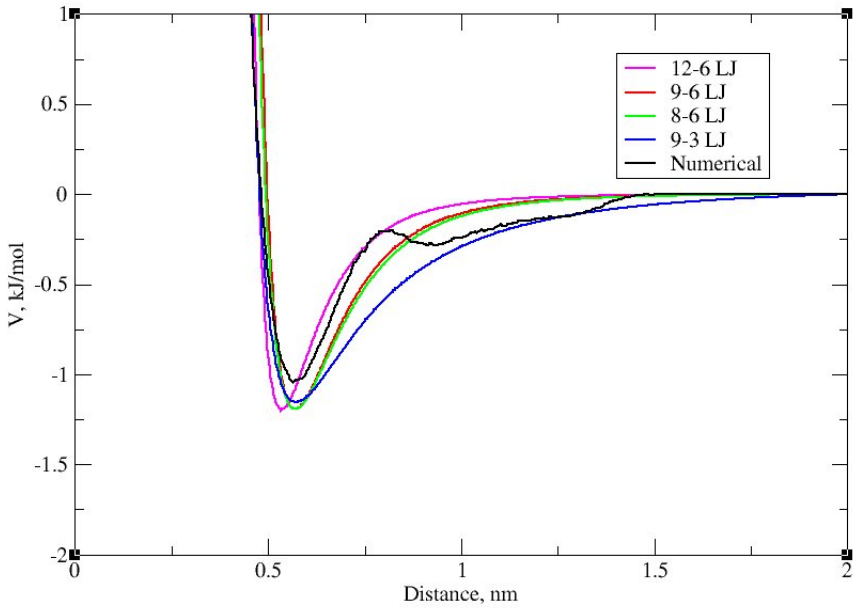

Figure 7.29: *Non bonded potential for E-C interaction: numerical (black) and analytical fit using parameters obtained by combination rule*

A dodecane system was simulated with five sets of potentials. We used 12–6, 9–6, 8–6 and 9–3 Lennard-Jones fitted by numerical values, as well as 9–3 potential with

E-C parameters generated by mixing rules from eqv. 3.10. In this work we focus on representing correctly the crystallisation temperature and density, for this reason the simulation is performed at 250 K, i.e. dodecane crystallisation point. Simulation parameters are given in Table 7.10.

Table 7.10: *Parameters for coarse grained calculation of dodecane with different analytical potentials*

Calculation parameters:	
System size	1000 molecules
Step size	4 fs
Length of calculation	8 ns each
Integration	Leap frog
Periodic boundary	xyz
Ensemble	*NPT*
Temperature	250 K
Thermostat	Velocity rescale
Pressure	1 bar
Barostat	Berendsen
Compressibility	9×10^{-5} bar^{-1}

The densities obtained in simulations using 12–6, 9–6 and 8–6 Lennard-Jones potentials are all around 0.52 g/cm^3. This value is very low compared to the density in the atomistic system (0.752 g/cm^3) and that obtained with the numerical potential (0.754 g/cm^3). The density of the system modelled with the 9–3 potential is 0.702 g/cm^3 and the model using E-C interaction from combined potentials is 0.718 g/cm^3.

Figure 7.30 compares the RDF of the four systems with the united-atom RDF, used to fit a numerical potential. Only the 9–3 potential for E–C interaction fitted by mixing rule is shown.

Figure 7.30 shows that only the 9–3 potential has the correct position of the first RDF peak, while all n–6 potentials are shifted further away. The position of the second peak is not as well modelled, even by the 9–3 interaction. This suggests that the presence of the second minima on the potentials is needed to create the necessary order in the system at transition temperature.

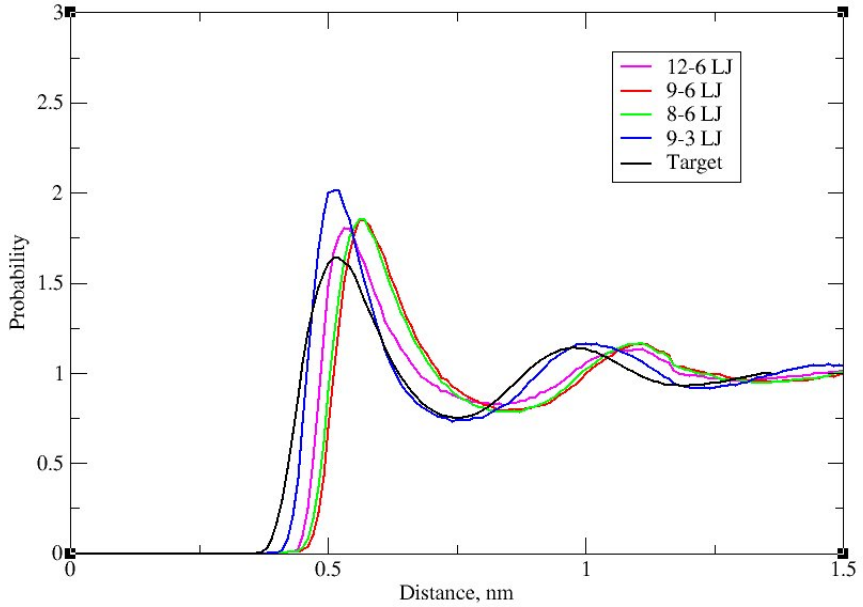

(a) Radial distribution function for E-E interaction

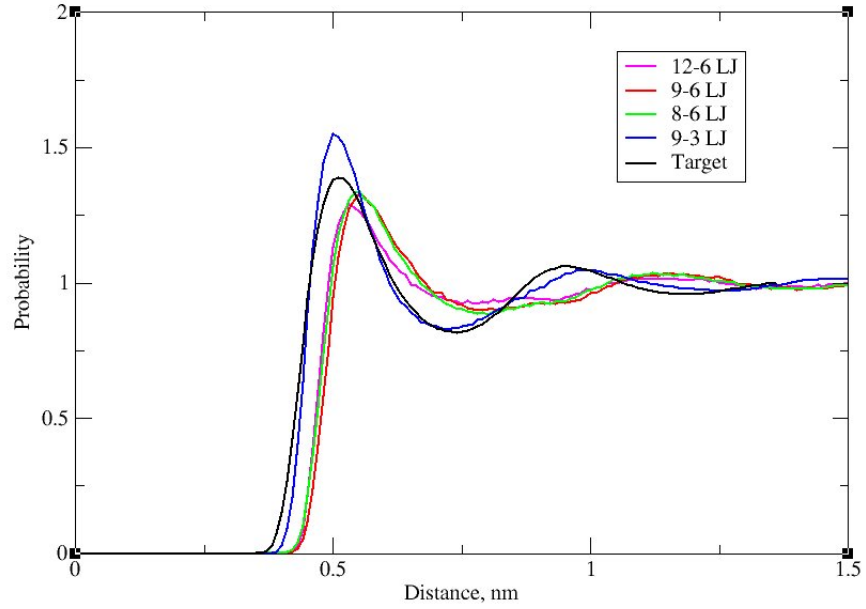

(b) Radial distribution function for E-C interaction

Figure 7.30: *Comparison of radial distribution functions from simulations with analytical non bonded potentials to the target (black) one [Continued]*

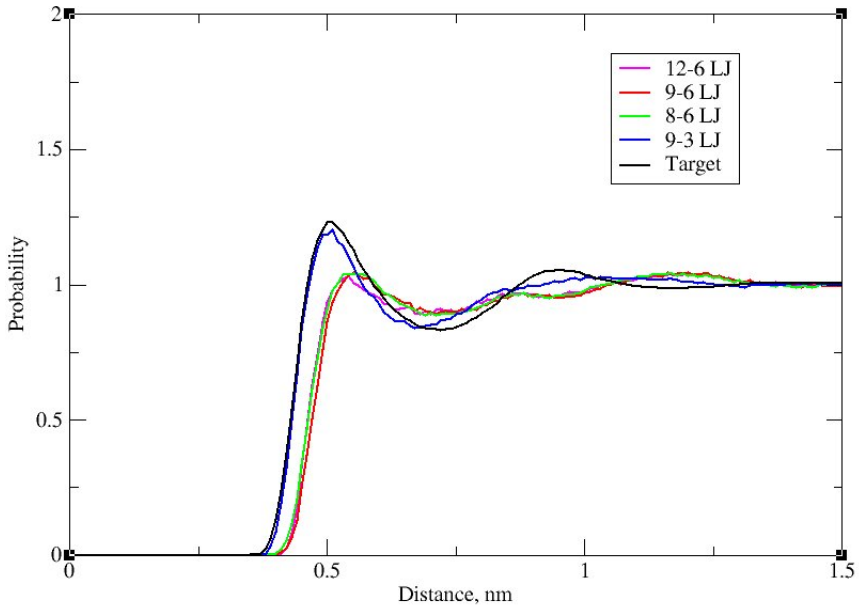

(c) Radial distribution function for C-C interaction

Figure 7.30: *[Continued] Comparison of radial distribution functions from simulations with analytical non bonded potentials to the target (black) one.*

The positions of the RDF obtained from the n–6 Lennard-Jones potentials resemble the trend for cubic packing: a, $\sqrt{2}a$, $2a$. For C-C interactions these are 0.56 nm, 0.85 nm and 1.15 nm. While the RDF from the 9–3 Lennard-Jones shows a trend towards hexagonal packing with a pattern: a, $\sqrt{3}a$, $2a$, corresponding to 0.50 nm, 0.84 nm and 1.01 nm for the C-C interaction. The hexagonal-like arrangements have been earlier observed in the united-atom studies of alkanes and so are desirable for the coarse grained model.

Even though the 9–3 Lennard-Jones produces an hexagonal-like packing, it fails to account for the long-range structure, essential for modelling the phase transition. To be able to fit the potential to the analytical form, more complicated expressions should be derived. This would however lead to an increase of computational cost and as such loose the original advantage. Similar observations were obtained by Reith *et al.* in the original paper on iterative Boltzmann inversion method [32], where the final potential also had multiple wells.

7.9 Binary alkane system

Our coarse grained model is used to simulate a binary mixture of 3000 tetracosane and 6000 dodecane molecules. The model is build and allowed to mix at 320 K for 4 ns. The system is then gradually cooled to 250 K by stepwise annealing, the parameters for calculation are given in Table 7.11.

Table 7.11: *Parameters for coarse grained calculation of dodecane and tetracosane binary mix over a range of temperatures*

Calculation parameters:	
System size	3000 tetracosane 6000 dodecane
Step size	4 fs
Length of calculation	4 ns 4 ns + 8 ns + 24 ns + 8 ns
Integration	Leap frog
Periodic boundary	xyz
Ensemble	*NPT*
Temperature	320 K 280 K, 270 K, 260 K, 250 K
Thermostat	Velocity rescale
Pressure	1 bar
Barostat	Berendsen
Compressibility	9×10^{-5} bar^{-1}

A linear increase in density is observed upon cooling, Figure 7.31. Crystal formation starts at 270 K, a further temperature reduction encourages steady crystal growth. During the formation of the tetracosane crystal dodecane solvent is displaced. This phenomena is highlighted by a change in the partial density of the components across the box, Figure 7.32. The phase separation between tetracosane and dodecane begins at 270 K (dashed line), where a decrease in the density of one component is accompanied by an increase of the other. This difference becomes greater as the temperature reaches 250 K.

A vectorial correlation analysis, described in section 4 has been performed on the formed crystal. Due to the differences in the sites of coarse grained model and united atom, these vector distributions cannot be directly compared. However the analysis

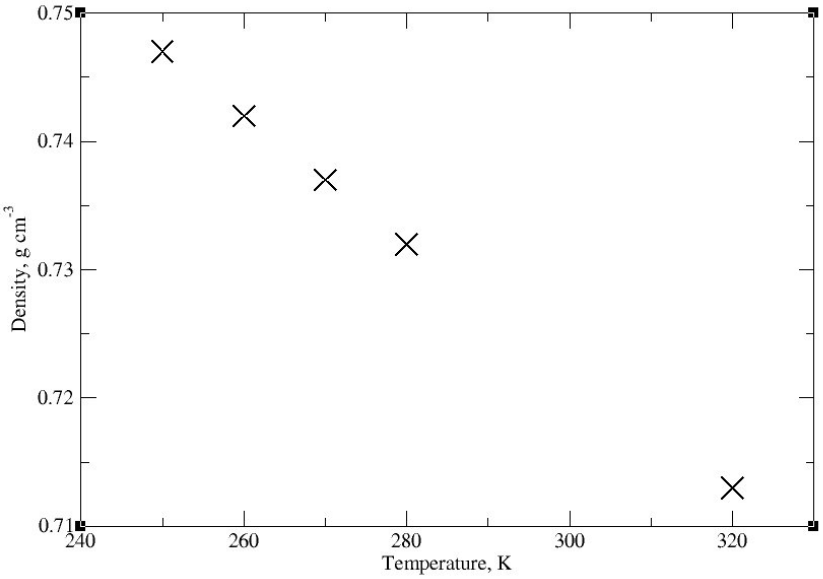

Figure 7.31: *Change of the density in the binary mixture of tetracosane and dodecane upon cooling from 320 K to 250 K*

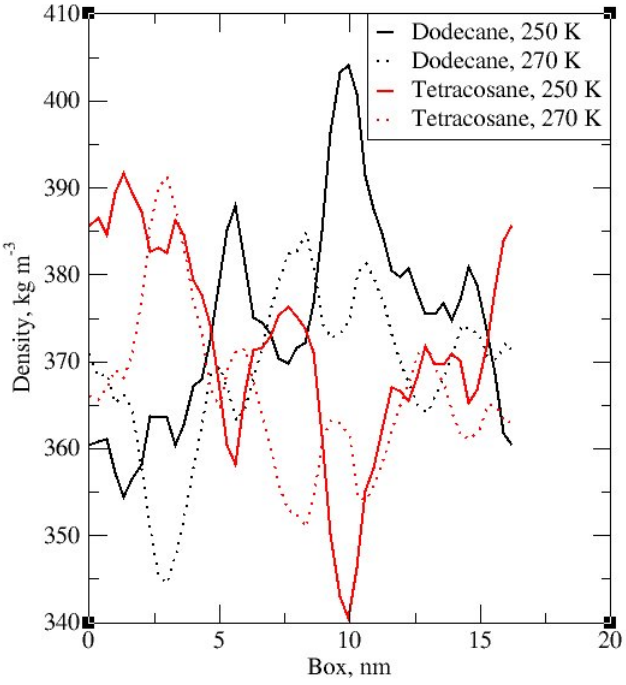

Figure 7.32: *Change of the partial density across the simulation box in the mixture of tetracosane (red) and dodecane (black) at 270 K (dotted line) and 250 K (solid line)*

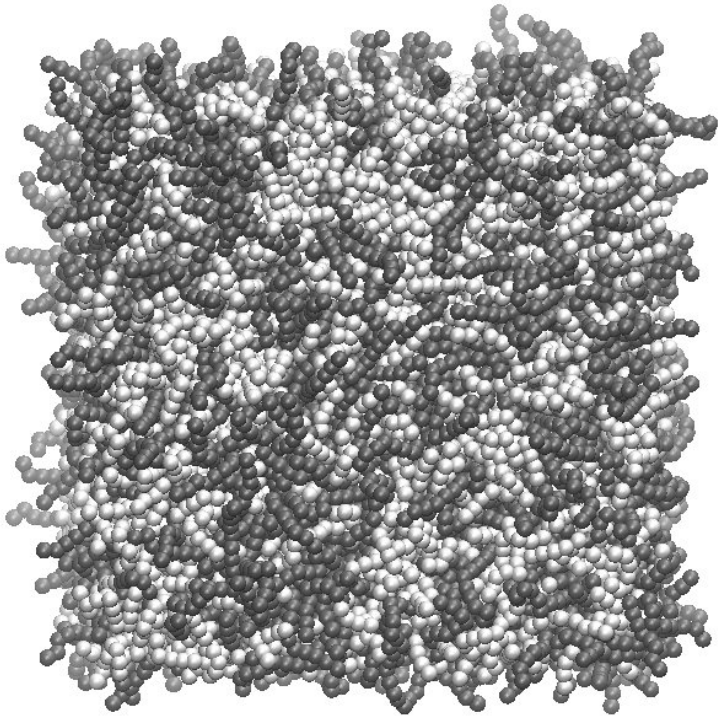

(a) Binary mixture at 280 K

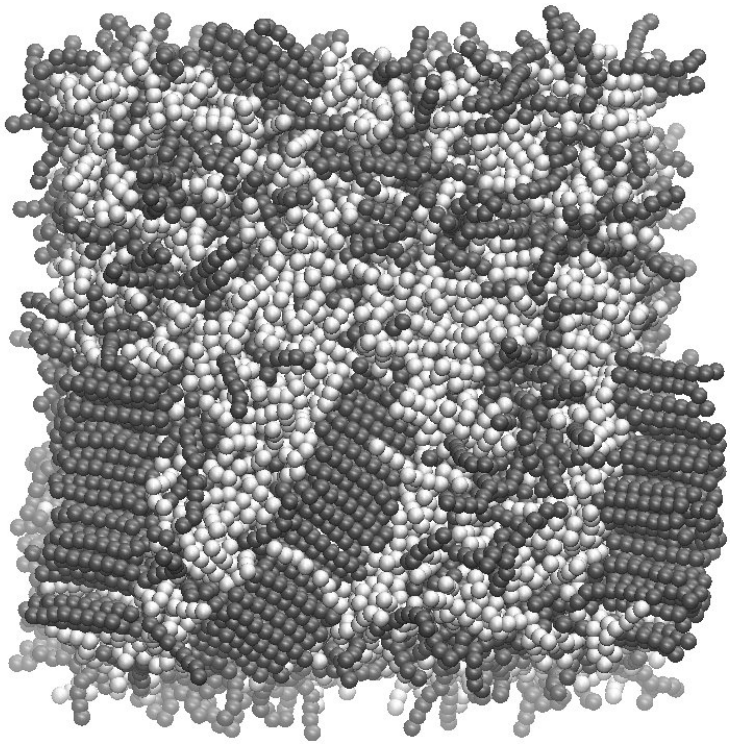

(b) Binary mixture at 250 K

Figure 7.33: *Snapshot of dodecane (white) and tetracosane (grey) binary mixture at 280 K and 250 K*

provides a useful measure of the ordering of molecules in the system.

Figure 7.34 shows the vector distribution, describing the molecular orientation of teracosane molecules at 280 K (a) and 250 K (b). At 280 K the graph has a uniform shape, corresponding to randomly oriented vectors. At 250 K (b) there are four narrow peaks in the probability due to a high alignment of the molecules in crystal stacks. Vectorial analysis was also performed on the dodecane molecules, showing a uniform vector orientation distributions at both temperatures.

The binary system of dodecane and tetracosane is able to represent well the relationship between pressure and temperature, as well as crystal formation and growth. Consistently with experimental studies [52], the crystal is homogeneous. Remarkably, the shorter time scales and smaller system size accessible by atomistic calculations, did not allow this phenomenon to be observed in our united atom models (Section 4).

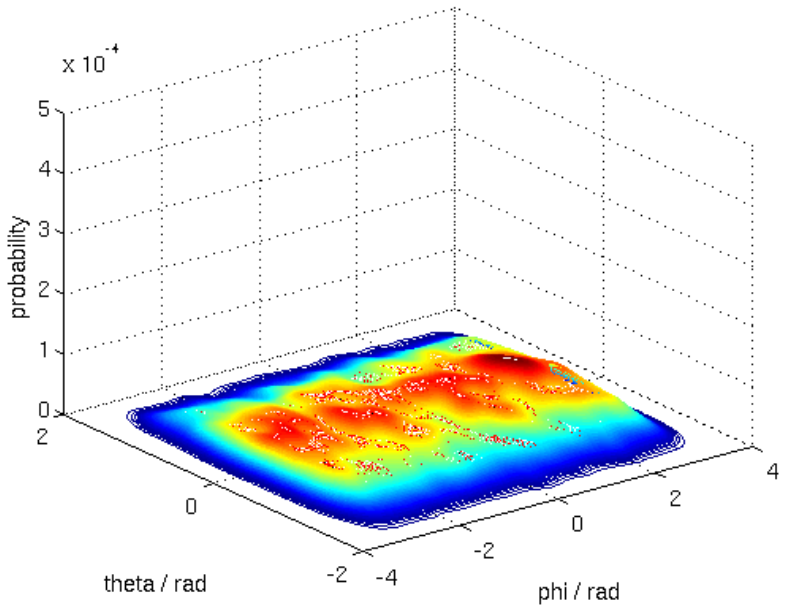

(a) Tetracosane at 280 K

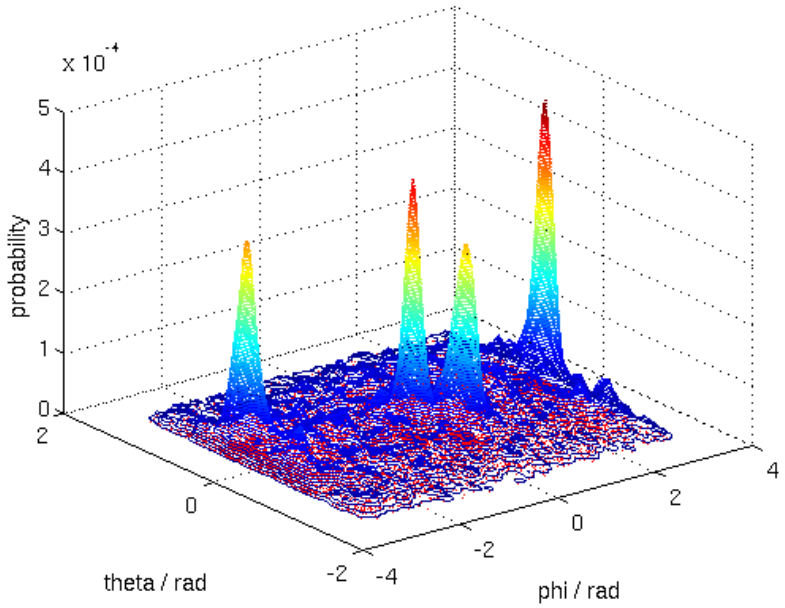

(b) Tetracosane at 250 K

Figure 7.34: *Vector orientation distribution of tetracosane molecules at 280 K and 250 K*

7.10 Comparison with a similar model and discussion

The coarse grained model developed in this chapter shows good transferability over both, alkane chain lengths and temperatures. It provides good representation of the transition from melt to crystal, describing well both structure and density of the system. To date there is only one coarse grained model of alkanes showing good temperature transferability [26]. It was developed to fit vapour-liquid co-existence, rather than the melt to crystal transition.

The coarse grained bead model, developed by Maerzke and Siepmann [26], like our model unites three carbon atoms. In that model all interactions are represented as distances between beads. The model, developed in this work, represents only bond and non bonded potentials as distances, while angles are given in degrees. Figure 7.35 shows the comparison between two coarse grained models for bond distances and non bonded potentials. Due to the differently defined angle in these studies, it is not possible to directly compare them. Figure 7.36 shows the shapes of the potentials on the same energy scale.

The bond potentials, dashed line in Figure 7.35, developed by Maerzke and Siepmann, have wider and lower minima at shorter distance, by such allowing a higher probability and amount and variation of *gauche* conformations. Through the development of the current model, it was noted that the exact shape of the bond potential can vary. The boundaries of the variation are shown in Figure 7.37. Importantly, if the bond potentials are changed, non bonded potentials should undergo refining and pressure correction to accommodate the changes in bond potential.

The non bonded potentials by Maerzke *et al.*, dashed lines on Figure 7.35(b), are 12–6 Lennard-Jones type. The attractive part was chosen to be set to 6, due to the previous tests by authors, that have proven term $1/r^6$ is best for representing the liquid-vapour transition within their united atom model [20]. In their study, numerous n–6 potentials were tested, showing the best match of thermodynamic properties with $n = 12$ and 11, while better structural agreement was found using $n \leq 9$. The main priority of Maerzke *et al.* was to fit the thermodynamic properties and this was achieved with higher n by sacrificing the quality of the RDF.

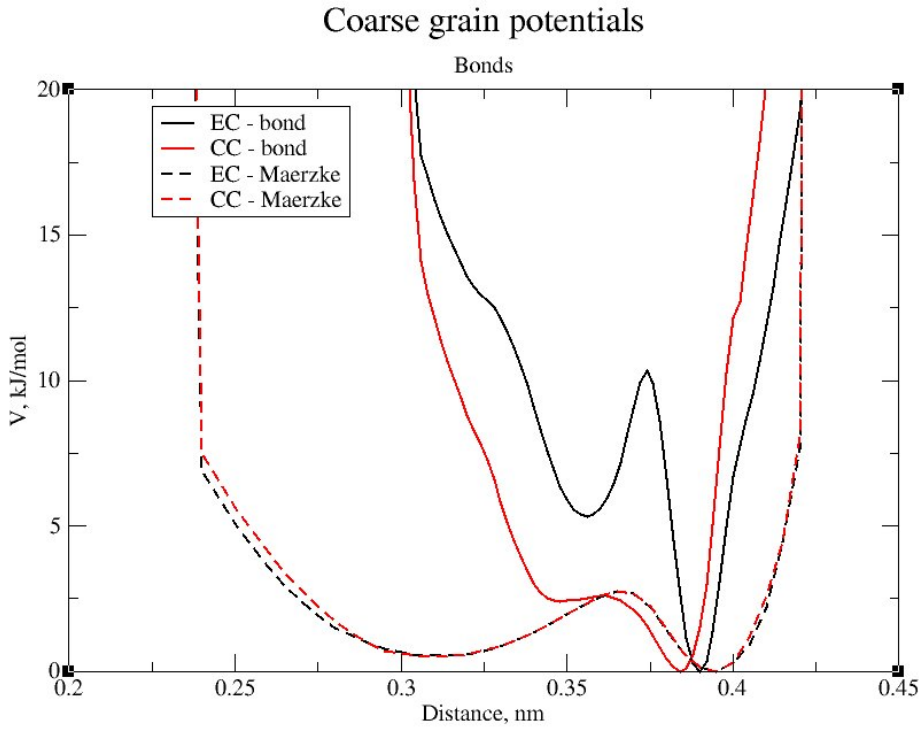

(a) Bond length potentials

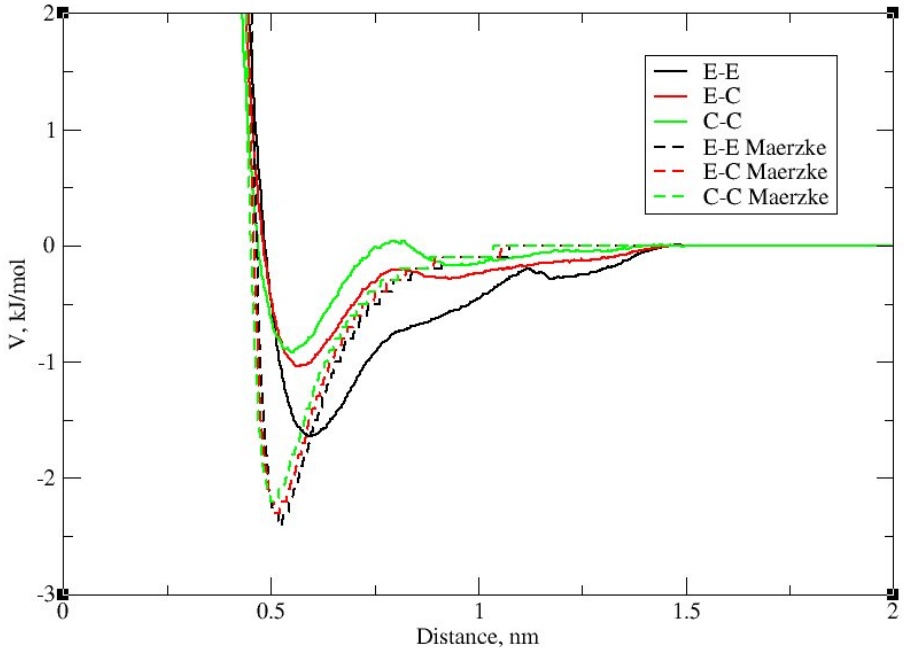

(b) Non bonded potentials

Figure 7.35: *Comparison of coarse grained potentials for this work and study by Maerzke and Siepmann [26]*

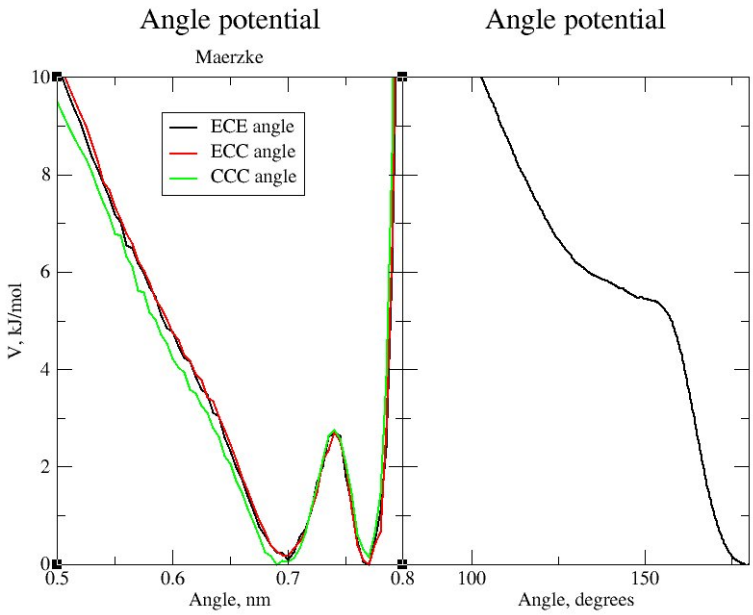

Figure 7.36: *Comparison of coarse grained angle potentials for this work and study by Maerzke and Siepmann [26]. The potentials cannot be compared directly, in work by Maerzke et al. the angle is given as a bond between 1-3 atoms, while in this work angles are in degrees*

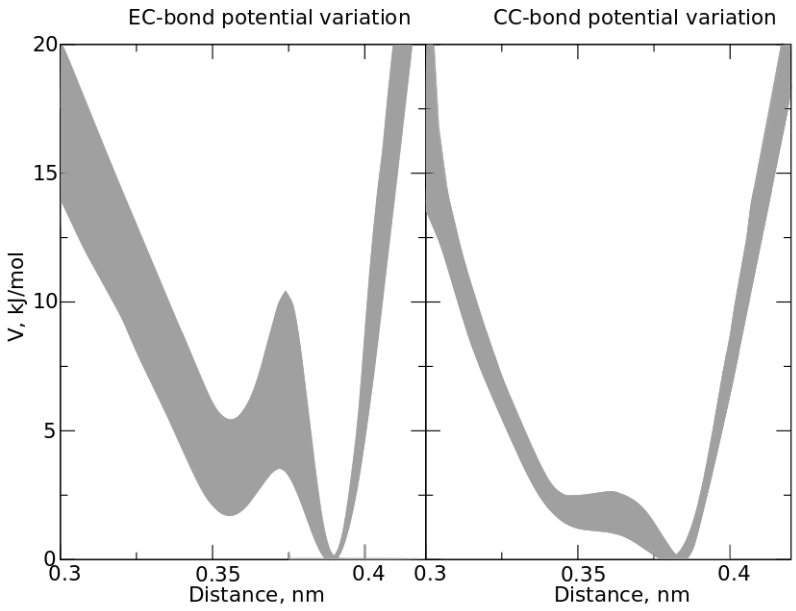

Figure 7.37: *Shaded area shows acceptable variation in the coarse grained bond potential*

In this work it was shown to be possible to fit potentials to a 9–3 Lennard-Jones, but that decreased the accuracy of prediction of both thermodynamic and structural properties. The numerical potentials have a second well at 0.8 - 0.9 nm, followed by a smaller third well. The presence of these wells is important in representing correctly the order in the system at the liquid-solid transition.

The correct representation of the crystal structure is achieved by making the potential for the non bonded E-E interaction (black line on Figure 7.35(b)) the deepest. This favours the end-to-end interaction over end-to-centre (E-C) interaction, red line on Figure 7.35(b). Three Lennard-Jones potentials by Maerzke *et al.* also show such a trend, but the differences in potential well depths are much smaller.

Similarly to the bond potentials, angle potentials by Maerzke *et al.* have a double well, Figure 7.36. This will lead to both *gauche* and *trans* conformations in near equal amounts. The angle potential in this work has a single minima at 180^o and a shoulder at 120^o-150^o, that permits the appearance of a small number of *gauche* conformations. The angle potential was shown to play an important role in the crystallisation process, driving the straightening of the molecule with the decrease of temperature.

The coarse grained force field by Maerzke *et al.* was parametrised over the liquid–vapour co-existence curve, like the TraPPE united atom force field by the same group [20]. In the case of the united atom, the model was able to represent the crystallisation process sufficiently well and was therefore used in our earlier study, and is the base of our coarse grained model. The force field by Maerzke *et al.* have been shown to represent the system well over 100 K range around the vaporisation point, but, there were no tests performed to access its transferability to lower temperatures. For this reason it is interesting to test their model for a liquid to crystal transition of tetracosane.

The system of 8000 teracosane molecules was modelled at 300 K, 280 K and 260 K. Parameters are given in the Table 7.12. It was found to be necessary to use the *NVT* ensemble to equilibrate the system at every new temperature, before allowing the volume to change. Even after equilibration, a 2 fs step had to be used.

Table 7.12: *Parameters for calculation of tetracosane with the TraPPE coarse grained [26] model over a range of temperatures*

Calculation parameters:	
System size	8000 molecules
Step size	2 fs
Length of calculation	5 ns each
Integration	Leap frog
Periodic boundary	xyz
Ensemble	*NVT* and *NPT*
Temperature	300 K, 280 K, 260 K
Thermostat	Velocity rescale
Pressure	1 bar
Barostat	Berendsen
Compressibility	9×10^{-5} bar^{-1}

The model was found to represent densities exceptionally well, as it was parametrised to fit thermodynamic properties. However, below the crystallisation point the alkane chains remained randomly curled, rather then extended. The RDF was also poorly represented. This is to be expected for this model, as it was not parametrised to fit structural properties that are essential for correct crystallisation.

Typically the step size limit is imposed by bonds, as the bonded potential is the steepest of all. In the model by Maerzke *et al.* all three sets of potentials are of a comparable steepness. It is possible that such a short step is due to the use of 12–6 Lennard-Jones. The 12–6 expression was originally developed for atoms and hard sphere models and as the consequence has stronger repulsion term (m=12) and has a shorter range attraction (n=6) than necessary for softer and larger coarse grained particles.

Both, the coarse grained model developed in this work and the model by Maerzke *et al.* are based on the united atom TraPPE force field and uses a 3:1 mapping. However the models are aimed at a different temperature range and are parametrised to fit different properties. In the parametrisation by Maerzke *et al.* a higher weight was given for matching thermodynamic properties and an excellent agreement was obtained. In our work the structure of the system was as important as the transition temperature and density, this results in a model that produces good crystallisation,

while underestimating the temperature and density by less than 5%.

7.11 Extension to the model: united atom - coarse grained interaction

An extension to the current coarse grained force field, to allow interaction between coarse grained beads and a terminal united atom CH_3 has also been developed. This provides potentials to allow a wider range of hydrocarbons to be studied. For this purpose a high resolution calculation of tricosane was used. Tricosane is a long molecule and so would not be ideal if the system had to be parametrised from scratch. However, since high resolution calculations have already been performed through earlier atomistic studies and coarse grained parameters for central beads have already been developed in the previous section, tricosane provides a convenient system to carry out further development work.

Bonded interactions were calculated, following the procedure, described in the section 7.3.1. The bonded potentials for interactions between united atom (*UA*) and coarse grained bead (*C*), as well as relevant coarse grained potentials obtained from earlier work are shown in Figure 7.38.

The bond between a single united atom and a coarse grained bead is shorter than between two coarse grained beads. The minimum of the angle potential between coarse grained beads is at 180^o, while in the presence of a united atom angle is at 165^o. This is intermediate between two types of angle – linear for coarse grained beads and 109^o for *sp3* united atoms.

The united atom *UA*-*UA* interaction is represented as a 12–6 Lennard-Jones potential with σ and ϵ from the original TraPPE force field [20]. Two approaches were tested for the interaction between the united atom and the coarse grained bead, *C*-*UA*. In the first approach, a 9–6 Lennard-Jones potential was used with σ=0.4218 nm and ϵ = 0.868 kJ mol^{-1}, calculated by Lorentz-Berthelot mixing rules, eqv. 3.10 and 3.11. In the second approach, a potential for the *C*-*UA* interaction was obtained iteratively with a pressure correction applied. The resulting non bonded potentials for tricosane are

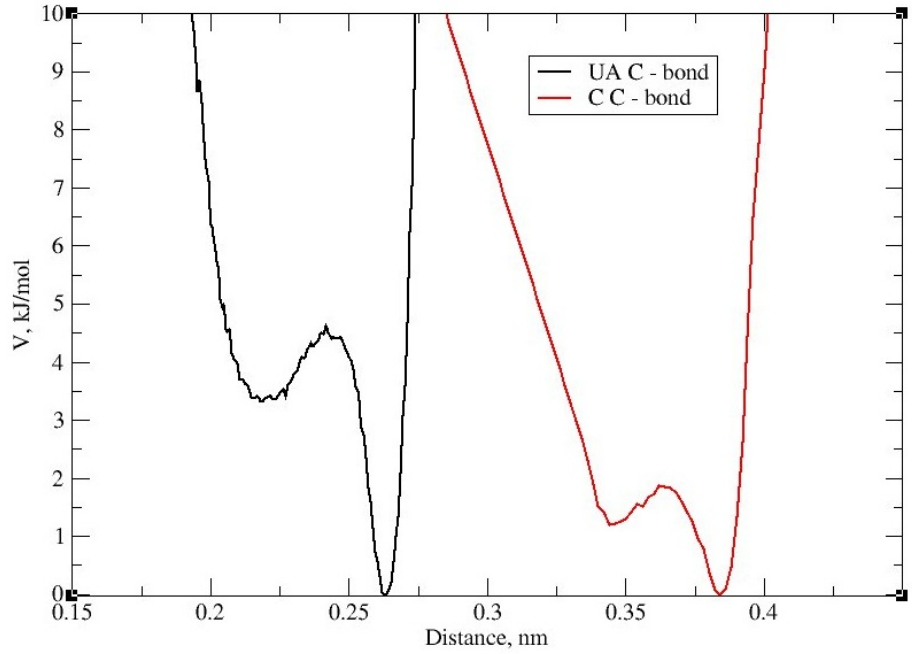

(a) Bond potential

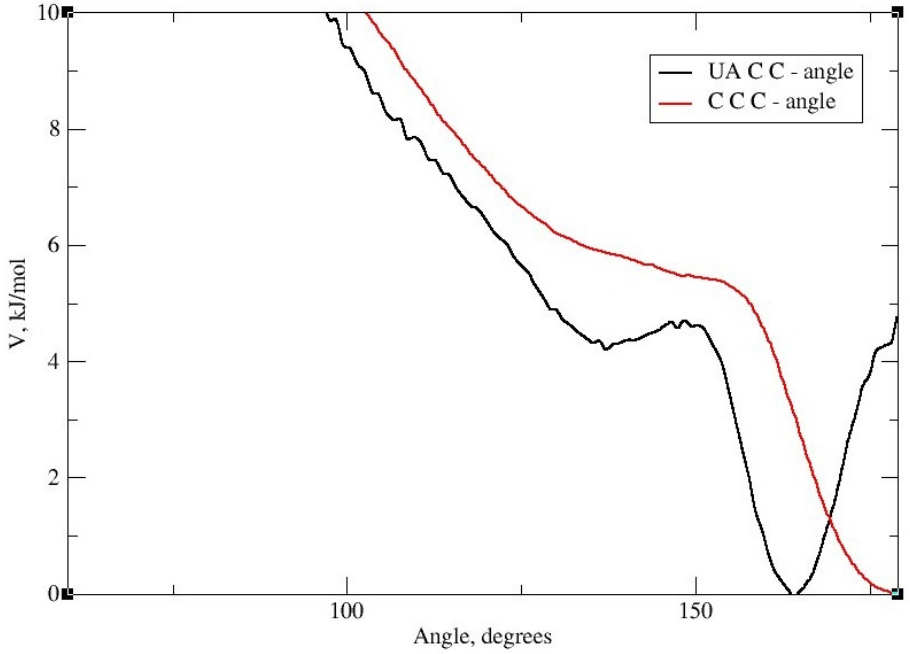

(b) Angle potential

Figure 7.38: *Bonded potentials describing interactions for a terminal united atom (UA) and a coarse grained bead (C)*

shown in Figure 7.39. It can be seen that the potential obtained iteratively (dashed line) has a smaller well depth than the 9–6 Lennard-Jones (solid black line) and has a second prominent well at a longer range.

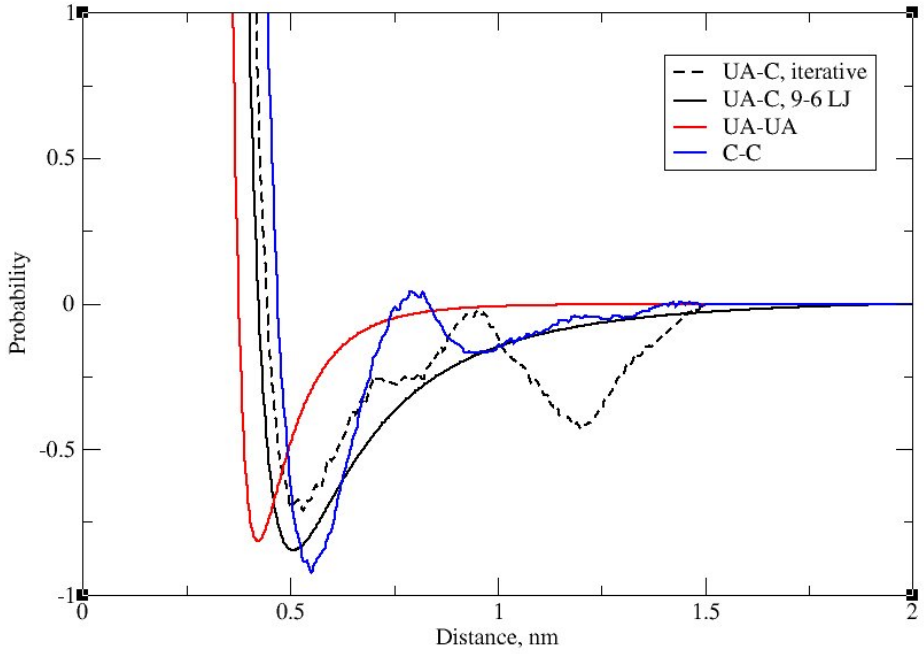

Figure 7.39: *Iteratively derived non bonded potentials (dashed line) and 9–6 Lennard-Jones non bonded potentials (solid line) for tricosane*

The performance of the two potentials have been accessed by simulations at temperatures around the crystallisation point, parameters are given in the table 7.13.

The system, using the 9–6 Lennard-Jones shows a poor packing, Figure 7.40(a). By the position of the terminal united atoms (yellow beads) it is possible to see that no lamellar arrangements are present. This is due to an overestimation of the attraction between *UA* and *C* beads by mixing rules, making the it more favourable than *UA-UA*. A similar packing was obtained by an iteratively derived potential, that had a first minima lower than the *UA-UA* well. All iteratively derived potentials had a second minima, that imposed higher order on the system and as a consequence a better packing and density.

Table 7.13: *Parameters for coarse grained calculations of tricosane over a range of temperatures*

Calculation parameters:	
System size	8000 molecules
Step size	4 fs
Length of calculation	4 ns
Integration	Leap frog
Periodic boundary	xyz
Ensemble	*NPT*
Temperature	250 K, 270 K, 320 K
Thermostat	Velocity rescale
Pressure	1 bar
Barostat	Berendsen
Compressibility	9×10^{-5} bar^{-1}

The best iteratively fitted potential is shown in Figure 7.39 (dashed black line). The well depth of the *UA-C* interaction is slightly smaller than *UA-UA* and *C-C*. This prioritises the interactions between similar type of beads over the heterogeneous ones, leading to lamellare arrangements in the crystal, Figure 7.40 (b). The shoulder at 0.7 nm and the second well at 1.2 nm create a long-range order, necessary for structuring the forming crystal.

The tricosane crystal, Figure 7.40 is not as well-structured, as tetracosane, Figure 7.25. Nevertheless, the system preserves the trend in density change, Figure 7.41. The density is lower than desired, which can be the result of a slight bend in the chain imposed by the terminal UA-C-C angle, that has a minima at 165^o. The difference in densities is still acceptable and preserves the crystallisation temperature at approximately 275 K. The agreement in the trend of crystallisation temperatures for the range of alkanes is essential for crystallisation studies of mixtures to be performed.

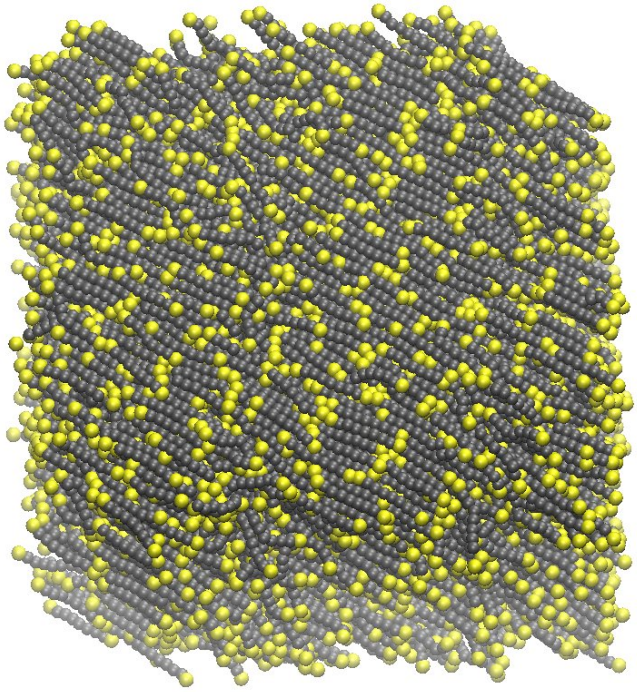

(a) Lennard-Jones potential for UA-C

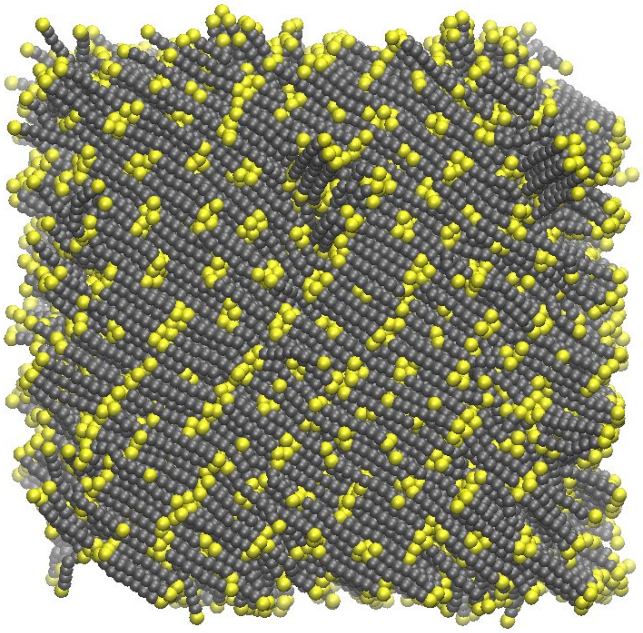

(b) Numerical potential for UA-C

Figure 7.40: *Tricosane system at 250 K, UA-C interaction modelled with Lennard-Jones (a) and numerical non bonded potential (b). The coarse grained beads are shown in grey, united atom terminal carbons in yellow*

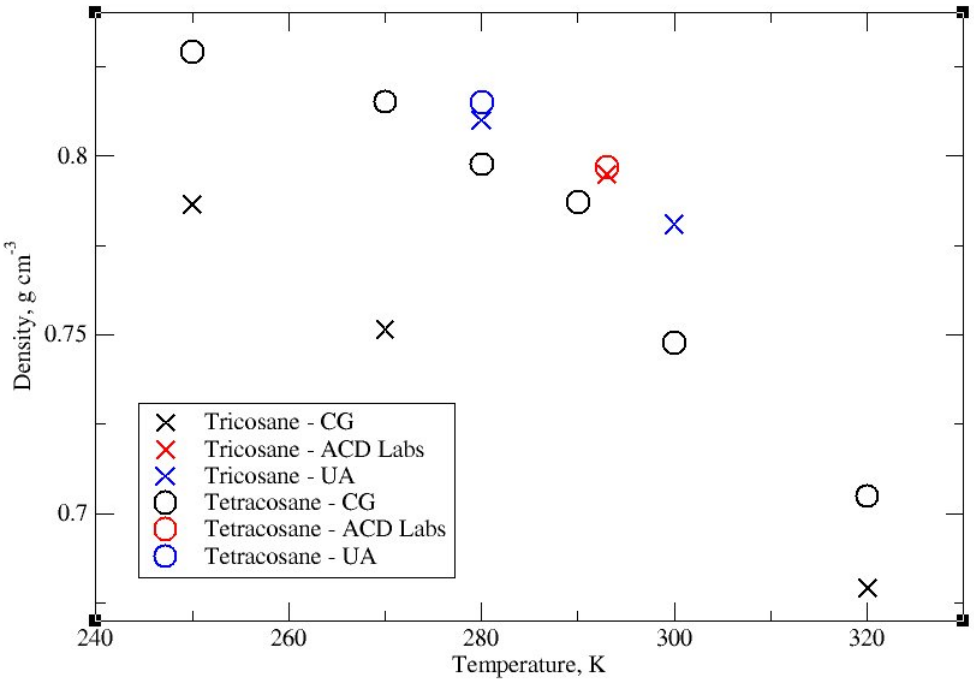

Figure 7.41: *Density of tricosane from coarse grained simulations (black crosses), from united atom simulations (blue crosses) and by ACD Labs [45] compared with the same set of densities of tetracosane (circles)*

7.12 Tertiary alkane system

A tertiary alkane system of 1000 tetracosane, 1000 tricosane and 4000 dodecane molecules was mixed at 320 K and then cooled stepwise, parameters are given in Table 7.14. It was noted that for this system to preserve the temperature, united atom and coarse grained groups have to be coupled to the thermal bath separately. Additionally, it was found to be necessary to start the simulation with a 2 fs timestep. Only after system equilibration the timestep can be increased to 4 fs. This is due to the two different sized beads used in the model.

Table 7.14: *Parameters for coarse grained calculation of tertiary mixture of tetracosane, tricosane and dodecane over the range of temperatures*

Calculation parameters:	
System size	1000 tetracosane 1000 tricosane 4000 dodecane
Step size	4 fs
Length of calculation	4 ns 8 ns + 30 ns + 8 ns
Integration	Leap frog
Periodic boundary	xyz
Ensemble	*NPT*
Temperature	320 K 280 K, 260 K, 250 K
Thermostat	Velocity rescale
Pressure	1 bar
Barostat	Berendsen
Compressibility	9×10^{-5} bar^{-1}

Similarly to the binary system of dodecane and tetracosane (Section 7.9) a steady increase in density upon cooling is observed. The overall density at 280 K is 0.753 g/cm^3, 0.758 g/cm^3 at 260 K and 0.753 g/cm^3 at 250 K. The analysis of partial density, Figure 7.42, shows a uniform distribution of components at 280 K. With a decrease of temperature towards 250 K, tetracosane separates and forms crystal domains. Tricosane stays evenly dispersed through the system, when at close distance to tetracosane it co-crystallises. By such tetracosane provides the initial crystal, that then acts as a nucleation centre. The binary crystal formed in the solvent is shown in Figure 7.44.

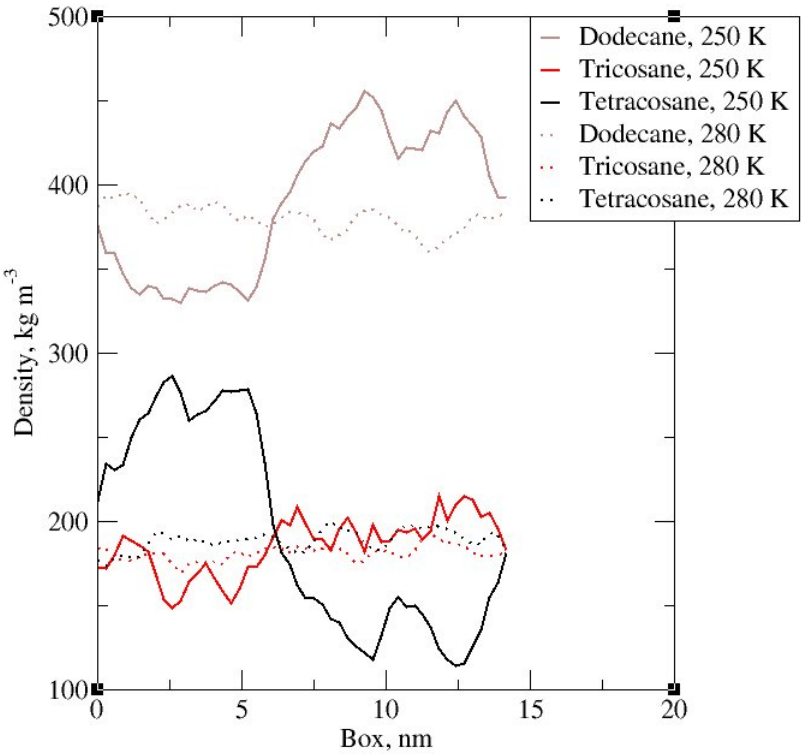

Figure 7.42: *Change of partial density in a tertiary mixture of dodecane (grey), tricosane (red) and tetracosane (black) at 280 K (dashed line) and 260 K (solid line)*

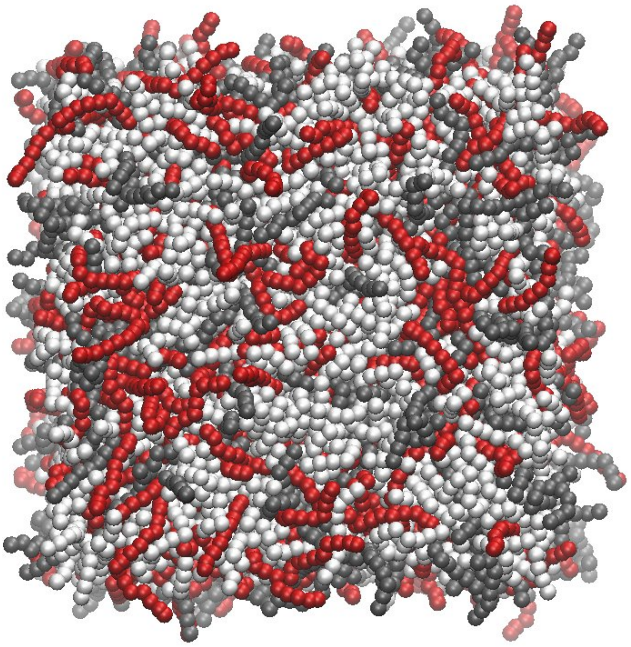

Figure 7.43: *Snapshot of tertiary system at 280 K. Dodecane is shown in white, tricosane in red and tetracosane in grey*

A vector orientation analysis was performed on the system at 250 K, Figure 7.45. The tetracosane molecules align well, leading to sharp peaks. This is comparable to the behaviour of tetracosane in the binary mixture at the same temperature, Figure 7.34 (b). Tricosane molecules are also aligned, but show a little less order than tetracosane (shorter and broader peaks). Both long chain alkanes have the same orientation, indicative of either co-crystallisation or tetracosane molecules acting as a nucleation centre. Dodecane shows only a slight order with alignment parallel to longer molecules. At 250 K dodecane molecules start to form crystals. Due to the observed co-alignment of dodecane molecules with longer paraffins, the latter are likely to act as a nucleation centre.

The model describes well the tertiary alkane mixture: it allows co-crystallisation of longer alkanes from melt, while solvent alkanes are removed from the crystal. Tricosane is shown to be less ordered in the forming crystal, likely as a result of a lower density and hence crystallisation temperature. Both co-crystallisation of similar length paraffins and separation of the solvent have been observed experimentally [52, 53]. The latter was not possible to observe with higher resolution calculations (Chapter 4)

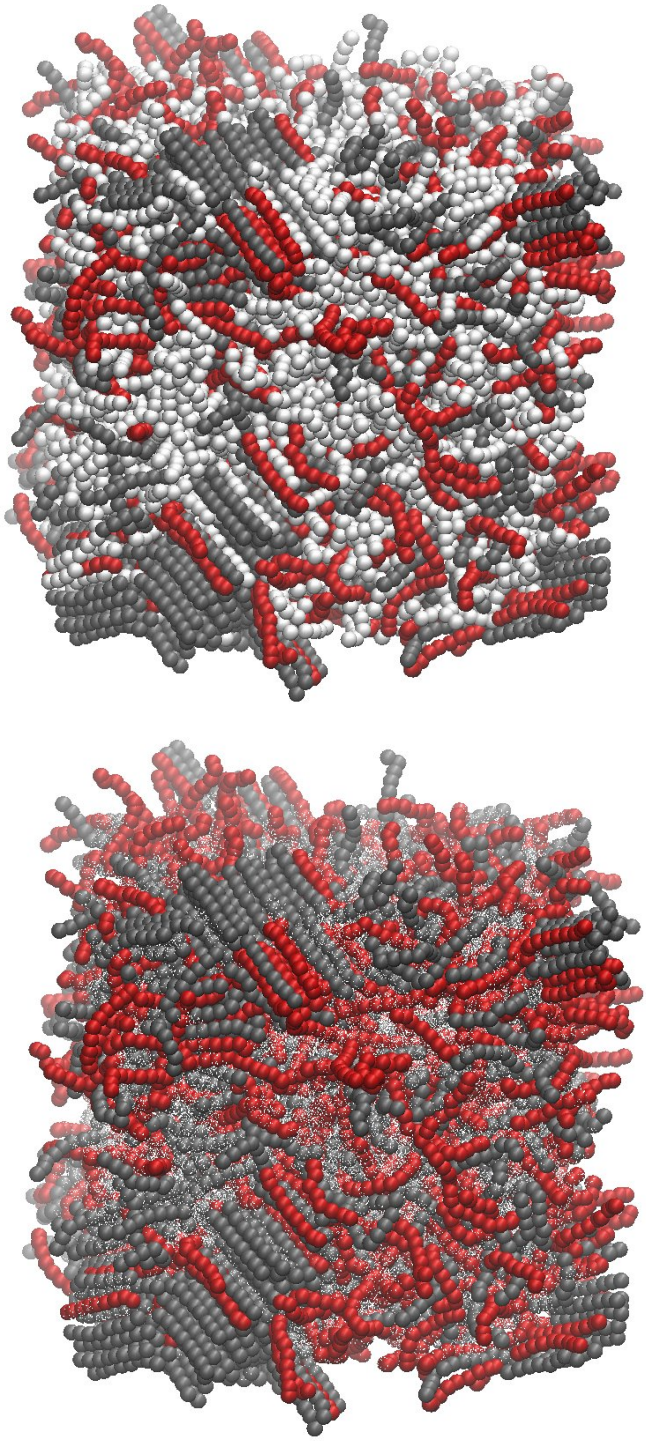

Figure 7.44: *Snapshot of tertiary system at 250 K. Dodecane is shown as white beads on the top figure and represented by white dots for easier visualisation of the crystallisation of tricosane (red) and tetracosane (grey)*

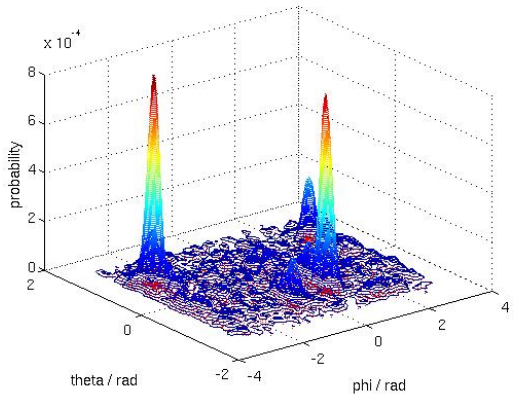

(a) Tetracosane at 250 K

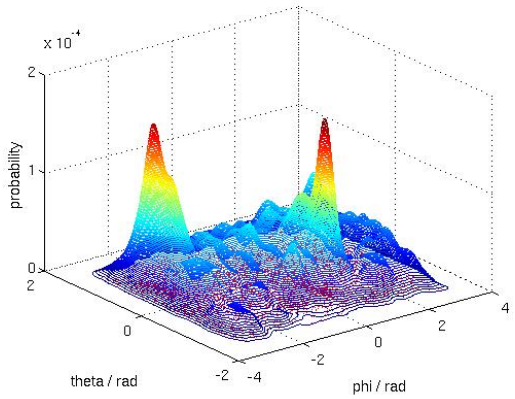

(b) Tricosane at 250 K

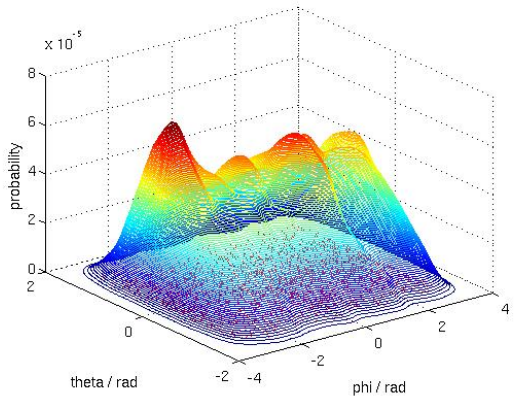

(c) Dodecane at 250 K

Figure 7.45: *Vectorial distribution in the tertiary mixture of tetracosane (a), tricosane (b) and dodecane (c) at 250 K*

due to the time and size restrictions in atomistic studies.

The choice of united atom beads to represent the end groups was done with the assumption that the non bonded interaction between terminal atoms is well parameterised and readily available. It was found that even though the interaction is well represented, the derivation of a non bonded potential between coarse grained and united atom beads still requires extensive fitting. Most importantly, it can force a smaller time step.

In the future it would be interesting to use a four-site bead $4CG$ to extend the range of parameters for hydrocarbons. This choice could potentially avoid the mismatch experienced between united atom and coarse grained beads observed in this work. Moreover, choosing a four-site coarse grained bead would prevent a timestep reduction.

When modelling linear alkanes it is important to preserve its symmetry of their corse grained representation. Hence, for alkanes that are $n(3CG)+2C$, the $4CG$ can become terminal beads. For alkanes that are $n(3CG)+1C$, the $4CG$ should be the central one. It is likely that the potential describing interactions between terminal $4CG$ and $3CG$ will differ significantly from the ones between central $4CG$ and $3CG$. Consequently, a coarse grained force field capable of describing well interactions for a wide range of hydrocarbons will need a large range of parameters.

7.13 Conclusions

In this chapter the development of a coarse grained model of linear alkanes from atomistic calculations has been performed. The model was fitted to reproduce the crystallisation process and matched to both thermodynamic and structural properties. Both molecular size and temperature transferability were shown over a 120 K range. A mixture of *n*-akanes exhibited crystallisation with a similar behaviour to that observed experimentally: the separation between different lengths of alkanes and co-crystallisation of similar ones. The model reproduces well the trend of density,

angle, bond and radial distributions over a range of temperatures.

The model was extended by introducing a terminal united atom bead. The parameterisation of two very different beads (three times the size) was difficult, though provided acceptable results. The use of different size beads caused some inconveniences in setting up the simulations and a major drawback was the reduction of the timestep.

The developed coarse grained force field is the first of its type to be able to simulate well the crystallisation process from the melt, while preserving thermodynamic and structural properties. This coarse grained force field constitutes the base for further developments aimed at molecules participating in the crystallisation of alkanes, such as diesel additives and solvents.

Bibliography

[1] Intel. Excerpts from a conversation with gordon moore: Moore's law. (Last checked 2011-10-10).

[2] S.J. Marrink, A.H. de Vries, and A.E. Mark. Coarse grained model for semiquantitative lipid simulations. *The Journal of Physical Chemistry B*, 108(2):750–760, 2004.

[3] S.J. Marrink, H.J. Risselada, S. Yefimov, D.P. Tieleman, and A.H. De Vries. The MARTINI force field: coarse grained model for biomolecular simulations. *The Journal of Physical Chemistry B*, 111(27):7812–7824, 2007.

[4] L. Monticelli, S.K. Kandasamy, X. Periole, R.G. Larson, D.P. Tieleman, and S.J. Marrink. The martini coarse-grained force field: extension to proteins. *Journal of Chemical Theory and Computation*, 4(5):819–834, 2008.

[5] C.A. López, A.J. Rzepiela, A.H. de Vries, L. Dijkhuizen, P.H. Hünenberger, and S.J. Marrink. Martini coarse-grained force field: extension to carbohydrates. *Journal of Chemical Theory and Computation*, 5(12):3195–3210, 2009.

[6] M. Winger, D. Trzesniak, R. Baron, and W.F. Van Gunsteren. On using a too large integration time step in molecular dynamics simulations of coarse-grained molecular models. *Physical Chemistry Chemical Physics*, pages 1934–1941, 2009.

[7] W. F. van Gunsteren and M. Winger. Reply to the 'Comment on "On using a too large integration time step in molecular dynamics simulations of coarse-grained molecular models"' by S. J. Marrink, X. Periole, D. Peter Tieleman and Alex H. de Vries, Phys. Chem. Chem. Phys., 2010, 12, DOI: 10.1039/b915293h. *Physical Chemistry Chemical Physics*, 12:2257–2258, 2010.

[8] S.O. Yesylevskyy, L.V. Schäfer, D. Sengupta, and S.J. Marrink. Polarizable water model for the coarse-grained MARTINI force field. *PLoS computational biology*, 6(6):e1000810, 2010.

[9] L. Darré, M.R. Machado, P.D. Dans, F.E. Herrera, and S. Pantano. Another coarse grain model for aqueous solvation: WAT FOUR? *Journal of Chemical Theory and Computation*, 6(12):3793–3807, 2010.

[10] A.J. Rader. Coarse-grained models: getting more with less. *Current Opinion in Pharmacology*, 10(6):753 – 759, 2010.

[11] S. Riniker and W.F. van Gunsteren. A simple, efficient polarizable coarse-grained water model for molecular dynamics simulations. *The Journal of Chemical Physics*, 134:084110, 2011.

[12] F. Müller-Plathe. Coarse-graining in polymer simulation: From the atomistic to the mesoscopic scale and back. *ChemPhysChem*, 3(9):754–769, 2002.

[13] W. Tschöp, K. Kremer, J. Batoulis, T. Bürger, and O. Hahn. Simulation of polymer melts. I. Coarse-graining procedure for polycarbonates. *Acta polymerica*, 49(2-3):61–74, 1998.

[14] R.L.C. Akkermans and WJ Briels. A structure-based coarse-grained model for polymer melts. *The Journal of Chemical Physics*, 114:1020, 2001.

[15] J. Fischer, D. Paschek, A. Geiger, and G. Sadowski. Modeling of aqueous poly (oxyethylene) solutions. 2. Mesoscale simulations. *The Journal of Physical Chemistry B*, 112(43):13561–13571, 2008.

[16] W. Shinoda, R. DeVane, and M.L. Klein. Coarse-grained molecular modeling of non-ionic surfactant self-assembly. *Soft Matter*, 4(12):2454–2462, 2008.

[17] S.O. Nielsen, C.F. Lopez, G. Srinivas, and M.L. Klein. A coarse grain model for n-alkanes parameterized from surface tension data. *The Journal of Chemical Physics*, 119:7043, 2003.

[18] S.-W. Chiu, H. L. Scott, and E. Jakobsson. A coarse-grained model based on Morse potential for water and n-alkanes. *Biophysical Journal*, 6(3):851–863, 2010.

[19] S.-W. Chiu and E. Jakobsson. A modified Morse potential for coarse grained water-alkane interaction. *Biophysical Journal*, 100:158, February 2011.

[20] M.G. Martin and J.I. Siepmann. Transferable potentials for phase equilibria. 1. United-atom description of n-alkanes. *The Journal of Physical Chemistry B*, 102(14):2569–2577, 1998.

[21] M.G. Martin and J.I. Siepmann. Novel configurational-bias Monte Carlo method for branched molecules. Transferable potentials for phase equilibria. 2. United-atom description of branched alkanes. *The Journal of Physical Chemistry B*, 103(21):4508–4517, 1999.

[22] C.D. Wick, M.G. Martin, and J.I. Siepmann. Transferable potentials for phase equilibria. 4. united-atom description of linear and branched alkenes and alkylbenzenes. *The Journal of Physical Chemistry B*, 104(33):8008–8016, 2000.

[23] B. Chen, J.J. Potoff, and J.I. Siepmann. Monte Carlo calculations for alcohols and their mixtures with alkanes. Transferable potentials for phase equilibria. 5. United-atom description of primary, secondary, and tertiary alcohols. *The Journal of Physical Chemistry B*, 105(15):3093–3104, 2001.

[24] J.M. Stubbs, J.J. Potoff, and J.I. Siepmann. Transferable potentials for phase equilibria. 6. united-atom description for ethers, glycols, ketones, and aldehydes. *The Journal of Physical Chemistry B*, 108(45):17596–17605, 2004.

[25] C.D. Wick, J.M. Stubbs, N. Rai, and J.I. Siepmann. Transferable potentials for phase equilibria. 7. primary, secondary, and tertiary amines, nitroalkanes and nitrobenzene, nitriles, amides, pyridine, and pyrimidine. *The Journal of Physical Chemistry B*, 109(40):18974–18982, 2005.

[26] K.A. Maerzke and J.I. Siepmann. Transferable potentials for phase equilibria-coarse-grain description for linear alkanes. *The Journal of Physical Chemistry B*, 2011.

[27] P. Carbone, H.A.K. Varzaneh, X. Chen, and F. Müller-Plathe. Transferability of coarse-grained force fields: The polymer case. *The Journal of Chemical Physics*, 128:064904, 2008.

[28] V.A. Harmandaris, D. Reith, N.F.A. van der Vegt, and K. Kremer. Comparison between coarse-graining models for polymer systems: Two mapping schemes for polystyrene. *Macromolecular chemistry and physics*, 208(19/20):2109, 2007.

[29] F. Ercolessi and J.B. Adams. Interatomic potentials from first-principles calculations: the force-matching method. *EPL (Europhysics Letters)*, 26:583, 1994.

[30] S. Izvekov and G.A. Voth. A multiscale coarse-graining method for biomolecular systems. *The Journal of Physical Chemistry B*, 109(7):2469–2473, 2005.

[31] S. Izvekov and G.A. Voth. Multiscale coarse graining of liquid-state systems. *The Journal of Chemical Physics*, 123:134105, 2005.

[32] D. Reith, M. Pütz, and F. Müller-Plathe. Deriving effective mesoscale potentials from atomistic simulations. *Journal of Computational Chemistry*, 24(13):1624–1636, 2003.

[33] A.P. Lyubartsev and A. Laaksonen. Calculation of effective interaction potentials from radial distribution functions: A reverse Monte Carlo approach. *Physical Review E*, 52(4):3730, 1995.

[34] C.D. Berweger, W.F. van Gunsteren, and F. Müller-Plathe. Force field parametrization by weak coupling. Re-engineering SPC water. *Chemical physics letters*, 232(5-6):429–436, 1995.

[35] A.J. Rzepiela, M. Louhivuori, C. Peter, and S.J. Marrink. Hybrid simulations: combining atomistic and coarse-grained force fields using virtual sites. *Physical Chemistry Chemical Physics*, 13(22):10437–10448, 2011.

[36] S. Jain, S. Garde, and S.K. Kumar. Do inverse Monte Carlo algorithms yield thermodynamically consistent interaction potentials? *Industrial & Engineering Chemistry Research*, 45(16):5614–5618, 2006.

[37] B. Hess, C. Kutzner, D. Van Der Spoel, and E. Lindahl. GROMACS 4: Algorithms for highly efficient, load-balanced, and scalable molecular simulation. *Journal of Chemical Theory and Computation*, 4(3):435–447, 2008.

[38] V. Rühle, C. Junghans, A. Lukyanov, K. Kremer, and D Andrienko. Versatile object-oriented toolkit for coarse-graining applications. *Journal of Chemical Theory and Computation*, 5(12):3211–3223, 2009.

[39] H.J. Qian, P. Carbone, X. Chen, H.A. Karimi-Varzaneh, C.C. Liew, and F. Muller-Plathe. Temperature-transferable coarse-grained potentials for ethylbenzene, polystyrene, and their mixtures. *Macromolecules*, 41(24):9919–9929, 2008.

[40] H. Wang, C. Junghans, and K. Kremer. Comparative atomistic and coarse-grained study of water: What do we lose by coarse-graining? *The European Physical Journal E: Soft Matter and Biological Physics*, 28(2):221–229, 2009.

[41] A. N. Vinogradov. Acoustic properties of dodecane-oleic acid system. *Vestnik Moskovskogo Universiteta, Seriya 2: Khimiya*, 45(5):305–308, 2004.

[42] B.J. Mair and A.J. Streiff. Separation of the aromatic hydrocarbons and the isolation of dodecane, naphthalene, 1-methylnaphthalene and 2-methylnaphthalene from the kerosene fraction of petroleum. *Journal of Research of the National Bureau of Standards*, 24:395–414, 1940.

[43] J. Troncoso, J.L. Valencia, M. Souto-Caride, D. Gonzalez-Salgado, and J. Peleteiro. Thermodynamic properties of dodecane+ 1-butanol and+ 2-butanol systems. *Journal of Chemical & Engineering Data*, 49(6):1789–1793, 2004.

[44] S. Wawzonek, P.D. Klimstra, and R.E. Kallio. Preparation of long chain alkyl hydroperoxides. *The Journal of Organic Chemistry*, 25(4):621–623, 1960.

[45] Calculated using Advanced Chemistry Development (ACD/Labs) Software V11.02, 1994–2012.

[46] J. E. Jones. On the determination of molecular fields. I. From the variation of the viscosity of a gas with temperature. *Proceedings of the Royal Society of London. Series A*, 106(738):441–462, 1924.

[47] Gustav Mie. Zur kinetischen Theorie der einatomigen Körper. *Annalen der Physik*, 316(8):657–697, 1903.

[48] A. Ahmed and R.J. Sadus. Solid-liquid equilibria and triple points of n-6 Lennard-Jones fluids. *The Journal of Chemical Physics*, 131(17):174504, 2009.

[49] A. Warshel and S. Lifson. Consistent force field calculations. II. Crystal structures, sublimation energies, molecular and lattice vibrations, molecular conformations, and enthalpies of alkanes. *The Journal of Chemical Physics*, 53:582, 1970.

[50] D.N.J. White. A computationally efficient alternative to the buckingham potential for molecular mechanics calculations. *Journal of Computer-Aided Molecular Design*, 11:517–521, 1997. 10.1023/A:1007911511862.

[51] Farid F. Abraham and Y. Singh. The structure of a hard-sphere fluid in contact with a soft repulsive wall. *The Journal of Chemical Physics*, 67(5):2384–2385, 1977.

[52] E. Sloutskin, E. B. Sirota, H. Kraack, B. M. Ocko, and M. Deutsch. Surface freezing in *n*-alkane solutions: The relation to bulk phases. *Physical Review E*, 64:031708, Aug 2001.

[53] I. Denicolo, A. F. Craievich, and J. Doucet. X-ray diffraction and calorimetric phase study of a binary paraffin: $C_{23}H_{48}$–$C_{24}H_{50}$. *The Journal of Chemical Physics*, 80(12):6200–6203, 1984.

Part IV Conclusions of this work

8 Conclusions and further work

This thesis describes a computational investigation into the crystallisation of diesel fuel and the effect that diesel additives have on crystallisation.

After an introduction to the problems under consideration, the first set of results discusses the development of a model for diesel fuel and a strategy for investigating its crystallisation. It was found that successful crystallisation can be seen in pure *n*-tricosane ($C_{23}H_{48}$) by employing a stepwise cooling procedure, where the system is allowed to re-equilibrate after each temperature drop. The time necessary for re-equilibration was found to be strongly temperature dependant, requiring long simulation times of over 20 ns for temperatures close to the crystallisation temperature.

It was found to be possible to produce well-formed crystals within the simulation, with the unit cell dimensions, *a* and *b*, in a reasonably good agreement with experiment. However, it was shown that it was difficult to approach the crystallisation temperature slowly enough to produce defect-free crystals, and to obtain a good measurement for the *c* axis. Moreover, the presence of periodic boundary conditions in the system, led to a tilting of individual lamellae so that they were no longer parallel to the crystallographic *c* axis, as the periodic boundary conditions were not commensurate with an integer number of unit cells.

Computer time is continuing to increase at a rapid rate, with the introduction of better parallel algorithms and the exploitation of new architectures (such as GPUs.) It would therefore be interesting to repeat these studies in the future with (potentially) much

larger systems and potentially longer simulation times.

Homogeneous crystallisation was also observed from binary and tertiary mixtures of paraffins of similar chain lengths. These systems were found to co-crystallise in to hexagonally arranged lamellae. The presence of different length alkanes was found to create *gauche* disorder, leading to the formation of lamellar layers with softer edges.

The presence of a nucleation centre in the system was also found to provide a faster, more efficient crystallisation (heterogeneous nucleation) and also reducing the effects of supercooling. In our simulations, the nucleation centre is a positionally restrained crystal, formed from the same molecules as the surrounding melt.

Crystallisation of paraffin from four solvents commonly present in the diesel fuel, was also studied. This allowed us to establish the behavioural trends by solvent type. Aromatic solvents were found to separate from the growing crystal, leading to higher structured crystals. Aliphatic solvents have similar interactions to paraffin waxes, displaying therefore lower expulsion rates. As a consequence, aliphatic solvents co-crystallised with paraffin waxes.

A number of additives are used in diesel fuels. In this thesis we focused on four common wax crystal modifiers: ethylene vinyl acetate (EVA), polymethilmethacrylate (PMA), polyalphaolefin (PAO) and alkylphenol formaldehyde condensate (APFC). Even though distinct mechanisms were observed, a common mode of action could be identified. All additives contained a linear aliphatic segment that co-crystallised with the paraffins. The additive then created additive-specific distortions to the alignment of forming crystal domains. Interestingly, it was observed that for the additive to be effective, the linear aliphatic segment must be approximately two times shorter than the targeted *n*-alkanes.

In EVA, the polymer backbone was found to co-crystallise with alkanes, while side chains created turns, distorting the arrangement of the lamellar stacks. The presence of vinyl acetate side groups further increases the potency of this additive.

PMA and PAO are comb-type additives having side chains of similar length. The side-chains incorporate into the growing crystal in the same manner as backbone of EVA. Their crystal distorting action arises from the conformation of the backbone. PAO has ethylene vinyl groups linking the side chains to the backbone. All of the side chains are of the same length and extend at the low temperatures. Depending on the tacticity, the backbone of PAO will either fully extend (in the atactic polymer) or remain curled ((in the isotactic polymer). In PMA, in addition to longer side chains, there is also a small number of short ones. These introduce kinks in the backbone, that are preserved even at low temperatures.

APFC side chains are commensurate to PMA and PAO ones. The major difference is presented by the molecule's core, constituted by six phenol rings. The core strongly interacts with itself through hydrogen bonding forming a plate or a crescent structure. While side chains can extend, co-crystallising with paraffin, the core does not rearrange and therefore is able to create imperfections in the structure of the surrounding crystal.

All of the additives in this study have a common structural feature: linear aliphatic chain of approximately half of the length of the crystallising paraffin. It would be interesting to observe how crystallisation is affected by changing the length of this aliphatic segment. The wax modifying action is achieved via structural deformations created by short side chains, or acetate groups, or both. Future work could involve a systematic study on the effects of a variation in proportions of side chains and acetate groups. Additional investigations into the use of other charged groups could be carried out using the methodologies introduced in this thesis.

A blend of numerous additives is frequently used in diesel fuels, as it leads to a more effective crystal modification. This suggests that additives could interact with each other. So far these interactions have not been studied in neither this work nor in any previously published works and so should provide an interesting area for further investigation.

All the performed atomistic simulations were subject to two common limitations: a

small system size and a short timescale. Additionally, due to the nature of this study, systems were cooled to crystallisation, but the temperature change was extremely rapid in comparison to a real experiment. To be able to increase the system size and simulation timescales we have developed a corse grained model of linear alkanes.

The coarse grained model was fitted to reproduce the crystallisation process of a variety of linear alkanes. Remarkably, our model is the first of its kind to have shown transferability over 120 K range, while preserving thermodynamic and structural properties of both melt and crystal.

The coarse grained model was then used to simulate crystallisation of *n*-alkane mixtures. Unlike atomistic simulations, coarse grained ones allowed us to observe the separation between different lengths of alkanes, and co-crystallisation of similar ones. This result matches the experimental observations. Our coarse grained models therefore allowed for the efficient simulation of systems that go beyond the size and timescale limitations of atomistic simulations.

The new coarse grained force field produced here forms the basis for further development of molecules participating in the crystallisation of alkanes, such as diesel additives and solvents.